

Classical and Quantum Field Theory of Bose-Einstein Condensates

Sebastian Wüster

January 2007

A thesis submitted for the degree of Doctor of Philosophy
at the Australian National University



Declaration

This thesis is an account of research undertaken between September 2003 and January 2007 at the Department of Physics, Faculty of Science, The Australian National University, Canberra, Australia. I also was affiliated with ACQAO, the Australian Research Council Centre of Excellence for Quantum-Atom Optics. Except where otherwise stated, I present my original results, obtained under the supervision of Dr. Craig M. Savage.

I worked jointly with Beata J. Dąbrowska-Wüster on the truncated Wigner simulations of collapsing condensates and quantum effects in the localisation of matter-waves in optical lattices. The latter project is not included in this thesis. The code for the truncated Wigner simulations of collapsing BECs was written by P. B. Blakie and M. J. Davis. We adapted it to allow dynamical noise terms.

Much of the results regarding Skyrmion stability benefited greatly from work done by T. E. Argue for his honours thesis, which I verified and extended.

Sebastian Wüster
August 1, 2007

For my bright star, Beatka.

Acknowledgements

A PhD spans about twenty-two-thousand waking hours, which is never enough for all the interesting physics to be looked into, but a rather longish time in many other respects. Many people have contributed to make mine enjoyable and productive. First and foremost, I thank Craig Savage for being a fantastic supervisor. The ingenious balance of reassurance, guidance and freedom that he provided, made my PhD such a rewarding adventure. Also the exciting selection of topics that I was allowed to dig into contributed to this. Many thanks go to Joe Hope, who complemented Craig to complete a truly great supervisory team, and particularly brought me up to speed in the struggle against the machine right from the start. During the two trips to Brisbane, Matthew Davis and Ashton Bradley splendidly filled the role of supervisor and co-worker simultaneously and were continuously helpful also beyond the two designated cooperation projects. Elena Ostrovskaya helped me significantly during my first experience with referees of PRL.

I wish to thank John Close and Nick Robins for much insight regarding the real world of BEC experiments, and Christina Figl for her notes on the Landé factor. Piyush Jain shared some important experience regarding condensate de-Laval nozzles, and Andrew Truscott, Dragomir Neshev and Wiesław Królikowski some of their knowledge about optical vortices. All members of the Department of Physics, the Nonlinear Physics Centre and ACQAO have provided a fun and comfortable working environment, and I particularly thank Hans Bachor and Ruth Wilson for creating such a stimulating workplace as our centre. While we stayed in Brisbane, the UQ Quantum-Atom-Optics theory group showed their warm hospitality.

Special thanks go to Robert Fischer, for tales about his work on optical vortices, which gave me the idea for the optical tunnel while we were having a pint of Guinness. More importantly, he read a poem at my wedding. For that, I also thank Ania and Stephen Beacom, who further helped me by proof-reading

some chapters of this thesis.

Several physicists whom I never met in person gave me useful assistance by e-mail: I would like to thank Rembert Duine for an email discussion regarding quantum evaporation and the HFB, Murray Holland for providing HFB code for the purpose of comparison, Stéphane Métens for explanations of his work, Boudeijn Verhaar for information regarding scattering lengths and Hanns-Christoph Nägerl for directions regarding cesium parameters.

Much of the practical work in this thesis would have been much more difficult without the crew at the ANU supercomputer facility and the UQ ACQAO cluster. I particularly would like to thank Margaret Kahn, David Singleton and Ian Mortimer for their patience.

All stages of life are connected, and I am in deep debt to my parents, Rosemarie and Christian Wüster for bringing me up the way they did and always encouraging my natural curiosity. Along the way in high school, Ullrich Braselmann and Karl-Heinrich Meyberg probably played a role in guiding me to where I am now, by means of their inspired way of teaching physics and mathematics respectively.

Finally and most deeply I am grateful to my wonderful wife Beatka. Thank you for countless hours of discussions about physics, many interesting ideas, the initiation of the collaboration projects and proof-reading of this thesis. But more importantly, thank you for dragging me to Australia, making my life funny and exciting, pushing me to my limits and providing me with a safehaven, support and love. You are the bright shining star, which guides me through my life.

Abstract

We study the application of Bose-Einstein condensates (BECs) to simulations of phenomena across a number of disciplines in physics, using theoretical and computational methods.

Collapsing condensates as created by E. Donley *et al.* [Nature **415**, 39 (2002)] exhibit potentially useful parallels to an inflationary universe. To enable the exploitation of this analogy, we check if current quantum field theories describe collapsing condensates quantitatively, by targeting the discrepancy between experimental and theoretical values for the time to collapse. To this end, we couple the lowest order quantum field correlation functions to the condensate wavefunction, and solve the resulting Hartree-Fock-Bogoliubov equations numerically. Complementarily, we perform stochastic truncated Wigner simulations of the collapse. Both methods also allow us to study finite temperature effects.

We find with neither method that quantum corrections lead to a faster collapse than is predicted by Gross-Pitaevskii theory. We conclude that the discrepancy between the experimental and theoretical values of the collapse time cannot be explained by Gaussian quantum fluctuations or finite temperature effects. Further studies are thus required before the full analogue cosmology potential of collapsing condensates can be utilised.

As the next project, we find experimental parameter regimes in which stable three-dimensional Skyrmions can exist in a condensate. We show that their stability in a harmonic trap depends critically on scattering lengths, atom numbers, trap rotation and trap anisotropy. In particular, for the ^{87}Rb $|F = 1, m_f = -1\rangle$, $|F = 2, m_f = 1\rangle$ hyperfine states, stability is sensitive to the scattering lengths at the 2% level. We find stable Skyrmions with slightly more than 2×10^6 atoms, which can be stabilised against drifting out of the trap by laser pinning.

As a stepping stone towards Skyrmions, we propose a method for the stabilisation of a stack of parallel vortex rings in a Bose-Einstein condensate. The method makes use of a “hollow” laser beam containing an optical vortex, which

realises an optical tunnel for the condensate. Using realistic experimental parameters, we demonstrate numerically that our method can stabilise up to 9 vortex rings.

Finally, we focus on analogue gravity, further exploiting the analogy between flowing condensates and general relativistic curved space time. We compare several realistic setups, investigating their suitability for the observation of analogue Hawking radiation. We link our proposal of stable ring flows to analogue gravity, by studying supersonic flows in the optical tunnel. We show that long-living immobile condensate solitons generated in the tunnel exhibit sonic horizons, and discuss whether these could be employed to study extreme cases in analogue gravity.

Beyond these, our survey indicates that for conventional analogue Hawking radiation, simple outflow from a condensate reservoir, in effectively one dimension, has the best properties. We show with three dimensional simulations that stable sonic horizons exist under realistic conditions. However, we highlight that three-body losses impose limitations on the achievable analogue Hawking temperatures. These limitations vary between the atomic species and favour light atoms.

Our results indicate that Bose-Einstein condensates will soon be useful for interdisciplinary studies by analogy, but also show that the experiments will be challenging.

Notation and Terminology

Notation

This summary gives an overview of the used symbols. They are grouped alphabetically, first Latin and then Greek.

| | |
|--------------------------|---|
| \sim | Signals dimensionless quantities. |
| a_0 | Bohr radius, $a_0 = 5.29177 \times 10^{-11}$ m. |
| a_{collapse} | Negative scattering length during collapse. |
| a_{ij} | New values of ^{87}Rb multi-component scattering lengths. |
| \bar{a}_{ij} | Old values of ^{87}Rb multi-component scattering lengths. |
| a_{init} | Initial scattering length. |
| a_s | Atomic s-wave scattering length. |
| c | Single-component condensate speed of sound. |
| c_+, c_- | Multi-component condensate speeds of sound. |
| E_{cut} | Energy cutoff. |
| $d\xi$ | Dynamical noise term in the TWA due to three-body losses. |
| D | Rapidity parameter for the horizon. Within $\Delta x = D\xi$ the Mach number is allowed to vary by ~ 1 . |
| g | Physical atom-molecule coupling. |
| g_0 | Bare atom-molecule coupling. |
| G_A | Anomalous correlations, $G_A(x, x') = \langle \chi(x')\chi(x) \rangle$. |
| \bar{G}_A | Pairing field, $\bar{G}_A(x) = G_A(x, x)$. |
| G_N | Normal correlations, $G_N(x, x') = \langle \chi^\dagger(x')\chi(x) \rangle$. |
| \bar{G}_N | Density of uncondensed atoms, $\bar{G}_N(x) = G_N(x, x)$. |
| $\tilde{G}_{N/A}(r, r')$ | Rescaled correlation functions, $G_{N/A}(r, r') = \tilde{G}_N(r, r')/r/r'$. |
| \hbar | Planck's constant, $\hbar = 1.05457 \times 10^{-34}$ Js. |
| \hat{H} | Many-body Hamiltonian. |
| $\hat{H}_0(\mathbf{x})$ | Single-particle Hamiltonian. |

| | |
|-----------------------|---|
| J | Atom flux. |
| k_B | Boltzmann's constant, $k_B = 1.38066 \times 10^{-23}$ J/K. |
| K | Momentum cutoff. |
| K_1, K_2, K_3 | One, two and three-body loss coefficient. |
| $\hat{\mathbf{L}}$ | Angular momentum operator. |
| m | Atomic mass. |
| M | Single component condensate Mach number $M = v/c$. |
| n, n_{cond} | Condensate density. |
| n_{peak} | Density peak value. |
| n_{unc} | Density of uncondensed atoms. |
| \hat{n}_1 | Density fluctuation operator. |
| N_1, N_2 | Condensate atom number in components one and two. |
| N_{cond} | Condensate atom number. |
| N_{init} | Initial condensate atom number. |
| N_r | Fraction of atoms in component 2, $N_r = N_2/N_{\text{tot}}$. |
| N_{remn} | Remnant atom number. |
| N_{tot} | Total atom number. In chapter 3: $N_{\text{tot}} = N_{\text{cond}} + N_{\text{unc}}$. In chapter 4: $N_{\text{tot}} = N_1 + N_2$. |
| N_{unc} | Number of uncondensed atoms. |
| $O(x)$ | Shape of outcoupling region. |
| t_{collapse} | Collapse time. Time after initiation of collapse until which only small atom loss occurs. |
| T_H | Analogue Hawking temperature. |
| U | Physical interaction strength. To be distinguished from the bare interaction strength U_0 when quantum effects are present. |
| U_0 | Interaction strength in the GPE and HFB equations. For quantum theory this is the bare coupling, to be distinguished from the physical coupling U . For semi-classical theory there is no distinction and we write U_0 or U . |
| U_{bg} | Background scattering length of atom-molecule resonance theory. This is the physical scattering strength far away from the resonance. Near the resonance this value is modified to $U(B)$, B is the magnetic field. |
| U_{ij} | Multi-component interaction strengths, $U_{ij} = \frac{4\pi\hbar^2 a_{ij}}{m}$. |
| v | Single component condensate speed $v = \mathbf{v} $. |
| \mathbf{v} | Single component condensate velocity. |
| V | External potential for the condensate. |
| V_0 | In chapter 4: Amplitude of laser pinning potential. In chapter 5: Amplitude of exit nozzle potential. |

| | |
|--|--|
| $V_{h,i}$ | Amplitude of hump potentials. |
| V_t, V_v | Trap potential and optical vortex potential for atom-light skyrmions. |
| w_0 | Assorted focal widths of laser beams used for optical manipulation. |
| w_i | Widths of hump potentials. |
| W | In chapter 4: Skyrmion winding number. In chapter 5: height of the hump potential. |
| Greek alphabet | $\alpha, \beta, \gamma, \Gamma, \delta, \Delta, \epsilon, \zeta, \eta, \theta, \Theta, \iota, \kappa, \lambda, \Lambda, \mu, \nu, \xi, \Xi, o, \pi, \Pi, \rho, \sigma, \Sigma, \tau, v, \phi, \Phi, \chi, \psi, \Psi, \omega, \Omega.$ |
| α | Constant related to the momentum cutoff. |
| $\alpha_i, \alpha(\mathbf{x})$ | Stochastic wave function. |
| γ | Outcoupling strength. |
| η | In chapter 3: Initial state quantum noise. In chapter 5: Trap anisotropy $\eta = \omega_x/\omega_\perp$. |
| ϑ | Condensate phase. |
| $\hat{\theta}$ | Phase fluctuation operator. |
| λ | Assorted wavelengths of laser beams used for optical manipulation. |
| μ | Chemical potential. |
| ν | Physical molecular field detuning. |
| ν_0 | Bare molecular field detuning. |
| τ_{evolve} | Evolution time. Time after initiation of collapse that the BEC is left to evolve freely before the atom number is measured. |
| $\phi(\mathbf{x})$ | Condensate wavefunction. |
| $\phi_a(\mathbf{x}), \phi_m(\mathbf{x})$ | Atom and molecule wavefunctions. |
| $\phi_1(x), \phi_2(x)$ | Wave functions of different hyperfine components. |
| $\tilde{\phi}_a(r)$ | Rescaled wave function, $\phi_a = \tilde{\phi}_a/r$. |
| $\hat{\chi}(\mathbf{x})$ | Fluctuating component of the field operator. |
| $\hat{\chi}_a(\mathbf{x}), \hat{\chi}_m(\mathbf{x})$ | Fluctuations of atom and molecule field. |
| $\hat{\rho}$ | The system's density operator. |
| ξ | Condensate healing length, $\xi = \hbar/(\sqrt{2}mc)$. |
| $\hat{\Psi}(\mathbf{x}), \hat{\Psi}_a(\mathbf{x})$ | Atomic field operator. |
| $\hat{\Psi}_m(\mathbf{x})$ | Molecular field operator. |
| $\omega_x, \omega_y, \omega_z$ | Trap frequencies along the cartesian axes. |
| ω_\perp | Transverse trap frequency of a cigar shaped trap or a waveguide. |
| $\boldsymbol{\Omega}, \Omega$ | Angular velocity of trap rotation. $\Omega = \boldsymbol{\Omega} $. |

Glossary

We provide brief definitions of frequently used terms and abbreviations, specified for our context and sorted alphabetically.

| | |
|------------------------|--|
| “analogy”, the | Mathematical equivalence between the equation for BEC excitations in the hydrodynamic regime and that for a scalar quantum field in curved spacetime. Also the operator commutation relations are identical, allowing the study of curved spacetime quantum effects in BECs. |
| BEC | Bose-Einstein condensate. |
| black hole horizon, BH | Surface in the BEC flow where the normal component of the flow turns from subsonic to supersonic. Analogue of the event horizon around an astrophysical black hole. |
| component | Part of the BEC with atoms in one specific hyperfine state. |
| de-Laval nozzle | Constriction of a tube to create supersonic flow in aerodynamics. In a BEC, we can also use a hump potential. |
| depletion | Presence of uncondensed atoms at zero temperature due to interactions. |
| downstream | In the direction of flow. |
| ergoregion | Region in the condensate where the velocity modulus exceeds the speed of sound. Phonons can escape from this region, but they cannot remain motionless as seen in the lab frame. |
| Feshbach resonance | Resonant bound state in atomic collisions. The energy of the resonance can be adjusted with a magnetic field. This allows steering of the interactions in a BEC using a magnetic field. |
| GPE | Gross-Pitaevskii equation. |
| GR | General relativity. |
| grey soliton | Dip in the condensate density to a fraction f of the background value. $f = 0$ would be a dark soliton. For $f > 0$ the dip is moving. |
| grid | Set of discrete points used to represent the spatial domain in numerical computations. |
| healing length | Natural length scale for variations of the condensate wave function. |
| HFB | Hartree-Fock-Bogoliubov. |
| horizon | See “black hole horizon” and “white hole horizon”. |

| | |
|------------------------|---|
| hump potential | Optically generated potentials, placed in the way of the BEC flow. |
| hydrodynamic equations | Bernoulli's equation (energy conservation) and continuity equation (number conservation). The BEC obeys these in the hydrodynamic regime. |
| hydrodynamic regime | A BEC only varies on length scales larger than the healing length. In this regime the condensate behaves like an inviscid, irrotational fluid. |
| line singularity | Line with undefined BEC phase due to circulating flow. |
| line vortex | Circular condensate flow around the line singularity. |
| leaking out | Condensate with just high enough chemical potential to leave a reservoir, streaming over the confining hump potential. |
| optical piston | Repulsive optical potential that is moving in time, creating a piston that pushes the condensate. |
| optical tunnel | Finite length tunnel formed by the core of a focussed optical vortex laser beam. |
| optical vortex | Laser beam with a phase singularity on its axis. Because of the singularity, the light intensity of the beam has a hollow profile. |
| phase imprinting | Engineering a phase and hence a flow field in the condensate by means of interaction with electromagnetic waves. |
| phase separation | Immiscibility of two hyperfine components of the BEC. Under the influence of dissipation, these separate spatially, leaving only a small overlap region at the contact surface. |
| phonon | BEC excitation with wavenumber q that fulfills $q\xi \ll 1$. |
| pinning potential | Repulsive optical potential, placed on the singularity of a matter wave vortex, to prevents its contraction or drift towards low density regions of the condensate. |
| Q1D | Quasi-one dimensional. A BEC with $\mu \ll \hbar\omega_{\perp}$. Transverse excitations are frozen out. |
| resonance theory | Description of a Feshbach resonance in a BEC by coupled atom and molecule fields. |
| ring singularity | Ring with undefined BEC phase due to condensate flow. |
| ring vortex | Condensate flow around the ring singularity. Imagine flow on the surface of a torus, threading the hole. |
| scattering length | Parameter a_s , describing the whole scattering behaviour of cold atoms in the s-wave regime. |
| SDE | Stochastic differential equation. |
| semi-classical theory | BEC mean field theory. Quantum field effects are neglected and the condensate can be described by a single wave function. |

NOTATION AND TERMINOLOGY

| | |
|--------------------------|--|
| singularity | See “ring singularity” and “line singularity”. |
| soliton | Used here synonymously with “solitary wave”. Localised solution of a wave equation that propagates without change of shape. |
| sonic horizon | See “black hole horizon” and “white hole horizon”. |
| stochastic wave function | Solution of a stochastic differential equation. For us the Gross-Pitaevskii mean-field with the addition of initial random noise. |
| three-body loss | Three atoms collide and form a molecule among them. All three atoms are lost from the condensate. |
| transsonic | A flow that turns from subsonic to supersonic (spatially). |
| TTF | Transverse Thomas-Fermi. A BEC with $\mu \gg \hbar\omega_{\perp}$. The transverse profile is determined in the Thomas-Fermi approximation. |
| TWA | Truncated Wigner approximation. |
| upstream | Against the direction of flow. |
| vortex charge | Topological invariant. Indicates how often the phase wraps over $U(1)$ on a line around the vortex singularity. |
| white hole horizon, WH | Surface in the BEC flow where the normal component of the flow returns from supersonic to subsonic. The analogue object exists in astrophysics as the inner horizon around an electrically charged black hole. |

Contents

| | |
|--|-----|
| Acknowledgements | vii |
| Abstract | ix |
| Notation and Terminology | xi |
| 1 Introduction | 1 |
| 1.1 Thesis Plan | 2 |
| 1.2 Bose-Einstein Condensation | 3 |
| 1.2.1 Manipulation and Trapping of Atoms | 6 |
| 1.2.2 Interactions between Atoms | 9 |
| 1.3 Bose-Einstein Condensates as Simulators | 12 |
| 1.4 List of Publications | 14 |
| 2 Theory | 15 |
| 2.1 Microscopic Description of an Interacting Bose-Gas | 16 |
| 2.1.1 Loss Processes and the Master Equation | 17 |
| 2.2 The Gross-Pitaevskii Equation | 18 |
| 2.2.1 Hydrodynamic Equations | 19 |
| 2.2.2 The Imaginary Time Method | 19 |
| 2.2.3 Rotating Frames | 21 |
| 2.2.4 Multi-component Condensates | 22 |
| 2.2.5 Atom Losses | 24 |
| 2.3 The Bogoliubov Equations | 24 |
| 2.3.1 Classical Excitations vs. Quasi-Particles | 25 |
| 2.3.2 The Bogoliubov Dispersion Relation | 26 |
| 2.3.3 Energetical and Dynamical Stability | 28 |
| 2.3.4 Hydrodynamic Representation of the Fluctuation Field . . | 28 |
| 2.4 Hartree-Fock-Bogoliubov Theory | 30 |

| | | |
|----------|--|-----------|
| 2.4.1 | Gap in the Excitation Spectrum and Goldstone's Theorem | 32 |
| 2.4.2 | Self-consistent Stationary States | 34 |
| 2.4.3 | Ultraviolet Renormalisation | 36 |
| 2.4.4 | Atom-Molecule Resonance Theory | 37 |
| 2.4.5 | Atom Losses | 39 |
| 2.5 | The Truncated Wigner Approximation | 40 |
| 2.5.1 | Stochastic Differential Equations | 42 |
| 2.5.2 | Initial Conditions and Correlation Function | 43 |
| 2.5.3 | Validity of the Truncation | 45 |
| 2.5.4 | Renormalisation | 46 |
| 2.5.5 | Atom Losses | 46 |
| 2.5.6 | Stochastic Equation in the Oscillator Basis | 47 |
| 2.5.7 | Outlook on further Phase-Space Methods | 49 |
| 2.6 | Numerical Solutions | 50 |
| 2.7 | Summary | 51 |
| 3 | Collapsing Bose-Einstein Condensates | 53 |
| 3.1 | Attractive Interactions | 55 |
| 3.2 | "Bosenova" | 56 |
| 3.2.1 | The Experiment | 56 |
| 3.2.2 | The Theory | 60 |
| 3.3 | Spherical Gross-Pitaevskii Model | 63 |
| 3.4 | Hartree-Fock-Bogoliubov Framework | 65 |
| 3.4.1 | Condensate Depletion | 67 |
| 3.4.2 | Resonance Theory | 71 |
| 3.4.3 | Discussion | 74 |
| 3.5 | Truncated Wigner Framework | 75 |
| 3.5.1 | Numerical Method | 76 |
| 3.5.2 | Collapse of a Cigar Shaped Condensate | 79 |
| 3.5.3 | Inclusion of a Thermal Cloud | 80 |
| 3.6 | Hartree-Fock-Bogoliubov vs. Wigner | 81 |
| 3.7 | Parallels to Cosmology | 84 |
| 3.8 | Conclusions and Outlook | 85 |
| 4 | Topological Structures in Condensates | 87 |
| 4.1 | Introduction to Skyrmions | 88 |
| 4.1.1 | Topological Solitons | 88 |

| | | |
|----------|---|------------|
| 4.1.2 | Skyrmion Topology | 89 |
| 4.1.3 | Skyrmions in Particle Physics | 92 |
| 4.1.4 | Skyrmions in Bose-Einstein Condensates | 94 |
| 4.2 | Stability of Trapped Skyrmions in Condensates | 99 |
| 4.2.1 | Atom Numbers in a Skyrmion | 99 |
| 4.2.2 | Skyrmion Core Flow | 101 |
| 4.2.3 | Gravitational Sag | 104 |
| 4.2.4 | Stabilisation against Drift | 108 |
| 4.2.5 | Variation of the Scattering Lengths | 111 |
| 4.2.6 | Supersonic Core Instability? | 115 |
| 4.2.7 | Summary and Outlook | 116 |
| 4.3 | High Charge Ring Flows in Condensates | 116 |
| 4.3.1 | Optical Vortices | 117 |
| 4.3.2 | Potentials and Method | 118 |
| 4.3.3 | Stabilisation of High Charge Ring Flow | 120 |
| 4.3.4 | Summary and Outlook | 123 |
| 4.4 | Conclusion | 124 |
| 5 | Analogue Gravity | 125 |
| 5.1 | Introduction | 126 |
| 5.1.1 | General Relativity | 126 |
| 5.1.2 | Quantum Field Theory in Curved Spaces | 127 |
| 5.2 | Analogue Gravity | 131 |
| 5.3 | Experimentally Utilisable Sonic Horizons | 134 |
| 5.3.1 | Sonic Horizons | 135 |
| 5.3.2 | Stability | 138 |
| 5.3.3 | Rapidity of Flow Variation | 140 |
| 5.3.4 | Limits on the Analogue Hawking Temperature | 141 |
| 5.3.5 | Signature of the Analogue Hawking Effect | 145 |
| 5.3.6 | Outlook | 146 |
| 5.4 | Supersonic Optical Tunnel | 146 |
| 5.4.1 | Flow Acceleration | 147 |
| 5.4.2 | Dynamical Instability | 149 |
| 5.4.3 | Single Soliton Horizons | 153 |
| 5.4.4 | Summary | 156 |
| 5.5 | Sonic Horizons in Atom Lasers | 156 |
| 5.5.1 | Dimensionless Formalism | 157 |

| | | |
|----------|--|------------|
| 5.5.2 | Horizon due to Strong Outcoupling | 158 |
| 5.5.3 | Horizon due to Obstacle | 161 |
| 5.5.4 | Summary | 166 |
| 5.6 | Reservoir Outflow | 167 |
| 5.6.1 | Outflow Scenario | 167 |
| 5.6.2 | Transverse Horizon Shape | 171 |
| 5.6.3 | Maintaining Pressure | 174 |
| 5.6.4 | Effects of Three-Body-Loss | 176 |
| 5.6.5 | Optimal Outflow Operation | 177 |
| 5.6.6 | Summary | 178 |
| 5.7 | Conclusions | 178 |
| 6 | Conclusions | 181 |
| A | Resonance Theory Renormalisation | 183 |
| A.1 | Lagrangian and Feynman Rules | 184 |
| A.2 | Summation of Ladder Diagrams | 185 |
| B | HFB Equations for Spherical Symmetry | 189 |
| C | Topological Structures: Technical Details | 195 |
| D | Numerical Methods | 197 |
| D.1 | Project Overview | 197 |
| D.1.1 | Programming | 197 |
| D.1.2 | Algorithms | 198 |
| D.2 | Runge-Kutta Fehlberg Method in XMDS | 199 |
| | Bibliography | 206 |

Chapter 1

Introduction

Bose-Einstein condensation in ultra-cold alkali gases, when thousands or millions of atoms gather in the same quantum state is an amazing phenomenon. After S. Bose [1] found that in the quantum world particles may obey Bose statistics, A. Einstein [2, 3] predicted that near the absolute zero of temperature, these would undergo condensation. The effect, later named Bose-Einstein condensation, is a manifestation of quantum physics in the macroscopic world. The gathering of many particles in the same quantum state appears to visualise the matter wave, whose modulus can be reconstructed from the particle density pictured in a single shadow image. Particularly since the first experimental realisations of gaseous Bose-Einstein condensates (BECs) in 1995 [4–6], the number of publications in the area has skyrocketed, on topics ranging from classical collective excitations [7] to quantum phase transitions [8].

However it was not until recent years that quantum-field effects in these ultra-cold many-body systems were studied in greater detail. Earlier, surprisingly many BEC phenomena could be explained using mean field theory, which neglects all quantum field correlations, and describes the condensate with an essentially classical nonlinear wave equation. But lately, experimental progress with dilute gas Bose-Einstein condensates has allowed increasingly detailed studies of the quantum nature of the atomic field [9–12]. This has been accompanied by advances in the numerical treatment of many body quantum field theory applied to BEC dynamics, most prominently in a better understanding of phase space methods [13] and Hartree-Fock-Bogoliubov (HFB) theory [14]. Due to these developments, BECs can now be used to explore concepts and ideas of both, classical and quantum field theory. Usually classical mean field effects are dominant, but if desired, the underlying quantum field nature can be brought to the surface.

Besides being thus intrinsically a testbed for advanced concepts of quantum many-body theory, BECs offer themselves as laboratory tools for the verification of ideas from a much wider range of physics. Ultracold quantum gases have astonishing similarities to diverse physical systems ranging from antiferromagnetic materials [15] to astrophysical black holes [16, 17]. Another example is the existence of Efimov states, genuine three particle bound states first studied in the context of nuclear physics [18, 19], which have recently been observed in an ultracold cesium gas [20]. Skyrmions, which were first introduced in particle physics [21–24], where their application [25] has recently triggered a controversial search for penta-quarks [26], have been shown to exist in trapped gaseous BECs [27]. Condensates collapsing under their own self-attraction [28] might give us clues about particle production in the inflationary phase of the universe’s expansion [17, 29].

Researching the application of BECs to simulations of phenomena across disciplines, using these analogies, lies at the heart of this thesis. We will show that simulations of black holes and Skyrmions can be done in present experiments. The common goals of our projects are to identify suitable experimental parameter regimes, or to improve our understanding of the underlying theory for cross-disciplinary experiments. This theoretical work is required at this time, as experiments on the analogies are hardly possible without guidance. Our emphasis on experiment facilitation requires the realistic modelling of our physical systems, generally necessitating numerical simulations, supported by simple analytical ideas.

For these our workhorse is condensate mean field theory, but we also consider quantum corrections in the Hartree-Fock-Bogoliubov and truncated Wigner theories.

1.1 Thesis Plan

The global structure of this thesis is as follows: The remainder of the introduction provides a brief overview of the basic physics underlying the research in this thesis, and then, in section 1.3, a quick introduction of the topics that we studied within the broader context of BECs as simulators.

Since many of the theoretical techniques that we require are used throughout this thesis, they are summarised in chapter 2. The reader who is familiar with the topics there, is encouraged to advance directly to chapters 3-5, which contain

our results. Access to our mathematical notation, which is defined in chapter 2, is also provided by the notation summary on page (xi).

In chapter 3, we consider the ground breaking “*Bosenova*” experiment on collapsing Bose-Einstein condensates [28]. The question is whether quantum depletion during the collapse can explain an existing discrepancy between experimental results and theoretical simulations that neglect quantum effects [30].

Solitonic *Skyrmion* solutions in two-component BECs will occupy us in a large part of chapter 4. As mentioned, these have connections to particle and nuclear physics. We thoroughly investigate the available parameter-space, in order to assess challenges in their experimental creation within BECs. The second part of chapter 4 concerns the stabilisation of high charge *ring vortices* in a BEC. These not only form an experimental stepping stone towards Skyrmions, but also hold promise for the realisation of supersonic optical BEC tunnels which will be of use in chapter 5. Both Skyrmions and ring vortices have a nontrivial topological structure, the overall theme of chapter 4 is thus the study of *topological solitons*.

In the final chapter, chapter 5, we present our suggestions for the first BEC experiment in the field of analogue gravity. The primary question addressed is “What is a *realistic* experimental setup for the study of analogue Hawking radiation, in which the effect can be seen with present technology?”.

After the presentation of our results, we finish with general conclusions in chapter 6.

Several appendices are devoted to technical details that might be most useful for the reader aiming to use any of the methods presented in this thesis.

Last but not least, this thesis comes with a multimedia CD. Most importantly, it contains quicktime and mpg movies of selected BEC dynamics. While we prepared figures for all important results, some scenarios are much better visualised in our movies and if so, we have indicated it in the text. Further contents of the CD are sample code and the source files for the figures within this thesis.

1.2 Bose-Einstein Condensation

Due to the wave-like nature of particles in the realm of quantum mechanics, identical quantum objects must be strictly indistinguishable. In classical mechanics even identical black marbles in a children’s game could be labelled individually according to their initial position on the game table. Paying careful attention when the marbles are brought to collide, one can track each marble’s path and thus

identify them at the final moment of the game. Conversely, in the quantum mechanical problem we are fundamentally unable to say which “marble” went which way once their wave functions have overlapped during a collision process. The resulting axiom is that all observables have to be invariant under the exchange of any two identical particles. This leaves only two options: wavefunctions which are symmetric or antisymmetric under particle exchange [31]. Particles with a symmetric wavefunction are called bosons, those with antisymmetric ones are called fermions. After second quantisation this translates into the requirement that a bosonic field operator obeys commutation relations, while anticommutation relations hold for fermionic operators. Demanding Lorentz invariance and causality, relativistic quantum mechanics requires that all particles with integer spin are bosons and those with half-integer spin are fermions (spin-statistics theorem [32]). The classification extends beyond fundamental particles to composite objects like atoms.

The simple symmetry properties of wave functions have enormous consequences. So does the antisymmetry of fermionic wave functions forbid any two fermions to occupy the same quantum state, a rule known as the Pauli exclusion principle. This creates the periodic table of elements, prevents white dwarfs and neutron stars from gravitational collapse and leads to the existence of semiconductors. In contrast, bosonic systems not only allow arbitrarily many occupants of a single quantum state, they downright prefer such a configuration. The dynamical transition of a boson into a state already occupied by N fellows is $N + 1$ -times enhanced (Bose enhancement).

Ultimately this gives rise to the phenomenon of Bose-Einstein condensation: At extremely low temperatures, all members of a bosonic ensemble will condense into the single quantum ground state of the system. The result is a giant macroscopically occupied matter-wave (compare Fig. 1.1). Macroscopic occupation of one single particle state is the simplest signature of BEC.

For the case of an ideal gas, basic features of the condensation effect can be easily derived, which is done in many textbooks. Here we just state the major results. Below a critical temperature T_{crit} , more and more bosons have to occupy the system’s single particle ground state. One finds [33]

$$T_{\text{crit}} = \left(\frac{\rho}{\zeta(3/2)} \right)^{3/2} \frac{2\pi\hbar^2}{mk_B}, \quad (1.1)$$

for a homogeneous ideal gas of atoms with mass m , which has density ρ . ζ is the Riemann zeta function. For N_{tot} atoms in the system, the occupation N_{cond} of

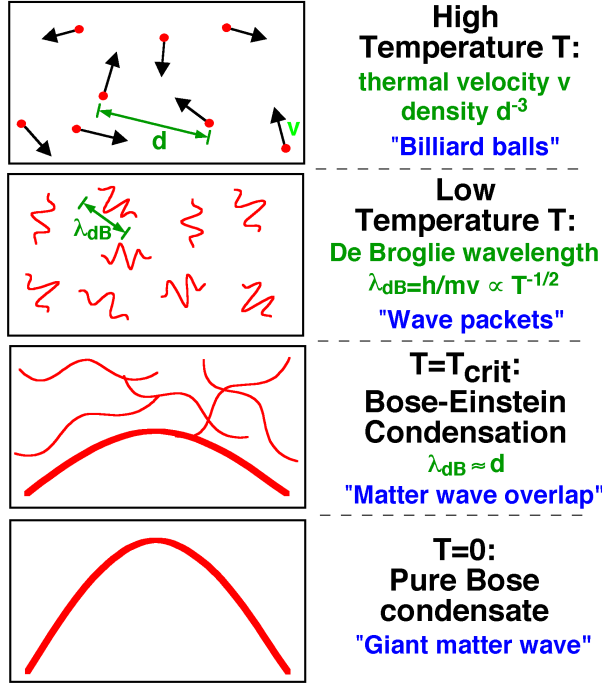


Figure 1.1: Illustration of the path to Bose-Einstein condensation. The image is taken from http://cua.mit.edu/ketterle_group/Nice_pics.htm. From top to bottom: At room temperature the average velocity of atoms is high enough to neglect quantum effects, they can be treated classically as “billiard balls”. Let d denote the inter particle spacing. The lower the temperature and hence the energy, the larger become the thermal de-Broglie wavelengths λ_{dB} of the atoms. At the critical temperature T_{crit} , λ_{dB} reaches the scale of d and matter waves begin to overlap. Near absolute zero, all atoms are forming essentially a single large matter wave.

the ground state increases like:

$$N_{\text{cond}} = N_{\text{tot}} \left[1 - \left(\frac{T}{T_{\text{crit}}} \right)^{3/2} \right], \quad (1.2)$$

if the temperature T is decreased below the critical temperature.

Interactions between the bosons quantitatively modify these results and also complicate the definition of Bose-Einstein condensation. One now resorts to the Penrose-Onsager criterion: A condensate is present when the matrix of expectation values $\langle \hat{\Psi}_i^\dagger \hat{\Psi}_j \rangle$ acquires an eigenvalue of the order of the total particle number. $\hat{\Psi}_j$ are field operators annihilating a particle in the j 'th single particle state.

Any bosonic system can condense, but probably the cleanest example is provided by a dilute gas of ultracold atoms. Among these, alkali atoms are easiest to manipulate in practice and form the BEC system that we have in mind throughout the thesis.

Typical critical temperatures for these gases are extremely low, around $0.1 \mu\text{K}$. This explains the decades-long gap between the theoretical prediction of BECs and their experimental creation in cold gases. To achieve ultracold temperatures, atoms are typically first subjected to laser cooling [34] within a magnetic trap. The remaining orders of magnitude in temperature are bridged by evaporative cooling [34], where the most energetic atoms in the trap are allowed to escape by continuously lowering the height of the trapping potential.

1.2.1 Manipulation and Trapping of Atoms

Interactions of atoms with electromagnetic fields are not only crucial for cooling the atoms by 10 orders of magnitude to obtain condensation, but also the primary means to manipulate condensates in experiments afterwards. In fact, the reason for the predominant use of alkali atoms in BEC experiments is that they have strong optical transitions, which are readily accessible with available lasers [35]. Atoms interact with radiation by their electric and magnetic dipole moments, which depend on the internal atomic state. Together with a wide range of available frequencies for the electromagnetic radiation, the accessible variety of internal states forms the basis for the flexibility of BEC experiments. In the following paragraphs, we provide details on those techniques that are frequently modelled in our numerical simulations. Specific details will be given for the most common BEC atom ^{87}Rb .

Magnetic Trapping and Hyperfine States

Neutral atoms can be confined in a magnetic trap. The basic principle is simple, but subtle details of the underlying physics turn out to be significant for our studies of Skyrmions in chapter 4.

Alkali atoms in their ground state have a magnetic dipole moment $\hat{\mu}$ and thus experience a potential $V_{\text{mag}} = \langle -\hat{\mu} \cdot \mathbf{B} \rangle^1$ in a magnetic field \mathbf{B} . Their electrons have no net orbital angular momentum, hence the magnetic moment is determined by

¹Without intending to be rigorous in the introduction, \hat{O} denotes an operator and $\langle \rangle$ an expectation value.

the nuclear spin $\hat{\mathbf{I}}$ and electronic spin $\hat{\mathbf{J}}$, coupled via the hyperfine interaction to the total spin $\hat{\mathbf{F}}$ [34]. For ^{87}Rb the electronic spin is $J = 1/2$ and couples to the nuclear spin $I = 3/2$, which can result in $F = 1$ or $F = 2$.

The magnetic moment is proportional to the total spin and its possible projections onto the magnetic field axis result in the discrete energy spectrum:

$$V_{\text{mag}} = m_F g_F \mu_B |\mathbf{B}|, \quad g_F = g_J \frac{F(F+1) - I(I+1) + J(J+1)}{2F(F+1)} \quad (1.3)$$

The projection of $\hat{\mathbf{F}}$ onto the magnetic field direction has eigenvalues $\hbar m_F$, g_F is the Landé g-factor, containing the total spin, nuclear spin and electronic spin quantum numbers (F, I, J respectively), as well as gyromagnetic factors for the electrons g_I and the nucleus g_J .² Finally, μ_B is the Bohr magneton.

As it is not possible to create a magnetic field maximum in a current-free region [36], a confining potential for the atoms can only be realised near a minimum of the magnetic field, using hyperfine states with $m_F g_F > 0$. In ^{87}Rb these are the *magnetically trappable states* $|F = 1, m_F = -1\rangle$, $|F = 2, m_F = 1\rangle$ and $|F = 2, m_F = 2\rangle$.

Eq. (1.3) is the low field limit of the Breit-Rabi equation [37]. The Breit-Rabi equation, discussed in section 4.2.3 gives the energy in a magnetic field for arbitrary magnetic field strengths. It deviates from Eq. (1.3) due to a magnetic field dependence of the magnetic moment. These deviations are relevant for Skyrmion stability, hence we discuss them in chapter 4.

According to Eq. (1.3), different hyperfine states can experience the same potential. This is the case for example for the $|F = 1, m_F = -1\rangle$ and $|F = 2, m_F = 1\rangle$ states of ^{87}Rb . These are useful for the creation of a two-component BEC.

Optical Trapping

Atoms interact with laser light predominantly via pre-existing or induced electric dipole moments. Alkali atoms in their ground state have no electric dipole moment unless one is induced by the electric field of a laser. As usual the interaction energy between a static electric field \mathbf{E} and a dipole $\hat{\mathbf{d}}$ is $V_{\text{dip}} = \langle -\hat{\mathbf{d}} \cdot \mathbf{E} \rangle$, which turns out quadratic in the field as the induced dipole strength itself is proportional to $|\mathbf{E}|$ to first order. The expression $V_{\text{dip}} = \alpha \mathbf{E}^2 / 2$ defines the static polarisability α of the atom. Extending the equation to oscillating laser fields

²We assumed $g_J \gg g_I$ to write Eq. (1.3).

$\mathbf{E}(t) = \mathbf{E}_\omega e^{-i\omega t} + \mathbf{E}_{-\omega} e^{i\omega t}$ one obtains [34]:

$$V_{\text{dip}} = -\frac{1}{2}\alpha(\omega)\overline{E(t)^2} = \frac{\hbar\Omega_R^2\delta}{\delta^2 + \Gamma_e^2/4}, \quad (1.4)$$

$$\Omega_R = \left| \langle e | \hat{\mathbf{d}} \cdot \mathbf{E}_\omega | g \rangle \right| / \hbar. \quad (1.5)$$

The time average of the electric field is denoted by $\overline{E(t)^2}$ and the polarisability $\alpha(\omega)$ is now frequency dependent. Ω_R is the Rabi frequency, proportional to $|\mathbf{E}|$. We also used the detuning $\delta = \omega - \omega_{eg}$ between the laser frequency ω and the frequency $\omega_{eg} = (E_e - E_g)/\hbar$ of a single dominant atomic transition between the ground state $|g\rangle$ with energy E_g and an excited state $|e\rangle$ with energy E_e . Γ_e is the spontaneous emission rate of this excited level.

The shift in atomic energy levels described by Eq. (1.4) is mainly due to virtual transitions to the upper level, hence it does not require a photon to be actually absorbed. It is due to this feature that the atom-light interaction can be applied to create potentials for BEC atoms. If photons were regularly absorbed, the recoil from the subsequent re-emissions would cause the atoms to leave the BEC. To avoid photon absorption, the laser light is therefore shone onto the BEC far detuned from the atomic resonance. Eq. (1.4) depends linearly on δ , hence we can create repulsive potentials for *blue-detuned* light ($\delta > 0$) and attractive potentials for *red-detuned* light ($\delta < 0$). Then it is possible to create versatile potentials for BEC atoms, and even optical traps based on the light shift alone. The latter usually exploit the spatially varying intensity profile of a laser beam near its focus.

Finally we point out that in an optical trap all hyperfine states feel the same potential. Unlike magnetic traps, optical traps therefore do not affect the atomic spin degree of freedom, allowing the creation of spinor condensates.

Phase Imprinting and Vortices

Trapped BEC atoms would be a lot less exciting if electromagnetic fields did not allow the further controlled manipulation of them. Here we briefly mention the phase imprinting technique. We have just seen how the interaction of atoms with laser light changes their energy levels. Roughly speaking, the amplitude of an atom with energy E evolves as $e^{iEt/\hbar}$. If laser light with spatially varying intensity is shone on the atoms for a short time, this effect can be used to modify the spatial profile of the phase of the atoms. As we will see in section 2.2.1, a phase-gradient thus imprinted on the condensate corresponds to a non-vanishing velocity

of the atoms. Phase imprinting is now a standard tool to create vortices [34, 38], for which the phase is chosen such that it corresponds to a circulating BEC flow around what is to become the vortex core. The technique has further been suggested for the creation of Skyrmions, which we study in chapter 4.

Vortices are the only way for a BEC to take up angular momentum. Around a vortex, the phase of the BEC wave function varies by an integer multiple of 2π . The phase singularity at the vortex centre forces the BEC density there to zero. The phase structure corresponds to a circulating flow around the vortex core, just as the flow in the water-vortex arising when a kitchen sink is emptied. If angular momentum is added to a BEC cloud, for example by rotating the confining trap, an increasing number of vortices is seeded which arrange themselves in a regular pattern, called a vortex array [38].

1.2.2 Interactions between Atoms

As mentioned before, the theory of Bose-Einstein condensation is complicated by the inherent interactions of atoms. These are however crucial for the actual achievement of condensation: The evaporative cooling stage requires the gas to remain in thermal equilibrium mediated by elastic collisions. Further, the final transition to the condensed state is accelerated by Bose enhanced scattering events.

Atoms interact primarily through the van der Waals potential, arising from dipole-dipole interactions. These are intrinsically weak; the attractive potential scales with distance r as $1/r^6$ [36]. For small r , the atomic electron orbitals begin to overlap, resulting in a strongly repulsive contribution to the interatomic potential. Both parts of the potential together are often modelled using the Lennard-Jones potential with a repulsive core $\sim 1/r^{12}$ and an attractive long range potential $\sim 1/r^6$.

The theoretical quantum treatment of a huge number of atoms interacting via this non-local potential V_{int} is extremely demanding. Fortunately, at the ultracold temperatures where BEC occurs, a simplification is possible.

Elastic collisions and s-wave approximation

Quantum scattering theory considers the transition probability from an incoming plane wave state $|\Psi_{\text{in}}\rangle \sim e^{i\mathbf{k}\cdot\mathbf{x}}$ into an outgoing scattered wave $|\Psi_{\text{out}}\rangle$ mediated by interaction with the potential $V_{\text{int}}(\mathbf{x})$ described above. We can write the complete wave function as the sum of both contributions, parametrised as $\Psi =$

$e^{i\mathbf{k}\cdot\mathbf{x}} + f(\theta)e^{ikr}/r$ [34]. We assumed an outgoing spherical wave, whose amplitude depends on the angle θ between the scattering direction and the axis of original beam propagation given by \mathbf{k} . r is the distance from the scattering centre and $f(\theta)$ the scattering amplitude. The axial symmetry of the problem, with respect to the propagation direction of the incoming atom, further allows us to perform a *partial wave expansion* of $f(\theta)$.

$$f(\theta) = \frac{1}{2ik} \sum_{l=0}^{\infty} (2l+1)(e^{2i\delta_l} - 1) P_l(\cos \theta), \quad (1.6)$$

in terms of Legendre polynomials $P_l(\cos \theta)$. In so doing, we have traded the unknown function $f(\theta)$ for the unknown set of constants δ_l .

The expansion essentially decomposes the wave function into components with definite orbital angular momentum with respect to the scattering centre. We know that for scattering by a central potential this orbital angular momentum is conserved and further that it is quantised. For low collision energies, as in a gas of very cold atoms, only the lowest angular momenta l have to be considered. A heuristic semi-classical argument is that low momentum atoms only have high angular momentum with respect to the potential centre if their classical trajectory misses the centre by a large distance. As the inter atomic potential has a short range, those atoms do not significantly feel the scattering potential. In a BEC the temperature is cold enough, so that we only have to consider the first term ($l = 0$) in Eq. (1.6). In such a case, scattering occurs in all directions with equal probability ($P_0(\cos \theta) = \text{const.}$), which is also true for a simple zero-range potential $\tilde{V}_{\text{int}} = U_0 \delta^{(3)}(\mathbf{x})$. Fitting U_0 to reproduce the correct overall scattering probability one obtains [34]

$$U_0 = \frac{4\pi\hbar^2 a_s}{m}. \quad (1.7)$$

Here a_s is the scattering length, whose magnitude we could for example find via

$$\sigma = 8\pi a_s^2, \quad (1.8)$$

where σ is the total cross section for atom scattering.

The sign of a_s determines whether the interactions are repulsive or attractive. The *s-wave approximation*, which consists of using \tilde{V}_{int} in place of V_{int} , is justified for dilute cold cases with density n which satisfy [35]

$$n|a_s|^3 \ll 1. \quad (1.9)$$

This condition is usually fulfilled for dilute gas BECs.

Feshbach resonances

Matters are more complicated if the potential V_{int} admits bound state solutions. However, these complications give rise to tunable interactions between atoms, an enormously powerful tool that will be frequently used³ in this thesis. Since V_{int} depends on the spin state of the colliding atoms, so does the fact whether or not V_{int} allows a bound state. For spin states allowing binding, the atoms are referred to as in a closed channel, otherwise they are in an open channel. Resonance phenomena occur, when the total energy of colliding atoms in the open channel matches that of a bound state (molecule) in a closed channel. The scattering probability near such a resonance consequently depends strongly on the collision energy, exhibiting a characteristic resonance peak.

The reason why these so-called Feshbach resonances [39] can be exploited to widely tune the interatomic interactions is the magnetic field dependence of the energy gap between two free atoms at rest and a bound pair. The gap is later referred to as the detuning ν . It arises from a difference between the magnetic moments of the open and closed channels. Further details can be found in [34]. The use of Feshbach resonances is central to the “Bosenova” experiment discussed in chapter 3 and we also consider Feshbach modified scattering lengths for Skyrmions in chapter 4.

Inelastic collisions and atom losses

The modified scattering behaviour outlined above arises due to the virtual presence of atoms in the molecular state. Colliding atoms in the open channel cannot combine to form a real molecule, as this would violate energy-momentum conservation. The situation changes when a third atom is present in a collision process. Among three atoms the formation of one molecule is allowed, with the last atom absorbing excess energy. As a result of such a process, all three atoms are generally lost from a BEC, because the molecule is not trappable and the third atom too energetic.

These inelastic collisions are referred to as three-body recombination. They are normally rare, as the BEC is dilute and the loss rate proportional to the probability of finding three atoms at the same spot. However for high BEC densities recombination becomes significant and is crucially important for collapsing BECs in chapter 3 and high density BECs in chapter 5.

³Here and in following similar statements, we refer to the modelling of the concerned tools in our theory.

There are rare situations, in which it is possible for atoms to be lost from the BEC due to a binary collision, for example if the collision changes the internal state of an atom such that it is no longer trapped by the magnetic field. Even an atom on its own might be lost, for instance due to spontaneous emission as a consequence of photon absorption from an optical field used for BEC manipulation. This can occur with a small probability despite the light field being off resonant. Such events contribute to what we summarise as one-body losses.

1.3 Bose-Einstein Condensates as Simulators

With some background provided, we now move on to the core theme of this thesis: The use of Bose-Einstein condensates as simulators for other physical systems, which are at first sight often not even related to cold atom physics. In this section, we provide an overview of those three phenomena and their simulation by analogy in a BEC, which are the subject of research in this thesis. Other fruitful cross-disciplinary uses of BECs, beyond the scope of this thesis, include most notably the study of condensed-matter like systems in optical lattices [40–44].

To begin, we consider a Bose-Einstein condensate collapsing under its attractive self-interaction. The groundbreaking experiment on such an event [28] uncovered that a simple kinematic initial state can give rise to complex dynamical results. It is found that after an initial delay time t_{collapse} , the BEC experiences a violent explosion, after which parts of the condensate are ejected outwards as bursts. In this sense, the experiment displays fascinating similarities to supernova type-II explosions from astrophysics. These parallels earned the experiment the nickname “Bosenova”.

There are however deeper analogies to be found between collapsing BECs and astrophysical phenomena, as shown by Calzetta and Hu [45, 46]. The behaviour of quantum fluctuations in the atom field during the collapse is reminiscent of quantum effects during the conjectured inflationary phase [29] of the universe’s expansion. In both physical systems fluctuations can be labelled as “frozen” or “thawed”, depending on whether their eigenfrequencies are smaller or larger than the rate of change of the background. The background is the expanding universe’s spacetime in the cosmological scenario or the condensate density and velocity distribution in the BEC. Frozen modes are exponentially amplified in contrast to the oscillatory behaviour of thawed modes. Predictions made using such cross-fertilisation of ideas from cosmology and condensate physics could be verified in

a collapse experiment [45, 46]. To prepare the exploitation of the similarities, we study the question whether existing quantum field theory of BECs can describe the collapse experiment quantitatively under realistic conditions in chapter 3. To this end our focus is on the simplest experimental observable, which is however unrelated to cosmology.

We then change scope, from the physics of the largest imaginable object, the Universe, to some of the smallest structures: nucleons. Besides the predominantly used theory of quantum chromo dynamics (QCD), many properties of nucleons can be studied in an alternative framework: Skyrme-theory [47]. Its basic feature is the nucleon’s construction as a soliton of a meson field, which is called a Skyrmion. The complex topological structure of Skyrms will be explained in detail in chapter 4. Interestingly it can be realised in a BEC with multiple hyperfine components and amounts to a line vortex in one component threaded through a ring vortex in the other component. We investigate in detail in which experimental parameter regimes stable Skyrms can be expected.

In the last chapter, we return to the realm of astrophysics and study the potentially most useful analogy between a BEC and an utterly distinct physical system: a black hole. We will later see that under some conditions a BEC can be treated as an inviscid fluid. In such a case its perturbations are sound waves (phonons). In 1981, W. Unruh discovered that quantised phonons in a moving fluid behave like scalar quantum particles in the curved spacetime of general relativity [16]. If the fluid undergoes a spatial transition from subsonic to supersonic flow, phonons (travelling with the speed of sound) can never escape the supersonic region against the direction of flow. In this sense, the supersonic region forms the analogue of an astrophysical black hole, from which not even light can ever escape again. The location of the transition from sub to supersonic flow is called a “sonic horizon”.

Due to the depth of this analogy, such a scenario should in principle afford us insight into Hawking radiation [16, 48, 49]. Other flow situations can help the study of cosmological particle production [50] and matter-wave superradiance [51]. The field of studying the consequences of Unruh’s discovery has become known as “analogue gravity” [17]. We will refer to the correspondence between scalar particles in curved spacetime and phonons in a BEC as “the analogy” throughout this thesis. Our contribution in chapter 5 is an in depth query to find the currently most promising experimental setup for the observation of analogue Hawking radiation. To create the flow profiles required, we will extensively use the BEC manipulation techniques introduced earlier in this chapter.

In all these projects, the motivation for our research stems from the analogies between BEC physics and the other physical disciplines listed above. Nonetheless, we strictly analyse the suitability of realistic BEC systems for analogue studies and hence the theories used and problems tackled are those of Bose-Einstein condensate physics.

1.4 List of Publications

The following is a complete list of articles published or submitted in conjunction with the authors PhD. The research described in articles 1 – 3 and 5 – 6 is presented in this thesis. Papers are sorted chronologically by the date of first submission.

1. “Collapsing Bose-Einstein Condensates beyond the Gross-Pitaevskii Approximation”; S. Wüster, J.J. Hope and C.M. Savage; Phys. Rev. A **71**, 033605 (2005).
2. “Numerical Study of the stability of Skyrmions in a Bose-Einstein Condensate”; S. Wüster, T.E. Argue and C.M. Savage; Phys. Rev. A **72**, 043616 (2005).
3. “Supersonic optical tunnels for Bose-Einstein condensates”; S. Wüster and B.J. Dąbrowska-Wüster; cond-mat/0602108 (2006).
4. “Quantum effects in the dynamical localization of Bose-Einstein condensates in optical lattices”; B.J. Dąbrowska-Wüster, S. Wüster, A.S. Bradley, M.J. Davis and E.A. Ostrovskaya; cond-mat/0607332 (2006).
5. “Quantum depletion of collapsing Bose-Einstein condensates”; S. Wüster, B.J. Dąbrowska-Wüster, A.S. Bradley, M.J. Davis, P.B. Blakie, J.J. Hope and C.M. Savage; cond-mat/0609417; Phys. Rev. A in press (2007).
6. “Limits to the analogue Hawking temperature in a Bose-Einstein condensate”; S. Wüster and C.M. Savage; in preparation (2007).

The contents of articles 1 and 5 are presented in chapter 3. Article 2 is included in chapter 4, which also contains contributions from article 3. The analogue gravity chapter 5 contains research from papers 3 and 6.

Chapter 2

Theory

This chapter briefly but systematically introduces the theoretical tools which are required in order to answer the questions posed in this thesis. In the process, we define our mathematical notation and highlight the relations between the approaches employed.

The most basic description of a Bose-Einstein condensate, on the mean-field level, is conceptually only slightly more involved than Schrödinger's equation. However the BEC's equation of motion is nonlinear, giving rise to a multitude of new phenomena [35]. Additionally, many of the topics covered in this thesis require more sophisticated tools: to deal with atom losses, supersonic flow, multi-component condensates, rotating traps and quantum corrections.

In our overview of the theory, we start from the many-body Hamiltonian, derive various incarnations of the Gross-Pitaevskii equation and finally include quantum corrections using two very different schemes: time dependent Hartree-Fock Bogoliobov theory and the truncated Wigner approach.

Our primary objective is a self-contained thesis. We also wish to offer practical guidance, regarding how and when subtleties in the theories have to be carefully considered and where they can be safely ignored.

This thesis is not primarily concerned with theory development. Some elements of the presented methods were however worked out (or re-developed) within the author's PhD, such as:

- The renormalisation of the HFB equations using Feynman diagrams (appendix A).
- The implementation of the time dependent Hartree-Fock Bogoliubov (HFB) equations in a spherical harmonic trap (appendix B).

- The sketch of the inclusion of three-body loss processes, also for the uncondensed component, in the HFB equations (section 2.4.5).

2.1 Microscopic Description of an Interacting Bose-Gas

After second quantisation [31], a system of interacting Bosons possesses the many-body Hamiltonian:

$$\begin{aligned} \hat{H} = & \int d^3\mathbf{x} \hat{\Psi}^\dagger(\mathbf{x}) \hat{H}_0(\mathbf{x}) \hat{\Psi}(\mathbf{x}) \\ & + \frac{1}{2} \iint d^3\mathbf{x} d^3\mathbf{x}' \hat{\Psi}^\dagger(\mathbf{x}) \hat{\Psi}^\dagger(\mathbf{x}') V_{int}(\mathbf{x} - \mathbf{x}') \hat{\Psi}(\mathbf{x}') \hat{\Psi}(\mathbf{x}), \end{aligned} \quad (2.1)$$

where $\hat{H}_0(\mathbf{x}) = -\frac{\hbar^2}{2m} \nabla_{\mathbf{x}}^2 + V(\mathbf{x})$ is the single particle Hamiltonian. Here $\hat{\Psi}(\mathbf{x})$ denotes the field operator in the Heisenberg picture that annihilates atoms of mass m at position \mathbf{x} . The fields obey the canonical commutation relations

$$[\hat{\Psi}(\mathbf{x}), \hat{\Psi}(\mathbf{x}')] = 0, \quad [\hat{\Psi}(\mathbf{x}), \hat{\Psi}^\dagger(\mathbf{x}')] = \delta^{(3)}(\mathbf{x} - \mathbf{x}'). \quad (2.2)$$

$V(\mathbf{x})$ is a potential, which the atoms experience, for example, due to interaction with external electromagnetic fields (section 1.2). A common example regularly encountered in this thesis is a cylindrically symmetric harmonic trap:

$$V(\mathbf{x}) = \frac{1}{2} m (\omega_\perp^2 x^2 + \omega_\perp^2 y^2 + \omega_z^2 z^2). \quad (2.3)$$

$V_{int}(\mathbf{x} - \mathbf{x}')$ parametrises the interaction between atoms at positions \mathbf{x} and \mathbf{x}' . Throughout this thesis we assume this interaction potential to be local:

$$V(\mathbf{x} - \mathbf{x}') = U_0 \delta^{(3)}(\mathbf{x} - \mathbf{x}'), \quad (2.4)$$

with interaction strength U_0 . We justified this step physically in section 1.2. Finally, we note that the Hamiltonian (2.1) is globally $U(1)$ symmetric, i.e. it is invariant under phase rotations of the field operator: $\hat{\Psi}(\mathbf{x}) \rightarrow \hat{\Psi}(\mathbf{x}) \exp(i\varphi)$, $\exp(i\varphi) \in U(1)$.

We can now derive the Heisenberg equation for the operator $\hat{\Psi}(\mathbf{x})$ from Eq. (2.1), using the above described contact potential:

$$i\hbar \frac{\partial}{\partial t} \hat{\Psi}(\mathbf{x}) = [\hat{\Psi}(\mathbf{x}), \hat{H}] = \hat{H}_0(\mathbf{x}) \hat{\Psi}(\mathbf{x}) + U_0 \hat{\Psi}^\dagger(\mathbf{x}) \hat{\Psi}(\mathbf{x}) \hat{\Psi}(\mathbf{x}). \quad (2.5)$$

The macroscopic occupation of a single mode of the interacting field is incorporated through the assumption that the atom field operator acquires an expectation value, which is the condensate wave function: $\phi(\mathbf{x}) = \langle \hat{\Psi}(\mathbf{x}) \rangle$. Equivalently, we can choose a particular many-body quantum state with a non-vanishing expectation value, such as a coherent state. The appearance of the condensate wave function breaks the $U(1)$ symmetry of the Hamiltonian, as condensates with different phase are macroscopically distinct objects.

The decomposition of $\hat{\Psi}(\mathbf{x})$ into its mean and fluctuations

$$\hat{\Psi}(\mathbf{x}) = \phi(\mathbf{x}) + \hat{\chi}(\mathbf{x}), \quad (2.6)$$

defines the fluctuation operator $\hat{\chi}(\mathbf{x})$. Inserting Eq. (2.6) into Eq. (2.5) and taking the expectation value yields:

$$\begin{aligned} i\hbar \frac{\partial}{\partial t} \langle \hat{\Psi}(\mathbf{x}) \rangle &= i\hbar \frac{\partial}{\partial t} \phi(\mathbf{x}) = \hat{H}_0(\mathbf{x})\phi(\mathbf{x}) + U_0 |\phi(\mathbf{x})|^2 \phi(\mathbf{x}) + 2U_0 \langle \hat{\chi}^\dagger(\mathbf{x})\hat{\chi}(\mathbf{x}) \rangle \phi(\mathbf{x}) \\ &\quad + U_0 \langle \hat{\chi}(\mathbf{x})\hat{\chi}(\mathbf{x}) \rangle \phi(\mathbf{x}) + U_0 \langle \hat{\chi}^\dagger(\mathbf{x})\hat{\chi}(\mathbf{x})\hat{\chi}(\mathbf{x}) \rangle. \end{aligned} \quad (2.7)$$

This equation forms our point of origin for the exploration of a couple of approximations to the full quantum evolution.

2.1.1 Loss Processes and the Master Equation

The Hermitian Hamiltonian in the previous section describes a system in which the number of particles is conserved. Atom losses can indeed often be neglected, as experiments are usually done in regimes where losses remain small. There are however cases where losses play a crucial role in the condensate dynamics. Two of these are covered in this thesis: (i) collapsing condensates and (ii) high density condensates for the creation of analogue Hawking radiation.

Due to the Hermiticity of any Hamiltonian, the loss has to be phenomenologically modelled at the level of the equation of motion. To do so, we represent our quantum system by its density operator $\hat{\rho}$. The evolution equation for $\hat{\rho}$, termed a *master equation*, in the presence of three-body losses with loss-constant K_3 has been derived by M. Jack in Ref. [52]:

$$\frac{d\hat{\rho}}{dt} = -\frac{i}{\hbar} [\hat{H}, \hat{\rho}] + \frac{K_3}{6} \int d^3 \mathbf{x} (2\hat{\Psi}(\mathbf{x})^3 \hat{\rho} \hat{\Psi}^\dagger(\mathbf{x})^3 - \hat{\Psi}^\dagger(\mathbf{x})^3 \hat{\Psi}(\mathbf{x})^3 \hat{\rho} - \hat{\rho} \hat{\Psi}^\dagger(\mathbf{x})^3 \hat{\Psi}(\mathbf{x})^3). \quad (2.8)$$

We can similarly include two-body (one-body) losses by replacing $\hat{\Psi}(\mathbf{x})^3$ with $\hat{\Psi}(\mathbf{x})^p$ and $\hat{\Psi}^\dagger(\mathbf{x})^3$ with $\hat{\Psi}^\dagger(\mathbf{x})^p$, where $p = 2$ ($p = 1$) [53]. In the density matrix

formalism, we have $\langle \hat{A} \rangle = \text{Tr}[\hat{\rho}\hat{A}]$ for an operator \hat{A} . From Eq. (2.8) we can then derive:¹

$$\frac{d\langle \hat{A} \rangle}{dt} = -\frac{i}{\hbar} \langle [\hat{A}, \hat{H}] \rangle + \frac{K_3}{6} \int d^3\mathbf{x}' (\langle [\hat{\Psi}^\dagger(\mathbf{x}')^3, \hat{A}] \hat{\Psi}(\mathbf{x}')^3 \rangle + \langle \hat{\Psi}^\dagger(\mathbf{x}')^3 [\hat{A}, \hat{\Psi}(\mathbf{x}')^3] \rangle). \quad (2.9)$$

We will make use of this result to include loss processes in the HFB formalism in sections 2.2.5 and 2.4.5. What we have presented so far applies to all theories of BEC contained in this chapter. As the next step, we focus our attention on the most basic and most popular one of these: the Gross-Pitaevskii theory.

2.2 The Gross-Pitaevskii Equation

For now we return to the conservative formulation (2.7), which we wish to cast into an approximate but easily applicable form. The most commonly used simplification is the *Gross-Pitaevskii* or *mean-field* approximation. It amounts to neglecting the operator $\hat{\chi}(\mathbf{x})$ in Eq. (2.7) and hence assuming that the quantum field is fully described by its mean field: $\hat{\Psi}(\mathbf{x}) \equiv \phi(\mathbf{x})$. This results in the famous Gross-Pitaevskii equation (GPE) [54, 55], also referred to as the Nonlinear Schrödinger equation (NLSE):

$$i\hbar \frac{\partial}{\partial t} \phi(\mathbf{x}) = \left(-\frac{\hbar^2}{2m} \nabla_{\mathbf{x}}^2 + V(\mathbf{x}) \right) \phi(\mathbf{x}) + U_0 |\phi(\mathbf{x})|^2 \phi(\mathbf{x}). \quad (2.10)$$

In the mean field picture, the interaction strength U_0 is related to the scattering length as discussed in the introduction: $U_0 = 4\pi\hbar^2 a_s/m$. The condensate wave function is normalised to the number of atoms in the condensate $\int d^3\mathbf{x} |\phi(\mathbf{x})|^2 = N$, which is conserved, as is the total energy defined in the next section. Since the Gross-Pitaevskii equation neglects all quantum fluctuations of the atomic field, we refer to it in the following also as the “semi-classical theory” of the BEC. One can derive a time-independent version (TIGPE) of the GPE using the Ansatz $\phi(\mathbf{x}, t) = \phi_0(\mathbf{x})e^{-i\mu t}$, where μ is the energy-eigenvalue, referred to as chemical potential. This makes $\phi_0(\mathbf{x})$ a stationary state of Eq. (2.10).

Due to their importance for this thesis, section 2.2.2 describes in quite a bit of detail how stationary and, in particular, ground states are most commonly found numerically. Before we get there, we would however like to present an alternative formulation of Eq. (2.10) that will also be tremendously useful in this thesis.

¹This is most easily seen by converting to the Schrödinger picture in an intermediate step and only assuming the Heisenberg picture again for the final result.

2.2.1 Hydrodynamic Equations

Using the Madelung representation $\phi = \sqrt{n} \exp(i\vartheta)$, we can define the atom number density n and velocity

$$\mathbf{v} = \hbar \nabla \vartheta / m. \quad (2.11)$$

By inserting these into Eq. (2.10) we can then derive the hydrodynamic equations for the BEC [34]:

$$\frac{\partial n}{\partial t} = -\nabla \cdot (n\mathbf{v}), \quad (2.12)$$

$$m \frac{\partial \mathbf{v}}{\partial t} = -\nabla \left[p_q + \frac{1}{2} m \mathbf{v}^2 + U n + V \right], \quad (2.13)$$

$$p_q = -\frac{\hbar^2 \nabla^2 \sqrt{n}}{2m\sqrt{n}}, \quad (2.14)$$

which are entirely equivalent to the Gross-Pitaevskii equation. (2.12) is an equation of continuity for the quantum fluid. Eq. (2.13) bears a close resemblance to Bernoulli's equation from fluid dynamics. The term that does not appear in Bernoulli's equation is the so-called "quantum pressure" p_q (2.14). If the condensate flow does not strongly vary on length scales shorter than the healing length

$$\xi = 1/\sqrt{8\pi n a_s} = \hbar/(\sqrt{2}mc), \quad (2.15)$$

p_q can be safely neglected. We call this situation the hydrodynamic regime. Under these circumstances, the BEC can be viewed as a viscosity-free, irrotational fluid.

For later reference we define the flow speed $v = |\mathbf{v}|$, the local speed of sound $c = \sqrt{Un/m}$ and the Mach number $M = v/c$. The expression for the local speed of sound stems from the dispersion relation for long wavelength perturbations around a stationary state of the GPE [34], a topic that we address in section 2.3.2.

As previously announced, we now turn towards the predominant method of constructing ground states for the GPE.

2.2.2 The Imaginary Time Method

In theoretical and experimental applications, the starting point for manipulations of the BEC is usually a well defined ground, or at least stationary state. Determining the existence and shape of particular stationary states is the main objective of our research in chapter 4 on Skyrmions and vortex rings. For the

analogue gravity project in chapter 5, we require a stationary BEC as the initial state for dynamical simulations. The most common method for the generation of stationary BEC states is imaginary time evolution.

Inserting $\hat{\Psi}(\mathbf{x}) \equiv \phi(\mathbf{x})$ into Eq. (2.1) we obtain the energy functional of $\phi(\mathbf{x})$:

$$E[\phi(\mathbf{x})] \equiv \langle \hat{H} \rangle = \int d^3\mathbf{x} \left(\phi^*(\mathbf{x}) \left[-\frac{\hbar^2}{2m} \nabla_{\mathbf{x}}^2 + V(\mathbf{x}) \right] \phi(\mathbf{x}) + \frac{U_0}{2} |\phi(\mathbf{x})|^4 \right). \quad (2.16)$$

We interpret Eq. (2.16) as a functional on a suitable vector space of functions \mathcal{F} (e.g. $\mathcal{F} = \mathcal{L}^{(2)}$, the space of all square integrable functions). Starting from a trial state $\phi_T(\mathbf{x}) \in \mathcal{F}$, we can find a local energy minimum by evolving $\phi(\mathbf{x})$ in the “direction” of steepest descent in energy within \mathcal{F} . This idea is explained more formally in Ref. [56]. Concretely, the state $\phi(\mathbf{x})$ is evolved in \mathcal{F} according to:

$$\frac{\partial \phi(\mathbf{x})}{\partial \tau} = -\nabla E[\phi(\mathbf{x})], \quad (2.17)$$

for a suitably chosen functional gradient ∇ and evolution parameter τ (the imaginary time coordinate). Using a functional derivative $\nabla E = \delta E / \delta \phi^*(\mathbf{x}) / \hbar$, we obtain the standard form of the imaginary time GPE :

$$\hbar \frac{\partial}{\partial \tau} \phi(\mathbf{x}) = - \left(-\frac{\hbar^2}{2m} \nabla_{\mathbf{x}}^2 + V(\mathbf{x}) \right) \phi(\mathbf{x}) - U_0 |\phi(\mathbf{x})|^2 \phi(\mathbf{x}). \quad (2.18)$$

This expression also follows from Eq. (2.10) by the substitution $t = -i\tau$, which gives rise to the method’s name. The normalisation of $\phi(\mathbf{x})$ is not conserved by Eq. (2.18). Therefore we narrow \mathcal{F} to the space of functions with fixed norm \mathcal{F}_N , to avoid evolution towards the trivial energy minimum $\phi(\mathbf{x}) \equiv 0$. In the practical implementation, this is achieved by rescaling $\phi(\mathbf{x})$ to the desired norm N after each numerical timestep. Using this rescaling procedure, $\phi(\mathbf{x})$ is propagated with Eq. (2.18) until it converges. If that occurs, $\phi(\mathbf{x})$ has to be a stationary state $\phi_0(\mathbf{x})$ of the GPE.

Occasionally, we know the chemical potential μ of the target state, rather than its atom number N . We can then use the equation

$$\hbar \frac{\partial}{\partial \tau} \phi(\mathbf{x}) = - \left(-\frac{\hbar^2}{2m} \nabla_{\mathbf{x}}^2 + V(\mathbf{x}) \right) \phi(\mathbf{x}) - U_0 |\phi(\mathbf{x})|^2 \phi(\mathbf{x}) + \mu \phi(\mathbf{x}), \quad (2.19)$$

without any rescaling of the norm. This procedure can be interpreted as minimisation of the free energy functional $F[\phi] = E[\phi] - \mu \int d^3\mathbf{x} |\phi|^2$ in the unconstrained space \mathcal{F} [56]. Our two choices of function space and functional to be minimised can be further combined with other choices for the derivative ∇ , such as *Sobolev-gradients* [56], which can improve convergence.

If the trial state $\phi_T(\mathbf{x})$ does not possess symmetries which Eq. (2.19) preserves, the method usually converges towards the global ground state. However, if we are interested in states with a particular topological structure or symmetry, choosing $\phi_T(\mathbf{x})$ in the same topological class (see section 4.1.1), often allows us to find local energy minima with the selected topology. In terms of the energy landscape defined by Eq. (2.16), we need to choose the initial state sufficiently “close” to the target, such that it lies within the energy valley containing the local minimum.

It is obvious that the parameter τ , while termed “imaginary time”, does not represent time in this formalism. There is however the expectation that a quasi-stationary system in the presence of a dissipative mechanism, whereby it can lower its energy, would evolve in a fashion qualitatively similar to the imaginary time trajectory. This idea can be formalised in a combined real-time and imaginary-time method [57].

In this thesis we make the most extensive use of the imaginary time method in chapter 4. There we require additional tools to deal with rotating reference frames and multi component BECs, which we discuss in the next two sections.

2.2.3 Rotating Frames

There are situations in which the BEC has to be treated in a reference frame which rotates with an angular velocity $\boldsymbol{\Omega}$ with respect to the laboratory. As an example we might want to determine the BEC ground state in a rotating harmonic trap, which has a slight deviation from spherical symmetry. This is done by imaginary time propagation in the rest frame of the trap. For sufficiently large $|\boldsymbol{\Omega}|$, the resulting ground state contains quantised vortices [38].

The transformation of the Hamiltonian (2.1) into the rotating frame yields [58]:

$$\hat{H}' = \hat{H} - \int d^3\mathbf{x} \hat{\Psi}^\dagger(\mathbf{x}) \boldsymbol{\Omega} \cdot \hat{\mathbf{L}} \hat{\Psi}(\mathbf{x}), \quad (2.20)$$

where $\hat{\mathbf{L}} = \hat{\mathbf{x}} \times \hat{\mathbf{p}}$ is the angular momentum operator. From this we obtain the real time GPE:

$$i\hbar \frac{\partial}{\partial t} \phi(\mathbf{x}) = \left(-\frac{\hbar^2}{2m} \nabla_{\mathbf{x}}^2 + V(\mathbf{x}) + U_0 |\phi(\mathbf{x})|^2 - \boldsymbol{\Omega} \cdot \hat{\mathbf{L}} \right) \phi(\mathbf{x}). \quad (2.21)$$

We choose the z -axis parallel to $\boldsymbol{\Omega}$, so that $\boldsymbol{\Omega} \cdot \hat{\mathbf{L}} = \Omega \hat{L}_z$. For the application mentioned initially in this sub-section, an imaginary time version of Eq. (2.21) can be easily obtained.

Rotating Frame Ehrenfest Relations

Care has to be taken when combining frame transformations with the hydrodynamic view presented in section 2.2.1. Let $\phi_R(\mathbf{x}) = \sqrt{n_R} \exp(i\vartheta_R)$ be the rotating frame wave function for which Eq. (2.21) holds. Counterintuitively, the gradient of its phase (see section 2.2.1) is still the condensate velocity in the *lab-frame*. To see this, we define $\mathbf{v}_R = \hbar \nabla \vartheta_R / m$ and derive a continuity equation from Eq. (2.21):

$$\frac{\partial n_R}{\partial t} = -\nabla \cdot (n_R \mathbf{v}_R - n_R \boldsymbol{\Omega} \times \mathbf{r}). \quad (2.22)$$

For this to have the same form as the continuity equation (2.12), the velocity in the rotating frame needs to be given by $\mathbf{v}' = \mathbf{v}_R - \boldsymbol{\Omega} \times \mathbf{r}$. A comparison with the velocity transformation from classical mechanics $\mathbf{v}' = \mathbf{v} - \boldsymbol{\Omega} \times \mathbf{r}$ [59], shows that we can identify \mathbf{v}_R with the velocity in the lab-frame.

To gain some feeling for the physics that is added to the GPE by the appearance of the angular momentum operator, we consider an Ehrenfest relation resulting from Eq. (2.21). Defining $\langle \hat{A} \rangle = \int d^3\mathbf{x} \phi_R^*(\mathbf{x}) \hat{A} \phi_R(\mathbf{x})$, we can derive the equation of motion for the expectation value of the momentum operator in the rotating frame:

$$\frac{\partial \langle \hat{\mathbf{p}}' \rangle}{\partial t} = - \left(\langle \nabla V \rangle + \langle \nabla U n_R \rangle + \langle 2(\boldsymbol{\Omega} \times \hat{\mathbf{p}}') \rangle + m \langle \boldsymbol{\Omega} \times (\boldsymbol{\Omega} \times \hat{\mathbf{r}}') \rangle \right). \quad (2.23)$$

It is apparent that due to the transformation to the rotating frame, the Ehrenfest relation contains terms reminiscent of the Coriolis and centrifugal forces.

2.2.4 Multi-component Condensates

Up till now, we assumed a BEC of atoms where no internal degree of freedom is relevant. This need not be the case. It is possible to create BECs with multiple components, which were introduced in section 1.2. In this thesis we study exclusively systems where the atom number within each component of the BEC is separately conserved. Let us consider the BEC as required for chapter 4, with two components $|1\rangle$ and $|2\rangle$. The situation requires the introduction of two field operators $\hat{\Psi}_1$ and $\hat{\Psi}_2$ in the Hamiltonian and the addition of interactions between the two fields. For brevity we only display the resulting two-component coupled Gross-Pitaevskii equations:

$$i\hbar \frac{\partial}{\partial t} \phi_i(\mathbf{x}) = \left(-\frac{\hbar^2}{2m} \nabla^2 + V(\mathbf{x}) + \sum_{j=1,2} U_{ij} |\phi_j(\mathbf{x})|^2 \right) \phi_i(\mathbf{x}). \quad (2.24)$$

Here the $\phi_i(\mathbf{x})$ for $i = 1, 2$ denote the BEC wave functions of the two components, for which we can define densities $n_i = |\phi_i|^2$ and velocities \mathbf{v}_i analogous to the single component case. The normalisation of the wave functions is taken as N_1 and N_2 , the numbers of atoms in each component respectively. The interaction parameters U_{ij} are proportional to the scattering lengths for intra (U_{11}, U_{22}) and inter component (U_{12}) interactions: $U_{ij} = 4\pi\hbar^2 a_{ij}/m$.

If the atom number in each component is not separately conserved, for example in a situation where hyperfine state changing collisions are allowed, we obtain the slightly more complicated situation of a spinor condensate [34] with different equations of motion.

Two Component Speed of Sound and Phase Separation

We now consider the dispersion relation of a two-component BEC to obtain an expression for its speed of sound. The long wavelength limit of the two-component excitation spectrum $\omega_{\pm}(k)$ can be found in Ref. [34] for a homogenous system:

$$c_{\pm} = \lim_{k \rightarrow 0} \frac{\omega_{\pm}(k)}{k} = \sqrt{\frac{U_{11}n_1 + U_{22}n_2}{2m}} \pm \frac{1}{2} \sqrt{\left(\frac{U_{11}n_1 - U_{22}n_2}{2m}\right)^2 + \frac{4U_{12}n_1n_2}{m^2}}. \quad (2.25)$$

It is easily shown, that the velocity c_- becomes imaginary if

$$U_{12}^2 > U_{11}U_{22}. \quad (2.26)$$

This indicates the presence of imaginary energy eigenvalues among the excitations, which signals dynamical instabilities, an issue that will be further discussed in section 2.3. If $U_{12}^2 > U_{11}U_{22}$, large mixtures of the two components are unstable, causing them to undergo “phase-separation”: The components $|1\rangle$ and $|2\rangle$ segregate into distinct spatial regions, with only a small zone of overlap at the contact surface. The depth of the overlap region is such that it only allows small-wavelength two-component excitations, for which c_- remains real.

Under the phase separation conditions (2.26), a fully mixed two component BEC is also energetically unstable, as can be easily shown for the untrapped case [60, 61]. The two mixed components can lower their energy by spatially segregating. We will give a more precise discussion of energetic vs. dynamic instability in section 2.3.3. The *phase-separation criterion* Eq. (2.26) will play a major role in chapter 4.

2.2.5 Atom Losses

Our final extension of the basic GP equation (2.10) is to describe atom losses. After previous preparations these are easily incorporated. We start from Eq. (2.9) by adding terms required for one and two-body losses as outlined in section 2.1.1. The operator \hat{A} will be the field operator $\hat{\Psi}(\mathbf{x})$. After making use of the commutation relations (2.2), we replace $\hat{\Psi}(\mathbf{x})$ by $\phi(\mathbf{x})$. The result is:

$$i\hbar \frac{\partial}{\partial t} \phi(\mathbf{x}) = \left(-\frac{\hbar^2}{2m} \nabla_{\mathbf{x}}^2 + V(\mathbf{x}) + U_0 |\phi(\mathbf{x})|^2 - i\frac{\hbar}{2} (K_1 + K_2 |\phi(\mathbf{x})|^2 + K_3 |\phi(\mathbf{x})|^4) \right) \phi(\mathbf{x}). \quad (2.27)$$

The total number of atoms N is no longer conserved due to the appearance of dissipative terms, and its time evolution is given by:

$$\frac{\partial N}{\partial t} = -K_1 \int d^3\mathbf{x} |\phi(\mathbf{x})|^2 - K_2 \int d^3\mathbf{x} |\phi(\mathbf{x})|^4 - K_3 \int d^3\mathbf{x} |\phi(\mathbf{x})|^6, \quad (2.28)$$

where we have introduced the one and two-body loss coefficients K_1 and K_2 . This concludes our introduction to the semi-classical theory of Bose-Einstein condensates. In the next section we go beyond the mean-field approximation to consider quantum excitations of the BEC.

2.3 The Bogoliubov Equations

A first step to include quantum corrections beyond the Gross-Pitaevskii mean field is the use of Bogoliubov theory [62]. We now no longer neglect the fluctuation operator $\hat{\chi}(\mathbf{x})$. Instead, we insert the definition (2.6) into Eq. (2.5), subtract the evolution of the mean field Eq. (2.10), and linearise the resulting equation with respect to $\hat{\chi}(\mathbf{x})$. This results in the operator equation [45]:

$$i\hbar \frac{\partial}{\partial t} \hat{\chi}(\mathbf{x}) = \hat{H}_0(\mathbf{x}) \hat{\chi}(\mathbf{x}) + U_0 \left(2|\phi(\mathbf{x})|^2 \hat{\chi}(\mathbf{x}) + \phi(\mathbf{x})^2 \hat{\chi}^\dagger(\mathbf{x}) \right). \quad (2.29)$$

In this section we only consider stationary scenarios. We thus assume that the condensate fulfills $\mu\phi(\mathbf{x}) = \hat{H}_0(\mathbf{x})\phi(\mathbf{x}) + U_0|\phi(\mathbf{x})|^2\phi(\mathbf{x})$. Now we expand $\hat{\chi}(\mathbf{x})$ in terms of *quasi-particle* annihilation and creation operators $\hat{\alpha}_i, \hat{\alpha}_i^\dagger$:

$$\hat{\chi}(\mathbf{x}) = \exp(-i\mu t/\hbar) \sum_i \left[u_i(\mathbf{x}) \exp(-i\epsilon_i t/\hbar) \hat{\alpha}_i - v_i^*(\mathbf{x}) \exp(i\epsilon_i t/\hbar) \hat{\alpha}_i^\dagger \right]. \quad (2.30)$$

Here i is a collective index numbering the possible excitation modes. The linearised equations for the mode functions u_i , v_i derived from Eq. (2.29) are called Bogoliubov equations:

$$\begin{aligned} \left(-\frac{\hbar^2}{2m} \nabla_{\mathbf{x}}^2 + V(\mathbf{x}) + 2U_0|\phi(\mathbf{x})|^2 - \mu - \epsilon_i \right) u_i(\mathbf{x}) - U_0\phi(\mathbf{x})^2 v_i(\mathbf{x}) &= 0, \\ \left(-\frac{\hbar^2}{2m} \nabla_{\mathbf{x}}^2 + V(\mathbf{x}) + 2U_0|\phi(\mathbf{x})|^2 - \mu + \epsilon_i \right) v_i(\mathbf{x}) - U_0\phi^*(\mathbf{x})^2 u_i(\mathbf{x}) &= 0. \end{aligned} \quad (2.31)$$

Being linear in the u_i and v_i , these equations do not fix the quantum depletion, i.e. the fraction of uncondensed particles that are present even at zero-temperature due to the interaction. The depletion is encoded in the amplitudes of the u_i and v_i . However, for the operators \hat{a}_i and \hat{a}_i^\dagger to obey the commutation relations of creation and destruction operators, we also have to demand [34]:

$$\int d^3\mathbf{x} [|u_i(\mathbf{x})|^2 - |v_i(\mathbf{x})|^2] = 1. \quad (2.32)$$

This condition determines the quantum depletion, as is most easily seen in a homogenous case [34]. There Eq. (2.32) can be used in conjunction with Eqns. (2.31) to obtain an explicit expression for the mode functions u_i and v_i . Their amplitudes depend on U_0 . The depletion in this simple case is:

$$\frac{n_{\text{unc}}}{n} = \frac{8}{3\sqrt{\pi}}(na_s^3)^{1/2}, \quad (2.33)$$

where we used the density of uncondensed atoms $n_{\text{unc}} = \langle \hat{\chi}^\dagger(\mathbf{x})\hat{\chi}(\mathbf{x}) \rangle$. For this result the BEC quantum state is assumed to be the *Bogoliubov vacuum* $|0\rangle$ defined by:

$$\hat{a}_i|0\rangle = 0 \quad \forall i. \quad (2.34)$$

2.3.1 Classical Condensate Excitations vs. Bogoliubov Quasi-Particles

The theory shown so far in this section deals explicitly with quantised excitations of the BEC. It can also be of interest to find the *classical* excitation modes of the condensate by inserting the Ansatz $\phi_0(\mathbf{x}) + \delta\phi(\mathbf{x}, t)$ into the GPE (2.10). In this expression we added some excitation $\delta\phi(\mathbf{x}, t)$ to $\phi_0(\mathbf{x})$, the stationary state². Our goal is to find the eigenfrequencies of $\delta\phi(\mathbf{x}, t)$.

²For simplicity, we assume a chemical potential $\mu = 0$ for the condensate.

Expanding $\delta\phi(\mathbf{x}, t) = \sum_i \tilde{u}_i(\mathbf{x})e^{-i\omega_j t} - \tilde{v}_i(\mathbf{x})e^{+i\omega_j t}$, we find that the condensate excitation modes \tilde{u}_i, \tilde{v}_i obey the same equation (2.31) as the quantum mode functions. Due to the algebraic similarities in the construction this is not surprising. However in the semi-classical treatment, the condensate modes \tilde{u}_i, \tilde{v}_i do not have to obey Eq. (2.32), they can be arbitrarily normalised³.

A mode represents a classical fluctuation *within* the condensate or has to be treated as part of the fluctuating field $\hat{\chi}$, depending on whether a coherent phase relation to the condensate wave function exists [63]. To be more specific, we can consider a quantum state where some $\langle \hat{a}_i \rangle = z \neq 0$ for $z \in \mathbb{C}$, i.e. the quasi-particle annihilation operator acquires an expectation value. By definition, such a mode forms part of the condensate. For incoherent excitations we have $\langle \hat{a}_i \rangle = 0$, identifying the mode as part of the fluctuation field. The difference can be understood nicely in the stochastic theory of BECs in section 2.5, where we will briefly revisit this topic.

To summarise: Perturbations of the classical condensate wave function $\delta\phi(\mathbf{x}, t)$ and quantised excitations $\hat{\chi}$ (quasi-particles) of the atom field are governed by the same equations (2.31) for their eigenmodes. Whether they are to be treated as one or the other depends entirely on the coherence relation between the modes and the condensate.

We now turn our attention to the energy spectrum of either kind of excitation.

2.3.2 The Bogoliubov Dispersion Relation

In the homogenous case the Bogoliubov equations are easy to solve. Due to translational symmetry we can write $u_q(\mathbf{x}) = u_q e^{i\mathbf{qx}}/\sqrt{V}$ and $v_q(\mathbf{x}) = v_q e^{i\mathbf{qx}}/\sqrt{V}$ for a continuous wave number q [34]. With this Ansatz, Eq. (2.31) yields nontrivial solutions for u_q and v_q only if:

$$\epsilon_q^2 = \frac{\hbar^2 q^2}{2m} \left(\frac{\hbar^2 q^2}{2m} + 2nU_0 \right). \quad (2.35)$$

This is the Bogoliubov dispersion relation [62]. n denotes the condensate density $n = |\phi(\mathbf{x})|^2 = \text{const.}$ We can further proceed to solve for explicit values of u_q and v_q once a specific normalisation is chosen. The result, together with the dispersion relation, is shown in Fig. 2.1. The graph displays the main feature of the Bogoliubov dispersion relation: At large wavelengths $\lambda = 2\pi/q$, the condensate

³The relative amplitude of \tilde{u}_j and \tilde{v}_j is constrained by Eqs. (2.31), however their common normalisation is arbitrary.

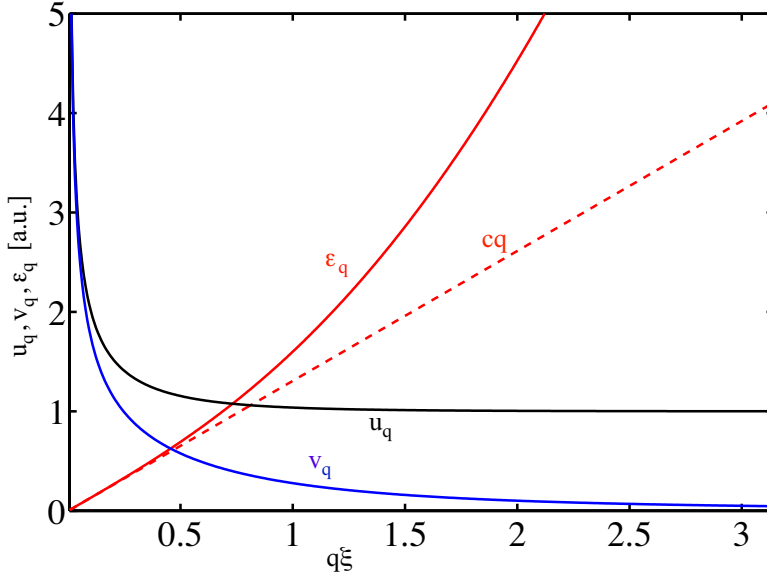


Figure 2.1: Bogoliubov dispersion relation ϵ_q (red) and mode functions u_q (black), v_q (blue). For the normalisation of the modes we took $|u_q|^2 - |v_q|^2 = 1$. All quantities are shown in arbitrary units. The maximal displayed value of q corresponds to a wavelength of $\lambda = 2\xi$.

excitations (whether classical or quantum) obey a linear dispersion relation. This is reminiscent of sound waves (phonons) with wave number k , whose frequency ω is connected to the speed of sound c by $\omega = ck$. In this limit we recover from Eq. (2.35) the result $c = \sqrt{Un/m}$ noted earlier. The large wavelength domain is thus called the *phononic* regime.

At smaller wavelengths the dispersion relation becomes quadratic, which is characteristic of a free particle. An interpretation of high energy modes as particle-like excitations is further supported by the behaviour of the amplitudes u_q , v_q . For $q \rightarrow \infty$, v_q tends to zero [34]. The excitation mode $\delta\phi(\mathbf{x})$ then just takes the shape of a single particle momentum eigenstate with momentum $\hbar q$, according to Eq. (2.30). The wavelength scale for this transition is given by $2\pi\xi$, where ξ is the healing length (2.15).

Another feature of the spectrum Eq. (2.35) is the absence of a gap, i.e. $\lim_{q \rightarrow 0} \epsilon_q = 0$. This will be relevant in section 2.4.1. In contrast, the excitation spectrum of a Cooper-pair condensate in a superconductor exhibits an energy-gap, giving rise to the superconductivity effect itself.

The gaplessness of the Bogoliubov spectrum persists also in inhomogenous situations, where Eqs. (2.31) can be shown to possess a mode $u_0 = \phi(\mathbf{x})$, $v_0 =$

$\phi^*(\mathbf{x})$ with vanishing energy⁴.

Beyond these basic results for a homogenous BEC, the Bogoliubov spectrum ϵ_i also offers a wealth of information in more complicated situations, as we will now see.

2.3.3 Energetical and Dynamical Stability

For any given stationary state of the GPE, the solutions of Eqs. 2.31 can appear with real or complex energy eigenvalues ϵ_i . Stable oscillatory solutions have real positive energies. An inspection of Eq. (2.30) shows that modes whose energy possesses an imaginary part will exponentially grow in time. The presence of imaginary eigenvalues in the Bogoliubov spectrum therefore signals *dynamical instability* of the underlying stationary BEC state.

A state is *energetically stable*, if it represents a local minimum of the energy functional (2.16). In this case, no small perturbation can lower the energy. The imaginary time method that we reviewed in section 2.2.2 thus determines energetic stability. Stationary states that are energetically unstable exhibit real negative eigenvalues in the Bogoliubov spectrum.

It has been shown that for solutions of the GPE, energetic stability implies dynamic stability [64]. The converse is however not true, and in energetically unstable situations, dynamical stability can be separately established. This is crucial in the context of analogue gravity (chapter 5).

2.3.4 Hydrodynamic Representation of the Fluctuation Field

The core result of analogue gravity (section 1.3), can be derived for a BEC by combining the Bogoliubov methodology with the hydrodynamic formulation of section 2.2.1. Our starting point is Eq. (2.29). We further recall from section 2.2.1 that we can write the condensate as $\phi(\mathbf{x}) = \sqrt{n(\mathbf{x})} \exp(i\vartheta(\mathbf{x}))$ to deduce its velocity $\mathbf{v} = \hbar \nabla \vartheta(\mathbf{x})/m$.

We now define Hermitian fields

$$\begin{aligned}\hat{n}_1(\mathbf{x}) &= \sqrt{n(\mathbf{x})} (e^{-i\vartheta(\mathbf{x})} \hat{\chi}(\mathbf{x}) + e^{i\vartheta(\mathbf{x})} \hat{\chi}^\dagger(\mathbf{x})), \\ \hat{\theta}(\mathbf{x}) &= \frac{i}{2\sqrt{n(\mathbf{x})}} (e^{-i\vartheta(\mathbf{x})} \hat{\chi}(\mathbf{x}) - e^{i\vartheta(\mathbf{x})} \hat{\chi}^\dagger(\mathbf{x})),\end{aligned}\tag{2.36}$$

⁴Which however is not normalisable according to Eq. (2.32).

i.e. $\hat{n}_1 = \hat{n}_1^\dagger$ and $\hat{\theta} = \hat{\theta}^\dagger$. These furnish the *acoustic representation* of the fluctuating field [50]:

$$\hat{\chi}(\mathbf{x}) = e^{i\vartheta(\mathbf{x})} \left(\frac{1}{2\sqrt{n(\mathbf{x})}} \hat{n}_1(\mathbf{x}) - i\sqrt{n(\mathbf{x})} \hat{\theta}(\mathbf{x}) \right). \quad (2.37)$$

With the hermiticity of \hat{n}_1 and $\hat{\theta}$ in mind, we see that $\hat{n}_1(\mathbf{x})$ is associated with density fluctuations and $\hat{\theta}(\mathbf{x})$ with phase fluctuations of the atom field.

Inserting Eq. (2.37) into Eq. (2.29) and extracting the self-adjoint and anti-self-adjoint parts of the equation we obtain [50]:

$$\frac{\partial \hat{n}_1(\mathbf{x})}{\partial t} = -\nabla \cdot \left(\nabla \cdot \mathbf{v}(\mathbf{x}) \hat{n}_1(\mathbf{x}) - \frac{\hbar n(\mathbf{x})}{m} \nabla \hat{\theta}(\mathbf{x}) \right), \quad (2.38)$$

$$\frac{\partial \hat{\theta}(\mathbf{x})}{\partial t} = \frac{U}{\hbar} \hat{n}_1(\mathbf{x}) - \mathbf{v}(\mathbf{x}) \cdot \nabla \hat{\theta}(\mathbf{x}) - \frac{\hbar^2}{2m} D_2 \hat{n}_1(\mathbf{x}), \quad (2.39)$$

where the operator D_2 is defined by:

$$D_2 \hat{n}_1(\mathbf{x}) = -\frac{1}{2} \frac{\nabla^2 \sqrt{n(\mathbf{x})}}{\sqrt{n(\mathbf{x})}^3} \hat{n}_1(\mathbf{x}) + \frac{1}{2} \frac{1}{\sqrt{n(\mathbf{x})}} \nabla^2 \left(\frac{\hat{n}_1(\mathbf{x})}{\sqrt{n(\mathbf{x})}} \right). \quad (2.40)$$

In the hydrodynamic regime of the background condensate flow, defined in section 2.2.1, the first term in $D_2 \hat{n}_1(\mathbf{x})$ can be neglected⁵. The following treatment also neglects the second term. Due to the involvement of the field operator $\hat{n}_1(\mathbf{x})$ itself, this cannot be justified by assumptions on the background flow alone. This *acoustic approximation* thus limits the validity of the following results to modes of the fluctuation field whose wave numbers are shorter than the inverse healing length $1/\xi$ [50]. It is possible to keep the operator D_2 in subsequent expressions, an approach which is elaborated in [50, 65] but not further treated here.

By combining Eqs. (2.38)-(2.39), we can derive a single second order partial differential equation for the field operator $\hat{\theta}(\mathbf{x})$:

$$\frac{1}{\sqrt{-g}} \partial_\mu (\sqrt{-g} g^{\mu\nu} \partial_\nu) \hat{\theta}(\mathbf{x}, t) = 0. \quad (2.41)$$

Here we imply the Einstein summation convention [66]. Further we have defined the 4-derivative $\partial_\mu = (\frac{\partial}{\partial t}, \frac{\partial}{\partial x}, \frac{\partial}{\partial y}, \frac{\partial}{\partial z})^T$ and the *effective inverse metric*:

$$g^{\mu\nu} = \frac{1}{n(\mathbf{x})c(\mathbf{x})} \begin{pmatrix} -1 & \vdots & -v_j \\ \cdots & \ddots & \cdots \\ -v_i & \vdots & (c(\mathbf{x})^2 \delta_{ij} - v_i v_j) \end{pmatrix}, \quad g = \det(g) = \frac{n(\mathbf{x})^2}{c(\mathbf{x})}. \quad (2.42)$$

⁵It is proportional to the quantum pressure term.

Equation (2.41) is the Klein-Gordon equation of a massless, minimally coupled, scalar quantum field in a curved space-time with metric $g_{\mu\nu}$ [16, 66], as we have claimed in the introduction.

This result motivates the whole of chapter 5 and with its presentation we conclude our discussion of the linearised quantum theory of a BEC.

2.4 Hartree-Fock-Bogoliubov Theory

The Bogoliubov equations for classical or quantised condensate fluctuations provide a limited way to study effects beyond the mean field. There are several aspects in which that formalism is incomplete: we neglect contributions to the mode energy by self-interactions of the constituent atoms. Further we take the condensate $\phi_0(\mathbf{x})$ as fixed when determining the Bogoliubov modes. In reality, for sufficiently large depletion, the interaction with the thermal cloud will change the shape of the condensate wave function.

Eq. (2.7) shows that a complete theory would require the time-evolution of the fluctuation operator $\hat{\chi}(\mathbf{x})$. A full quantum treatment of the nonlinear, multimode, many particle problem poses a formidable challenge. Here we only provide an approximation of the quantum evolution, which does however go beyond the simple Bogoliubov method of the previous section.

To this end, one describes the quantum fluctuations in terms of their correlation functions. We define the normal and anomalous correlation functions of $\hat{\chi}(\mathbf{x})$:

$$G_N(\mathbf{x}, \mathbf{x}') = \langle \hat{\chi}^\dagger(\mathbf{x}') \hat{\chi}(\mathbf{x}) \rangle, \quad G_A(\mathbf{x}, \mathbf{x}') = \langle \hat{\chi}(\mathbf{x}') \hat{\chi}(\mathbf{x}) \rangle. \quad (2.43)$$

Throughout this section we will make the simplifying assumption that the many body quantum state is gaussian. For example a single mode gaussian quantum state is defined as one whose density matrix takes the form: [13]

$$\hat{\rho} = \mathcal{N} \exp \left(-n \hat{a}^\dagger \hat{a} - \frac{1}{2} m \hat{a}^{\dagger 2} - \frac{1}{2} m^* \hat{a}^2 \right), \quad (2.44)$$

for some constants n, m , a normalisation factor \mathcal{N} and single mode creation and annihilation operators \hat{a}^\dagger, \hat{a} . Also the multimode generalisation can be written as an exponential of a quadratic form of single particle ladder operators [67]. A special case of this (the coherent state) was already underpinning the spontaneous symmetry breaking idea in section 2.1. We can then make use of *Wick's*

theorem from quantum field theory, which states that for a gaussian quantum state averages of arbitrary operators \hat{O}_i can be factorised as follows [67]:

$$\langle \hat{O}_1 \hat{O}_2 \hat{O}_3 \rangle = \underline{\hat{O}_1} \hat{O}_2 \langle \hat{O}_3 \rangle + \hat{O}_1 \underline{\hat{O}_3} \langle \hat{O}_2 \rangle + \langle \hat{O}_1 \rangle \underline{\hat{O}_2} \hat{O}_3 + \langle \hat{O}_1 \rangle \langle \hat{O}_2 \rangle \langle \hat{O}_3 \rangle \quad (2.45)$$

$$= \langle \hat{O}_1 \hat{O}_2 \rangle \langle \hat{O}_3 \rangle + \langle \hat{O}_1 \hat{O}_3 \rangle \langle \hat{O}_2 \rangle + \langle \hat{O}_1 \rangle \langle \hat{O}_2 \hat{O}_3 \rangle - 2 \langle \hat{O}_1 \rangle \langle \hat{O}_2 \rangle \langle \hat{O}_3 \rangle,$$

$$\langle \hat{O}_1 \hat{O}_2 \hat{O}_3 \hat{O}_4 \rangle = \underline{\hat{O}_1} \hat{O}_2 \underline{\hat{O}_3} \hat{O}_4 + \hat{O}_1 \underline{\hat{O}_3} \underline{\hat{O}_2} \hat{O}_4 + \hat{O}_1 \underline{\hat{O}_4} \underline{\hat{O}_2} \hat{O}_3 + \langle \hat{O}_1 \rangle \langle \hat{O}_2 \rangle \langle \hat{O}_3 \rangle \langle \hat{O}_4 \rangle, \quad (2.46)$$

$$\underline{\hat{O}_a} \hat{O}_b = \langle \hat{O}_a \hat{O}_b \rangle - \langle \hat{O}_a \rangle \langle \hat{O}_b \rangle.$$

They can thus be re-written as the sum over all possible factorisations into *contractions*⁶ of operators.

Using Wick's theorem Eq. (2.7) becomes:

$$\begin{aligned} i\hbar \frac{\partial}{\partial t} \phi(\mathbf{x}) &= \hat{H}_0(\mathbf{x})\phi(\mathbf{x}) + U_0 |\phi(\mathbf{x})|^2 \phi(\mathbf{x}) \\ &\quad + 2\tilde{U}_0 G_N(\mathbf{x}, \mathbf{x})\phi(\mathbf{x}) + U_0 G_A(\mathbf{x}, \mathbf{x})\phi^*(\mathbf{x}). \end{aligned} \quad (2.47)$$

The notation \tilde{U}_0 is introduced in anticipation of the next section, for now there shall be no distinction between \tilde{U}_0 and U_0 . To obtain the above result we have combined Eq. (2.45) with $\langle \hat{\chi}(\mathbf{x}) \rangle = \langle \hat{\chi}^\dagger(\mathbf{x}) \rangle = 0$ to reach $\langle \hat{\chi}^\dagger(\mathbf{x}) \hat{\chi}(\mathbf{x}) \hat{\chi}(\mathbf{x}) \rangle = 0$. From now on, we use the shorthand $\bar{G}_N(\mathbf{x}) = G_N(\mathbf{x}, \mathbf{x})$ and $\bar{G}_A(\mathbf{x}) = G_A(\mathbf{x}, \mathbf{x})$. Due to the relation $\bar{G}_N = \langle \hat{\Psi}^\dagger(\mathbf{x}) \hat{\Psi}(\mathbf{x}) \rangle - |\phi(\mathbf{x})|^2$ between \bar{G}_N , the total density of atoms $\langle \hat{\Psi}^\dagger(\mathbf{x}) \hat{\Psi}(\mathbf{x}) \rangle$ and the density of condensate atoms $|\phi(\mathbf{x})|^2$, we identify \bar{G}_N as the density of the uncondensed component of the atomic cloud.

Eq. (2.47) thus includes the interaction between the condensed and uncondensed components. To obtain a closed set of equations, we also require time evolution expressions for G_A and G_N . These are obtained from the Heisenberg

⁶We refer to $\underline{\hat{O}_1} \hat{O}_2$ as the contraction of the operators \hat{O}_1, \hat{O}_2 .

equations for the operators $\hat{\chi}^\dagger(\mathbf{x}')\hat{\chi}(\mathbf{x})$ and $\hat{\chi}(\mathbf{x}')\hat{\chi}(\mathbf{x})$ which gives us:

$$\begin{aligned} i\hbar \frac{\partial G_A(\mathbf{x}, \mathbf{x}')}{\partial t} &= \langle [\hat{\chi}(\mathbf{x}')\hat{\chi}(\mathbf{x}), \hat{H}] \rangle = \\ &\left[\hat{H}_0(\mathbf{x}) + \hat{H}_0(\mathbf{x}') \right] G_A(\mathbf{x}, \mathbf{x}') + 2\tilde{U}_0 \left[|\phi(\mathbf{x})|^2 + |\phi(\mathbf{x}')|^2 + \bar{G}_N(\mathbf{x}) + \bar{G}_N(\mathbf{x}') \right] G_A(\mathbf{x}, \mathbf{x}') \\ &+ U_0 \left[\phi(\mathbf{x})^2 G_N^*(\mathbf{x}, \mathbf{x}') + \phi(\mathbf{x}')^2 G_N(\mathbf{x}, \mathbf{x}') + \bar{G}_A(\mathbf{x}) G_N^*(\mathbf{x}, \mathbf{x}') + \bar{G}_A(\mathbf{x}') G_N(\mathbf{x}, \mathbf{x}') \right] \\ &+ U_0 \left[\phi(\mathbf{x})^2 + G_A(\mathbf{x}, \mathbf{x}) \right] \delta^{(3)}(\mathbf{x} - \mathbf{x}'), \end{aligned} \quad (2.48)$$

$$\begin{aligned} i\hbar \frac{\partial G_N(\mathbf{x}, \mathbf{x}')}{\partial t} &= \langle [\hat{\chi}^\dagger(\mathbf{x}')\hat{\chi}(\mathbf{x}), \hat{H}] \rangle = \\ &\left[\hat{H}_0(\mathbf{x}) - \hat{H}_0(\mathbf{x}') \right] G_N(\mathbf{x}, \mathbf{x}') + 2\tilde{U}_0 \left[|\phi(\mathbf{x})|^2 - |\phi(\mathbf{x}')|^2 + \bar{G}_N(\mathbf{x}) - \bar{G}_N(\mathbf{x}') \right] G_N(\mathbf{x}, \mathbf{x}') \\ &+ U_0 \left[\bar{G}_A(\mathbf{x}) G_A^*(\mathbf{x}, \mathbf{x}') - \bar{G}_A^*(\mathbf{x}') G_A(\mathbf{x}, \mathbf{x}') \right] \\ &+ U_0 \left[\phi(\mathbf{x})^2 G_A^*(\mathbf{x}, \mathbf{x}') - \phi^*(\mathbf{x}')^2 G_A(\mathbf{x}, \mathbf{x}') \right]. \end{aligned} \quad (2.49)$$

Equations (2.47)-(2.49) constitute the dynamical Hartree-Fock Bogoliubov equations. In the following sub-sections (2.4.1)-(2.4.3), we discuss various subtleties in their application and investigate the validity of this framework for quantum corrections to the semi-classical BEC evolution. Section 2.4.4 will introduce a molecular field into the theory, in order to describe the appearance of Feshbach resonances. In section 2.4.5 we incorporate loss processes and in section 2.4.2 propose a scheme to obtain a stationary state of the system of coupled PDEs (2.47)-(2.49).

2.4.1 Gap in the Excitation Spectrum and Goldstone's Theorem

It is a general result of quantum field theory that the spontaneous breaking of a continuous global symmetry of the Hamiltonian implies the presence of excitation modes with vanishing energy. This result is known as the Goldstone theorem, first shown in elementary particle physics [68, 69]. The analogous result for a bosonic many-body problem is known as Hugenholtz-Pines theorem [70]. The Goldstone theorem predicts massless particles, termed Goldstone bosons. An example are the pi-mesons $\pi_0, \bar{\pi}_0, \pi_\pm$ in the quantum chromo dynamics of two approximately massless quark flavours, where the chiral-symmetry of the Lagrangian is spontaneously broken by the appearance of the quark condensate [69, 71].

In section 2.1 we alluded to the global U(1) symmetry of the atomic Bose gas Hamiltonian. This symmetry is spontaneously broken by the ground state of the Hamiltonian in the presence of a Bose-Einstein condensate. The Goldstone or Hugenholtz-Pines theorems hence predict excitations with vanishing energy. As mentioned in section 2.3.2, these are indeed found in the linearised Bogoliubov theory.

However in the full HFB framework, beyond the linearised theory, the Hugenholtz-Pines theorem is violated. The excitation frequencies now can be determined with a Green's functions approach. In the homogeneous case one finds [72]:

$$\epsilon_q^2 = \left(\frac{\hbar^2 q^2}{2m} + U_0 n - U_0 \bar{G}_A \right)^2 - U_0^2 (\phi^2 + \bar{G}_A^2), \quad (2.50)$$

$$\lim_{q \rightarrow 0} \epsilon_q^2 = 4U_0^2 |\bar{G}_A| n. \quad (2.51)$$

Due to the presence of the anomalous density \bar{G}_A , this spectrum exhibits an energy gap at large wavelengths. We recover a result compatible with Goldstone's theorem in the Popov approximation where the anomalous density $\bar{G}_A(\mathbf{x})$ is neglected [72]. However in the time-dependent HFB equations this allows only for the treatment of a condensate in the presence of a pre-existing thermal cloud (\bar{G}_N), but neglects inter-conversion between the condensed and uncondensed fractions. For our study of quantum depletion in chapter 3, where the initial quantum state contains no uncondensed atoms, the Popov approximation is therefore of no use.

The appearance of the gap in the HFB spectrum can be traced back to our factorisation of the term $\langle \hat{\chi}^\dagger(\mathbf{x}) \hat{\chi}(\mathbf{x}) \hat{\chi}(\mathbf{x}) \rangle$ in Eq. (2.7) with Wick's theorem [73]. Without this step, the set of dynamical equations does not close. To determine the condensate evolution, we would then require knowledge of second and third order correlation functions, which in turn would necessitate solving the evolution of even higher order correlation functions. A systematic expansion along these lines is presented in Refs. [74, 75] and makes use of cumulants.

Having identified the origin of the energy gap, we can define the *gapless* Hartree-Fock Bogoliubov (GHFB) scheme. The core idea is to approximately include the effect of the missing component of the third order correlations. This can be achieved by replacing the couplings \tilde{U}_0 in Eqs. (2.47)-(2.49) with the effective interaction [73]:

$$\tilde{U}_0 \rightarrow U_{eff} = U_0 \left(1 + \frac{\bar{G}_A(\mathbf{x})}{\phi(\mathbf{x})^2} \right). \quad (2.52)$$

Note that a combination of functions giving rise to this effective interaction is naturally realised in the remaining terms of the HFB equations. They are therefore proportional to the untilded interaction U_0 in Eqs. (2.47)-(2.49). This treatment removes the unphysical gap from the HFB excitation spectrum [73]. The resulting theory correctly accounts for excitation frequencies even as the condensation temperature is approached [76]. From Eqs. (2.51) and (2.52), we see that for small \bar{G}_A , it is possible to ignore the effect of the gap in the spectrum.

One can calculate deviations in the excitation energies from the result in Eq. (2.35) due to the presence of an uncondensed component. If this is done perturbatively, rather than with the Green's functions approach mentioned earlier, unphysical *infrared divergences* occur (i.e. $\lim_{q \rightarrow 0} \epsilon_q = \infty$) [77]. This problem disappears if Eqs. (2.47) and (2.31) are solved self-consistently [78]. Such a procedure, the subject of the following section, has the added advantage that it supplies us with a stationary state of the evolution equations (2.47)-(2.49).

2.4.2 Self-consistent Stationary States

The introductory remarks in section 2.2.2 illustrate the usefulness of stationary states as a point of origin for numerical simulations. This is also the case for the time dependent HFB equations (2.47)-(2.49). For the work presented in this thesis, we fortunately only require an initial state for the trivial case $U_0 = 0$. Nonetheless, we briefly outline how a nontrivial stationary state for the HFB equations can be found. Before we set off, it will be useful to define the time-independent modified GPE:

$$\begin{aligned} \mu_a \phi(\mathbf{x}) &= \hat{H}_0(\mathbf{x})\phi(\mathbf{x}) + U_0 |\phi(\mathbf{x})|^2 \phi(\mathbf{x}) \\ &\quad + 2\tilde{U}_0 G_N(\mathbf{x}, \mathbf{x})\phi(\mathbf{x}) + U_0 G_A(\mathbf{x}, \mathbf{x})\phi^*(\mathbf{x}). \end{aligned} \quad (2.53)$$

The target of our construction is a set of functions that fulfill:

$$\begin{aligned} \phi(\mathbf{x}, t) &= \phi(\mathbf{x}) \exp(-i\mu_a t/\hbar), \\ G_N(\mathbf{x}, \mathbf{x}', t) &= G_N(\mathbf{x}, \mathbf{x}') \exp(-i\mu_{GN} t/\hbar), \\ G_A(\mathbf{x}, \mathbf{x}', t) &= G_A(\mathbf{x}, \mathbf{x}') \exp(-i\mu_{GA} t/\hbar). \end{aligned} \quad (2.54)$$

If we assume that the initial quantum state $|\Psi\rangle$ is the Bogoliubov vacuum $|0\rangle$, see Eq. (2.34), we obtain the correlation functions:

$$G_N(\mathbf{x}, \mathbf{x}') = \sum_i v_i(\mathbf{x}') v_i^*(\mathbf{x}), \quad G_A(\mathbf{x}, \mathbf{x}') = - \sum_i u_i(\mathbf{x}') v_i^*(\mathbf{x}). \quad (2.55)$$

Inserting Eq. (2.55) into Eq. (2.48) and Eq. (2.49) we see that for u_i, v_i which solve Eqs. (2.31), these G_A, G_N are stationary solutions if the backreaction is neglected. That is, we discard the terms quadratic in G_A, G_N in Eqs. (2.48) and (2.49) and all correlation functions in Eq. (2.53). With these approximations, it is straightforward to see that Eq. (2.55) together with an eigenfunction ϕ_0 of the TIGPE with eigenvalue μ represents a stationary solution⁷. The set of eigenvalues in Eq. (2.54) is then $\mu_a = \mu, \mu_{GA} = 2\mu, \mu_{GN} = 0$.

To obtain a stationary state of the full equations we can employ an iteration scheme:

1. We solve Eq. (2.53) for given $V(\mathbf{x})$ and $\bar{G}_N(\mathbf{x}) = \bar{G}_A(\mathbf{x}) = 0$, using for example the imaginary time method of section 2.2.2. We call the solution $\phi_{0,0}(\mathbf{x})$. We further define $\bar{G}_N(\mathbf{x})_0 = \bar{G}_A(\mathbf{x})_0 = 0$.
2. We solve the *modified* Bogoliubov equations [72]:

$$\begin{aligned} & \left(-\frac{\hbar^2}{2m} \nabla^2 + V(\mathbf{x}) + 2U_0 (|\phi_{0,n}(\mathbf{x})|^2 + \bar{G}_N(\mathbf{x})_n) - \mu - \epsilon_i \right) u_{i,n+1}(\mathbf{x}) \\ & - U_0 (\phi_{0,n}(\mathbf{x})^2 + \bar{G}_A(\mathbf{x})_n) v_{i,n+1}(\mathbf{x}) = 0, \\ & \left(-\frac{\hbar^2}{2m} \nabla^2 + V(\mathbf{x}) + 2U_0 (|\phi_{0,n}(\mathbf{x})|^2 + \bar{G}_N(\mathbf{x})_n) - \mu + \epsilon_i \right) v_{i,n+1}(\mathbf{x}) \\ & - U_0 (\phi_{0,n}^*(\mathbf{x})^2 + \bar{G}_A^*(\mathbf{x})_n) u_{i,n+1}(\mathbf{x}) = 0, \end{aligned} \quad (2.56)$$

for $n = 0$ to obtain mode functions $u_{i,1}, v_{i,1}$.

3. From the solutions $u_{i,1}$ and $v_{i,1}$, we calculate $G_N(\mathbf{x}, \mathbf{x}')_1$ and $G_A(\mathbf{x}, \mathbf{x}')_1$ according to Eq. (2.55).
4. We then solve Eq. (2.53) again, with $\bar{G}_N(\mathbf{x}) = \bar{G}_N(\mathbf{x})_1$ and $\bar{G}_A(\mathbf{x}) = \bar{G}_A(\mathbf{x})_1$ to obtain $\phi_{0,1}(\mathbf{x})$
5. Steps (1) to (4) are iterated until the solutions $\phi_{0,n}(\mathbf{x}), G_N(\mathbf{x}, \mathbf{x}')_n, G_A(\mathbf{x}, \mathbf{x}')_n$ converge.

It can be seen that a self-consistent result of the above iteration scheme represents a solution fulfilling Eq. (2.54).

A final point has to be addressed before we can obtain a well-defined summation in Eq. (2.55). The anomalous density \bar{G}_A is formally divergent and must

⁷For Eq. (2.48) this is best seen by first inverting the commutation operation that resulted in the delta function, i.e. $G_N(\mathbf{x}, \mathbf{x}') = \langle \hat{\chi}(\mathbf{x}) \hat{\chi}^\dagger(\mathbf{x}') \rangle - \delta^{(3)}(\mathbf{x} - \mathbf{x}')$.

be renormalised [14, 78, 79]. This is a consequence of approximating the atomic interactions as local. We will discuss renormalisation in the next section, at the end of which the prescription for a well defined \bar{G}_A in the self-consistent solution scheme is given.

2.4.3 Ultraviolet Renormalisation

The calculation of quantum effects in a local quantum field theory naturally leads to divergences [71]. This necessitates a renormalisation of the theory.

Renormalisation absorbs infinite quantities into the a priori unknown parameters of the Hamiltonian. These parameters hence become formally infinite, but all physical observables calculated with the renormalised theory turn out finite. Such a scheme is justified as the divergences arise from intermediate states with arbitrarily high energy (hence *ultraviolet* divergences) which have to be considered in quantum mechanics. However our local quantum field theory (2.1) is surely not valid at all energy scales. Divergent integrals in a calculation can thus be regularised by a momentum or energy cutoff K .

We then demand that the amplitude for low energy atom scattering derived from the Hamiltonian (2.1) in this way is given by $U = 4\pi\hbar^2 a_s/m$ where a_s is the s-wave scattering length [34]. This forms the *renormalisation condition*. The usual tool for these calculations is the Lippmann-Schwinger equation of quantum scattering theory [31]. One obtains a relation between the physical interaction strength U and the parameter U_0 in the Hamiltonian involving the momentum cutoff K . Following this procedure, Kokkelmans *et al.* [80] find:

$$U_0 = \frac{U}{1 - \alpha U}, \quad \alpha = \frac{mK}{2\pi^2\hbar^2}. \quad (2.57)$$

For a static calculation such as that outlined in the previous section, another approach is possible. Instead of renormalising the coupling constant U , one can make use of a renormalised anomalous average [14, 78, 79]

$$\tilde{\bar{G}}_A(\mathbf{x}) = \bar{G}_A(\mathbf{x}) + U_0 \phi(\mathbf{x})^2 \int_{|\mathbf{k}| < K} \frac{d^3\mathbf{k}}{(2\pi)^3} \frac{1}{2(\hbar^2\mathbf{k}^2/2m)}. \quad (2.58)$$

This procedure can also be used in a modal time dependent HFB method, constructed in terms of time varying mode functions u_i, v_i [79], but not for our time dependent correlation function approach.

2.4.4 Atom-Molecule Resonance Theory

Instead of the simple energy independent scattering by the quartic coupling term in Eq. (2.1) the situation can be more complicated. In this and the next section, we discuss the example of resonance scattering, which can be naturally included in the HFB framework.

In the vicinity of a Feshbach resonance, the atomic interactions are strongly dependent on the collision energy. This Feshbach resonant interaction can be modelled by adding a molecular field $\hat{\Psi}_m(\mathbf{x})$ to the theory [81, 82]. We briefly study this extension in chapter 3 and therefore give a quick overview here. For the situations studied in this thesis, an inclusion of the molecular resonance proved unnecessary, however this observation by itself is an important result.

The extra terms in the Hamiltonian, which describe the molecular field are:⁸

$$\begin{aligned} & \int d^3\mathbf{x} \hat{\Psi}_m^\dagger(\mathbf{x}) \left(-\frac{\hbar^2}{4m} \nabla_{\mathbf{x}}^2 + 2V(\mathbf{x}) - \nu_0 \right) \hat{\Psi}_m(\mathbf{x}) \\ & + \frac{g_0}{2} \int d^3\mathbf{x} \hat{\Psi}_m^\dagger(\mathbf{x}) \hat{\Psi}_a(\mathbf{x}) \hat{\Psi}_a(\mathbf{x}) + H.c. \end{aligned} \quad (2.59)$$

The molecules have mass $2m$ and their coupling to atoms is parametrised by g_0 . Any self-interaction of the molecules is neglected. The constituent atoms of a molecule shall experience the same spatial potential $V(\mathbf{x})$ as if they were unbound, but the overall energy of the bound pair is *detuned* from the unbound state by ν_0 .

The molecular field is now decomposed as previously the atom field:

$$\hat{\Psi}_m(\mathbf{x}) = \phi_m(\mathbf{x}) + \hat{\chi}_m(\mathbf{x}). \quad (2.60)$$

From the averages of the Heisenberg equations for $\hat{\Psi}_a(\mathbf{x})$ and $\hat{\Psi}_m(\mathbf{x})$, we obtain equations for the atomic and molecular condensates:

$$\begin{aligned} i\hbar \frac{\partial \phi_a(\mathbf{x})}{\partial t} &= \left(-\frac{\hbar^2}{2m} \nabla_{\mathbf{x}}^2 + V(\mathbf{x}) + U_0 |\phi_a(\mathbf{x})|^2 \right) \phi_a(\mathbf{x}) \\ &+ 2U_0 \bar{G}_N(\mathbf{x}) \phi_a(\mathbf{x}) + U_0 \bar{G}_A(\mathbf{x}) \phi_a^*(\mathbf{x}) \\ &+ g_0 (\phi_m(\mathbf{x}) \phi_a^*(\mathbf{x}) + \langle \hat{\chi}_m(\mathbf{x}) \hat{\chi}_a^\dagger(\mathbf{x}) \rangle), \end{aligned} \quad (2.61)$$

$$i\hbar \frac{\partial \phi_m(\mathbf{x})}{\partial t} = \left(-\frac{\hbar^2}{4m} \nabla_{\mathbf{x}}^2 + 2V(\mathbf{x}) - \nu_0 \right) \phi_m(\mathbf{x}) + \frac{g_0}{2} (\bar{G}_A(\mathbf{x}) + \phi_a(\mathbf{x})^2). \quad (2.62)$$

⁸Throughout this section, a subscript a denotes atomic field operators and condensates, m the molecular counterparts.

We will refer to this formalism as HFB-resonance theory. The remaining two Hartree-Fock Bogoliubov equations (2.48)-(2.49) are also modified by the coupling to molecules. For the case $\hat{\chi}_m(\mathbf{x}) = 0$ we can refer the reader to Ref. [82]. In the literature $\hat{\chi}_m(\mathbf{x})$ has usually been neglected on the grounds of a small molecular fraction and the expectation of an even smaller uncondensed molecular component. However, even small molecule numbers have to be treated on equal footing to atoms if g_0 is much larger than U_0 . We show in chapter 3 that this is the case for our scenario.

To extend the formalism consistently we would have to include correlation functions involving $\hat{\chi}_m(\mathbf{x})$ namely: $\langle \hat{\chi}_m(\mathbf{x}') \hat{\chi}_a^\dagger(\mathbf{x}) \rangle$, $\langle \hat{\chi}_m^\dagger(\mathbf{x}') \hat{\chi}_a^\dagger(\mathbf{x}) \rangle$, $\langle \hat{\chi}_m(\mathbf{x}') \hat{\chi}_a(\mathbf{x}) \rangle$, $\langle \hat{\chi}_m^\dagger(\mathbf{x}') \hat{\chi}_a(\mathbf{x}) \rangle$, $\langle \hat{\chi}_m(\mathbf{x}') \hat{\chi}_m(\mathbf{x}) \rangle$, $\langle \hat{\chi}_m^\dagger(\mathbf{x}') \hat{\chi}_m(\mathbf{x}) \rangle$. It is obvious that this substantially complicates the theory. We will give no further details here.

Renormalisation of the Resonance Theory

The renormalisation formalism also has to be extended for the resonance theory. This was done in Ref. [80]. Let U_{bg} denote the atomic background interaction strength far from the resonance where molecular effects can be neglected. If molecules are present, the renormalisation equations connect the physical atom-molecule coupling g , molecular detuning ν and background atom-atom scattering U_{bg} with the effective interaction U_{eff} that the atoms experience due to their resonant coupling to the molecular field:

$$U_0 = \frac{U_{\text{bg}}}{1 - \alpha U_{\text{bg}}}, \quad (2.63)$$

$$g_0 = \frac{g}{1 - \alpha U_{\text{bg}}}, \quad (2.64)$$

$$\nu_0 = \nu - \alpha \frac{gg_0}{2} = \nu - \alpha \frac{g^2}{2(1 - \alpha U_{\text{bg}})}, \quad (2.65)$$

$$U_{\text{eff}} = U_{\text{bg}} \left(1 + \frac{g^2}{2U_{\text{bg}}\nu} \right). \quad (2.66)$$

The same result can be obtained from the Hamiltonian (2.1) using Feynman diagrams in non-relativistic quantum field theory. For illustrative purposes we follow this route in appendix A. The physical parameters U_{bg} , g , ν are distinct from the bare quantities U_0 , g_0 , ν_0 , which are just parameters in the Hamiltonian and depend on the chosen cut-off. The atom-molecule coupling is related to the width of the Feshbach resonance κ by:

$$g = \sqrt{\kappa U_{\text{bg}}} = \sqrt{\Gamma \Delta \mu_{\text{bg}}}. \quad (2.67)$$

Here κ is a width parameter, Γ is the width in units of the magnetic field [83] and $\Delta\mu_{\text{bg}}$ is the difference between the magnetic moments of the molecular and unbound atomic states [84]. The coupling is therefore fixed by the experimental situation we wish to model, as is the background scattering length U_{bg} [83].

This concludes our introduction to atom-molecule resonance theory. The formalism is involved and only briefly employed to rule out unexpected effects in chapter 3, hence we kept our review of this theory brief.

The following sub-section also represents bonus material, in the sense that a more straightforward approach was taken in our work. We nonetheless present a sketch of how to accurately include atom losses in the full set of HFB equations, to complete the picture of the theory.

2.4.5 Atom Losses

We have shown in section 2.2.5 how loss processes can be included in the semi-classical treatment of the BEC. The resulting loss-terms are concerned with condensate particles only. Beyond the mean-field additional inelastic collisions can occur between condensed and uncondensed particles. To consistently extend our framework, we start from Eq. (2.9) using $\hat{A} = \hat{\Psi}(\mathbf{x})$ and obtain:

$$i\hbar \frac{\partial}{\partial t} \phi(\mathbf{x}) = \mathcal{L}_{\text{hfb}} [\phi(\mathbf{x}), \bar{G}_N(\mathbf{x}), \bar{G}_A(\mathbf{x})] - i\frac{\hbar}{2} K_3 \langle \hat{\Psi}^\dagger(\mathbf{x})^2 \hat{\Psi}(\mathbf{x})^3 \rangle. \quad (2.68)$$

Here \mathcal{L}_{hfb} is a shorthand for the “HFB functional” defined by the rhs. of Eq. (2.47). Using Eq. (2.6) and Wick’s theorem for expectation values with five operators, in the spirit of Eqs. (2.45), (2.46), we reach:

$$\begin{aligned} i\hbar \frac{\partial}{\partial t} \phi(\mathbf{x}) = & \mathcal{L}_{\text{hfb}} [\phi(\mathbf{x}), \bar{G}_N(\mathbf{x}), \bar{G}_A(\mathbf{x})] - i\frac{\hbar}{2} K_3 \left(\left[|\phi(\mathbf{x})|^4 + 3\bar{G}_A(\mathbf{x}) \phi^*(\mathbf{x})^2 \right. \right. \\ & + 6\bar{G}_N(\mathbf{x}) |\phi(\mathbf{x})|^2 + \bar{G}_A^*(\mathbf{x}) \phi(\mathbf{x})^2 + 6\bar{G}_N(\mathbf{x})^2 + 3|\bar{G}_A(\mathbf{x})|^2 \left. \left. \right] \phi(\mathbf{x}) \right. \\ & + 6\bar{G}_N(\mathbf{x}) \bar{G}_A(\mathbf{x}) \phi^*(\mathbf{x}) \left. \right), \end{aligned} \quad (2.69)$$

This includes the loss of condensate atoms due to inelastic collisions with uncondensed atoms. Similar modifications can arise from Eq. (2.9) to the evolution of G_A , G_N in Eqs. (2.48)-(2.49). These become increasingly unwieldy, involving expectation values of six operators.

For our applications in chapter 3, it is sufficient to consider loss processes between condensate atoms only, hence Eq. (2.69) shall suffice for our illustration

of the method. Our results in chapter 3 will show that quantum field studies in the presence of loss effects are much easier using the method that we will explain next: The truncated Wigner approximation.

2.5 Stochastic Methods: the Truncated Wigner Approximation

The HFB formalism tackles the complexity of solving the operator equation (2.5) by a reduction of the quantum evolution to that of the lowest order correlation functions. An alternative approach that has been widely successful in the field of quantum optics and is becoming increasingly popular in the study of quantum gases [85–88] is to make use of powerful *phase-space methods* [13, 89–91]. They are pedagogically described in [13, 92], nonetheless we aim to provide a compact but self-contained introduction in this chapter.

At the heart of the methods is a representation of the system’s density matrix $\hat{\rho}$ in terms of a suitable operator basis. Instead of evolving the density matrix it allows us to study the evolution of the expansion coefficients: the phase-space distribution. A generic expansion of $\hat{\rho}$ in terms of the operator basis $\hat{\Lambda}$ reads:

$$\hat{\rho}(t) = \int d\lambda P(\lambda, t)\hat{\Lambda}(\lambda). \quad (2.70)$$

Here $P(\lambda, t)$ is the phase space distribution onto which we want to reduce the problem. The vector λ is a parametrisation of our operator basis. By inserting Eq. (2.70) into Eq. (2.8), we can obtain an evolution equation for P .

We now choose P as the Wigner distribution W [13]. At the end of the section we make some general remarks on other possible choices of representation. Due to the inhomogeneity of the Bose gas in a harmonic trap, we have to define a multimode Wigner function:

$$\begin{aligned} W(\{\alpha_k\}, \{\alpha_k^*\}, t) &= \prod_k \left(\int \frac{1}{\pi^2} d^2 \beta_k \right) \exp \left(\sum_k \beta_k^* \alpha_k - \beta_k \alpha_k^* \right) \\ &\quad \text{Tr} \left[\exp \left(\sum_j \beta_j \hat{a}_j^\dagger - \beta_j^* \hat{a}_j \right) \hat{\rho}(t) \right], \end{aligned} \quad (2.71)$$

Here \hat{a}_j^\dagger (\hat{a}_j) annihilates (creates) atoms in the j ’th single particle mode. The α_k, α_k^* form the phase-space in which W is defined, they correspond to the λ in Eq. (2.70). These could be eigenstates of the harmonic oscillator or position eigenstates on a discrete grid, without changing the form of Eq. (2.71). In what follows

we will however have discretised position eigenstates in mind, while attempting to point out subtleties arising from other choices of basis.

We now consider a master equation analogous to Eq. (2.8), in which the continuous spatial coordinate \mathbf{x} has been replaced by a discrete index k : $\hat{\Psi}(\mathbf{x}) \rightarrow \hat{\Psi}_k$. Using Eq. (2.71) we can then derive the evolution of the Wigner function $W(\{\alpha_k\}, \{\alpha_k^*\})$ from Eq. (2.8). For our illustration of the method here, we assume $K_3 = 0$. The case $K_3 \neq 0$ is thoroughly treated in Refs. [93, 94].

The transition from the discretised master equation to an evolution equation for W is made easy by the following set of operator correspondences:⁹

$$\begin{aligned}\hat{\Psi}_k \hat{\rho} &\leftrightarrow \left(\alpha_k + \frac{1}{2} \frac{\partial}{\partial \alpha_k^*} \right) W, & \hat{\Psi}_k^\dagger \hat{\rho} &\leftrightarrow \left(\alpha_k^* - \frac{1}{2} \frac{\partial}{\partial \alpha_k} \right) W, \\ \hat{\rho} \hat{\Psi}_k &\leftrightarrow \left(\alpha_k - \frac{1}{2} \frac{\partial}{\partial \alpha_k^*} \right) W, & \hat{\rho} \hat{\Psi}_k^\dagger &\leftrightarrow \left(\alpha_k^* + \frac{1}{2} \frac{\partial}{\partial \alpha_k} \right) W.\end{aligned}\quad (2.72)$$

Either with these rules or explicitly using Eq. (2.71) and Eq. (2.8), we obtain [13, 92]¹⁰:

$$\frac{\partial W}{\partial t} = -\frac{i}{\hbar} \sum_j \left\{ \frac{\partial}{\partial \alpha_j} \left[\hat{H}_0 \alpha_j + U_0 \left(|\alpha_j|^2 - \frac{1}{\Delta V} \right) \alpha_j \right] - \frac{U_0}{4} \frac{\partial^3}{\partial^2 \alpha_j \partial \alpha_j^*} \alpha_j \right\} W + \text{c.c.} \quad (2.73)$$

W is a function of the sets $\{\alpha_k\}$, $\{\alpha_k^*\}$ and t as indicated before. These arguments are suppressed in Eq. (2.73) and what follows in order to compactify notation. ΔV denotes the volume associated with one discrete spatial point. Partial derivatives in Eq. (2.73) act on all functions to their right.

A few comments are in order regarding the peculiar $\frac{1}{\Delta V}$ term. The factor arises from consistently discretising Eq. (2.8) and the field operator, as well as taking into account that the replacement-rules Eq. (2.72) assume commutation relations like $[\hat{\psi}_i, \hat{\psi}_j^\dagger] = \delta_{ij}$. In a more general treatment for an arbitrary *restricted* single particle basis, this particular term is identified with an approximation of the commutator of the original field operator (2.2) (i.e. a delta-function) in the chosen restricted basis [93, 94].

For an n -mode, N particle problem, Eq. (2.73) determines the time evolution of a $2n$ dimensional function, a problem that remains numerically intractable for

⁹In using these rules, the operators furthest away from $\hat{\rho}$ in the master equation have to be replaced first, forming the left-most terms in the resulting product.

¹⁰For a generic treatment using arbitrary modes, this expression would contain matrix elements of \hat{H}_0 and the interaction Hamiltonian [94]. We assumed the discrete position basis and imply a discretised representation also for the spatial derivatives contained in \hat{H}_0 .

large n . However, compared to the n^N dimensional Hilbert space of the original operator equation, we made great progress, if N was large.

The problem could be cast into an even more accessible form, if Eq. (2.73) was of the form of a Fokker-Planck equation (FPE):

$$\frac{\partial W}{\partial t} = - \sum_j \frac{\partial}{\partial \alpha_j} A_j W + \frac{1}{2} \sum_{n,j} \frac{\partial}{\partial \alpha_n} \frac{\partial}{\partial \alpha_j^*} D_{nj} W + \text{c.c} \quad (2.74)$$

In this generic expression, besides W , also A_j and D_{nj} depend on the phase-space variables $\{\alpha_k\}$, $\{\alpha_k^*\}$ and time. \mathbf{A} is termed the drift vector, while the D_{nj} make up the diffusion matrix. Most importantly, if the diffusion matrix D is positive definite, there exists a precise correspondence between the FPE and a specific *stochastic differential equation* (SDE) [13, 95]. We will see in the following section, that the numerical solution of a SDE is tractable, at least in principle, even for many-mode, many-particle problems.

But first we return our attention to the Wigner representation: unfortunately Eq. (2.73) is not of the Fokker-Planck type. For the third order derivatives, no mapping to a stochastic equation exists [92]. Under special circumstances it can however be shown that these derivative terms can be neglected in comparison with the remainder of Eq. (2.73). This approach is known as the *truncated Wigner approximation* (TWA). We will discuss the situations in which this approximation is justified in section 2.5.3.

2.5.1 Stochastic Differential Equations

Having truncated Eq. (2.73) by neglecting all derivatives higher than second order, it takes the Fokker-Planck form (2.74). We can now use the general correspondence between Eq. (2.74) and the SDE [13]:

$$d\alpha_n = A_n dt + \sum_j B_{nj} dE_j(t), \quad (2.75)$$

Here $d\mathbf{E}(t)$ is a complex dynamic noise vector that fulfills: $\overline{dE_j(t)} = 0$ and $\overline{dE_i^*(t')dE_j(t)} = \delta_{ij}\delta(t-t')dt$. The drift vector \mathbf{A} of the FPE enters the deterministic part of Eq. (2.75). The matrix \mathbf{B} derives from the diffusion matrix via $\mathbf{D} = \mathbf{BB}^T$ and enters the random noise terms.

Care needs to be taken, as two common definitions of the integral over a stochastic function exist. This divides stochastic calculus into the Ito and Stratonovich forms [95]. The stochastic differential equation (2.75) has to be interpreted as

of the Ito-type [95]. However, the numerical algorithm SIIP [96], with which we would like to solve Eq. (2.75), assumes a Stratonovich type SDE [95].

The difference is only relevant when the diffusion terms are non-constant. Fortunately simple rules for an ‘‘Ito to Stratonovich’’ conversion exist: An Ito SDE like Eq. (2.75) is converted into the Stratonovich SDE [95]:

$$d\alpha_n = \left(A_n - \frac{1}{2} \sum_{jk} B_{kj} \frac{\partial}{\partial \alpha_k} B_{nj} \right) dt + \sum_j B_{nj} dE_j(t), \quad (2.76)$$

In the discrete position basis, we can interpret the phase-space variables α_k as the discretised stochastic wave function. We thus return to our usual notation for the wave function by replacing $\alpha_k \rightarrow \phi(\mathbf{x})$. Converting Eq. (2.73) without the highest derivative terms to a SDE, we obtain:

$$\frac{d\phi(\mathbf{x})}{dt} = -\frac{i}{\hbar} \left(-\frac{\hbar^2}{2m} \nabla^2 + V(\mathbf{x}) + U_0 \left(|\phi(\mathbf{x})|^2 - \frac{1}{\Delta V} \right) \right) \phi(\mathbf{x}). \quad (2.77)$$

In the truncated Wigner approximation and for the usual atomic interactions, there are no dynamical noise terms. Hence Eq. (2.77) takes the same form as the ordinary GPE (2.10) after adjusting our zero of energy. We only have to keep in mind that Eq. (2.77) has to evolve the Wigner distribution W of the initial quantum state of the BEC. This is achieved by picking the initial state $\phi_0(\mathbf{x})$ randomly according to the distribution W . For all these initial configurations, we can solve Eq. (2.77) numerically. Each such solution is referred to as *trajectory*. The distribution of the $\phi(\mathbf{x}, t)$ in the N_{traj} trajectories provides an approximation to the full distribution W at time t .

2.5.2 Initial Conditions and Correlation Function

Now knowing that the initial state of the stochastic wave function ϕ is randomly distributed according to the initial Wigner function of the BEC, we move on to specify the form of W . As the quantum state of the BEC is most commonly assumed to be coherent (section 2.1), we require a coherent state Wigner function for each mode [13]. This is achieved by

$$W(\{\alpha_k\}, \{\alpha_k^*\}, t) = \prod_k \left\{ \frac{\Gamma_k}{\pi} \exp \left[-\Gamma_k (\alpha_k - \alpha_{k,0}) (\alpha_k^* - \alpha_{k,0}^*) \right] \right\}, \quad (2.78)$$

with $\Gamma_k = 2 \forall k$. We represent this by adding random noise $\eta(\mathbf{x})$ according to:

$$\phi(\mathbf{x}, t=0) = \phi_0(\mathbf{x}) + \frac{1}{\sqrt{2}} \eta(\mathbf{x}). \quad (2.79)$$

$\eta(\mathbf{x})$ is a Gaussian distributed complex random function that fulfills the conditions $\overline{\eta(\mathbf{x})\eta(\mathbf{x}')} = 0$ and $\overline{\eta(\mathbf{x})^*\eta(\mathbf{x}')} = \delta(\mathbf{x} - \mathbf{x}')$, where \overline{f} denotes the stochastic average of f . From Eq. (2.78) to Eq. (2.79) we again made the conversion from the discrete to the continuous spatial notation. As usual $\phi_0(\mathbf{x})$ denotes the initial BEC wave function. Its value on a specific grid point $\phi_0(\mathbf{x}_k)$ corresponds to the $\alpha_{k,0}$ in Eq. (2.78).

We are later also interested in a thermal distribution of uncondensed atoms around the BEC. To define the quantum ground state for a small uncondensed component, the Bogoliubov modes of section 2.3 can be used. Following essentially Eq. (2.30) the noise is added in the Bogoliubov basis according to [97]:

$$\phi(\mathbf{x}, t = 0) = \phi_0(\mathbf{x}) + \sum_k [\sqrt{p_k} \eta_k u_k(\mathbf{x}) - \sqrt{p_k} \eta_k^* v_k^*(\mathbf{x})], \quad (2.80)$$

$$\sqrt{p_k} = \left[2 \tanh \left(\frac{\epsilon_k - \mu}{2k_B T} \right) \right]^{-1/2}. \quad (2.81)$$

Here $\phi_0(\mathbf{x})$ is the condensate ground state as before, T is the temperature, the ϵ_k are the Bogoliubov mode energies as determined by Eq. (2.31), and η is again a Gaussian noise.

As the spread of the variables α_k in the stochastic treatment samples the phase-space distribution P , we can obtain information about quantum correlation functions from suitable averages over the stochastic variables. If the Wigner representation is used, stochastic averages correspond to symmetrically ordered quantum averages [13], e.g.

$$\overline{\alpha_k^* \alpha_n} = \frac{1}{2} \langle \hat{\Psi}_k^\dagger \hat{\Psi}_n + \hat{\Psi}_n \hat{\Psi}_k^\dagger \rangle. \quad (2.82)$$

Because all interesting quantities in the stochastic method are based on averages over trajectories, we need to ensure that sufficiently many trajectories are sampled. A comparison of averaged quantities obtained from different numbers of trajectories, or equivalently the quantities' standard deviation, give us information about the residual error due to the unavailability of infinitely many trajectories, termed *sampling error*.

At this stage the distinction between condensate excitations and uncondensed fluctuations that we discussed in section 2.3.1 becomes particularly clear. Let us consider Eq. (2.81). According to Eq. (2.82), the condensate is given by $\overline{\phi_k}$. In this statistical average, the component of Eq. (2.81) proportional to the random noise term averages out. It has a different phase in each realisation and hence no fixed phase relation to the condensate. We thus have $\overline{\phi_k} = \phi_{0,k}$. In contrast $\overline{\phi_k^* \phi_k}$ is insensitive to the phase and acquires a contribution from the noise

terms, which is essentially the variance of the noise. In the nomenclature of section 2.3.1 a classical condensate excitation would contribute to $\phi_{0,k}$ in Eq. (2.81), whereas the quasi-particle population enters the noise part of the expression. In section 2.5.6 it can finally be seen, that the noise variance is essentially made up of the uncondensed population and virtual particles due to vacuum fluctuations within each mode.

2.5.3 Validity of the Truncation

In previous sub-sections we outlined how the TWA allows us to numerically evolve quantum averages of Bose gas field operators. However, to safely apply the truncated Wigner method, it is indispensable to establish the conditions for which the required truncation represents a justified approximation. Sinatra *et al.* [98] showed that the truncation is valid in a regime where all the modes under consideration are highly occupied.

Norrie *et al.* [93, 94] later found that this condition can be slightly relaxed. We only have to ensure that the particle density exceeds the mode density, where the former is significant. Concretely this means:

$$\left| \langle \hat{\Psi}^\dagger(\mathbf{x}) \hat{\Psi}(\mathbf{x}) \rangle - \frac{1}{2} \delta_C(\mathbf{x}, \mathbf{x}) \right|^2 \gg \sum_j \frac{\Gamma_j}{4} |\varphi_j(\mathbf{x})|^2, \quad (2.83)$$

$$\delta_C(\mathbf{x}, \mathbf{x}') \equiv \sum_k \varphi_k^*(\mathbf{x}') \varphi_k(\mathbf{x}). \quad (2.84)$$

Here we recognise the overall particle density $\langle \hat{\Psi}^\dagger(\mathbf{x}) \hat{\Psi}(\mathbf{x}) \rangle$ on the l.h.s. The function $\delta_C(\mathbf{x}, \mathbf{x}')$ is the commutator of the atomic field represented in the restricted single particle basis $\{\varphi_k(\mathbf{x})\}$ employed for practical computations, i.e. an approximate delta-function. The details of its origin can be found in [94]. To define the remaining components on the r.h.s. we have to specify the foremost assumption under which Eq. (2.83) was derived: one takes the system's Wigner function W to be of the form Eq. (2.78), with unspecified widths Γ_k . If we take the discrete position basis for illustration as we did earlier, we can write $\delta_C(\mathbf{x}, \mathbf{x}) = 1/\Delta V$ and $|\varphi_j(\mathbf{x})|^2 = \delta(x - x_j)/\Delta V$.

From a practical point of view, the criterion (2.83) ensures that the real particle density represented within the stochastic wave function $\phi(\mathbf{x})$ is not overwhelmed by the noise added. Since Eq. (2.83) relies on the assumption that W factorises as in Eq. (2.78), we cannot be sure of its validity for long times, because the factorisation assumption might break down under time evolution.

That this very likely occurs, has been demonstrated by Polkovnikov *et al.* [99, 100]. They showed for a highly occupied two-mode problem, that the TWA fails to reproduce a revival in oscillations of the number variance within one mode. It is also shown that the time for which the TWA correctly reproduces the known exact result increases, when the mode occupation increases.

To summarise, it has been established that the TWA is an approximation for highly occupied modes *and* short times.

2.5.4 Renormalisation

Since the TWA is a local quantum field theory, just like the HFB method, it also requires ultraviolet renormalisation. The steps necessary in the case of the TWA have been worked out in Ref. [98], and are based on essentially the same considerations as our discussion in section 2.4.3. Sinatra *et al.* find the connection [98]

$$U = \frac{U_0}{1 + \frac{1}{V} \sum_{k \neq 0} \frac{U_0}{\hbar^2 \mathbf{k}^2 / m}}. \quad (2.85)$$

between renormalised and bare couplings. If we replace the summation by a momentum space integration $\sum_k / V \rightarrow \int d^3 \mathbf{k} / (2\pi)^3$, and introduce a momentum cut-off K we obtain:

$$U = \frac{U_0}{1 + \frac{mK}{2\pi^2 \hbar^2} U_0}, \quad (2.86)$$

which is equivalent to Eq. (2.57).

2.5.5 Atom Losses

We have illustrated the Wigner method for the case $K_3 = 0$, but previously claimed that the inclusion of loss processes in the truncated Wigner scheme would be more straightforward than in the HFB. While this is true, three-body losses also in the stochastic approach complicate the treatment significantly. We thus just mention the most important consequences. A thorough discussion of the necessary adaptations in a situation with three-body losses can be found in Refs. [94, 101].

The use of the full master equation (2.8) creates additional terms in Eq. (2.73), including derivatives with respect to the α_k , α_k^* of up to order six. As previously, we have to truncate the equation to obtain a genuine FPE. If loss is included, the

evolution equation for W contains terms with second derivatives proportional to K_3 , which results in the presence of dynamical noise terms in the Ito SDE:

$$\begin{aligned} d\phi(\mathbf{x}) = & -\frac{i}{\hbar} \left(-\frac{\hbar^2}{2m} \nabla^2 + V(\mathbf{x}) + U_0 \left(|\phi(\mathbf{x})|^2 - \frac{1}{\Delta V} \right) \right) \phi(\mathbf{x}) dt \\ & - \frac{K_3}{2} \left(|\phi(\mathbf{x})|^4 - 3 \frac{|\phi(\mathbf{x})|^2}{\Delta V} + \frac{3}{2\Delta V^2} \right) \phi(\mathbf{x}) dt \\ & + \sqrt{\frac{3K_3}{2} |\phi(\mathbf{x})|^4 - 3K_3 \frac{|\phi(\mathbf{x})|^2}{\Delta V}} d\xi(x, t). \end{aligned} \quad (2.87)$$

The properties of the dynamical noise $d\xi(x, t)$ are explained in detail in the next section. Unlike the previously discussed commutator term proportional to $U_0/\Delta V$, the other terms including factors $1/\Delta V$ cannot be removed by fixing the energy scale origin. These terms can also be traced back to field operator commutators. However in the regime where the Wigner truncation itself is justified, these can be shown to be negligible [101]. Their removal is in fact required for a consistent treatment [101]. Corrections arising from a conversion to the Stratonovich form (see section 2.5.1) are of the same order as these $1/\Delta V$ terms, and consequently also have to be neglected. The correct Wigner SDE for a trapped BEC with three-body loss is therefore [101]:

$$\begin{aligned} d\phi(\mathbf{x}) = & -\frac{i}{\hbar} \left(-\frac{\hbar^2}{2m} \nabla^2 + V(\mathbf{x}) + U_0 |\phi(\mathbf{x})|^2 \right) \phi(\mathbf{x}) dt \\ & - \frac{K_3}{2} |\phi(\mathbf{x})|^4 \phi(\mathbf{x}) dt + \sqrt{\frac{3K_3}{2} |\phi(\mathbf{x})|^2} d\xi(x, t). \end{aligned} \quad (2.88)$$

2.5.6 Stochastic Equation in the Oscillator Basis

At this point, we have laid the theoretical basis for the truncated Wigner description of the quantum evolution of Bose gases. It remains for us to actually solve Eq. (2.88) for a realistic situation, fighting complications arising from the addition of quantum noise. Simply solving Eq. (2.88) on a spatial grid as usual for other problems, leads to aliasing effects [102] as the noise extends to the edge of the computational grid. These can be overcome in periodic situations by means described in Ref. [42], but not in a harmonic trap. Further, in the position basis we also cannot fulfill the criterion (2.83) for the problems we wish to address in chapter 3.

For our studies, we hence choose a powerful method to solve the Gross-Pitaevskii equation in the oscillator (energy) basis. The method was presented

in [103] and applied to BECs at finite temperature in [104, 105]. Here we extend the formalism in order to solve Eq. (2.88) with it. The stochastic field in Eq. (2.88) can be expanded in terms of eigenstates φ of the 1D harmonic oscillator:

$$\phi(\mathbf{x}, t) = \sum_{\{l,m,n\} \in \mathcal{C}} c_{lmn}(t) \varphi_l(x) \varphi_m(y) \varphi_n(z), \quad (2.89)$$

which fulfill:

$$\left(-\frac{\hbar^2}{2m} \frac{\partial^2}{\partial x^2} + \frac{1}{2} m \omega_x^2 x^2 \right) \varphi_n(x) = \epsilon_{x,n} \varphi_n(x). \quad (2.90)$$

Similarly $\varphi_m(y)$ and $\varphi_n(z)$ solve the oscillator equation for the dimensions y and z . The summation in Eq. (2.89) is restricted to all modes with total energy below a certain cutoff E_{cut} :

$$\mathcal{C} = \{l, m, n : \epsilon_l + \epsilon_m + \epsilon_n \leq E_{\text{cut}}\}. \quad (2.91)$$

To define condensed and uncondensed mode populations, we also expand the field operator in the energy basis:

$$\hat{\psi}(\mathbf{x}, t) = \sum_{\{l,m,n\} \in \mathcal{C}} \varphi_l(x) \varphi_m(y) \varphi_n(z) \hat{\Psi}_{lmn}(t), \quad (2.92)$$

The $\hat{\Psi}_{lmn}$ ($\hat{\Psi}_{lmn}^\dagger$) are operators that annihilate (create) an atom in the mode with quantum numbers l, m, n . Recall from section 2.5.2 that symmetrised quantum averages can be determined from averages over all trajectories. As the condensate is defined as the quantum average of the field operator, we write:

$$n_{\text{cond}}^{lmn} = \left| \langle \hat{\Psi}_{lmn} \rangle \right|^2 = |\overline{c_{lmn}}|^2, \quad (2.93)$$

$$\begin{aligned} n_{\text{unc}}^{lmn} &= \langle \hat{\Psi}_{lmn}^\dagger \hat{\Psi}_{lmn} \rangle - \left| \langle \hat{\Psi}_{lmn} \rangle \right|^2 \\ &= |\overline{c_{lmn}}|^2 - n_{\text{cond}}^{lmn} - \frac{1}{2}. \end{aligned} \quad (2.94)$$

The numbers of condensed and uncondensed atoms (N_{cond} , N_{unc}) are obtained by summing the populations in all the modes. The total atom number is $N_{\text{tot}} = N_{\text{cond}} + N_{\text{unc}}$.

Using the expansion (2.89), the stochastic equation (2.88) becomes:

$$\begin{aligned} dc_{lmn} &= -\frac{i}{\hbar} (\epsilon_l + \epsilon_m + \epsilon_n + U_0 F_{lmn}) dt \\ &\quad - \frac{K_3}{2} G_{lmn} dt + \sqrt{\frac{3K_3}{2}} dH_{lmn}. \end{aligned} \quad (2.95)$$

The F , G and dH are overlap integrals defined by:

$$F_{lmn} = \int d^3\mathbf{x} \varphi_l^*(x) \varphi_m^*(y) \varphi_n^*(z) |\phi(\mathbf{x})|^2 \phi(\mathbf{x}), \quad (2.96)$$

$$G_{lmn} = \int d^3\mathbf{x} \varphi_l^*(x) \varphi_m^*(y) \varphi_n^*(z) |\phi(\mathbf{x})|^4 \phi(\mathbf{x}), \quad (2.97)$$

$$dH_{lmn} = \int d^3\mathbf{x} \varphi_l^*(x) \varphi_m^*(y) \varphi_n^*(z) |\phi(\mathbf{x})|^2 d\xi(\mathbf{x}), \quad (2.98)$$

$$d\xi(\mathbf{x}) = \sum_{\{l,m,n\} \in \mathcal{C}} d\xi_{lmn}(t) \varphi_l(x) \varphi_m(y) \varphi_n(z). \quad (2.99)$$

$d\xi_{lmn}(t)$ in Eq. (2.99) are complex Gaussian noises that fulfill $\overline{d\xi_{lmn}(t) d\xi_{l'm'n'}(t')} = 0$ and $\overline{d\xi_{lmn}^*(t) d\xi_{l'm'n'}(t')} = \delta_{ll'} \delta_{mm'} \delta_{nn'} dt$.

To check the validity criterion (2.83) for the Wigner truncation in energy basis calculations, we later have to compute:

$$\delta_C(\mathbf{x}, \mathbf{x}) \equiv \sum_{\{l,m,n\} \in \mathcal{C}} |\varphi_l(x) \varphi_m(y) \varphi_n(z)|^2. \quad (2.100)$$

2.5.7 Outlook on further Phase-Space Methods

Many other choices for the operator basis can be made in Eq. (2.70). Generally one will attempt to choose a basis whose elements already capture essential features of the problem's density matrix $\hat{\rho}$, resulting in a simpler structure of the distribution P with which we operate [91]. Besides the Wigner distribution other popular options result in the positive-P or gauge-P phase space methods [89, 90]. These can, in principle, describe the *exact* quantum evolution of a BEC, as they result in a FPE without the need of any truncation¹¹. The positive-P method when applied to highly nonlinear, weakly damped problems such as BECs, suffers from stochastic instabilities: the number of trajectories required for a converged result increases beyond all scales after evolution times, which are usually too short [92]. There are however counter examples to this statement [86, 88]. Gauge-P methods have been designed to tackle precisely this problem, but their implementation is vastly more involved than that of the TWA. Further research is directed towards hybrid Wigner and positive-P techniques, in which highly occupied modes are represented by Wigner functions but modes which have small occupation by the positive-P representation [106].

For problems considered in this thesis, the TWA works well, thus we did not require any of the above “heavy artillery”.

¹¹If $K_3 = 0$.

2.6 Numerical Solutions

We only consider scenarios that either correspond to an existing BEC experiment or are intended as proposals for future experiments. This restricts the possibilities for simplifications. In either case, we found the usefulness of analytical calculations limited to providing guidance for more complete numerical solutions of the relevant equations. As a result, the research we present is heavily based on computer simulations of Bose-Einstein condensates. Specifically, we find numerical solutions to the equations of motion presented in this chapter, primarily the Gross-Pitaevskii equation (2.10), the imaginary time Gross-Pitaevskii equation (2.18), the time dependent Hartree-Fock-Bogoliubov equations (2.47)-(2.49) and the truncated Wigner SDE with loss (2.88).

All these equations are partial differential equations (PDEs) for a function $f(\mathbf{x}, t)$ of one time (or imaginary time) variable t and from one to three spatial variables. We exclusively encounter initial value problems where we know $f(\mathbf{x}, t = 0)$ and have to determine the function f at later times. To solve the equations numerically, space and time have to be discretised. This can be done in a variety of ways [102]. For the discretisation of spatial dimensions we either make use of equidistant grids or of an expansion of f in terms of a finite part of a complete set g_i . In the case of the HFB equations we use a mixture of the latter two approaches. For the discretisation of the time dimension we use both fixed stepsize algorithms and adaptive stepsize algorithms, as appropriate. The specific algorithms employed are listed in appendix D. There we also mention our original contributions to the numerical software **xmds**.

Now we outline the most important steps of validation of our numerical results. This reflects their central importance for a PhD-thesis with strong computational elements. To accurately represent the mathematical solution of a given PDE, the spatial and temporal grids must be fine and wide enough. If they are not, the simulation results no longer correspond to a solution of the continuous PDE. Unfortunately, the recognition of inappropriate grids is not always straightforward. A first step of verification can be the monitoring of conserved quantities, such as the atom number for the GPE without losses. Numerical inaccuracy often leads to a violation of conservation laws or other obvious signatures in the simulation output, such as a scrambled condensate due to a too small spatial grid extension. But the deviations from the true solution can appear innocent. For example, we encountered final “Skyrmion” states in the imaginary time evolution which looked as expected, but proved not to be a stationary state of the real time GPE.

This occurred for a too large imaginary time step.

Due to the subtlety with which numerical imprecision can affect physical conclusions, the only reliable means of ensuring convergence is the repetition of simulations with varied numerical parameters: grid spacing, grid extent and timestep or tolerance¹². All results presented in this thesis have been thus verified, with one qualification: For the demanding parameter space surveys of Skyrmions in chapter 4, it was not feasible to verify each individual datapoint, instead the verification was done in the form of spot checks. Further details regarding the verification steps undertaken will be provided throughout the thesis.

In addition to the above, it is always valuable to compare the results of independently coded programs, or compare simulation results quantitatively with existing results in the literature.

2.7 Summary

This concludes our introduction of the theoretical tools that we employ in this thesis, as well as some interesting details that went beyond the required scope.

The Gross-Pitaevskii theory presented in section 2.2 is the work-horse of this thesis. Numerical solutions to it are of prime interest for all of the following chapters. Even when we are interested in quantum effects beyond the GPE, we require its solutions as points of comparison, and to understand the numerical limitations imposed by the condensate dynamics.

Bogoliubov’s theory of elementary excitations in section 2.3 is particularly important to show the relation between quantised condensate fluctuations and quantum fields in curved space time, which forms the basis for chapter 5. But it also underpins our understanding of dynamic and energetic stability properties that pop-up all over chapters chapter 3 and chapter 4.

The time-dependent Hartree-Fock Bogoliubov theory that we outlined in section 2.4 and the truncated Wigner approximation in section 2.5 are the two quantum field theories that we confront with experimental results regarding collapsing condensate dynamics in chapter 3.

The notation defined in this chapter is used throughout the results chapters 3-5. To further simplify reference to mathematical definitions, a list of symbols is provided at the beginning of this thesis.

¹²The adaptive time step method ARK45 operates with a tolerance instead of a step size.

Chapter 3

Collapsing Bose-Einstein Condensates

Bose-Einstein condensates are suitable as simulators for classical and quantum effects across disciplines, as outlined in section 1.3. To make full use of their potential, the quantum field theory underlying ultracold quantum gases must be well understood. The objective of this chapter is to determine the extent to which this is the case.

Experimental progress in dilute gas Bose-Einstein condensates (BECs) has recently allowed increasingly detailed studies of the quantum nature of the atomic field [9–12]. This has been accompanied by advances in the numerical treatment of many-body quantum field theory applied to BEC dynamics, most notably in a better understanding of phase space methods [13] and Hartree-Fock-Bogoliubov theory [14], both of which we introduced in chapter 2. To test our understanding of these theories, experiments in which the physics is sufficiently straight-forward that *quantitative* agreement with many-body quantum theory can be expected are especially appealing.

In this chapter we concentrate on one of these, already mentioned in the introduction: the JILA¹ “Bosenova” experiment of E. Donley *et al.* [28], in which ^{85}Rb Bose-Einstein condensates were made to collapse by switching their atomic interactions from repulsive to attractive. In particular we are concerned with its most basic aspect: the time to collapse t_{collapse} . The abrupt onset of atom losses in the experiment allows a precise determination of this observable. It has previously been shown that the Gross-Pitaevskii (GP) theory substantially

¹Former Joint Institute for Laboratory Astrophysics, Boulder, Colorado, U.S.A., see <http://jila.ww.colorado.edu/jilameans.html>

overestimates these collapse times [30].

The Bosenova experiment exhibits many intricate features, most of which have been more widely studied in the literature than the collapse times. In contrast, this chapter is exclusively focussed on the collapse time observable, attacking the problem with quite heavy theoretical machinery. The reason for this enthusiasm is the prospect of eventually considering the more complicated experimental features in the light of cosmological analogies as briefly mentioned in section 1.3. Such studies of collapsing condensates would benefit greatly from an identification of a suitable quantum theory which describes the Bosenova experiment in a quantitatively correct fashion. This identification can best be done using the simplest observable for which experimental data exists: the collapse times.

While the BEC dynamics at and after the moment of collapse is complicated and violent, the evolution leading up to the collapse is fairly simple and should be very well described by the GPE as we will soon see. It is only during this initial stage that effects can have an influence on t_{collapse} . As the GPE does not yield the correct collapse times, quantum effects or other physics not included in the semi-classical theory must play a role in the collapse scenario. We have thus the opportunity to confront our quantum theories of BEC with a well-defined but comparatively simple experimental test.

The most straightforward reason to expect a reduction of the collapse time in a more complete quantum treatment is manifest in Eq. (2.47) of section 2.4, even though the argument is general and not confined to the HFB approach. The equation in question explicitly shows that the interaction between condensed and uncondensed atoms is twice that between condensate atoms themselves. This is an effect of the quantum mechanics of identical particles, which provides two distinct scattering channels if the atoms can be distinguished but only one for indistinguishable (both condensate) atoms. If enough atoms are transferred from the condensed to the uncondensed fraction by dynamical effects during the collapse, the overall mean field attraction could be significantly enhanced, reducing the collapse time.

The outline of this chapter is as follows. Initially, in sections 3.1 and 3.2, we provide the necessary background on condensates with attractive interactions, the Bosenova experiment and associated theoretical literature. To paint a clear picture of the semi-classical collapse dynamics, we draw on numerical work predating this thesis, most notably of Ref. [30]. In section 3.3 we present our own Gross-Pitaevskii studies of collapsing BECs in a spherical trap, which are required as a point of comparison with the spherical Hartree-Fock Bogoliubov model in

which we study quantum corrections in section 3.4. In section 3.4.2 we show that the influence of the molecular field, principally present near a Feshbach resonance, can be neglected. To check the validity of our results and extend the studies to the exact experimental geometry (cylindrically symmetric), we used the stochastic truncated Wigner method for simulations of collapsing condensates. Those results are presented in section 3.5. In section 3.6 we directly compare the two quantum field models in the case of a spherical collapse. Finally, in section 3.7 we give some more details on the cosmological analogue physics that could be studied in Bosenova-like experiments, once a quantitatively accurate quantum theory is identified.

3.1 Bose-Einstein Condensates with Attractive Interactions

Even with attractive interactions BECs do not necessarily collapse. A perfectly homogenous condensate with attractive interactions can be stationary, but would be highly unstable with respect to small density perturbations. Also a trapped, inhomogenous BEC need not collapse. The competition between the interaction energy, favouring a strongly localised BEC, and the kinetic energy, which counteracts localisation, can yield a metastable configuration in which the attraction is balanced by the zero-point motion of the atoms in the harmonic trap. This is only possible if the interaction energy does not become too large, posing a limit on the atom number of a stable, attractive BEC. If a critical atom number N_{crit} is exceeded, the BEC collapses, developing extremely high densities so that most atoms are lost due to inelastic collisions, which we alluded to in section 1.2.2. This critical number is [30, 83]

$$N_{\text{crit}} = \frac{k\bar{\sigma}_{\text{ho}}}{|a_s|}. \quad (3.1)$$

Here k is a numerical factor dependent on the trap geometry [30], $\bar{\sigma}_{\text{ho}} = \sqrt{\hbar/(m\bar{\omega})}$, where $\bar{\omega} = \sqrt[3]{\omega_x\omega_y\omega_z}$ is the geometric mean of harmonic trap frequencies. For the cylindrical JILA trap of Ref. [28] we have $k = 0.55$ [30].

The stability properties of condensates with attractive interactions can be further understood using Bogoliubov theory (section 2.3). For attractive interaction, $U_0 < 0$, we see that low wave number excitation energies in the Bogoliubov spectrum (2.35) become complex. According to section 2.3.3 this signals dynamical

instability, in agreement with our discussion above. Excitations with higher wave numbers q in Eq. (2.35) can remain stable even for $U_0 < 0$. This qualitatively² explains the meta-stability of small condensates with attractive interactions expressed in Eq. (3.1). If the BEC is small enough, excitations with wavelengths smaller than the condensate extension are not unstable for the chosen strength of attraction [34].

The collapse experiments at JILA [28, 107] represent the first completely controlled studies of collapsing, attractive BECs. Earlier experiments on unstable ^7Li condensates [108, 109] could not provide such a well defined initial state for the collapse. In the early experiments, a condensate below N_{crit} was continuously fed by a thermal cloud until the critical number was exceeded, initiating collapse. The collapse was therefore triggered in a random fashion. Nonetheless these were the first experiments to verify theoretical predictions about the critical atom number in attractive BECs.

3.2 “Bosenova”

3.2.1 The Experiment

Crucial to the collapse experiment of E. Donley *et al.* [28] was the use of Feshbach resonances. The experiment utilised the Rubidium isotope ^{85}Rb , which possesses particularly broad and therefore experimentally accessible Feshbach resonances [110]. The ^{85}Rb atoms require the use of resonances already for condensation, as they have a negative scattering length at zero magnetic field. Fig. 3.1 (a) shows the magnetic-field dependence of a_s for ^{85}Rb . To evaporatively cool, the magnetic field was adjusted to 162G, indicated by the green dot in the figure. Once the experimentalists successfully created a BEC, they ramped the magnetic field adiabatically to values a_{init} corresponding to the red or blue dots, where the scattering length is +7 Bohr-radii or 0 respectively. Together with the initial atom number of choice N_{init} , these initial states for the experiment are detailed in table 3.1. The Bosenova experiment used a cylindrically symmetric harmonic trap with $\omega_{\perp} = 2\pi \times 17.5$ Hz, $\omega_{\parallel} = 2\pi \times 6.8$ Hz. From the initial value a_{init} the scattering length was suddenly switched to a negative, attractive value a_{collapse} , see Fig. 3.1 (b). For $|a_{\text{collapse}}|$ above the critical value in Eq. (3.1), this initiated collapse. The scattering length was kept at a_{collapse} for a hold time τ_{evolve} . During

²Strictly Eq. (2.35) applies to homogeneous condensates only.

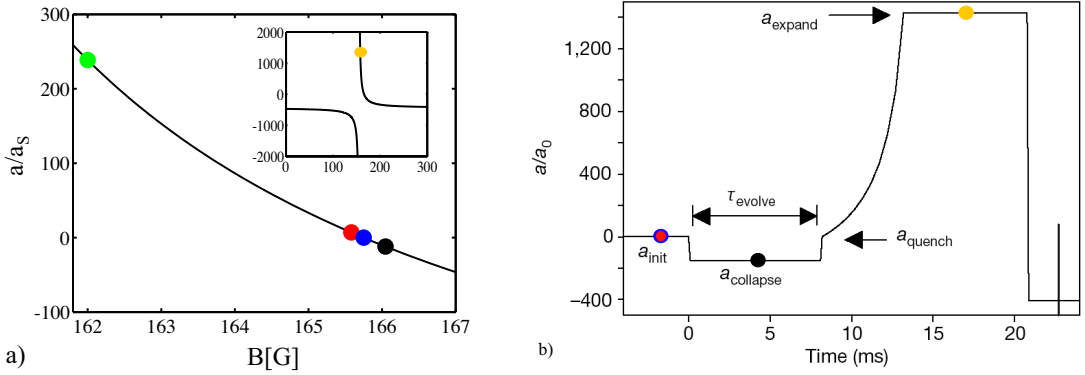


Figure 3.1: (a) ^{85}Rb Feshbach resonance of the Bosenova experiment. The main plot shows the magnetic field dependence of the scattering length in the region most relevant for the experiment. The inset covers a larger range across the resonance at $B_{res} = 155.04\text{G}$. Colorful dots indicate experimental stages: evaporation (green), initial state for case (i) in table 3.1 (red), initial state for case (ii) (blue), collapse (black), expansion for imaging (yellow). (b) Experimental sequence for the magnetic field. Color codes as in (a). The graph in (b) is taken with kind permission from Ref. [28].

| | N_{init} | a_{init} |
|------------|-------------------|-------------------|
| case (i) | 16000 | $+7a_0$ |
| case (ii) | 6000 | 0 |
| case (iii) | 4000 | $+2500a_0$ |

Table 3.1: Initial states for different collapse scenarios. a_0 is the hydrogen Bohr radius. The first two cases appear in Ref. [28], the third is described in [111] but is based on unpublished data.

this period the condensate experiences a violent collapse, which we visualise in section 3.3. The evolution of the BEC was then interrupted in such a way as to allow for precise information about the remaining atom number in the condensate at the moment of interest. This is the sole purpose of the sequence in Fig. 3.1 (b) after τ_{evolve} . The large scattering length a_{expand} was used for an expansion of the cloud to make reliable atom counting with absorption imaging techniques possible [28]. After the jump to a_{quench} , the remaining sequence of Fig. 3.1 (b) no longer influences the evolution of the atom number. The authors of Ref. [28] drew this conclusion from the independence of their results of the precise value

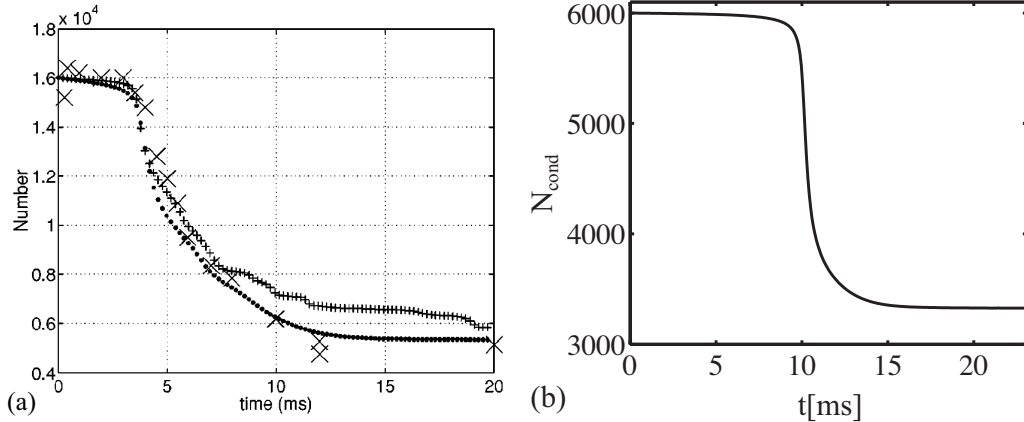


Figure 3.2: (a) Collapse of a case (i) initial state for $a_{\text{collapse}} = -30a_0$. Shown are the experimental results from [28] (\times), and numerical results (\bullet), ($+$) of Ref. [30]. (b) Collapse of a case (ii) initial state for $a_{\text{collapse}} = -10a_0$. We show a numerical result [30] as experimental curves of $N_{\text{cond}}(t)$ have not been published for this case.

of a_{quench} .

The collapsing condensate was observed to lose atoms, until the atom number reduced to about the critical value below which a stable condensate can exist [28]. The dependence of the remaining atom number on time since initiation of the collapse τ_{evolve} was measured for the case (i) of table 3.1. An exemplary graph is shown in Fig. 3.2 (a) together with theoretical results that we comment on in the following section. The experimental data points are obtained by repeated collapse experiments, starting from the same initial state with different τ_{evolve} . For later reference, let N_{remn} be the number of remaining atoms after the completion of the collapse, e.g. $N_{\text{remn}} \sim 5500$ in Fig. 3.2 (a).

The onset of number loss is quite sudden, with milliseconds of very little loss followed by a rapid decay of condensate population. This behaviour results from the scaling of the loss rate with the cube of the density, the peak value of which rises as $1/(t_{\text{collapse}} - t)$ near the collapse point [112]. This allows a precise definition of the collapse time t_{collapse} , the time after initiation of the collapse up to which only negligible numbers of atoms are lost from the condensate.

Another quantitative result of the experiment is the dependence of t_{collapse} on the magnitude of the attractive interaction that causes the collapse, parametrised by a_{collapse} . These measurements are performed from the case (ii) initial state, corresponding to an ideal gas. A typical case (ii) collapse is shown in Fig. 3.2 (b).

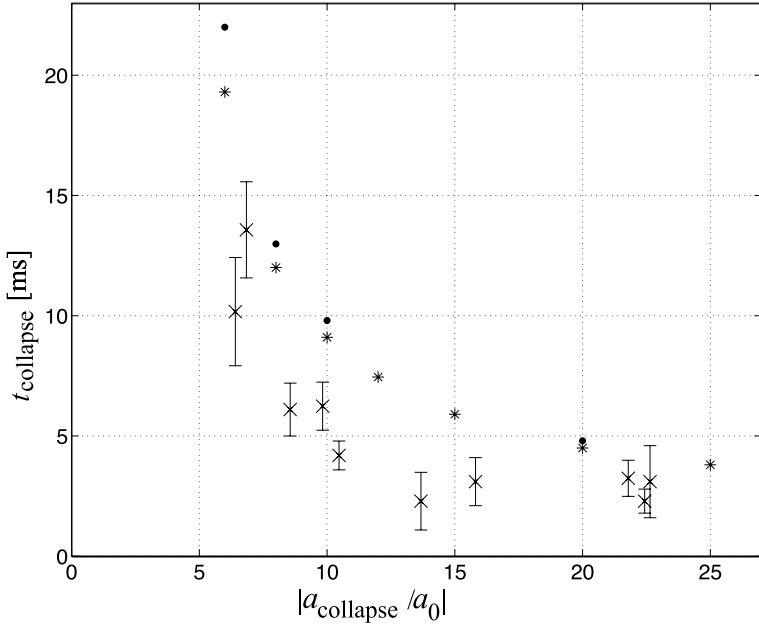


Figure 3.3: Experimental and numerical results for the collapse time t_{collapse} versus scattering length a_{collapse} , after a switch from $a = 0$ to a_{collapse} in case (ii). The experimental points (\times) and their error bars are from Fig. 2 of Ref. [28] taking into account the revision of scattering length values in Ref. [83]. Numerical results are given for exact, cylindrical geometry (\bullet) [30] and for spherical geometry ($*$) with trap frequency equal to the geometric mean of the experimental values. $K_3 = 1 \times 10^{-27} \text{ cm}^6 \text{s}^{-1}$ (results of section 3.3 in this thesis).

Here the decay of the condensate number is even faster (within ~ 0.5 ms) than in the case (i) scenario. Directly after the moment of collapse, the condensate number stabilises again.

The dependence of t_{collapse} on a_{collapse} deduced from the experiment is shown in Fig. 3.3 together with various theoretical results that we discuss shortly. The t_{collapse} datapoints presented in the original paper have undergone one revision of their a_{collapse} values by a factor of 1.166(8) due to a more precisely determined background scattering length [83], which is included in the figure. Graph 3.3 is central to this chapter, as it shows significant disagreement between theoretical and experimental results, discussed in more detail shortly.

There are several other striking features of the experiment, most notably the appearance of “bursts” and “jets”. One fraction of the atoms that are lost during the collapse is expelled from the condensate at quite high energies (~ 100 nK to ~ 400 nK, while the condensate temperature is 3 nK); this phenomenon

was referred to as “bursts”. Finally, when the collapse was interrupted *during the period of number loss* by a sudden jump in the scattering length to e.g. $a_{\text{quench}} = 0$, another atom ejection mechanism was observed: “jets” of atoms emerge, almost purely in the radial direction and with temperatures a lot lower than that of the bursts (a few nK). The experimental sequence triggering the jets is not to be confused with the standard sequence described earlier. Usually the abortion of undisturbed condensate evolution by a scattering length jump to a_{quench} is immediately followed by the atom number and cloud shape measurement. To observe the jets, the condensate is again left to evolve for a varying time *after* the switch to a_{quench} .

3.2.2 The Theory

Collapse time discrepancy

The unstable BEC with attractive interactions and loss of atoms during collapse has been modelled numerically with the Gross-Pitaevskii equation, including loss terms as in section 2.2.5. Numerical solutions to Eq. (2.27) for exact experimental parameters and geometry have been reported by Adhikari [113, 114], Saito and Ueda [115–118], Santos and Shlyapnikov [112], Savage, Robins and Hope [30] as well as Bao, Jaksch and Markovich [119]. They all use $K_1 = K_2 = 0$ as three-body losses dominate once any losses are important. Where these studies consider the initial situation of case (ii), their solutions agree on collapse times that qualitatively describe the experiment but systematically exceed the experimental values. Note that while the remnant atom number after collapse depends strongly on the three-body recombination rate K_3 , which is not well determined near the Feshbach resonance, and for which different values were employed in the references above, the collapse time in case (ii) does not vary much for experimentally reasonable values of K_3 [30]. The reason for this is that the three-body loss acts only as a diagnostic for a rapid increase in density at the point of collapse. In the time leading to this increase, the density of the contracting BEC remains low enough for three-body loss to play no role in the dynamics. Only at and after the actual time of collapse does the precise value of K_3 become relevant.

Fig. 3.3 shows a comparison between GP theory (\bullet) and the revised experimental data (\times) for case (ii). The change in a_{collapse} by a factor of 1.166(8) due to the revision has moved the experimental and theoretical points closer together compared to earlier works, but they still do not agree.

In Refs. [112, 115, 119] this situation is accepted as agreement between theory

and experiment. But if the GP equation indeed contains all the essential physics to describe t_{collapse} , one should expect better agreement since all crucial parameters of the model are experimentally fixed. In addition there exists another case where the GPE can apparently not account for t_{collapse} accurately, and that is the above mentioned case (iii) [111]. One reason for the controversy in the literature might be the fact that the GPE describes collapse times and remnant numbers well for case (i) [30, 113, 115, 119]. The condensates for cases (i) and (ii) are similar in peak density, ruling out a simple qualitative difference of the densities involved as an explanation for this distinct behaviour. Resolutions of this issue are hindered by the fact that only one published data point exists for the case (i) collapse time, compared to a whole set for case (ii).

Complementary to the numerical approach to the problem, one can attempt to find an analytic approximation that describes the essential features of the BEC collapse. Métens *et al.* [120] employ a variational approach assuming a Gaussian condensate shape. For values $\|a| - |a_{cr}\||/|a_{cr}| \ll 1$, where a_{cr} is the critical scattering length above which the BEC does not collapse, Eq. (3.1), they obtain $t_{\text{collapse}} \sim (|a/a_{cr}| - 1)^{-1/4}$, in agreement with Ref. [117]. But this parameter regime does not apply to the experiment, and it turns out that the scaling law becomes modified to $t_{\text{collapse}} \sim (|a/a_{cr}| - 1)^{-1/2}$ for scattering lengths away from the critical value [120]. Calzetta *et al.* [45] derive a scaling law for the collapse time from the growth of unstable perturbations of the atom field. Their result agrees with the one cited above, which seems to capture the shape of the function correctly. However both methods are unable to account for the proportionality constant, as both groups fit this parameter or the initial state to obtain agreement with experimental data.

In summary, mean field theory can describe the shape of the dependence of t_{collapse} on a_{collapse} correctly, but for case (ii) the real collapse seems significantly accelerated compared to these predictions. Naturally, one would suspect deviations from GP theory to be the cause of this phenomenon [30, 45].

Yurovsky [121] investigates quantum effects in homogeneous BECs with attractive interaction analytically, using an approximate solution to the operator equation for the condensate fluctuations. Results from Ref. [121] regarding the growth of an initially seeded unstable momentum-mode have been experimentally verified [122]. Yurovsky also derives an expression for the time evolution of condensate depletion.

Jets

Another prominent feature of the JILA experiment was the appearance of radial atomic jets when the collapse was suddenly interrupted. Numerical simulations were able to reproduce them using the GPE [114, 115, 119]. The phenomenon can be explained as interference of atom emission from highly localised density spikes that are formed during collapse [115]. The simulations seem to reproduce jet-shapes, anisotropy and dependence on t_{evolve} (Fig. 5 of [28]). By contrast Calzetta *et al.* [45] present a mechanism for jet production that is essentially a quantum effect. Their model reproduces the features of the experimental data for atom numbers in jets (Fig. 6 of [28]) for the range of validity of the approximations involved. Regarding this, the numerical simulations in [114, 119] yield a similar (partial) agreement with experiment, but do not agree with each other. Another feature of the jets in the collapse experiment is the existence of large fluctuations in the atom number in jets. Calzetta *et al.* [45] attribute this to a large number uncertainty in squeezed quantum states, while Bao *et al.* [119] reproduce these fluctuations by slight variations in the position of the initial state condensate wave function. The existence of jets can thus be predicted by GP theory alone, but it is not yet clear what role quantum effects play.

Bursts

Finally, one has to explain the bursts. These are atoms that remain in a detectable, trapped state during collapse but are found performing large amplitude oscillations in the trap. Numerical solutions of the GPE generally show atoms being ejected from the condensate at the time of collapse. In order to be candidates for the burst atoms in the JILA experiment, they need to have rather high energies ~ 100 nK (compare Fig. 4 of [28]). The ejected atoms within the condensate gain their energy due to a loss in (negative) mean field energy by three-body recombination, which is sensitive to the three body loss rate K_3 . Since K_3 is experimentally not very well constrained in the parameter regime in question [123], it is possible to reproduce the atom burst by matching K_3 to the energy spectrum [118]. But in Ref. [112] it is shown, that even if K_3 is fitted to the energy spectrum for *each* value of a_{collapse} , one cannot obtain simultaneous agreement for cases (i) and (ii) described in Ref. [28]. Furthermore, the remnant atom number after collapse N_{remn} also depends on K_3 and the values for K_3 that are necessary to obtain high energy bursts in agreement with the experiment, yield N_{remn} that disagree with the experiment. Calzetta *et al.* [45] also suggest a

quantum treatment of the bursts but do not put forward any quantitative predictions. Milstein, Menotti and Holland [82] present a model calculation showing that atom-molecule coupling can yield sufficiently energetic atoms, however they do not examine the experimental parameter regime. In this thesis, we will follow the formalism developed by Milstein *et al.*, but derive and utilise a slightly different position space representation of the approach taken in Ref. [82], using mostly the atomic field only.

An alternate model that describes physics beyond the GPE has been proposed by Duine and Stoof [111, 124] and applied to the collapse case (iii). They suggest elastic collisions between condensate atoms as the origin of the burst, and an additional channel by which the condensate can eject atoms. One of the collision partners gets ejected into the noncondensate in the process, while the other one is stimulated back into the condensate. This process is termed quantum evaporation. The model yields results that describe well the experimental data for the case (iii) collapse. But case (ii) cannot be treated with a Gaussian variational ansatz [124], and it is not clear how to incorporate these elastic collisions into a treatment that is focussed on the backreaction of uncondensed atoms on the condensate. We will comment further on the relation to our model in the last section.

A numerical study that accurately reproduces the bursts *and* all other results of the experiment therefore does not yet exist.

3.3 Spherical Gross-Pitaevskii Model

In the introduction to this chapter we stated our intention to apply the Hartree-Fock-Bogoliubov formalism of section 2.4 to the Bosenova experiment. This is an ambitious plan. Quantum corrections are included in the HFB framework as correlation functions $G_N(\mathbf{x}, \mathbf{x}')$, $G_A(\mathbf{x}, \mathbf{x}')$. For three spatial dimensions these represent six dimensional functions. Due to the cylindrical symmetry of the experimental system, the number of dimensions can be reduced to five. However, with reasonable numbers of numerical grid points per dimension, 3D numerical solutions of Eqns. (2.47)-(2.48) are unfeasible with the available computational resources, even exploiting cylindrical symmetry.

This forces us to model the experiment in spherically symmetric confinement. The trap frequency is chosen to equal the geometric mean of the experimental trap frequencies: $\omega = (\omega_\perp^2 \omega_\parallel)^{1/3}$. As $\omega_\perp = 17.5$ Hz and $\omega_\parallel = 6.8$ Hz [28], we have

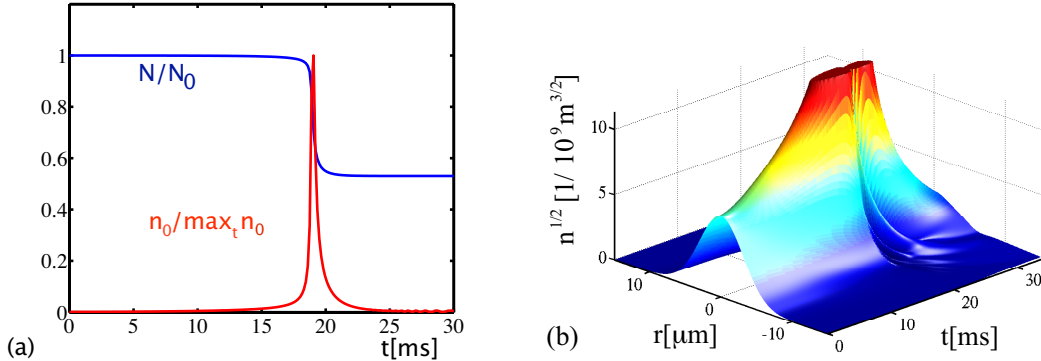


Figure 3.4: Numerical solution of the GPE for a spherically symmetric collapse with $a_{\text{collapse}} = -6a_0$ and $\omega = 12.8$ Hz. Time evolution of (a) atom number and peak density n_0 , both normalised to have unit maximum and (b) the spatial dependence of the condensate’s modulus. $N_0 = 6000$ and $\max_t n_0 = 2.0 \times 10^{22}/\text{m}^3$.

$\omega = 12.8$ Hz. Assuming a spherically symmetric system, the dimensionality of the correlation functions can be reduced to three. This process is detailed explicitly in appendix B.

Even if the geometry now no longer corresponds precisely to the Bosenova experiment, we can still compare the result of semi-classical Gross-Pitaevskii simulations with the predictions of Hartree-Fock-Bogoliubov theory, both for the spherical case. This tells us whether quantum depletion can accelerate a collapse in a situation similar to the experiment. The twice stronger interaction between condensed and uncondensed atoms should accelerate a collapse for sufficient depletion independent of the trapping geometry.

We thus first solve the GP equation (2.27) for the spherical case, with $K_1 = K_2 = 0$. Following [30], we choose $K_3 = 1 \times 10^{-39} \text{ m}^6 \text{s}^{-1}$. As argued in section 3.2.2 the precise value of K_3 is not important for collapse time results. The dependence of the collapse time on the strength of attraction is our main result for this section and included in Fig. 3.3. The spherical situation gives quite a good estimate of the complete three dimensional GPE collapse time. The purpose of these results, however, is as a point of comparison for the quantum theory results in section 3.4.1.

To give the reader an idea of the BEC collapse dynamics, we show graphs of the condensate GP evolution in Fig. 3.4. At the moment of collapse, the density develops an extremely high and narrow peak, shown in Fig. 3.4 (a). The peak has been cut off in Fig. 3.4 (b), to keep the remaining evolution visible. Its true

amplitude in the units of panel (b) is $\sqrt{n_{\max}} = 1.4 \times 10^{11}/m^{3/2}$. Directly after the collapse, atoms are rapidly propagating outwards. They form the spherical equivalent of the burst atoms described earlier. Together, these effects are the reason why the numerical simulation of semi-classical collapse dynamics is comparatively challenging. To represent the collapse peak accurately we require a fine grid spacing. To capture the ejected burst, the spatial domain has to be large, much larger than the fraction shown in Fig. 3.4 (b). Additionally, the extreme densities and high momentum components during the collapse enforce a small discrete time step. Many of the collapse features can be seen in the movie `bosenova-collapse-gpe.mov` on the CD, which shows a GPE simulation in cylindrical symmetry corresponding to the collapse in Fig. 3.2 (b).

The large discrepancy in numerical demands between the relatively calm period leading up to the collapse and the collapse point itself, makes studies of the Bosenova ideally suited for adaptive time step methods, such as the Runge-Kutta-Fehlberg ARK45 algorithm [102]. Adaptive spatial grid methods might be also highly beneficial, but have not been studied within this thesis.

3.4 Quantum Corrections in the Hartree-Fock-Bogoliubov Framework

Having established the semi-classical collapse time results for spherically symmetric condensates in the previous section, we are now ready to proceed to quantum theory. The full set of coupled Hartree-Fock-Bogoliubov equations has been given in Eqns. (2.47)-(2.48). Our first task is to cast them into a simpler form, utilising the spherical symmetry of the system. In the following, we elaborate only the major points of this adaptation, full details are given in appendix B.

Most importantly, we work in coordinates:

$$R = |\mathbf{x}|, \quad R' = |\mathbf{x}'|, \quad \beta = \cos \gamma, \quad (3.2)$$

where γ is the angle between the vectors \mathbf{x} and \mathbf{x}' . Due to the restriction to spherical symmetry the correlation functions will not depend on the overall orientation of \mathbf{x} and \mathbf{x}' , or on the azimuthal angle of \mathbf{x}' around \mathbf{x} , reducing the dimensionality of G_A and G_N from six to three. Following [82] the β dependence is expanded in terms of Legendre polynomials $P_n(\beta)$. Numerically, we model the delta function in Eq. (2.48) by a step function on one spatial grid point. The corresponding cut-off for renormalisation purposes is $K = \pi/\Delta R$, where ΔR is

our grid spacing (compare section 2.4.3). We now define:

$$\phi_a(R) = \frac{\tilde{\phi}_a(R)}{R}, \quad G_{N/A}(R, R', \beta) = \frac{\tilde{G}_{N/A}(R, R', \beta)}{RR'}, \quad (3.3)$$

and expand the correlation functions as:

$$\tilde{G}_N(R, R', \beta) = \sum_{n=0}^{M-1} \tilde{G}_N^{(n)}(R, R') P_n(\beta), \quad (3.4)$$

$$\tilde{G}_A(R, R', \beta) = \sum_{n=0}^{M-1} \tilde{G}_A^{(n)}(R, R') P_n(\beta), \quad (3.5)$$

where M is the number of Legendre Polynomials employed. We use the additional notation:

$$\bar{G}_{N/A}(R) \equiv \tilde{G}_{N/A}(\mathbf{R}, \mathbf{R}) = \sum_{n=0}^{M-1} \tilde{G}_{N/A}^{(n)}(R, R). \quad (3.6)$$

Our final form for the condensate equation is:

$$i\hbar \frac{\partial \tilde{\phi}(R)}{\partial t} = \left(-\frac{\hbar^2}{2m} \frac{\partial^2}{\partial R^2} + V(R) - i\frac{\hbar K_3}{2} |\tilde{\phi}(R)|^4 \right) \tilde{\phi}(R) + \frac{U_0}{R^2} \left(2\bar{G}_N(R) + |\tilde{\phi}(R)|^2 \right) \tilde{\phi}(R) + \frac{U_0}{R^2} \bar{G}_A(R) \tilde{\phi}^*(R), \quad (3.7)$$

The expansion coefficients obey the following equations of motion:

$$i\hbar \frac{\partial \tilde{G}_N^{(n)}(R, R')}{\partial t} = \left[-\frac{\hbar^2}{2m} \left(\frac{\partial^2}{\partial R^2} - \frac{\partial^2}{\partial R'^2} - n(n+1) \left(\frac{1}{R^2} - \frac{1}{R'^2} \right) \right) + V(R) - V(R') + 2U_0 \frac{|\tilde{\phi}(R)|^2 + \bar{G}_N(R)}{R^2} - 2U_0 \frac{|\tilde{\phi}(R')|^2 + \bar{G}_N(R')}{R'^2} \right] \tilde{G}_N^{(n)}(R, R') + U_o \frac{\tilde{\phi}(R)^2 + \bar{G}_A(R)}{R^2} \tilde{G}_A^{(n)*}(R, R') - U_o \frac{\tilde{\phi}^{2*}(R') + \bar{G}_A^*(R')}{R'^2} \tilde{G}_A^{(n)}(R, R'), \quad (3.8)$$

$$i\hbar \frac{\partial \tilde{G}_A^{(n)}(R, R')}{\partial t} = \left[-\frac{\hbar^2}{2m} \left(\frac{\partial^2}{\partial R^2} + \frac{\partial^2}{\partial R'^2} - n(n+1) \left(\frac{1}{R^2} + \frac{1}{R'^2} \right) \right) + V(R) + V(R') + 2U_0 \frac{|\tilde{\phi}(R)|^2 + \bar{G}_N(R)}{R^2} + 2U_0 \frac{|\tilde{\phi}(R')|^2 + \bar{G}_N(R')}{R'^2} \right] \tilde{G}_A^{(n)}(R, R') + U_o \frac{\tilde{\phi}(R)^2 + \bar{G}_A(R)}{R^2} \tilde{G}_N^{(n)*}(R, R') + U_o \frac{\tilde{\phi}(R')^2 + \bar{G}_A(R')}{R'^2} \tilde{G}_N^{(n)}(R, R') + U_o \left(\tilde{\phi}(R)^2 + \bar{G}_A(R) \right) \frac{2n+1}{4\pi R^2} \delta(R - R'). \quad (3.9)$$

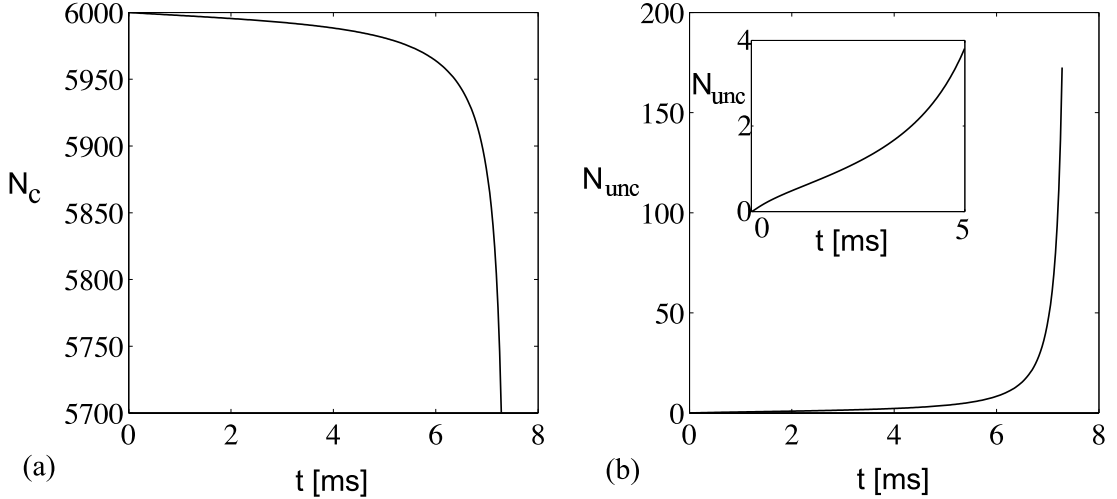


Figure 3.5: Number of condensed (a) and uncondensed (b) atoms during a case (ii) collapse with $a_{\text{collapse}} = -12a_o$ until $t = 7.3$ ms. The initial atom number was $N_o = 6000$, all in the condensate. A three-body loss term with $K_3 = 1 \times 10^{-27}$ cm⁶s⁻¹ is included for the condensate. The GPE value for $t_{\text{collapse}}(a/a_o = -12)$ is 7.45 ms. Numerical requirements prevent the simulations from reaching the exact GPE collapse point. Inset of (b): initial evolution of uncondensed-atom number.

3.4.1 Condensate Depletion

Having cast the HFB equation into a form suitable for a harmonic trap, we can now determine the time evolution of the quantum depletion and condensate number for the same cases considered in section 3.3 with the GPE only. We compute a solution to Eqs. (3.7)-(3.9) for the experimental parameters [28] of a case (ii) collapse ($a_{\text{collapse}} = -12a_o$), starting with a gaussian initial state and no uncondensed atoms ($G_A = G_N \equiv 0$) due to the absence of interactions in the initial state, $a_{\text{init}} = 0$.

We found that the BEC does not collapse earlier than in the corresponding spherical GPE simulations. The number of atoms in excitation modes, shown in Fig. 3.5, does not grow fast enough to accelerate the collapse. Only just before the collapse time predicted by the GPE are large numbers of uncondensed atoms created.

We do not simulate the collapse beyond or in fact even precisely until the GPE point of collapse. This is due to the numerical complications described at the end of the previous section. The large numbers of radial grid points required in the collapse are even more prohibitive for solutions of the HFB equations than for the

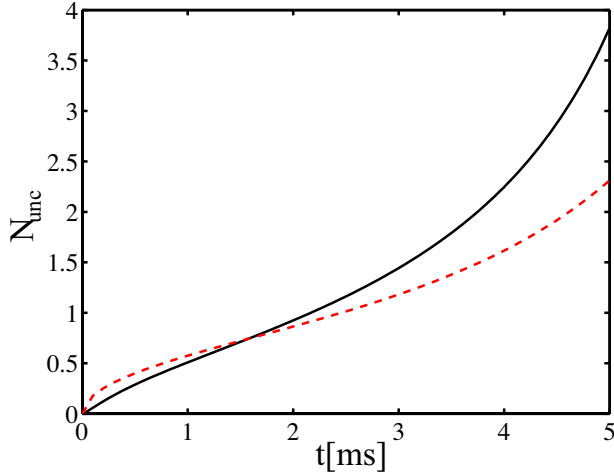


Figure 3.6: Comparison of the uncondensed atom number in our HFB formalism (black, solid), for parameters as in Fig. 3.5, with analytical predictions using Eq. (3.10) (red, dashed) in a local density approximation.

GPE, as the correlation functions possess two “radial” dimensions. However, in order to conclude that no acceleration of the collapse due to quantum depletion has occurred, we do not have to push the simulations into the collapse.

We compared the uncondensed atom numbers occurring in our simulations with the predictions of Yurovsky [121]. Yurovsky analytically derives an expression for the number of atoms transferred to uncondensed modes in a homogeneous condensate. Similar to the Bosenova experiment, the system is assumed to be in a pure BEC state at time $t = 0$, i.e. $n_{\text{unc}}(t = 0) = 0$. Yurovsky finds that the depletion after a period t in the presence of attractive interaction is given by:

$$n_{\text{unc}}(t) = 8a_S^2 n_{\text{cond}}^2 \sqrt{\frac{2\pi\hbar t}{m}}, \quad (3.10)$$

for times much smaller than $t_{\text{NL}} = (U|\phi(0)|^2/\hbar)^{-1}$, the nonlinear interaction time [121]. This time is approximately 4 ms for the collapse case presented here. We compare Eq. (3.10) with our results in Fig. 3.5 using a local density approximation³ and found agreement between the results until t_{NL} , to the extent shown in Fig. 3.6.

The main effort in our simulations went into the computation of the correlation functions of the condensate fluctuations G_N and G_A from which the uncondensed density \bar{G}_N is derived. Fig. 3.7 shows the initial evolution of the densities of the

³We take $n_{\text{unc}}(r, t) = 8a_S^2 n_{\text{cond}}(r, t)^2 \sqrt{2\pi\hbar t/m}$ ignoring other effects of inhomogeneity.

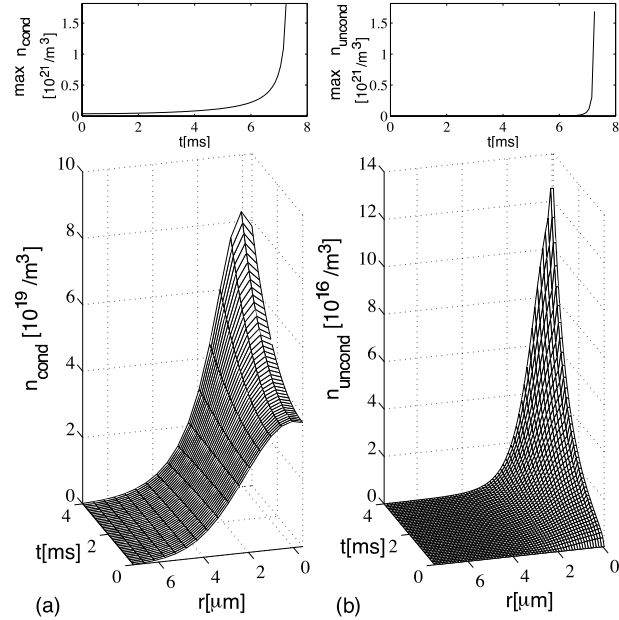


Figure 3.7: a) Time evolution of condensate density $n_{\text{cond}} = |\phi|^2$ and b) density of uncondensed atoms $n_{\text{uncond}} = \bar{G}_N$ for a case (ii) collapse with $a_{\text{collapse}} = -12a_o$. Above we display the corresponding peak densities until $t = 7.3$ ms.

condensed and uncondensed atoms and the corresponding peak densities for the simulated period of time. To illustrate the structure of the complete correlation functions $G_{N/A}(\mathbf{R}, \mathbf{R}')$, some representative samples are displayed in Fig. 3.8.

The results presented were computed on a grid with $N_r = 256$ points for R and R' , ranging from $-15 \mu\text{m}$ to $+15 \mu\text{m}$ each⁴, and eight Legendre polynomials. We checked that the results do not vary for changed spatial grid size or number of Legendre polynomials. The timesteps were 50 ns and 100 ns to check convergence. The variation of N_r also verified the cut-off independence of our simulations. Our multiprocessor code was run on 8 or 16 CPUs and employed the RK4IP algorithm developed by the BEC theory group of R. Ballagh at the University of Otago⁵. Parts of the simulations were done with the aid of the high level language XMDS⁶. Some comments regarding the parallel implementation can be found in appendix B.

⁴We employed artificial negative radii to allow the use of Fast Fourier transforms, see section D.1.2.

⁵The RK4IP method is described in the Ph.D. thesis of B.M. Caradoc-Davies which is online at: <http://www.physics.otago.ac.nz/bec2/bmcd/>. This is a pseudo-spectral method with a Runge-Kutta time step.

⁶Online at www.xmds.org.

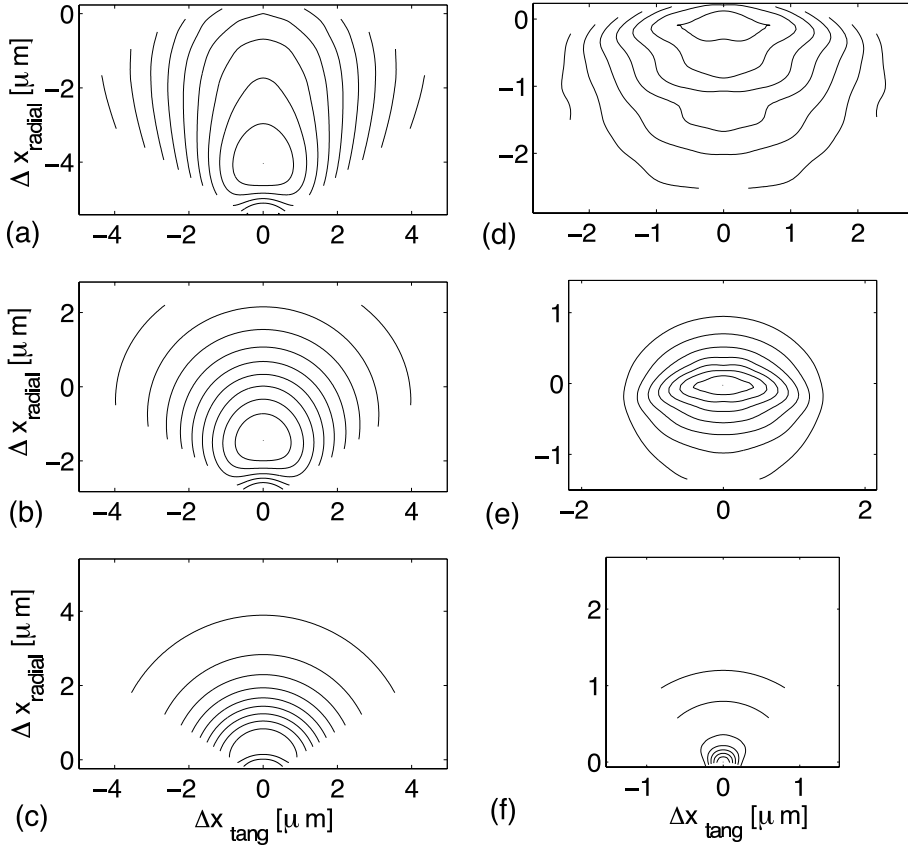


Figure 3.8: Equal amplitude contours of correlation functions $G_{N/A}(\mathbf{R}_0, \mathbf{R})$ for fixed \mathbf{R}_0 . We plot correlations for \mathbf{R} varying in a plane that contains the trap centre and the point \mathbf{R}_0 . The origin of cartesian coordinates $(\Delta x_{\text{tang}}, \Delta x_{\text{radial}})$ in this plane is taken to be \mathbf{R}_0 , a distance $|\mathbf{R}_0| = R_o$ from the trap centre. The Δx_{radial} axis connects \mathbf{R}_0 with the trap centre, which is thus located at the bottom-centre of each plot. The contours are equally spaced between the maximum value and 1/10 (3/10) of it, for G_N (G_A). The data was sampled on a $128 \times 128 \times 128$ grid in (R, R', θ) and subsequently interpolated to four times higher resolution, using standard matlab routines. Normal density G_N around a) $R_0 = 5.8 \mu\text{m}$, b) $R_0 = 3.2 \mu\text{m}$, c) $R_0 = 0.6 \mu\text{m}$. Anomalous density G_A around d) $R_0 = 5.8 \mu\text{m}$, e) $R_0 = 3.2 \mu\text{m}$, f) $R_0 = 0.6 \mu\text{m}$. The snapshot is taken during a case (ii) collapse with $a = -12a_0$ at $\tau_{\text{evolve}} = 5 \text{ ms}$. Panels (a), (b), (d), (e) show a difference in normal and anomalous atomic correlations, depending on whether \mathbf{R}_0 and \mathbf{R} are separated radially or tangentially in our spherical coordinate system. (c) If \mathbf{R}_0 is chosen near the origin, the direction of \mathbf{R} becomes irrelevant.

A drawback of the basic HFB method that we discussed in section 2.4.1 is the unphysical gap in the excitation spectrum. The gap can be viewed as a consequence of an incomplete renormalisation of certain terms in the HFB equations [125]. As described in section 2.4.1, the correct renormalisation would require the inclusion of higher order correlation functions [73, 125]. Since the effects of renormalisation on the coupling constant are small in the parameter regime of case (ii), it is not a priori clear whether a more complete renormalisation would significantly alter the number of uncondensed atoms.

In order to clarify this point, we applied the gapless HFB method of [73] (see section 2.4.1) to a case (ii) collapse and found no changes in our results. This can be easily explained, as for the undepleted initial state and relatively short evolution times, $\bar{G}_A(\mathbf{x})$ remains small compared to the condensate density throughout our simulations. It follows from Eq. (2.52), that the effective interaction strength of the gapless HFB method is essentially unchanged compared to the uncorrected coupling. In the regime of interest, many-body effects on the interatomic interactions are thus of minor significance.

3.4.2 Resonance Theory

The Feshbach resonance is a crucial element of the Bosenova experiment. The enhancement of atom scattering due to a Feshbach resonance and the associated appearance of a molecular condensate can be an important piece of cold atom physics. For example coherent transfers of condensate population from the atomic to the molecular fraction have been observed in [126]. This experiment has been successfully described using the resonance theory of section 2.4.4 [84]. For a Bosenova collapse, the full atom-molecule resonance theory is however not required, as we will show in this section.

The inclusion of the molecular field is important for magnetic fields closer to the resonance than is the case in the Bosenova experiment [45]. For magnetic fields further from the resonance, the molecular field can be adiabatically eliminated, following [45]. We outline the procedure for semi-classical theory, neglecting $\hat{\chi}(\mathbf{x})$ and atomic correlations. The reasoning is analogous but more complicated if quantum corrections are included.

According to section 2.4.4, the semi-classical evolution equation for the molecules is:

$$i\hbar \frac{\partial \phi_m(\mathbf{x})}{\partial t} = \left(\hat{H}_{\text{mol}} - \nu_0 \right) \phi_m(\mathbf{x}) + \frac{g_0}{2} \phi_a(\mathbf{x})^2. \quad (3.11)$$

Here the single particle Hamiltonian \hat{H}_{mol} describes a particle of mass $2m$ subject to a potential $2V$, i.e. $\hat{H}_{\text{mol}} = -\hbar^2 \nabla_{\mathbf{x}}^2 / 4m + 2V(\mathbf{x})$. If the detuning ν_0 is much larger than the kinetic and potential energy of the populated molecular field modes, \hat{H}_{mol} can be neglected in Eq. (3.11). From

$$i\hbar \frac{\partial \phi_m(\mathbf{x})}{\partial t} = -\nu_0 \phi_m(\mathbf{x}) + \frac{g_0}{2} \phi_a(\mathbf{x})^2 \quad (3.12)$$

we can then obtain an expression for the molecular field using the rotating wave approximation: If the period of rapid oscillations set by ν_0 is much shorter than the time scale of variations in $\phi_a(\mathbf{x})$, the term $\partial \phi_m(\mathbf{x})/\partial t$ averages out in Eq. (3.12). We are left with:

$$\phi_m(\mathbf{x}) = \frac{g_0}{2\nu_0} \phi_a(\mathbf{x})^2. \quad (3.13)$$

Still ignoring quantum correlations, the GP Eq. (2.61) for the atom field becomes:

$$i\hbar \frac{\partial \phi_a(\mathbf{x})}{\partial t} = \left(-\frac{\hbar^2}{2m} \nabla_{\mathbf{x}}^2 + V(\mathbf{x}) + U_0 |\phi_a(\mathbf{x})|^2 \right) \phi_a(\mathbf{x}) + g_0 \phi_m(\mathbf{x}) \phi_a^*(\mathbf{x}) \quad (3.14)$$

$$= \left(-\frac{\hbar^2}{2m} \nabla_{\mathbf{x}}^2 + V(\mathbf{x}) + U_0 \left(1 + \frac{g_0}{2\nu_0 U_0} \right) |\phi_a(\mathbf{x})|^2 \right) \phi_a(\mathbf{x}). \quad (3.15)$$

By comparison with the expression for the effective resonant interaction (2.66)⁷, we see that the effect of the molecular field is merely to adjust the atomic scattering length to an effective value. In this situation, it is sufficient to use the resonance mediated interaction strength for the interatomic interactions. For the coupling U_0 in the HFB equations (section 2.4), we can thus directly employ U_{eff} from Eq. (2.66) (section 2.4.4) and remove the molecular field, as its effect is then already taken into account.

To explicitly verify the negligibility of molecular field effects on a Bosenova collapse, we nonetheless simulate the condensate collapse using HFB resonance theory according to section 2.4.4. We include quantum correlation functions for the atomic but not for the molecular field. We find that a molecular field does not alter our main result: Condensate depletion is not sufficient to significantly accelerate the collapse.

The coupled set of equations for HFB resonance theory consists of (2.61), (2.62), (2.48) and (2.49), where the latter two contain additional terms involving the molecular field. These modifications are detailed in Ref. [82]. We also employed the same representation of correlation functions as the authors of Ref. [82].

⁷For the comparison we have to identify $U_0 = U_{\text{bg}}$, as we neglect quantum fluctuations.

From the arguments \mathbf{x} , \mathbf{x}' of the functions $G_A(\mathbf{x}, \mathbf{x}')$, $G_N(\mathbf{x}, \mathbf{x}')$ we change variables to $\mathbf{R} = (\mathbf{x} + \mathbf{x}')/2$ and $\mathbf{r} = \mathbf{x} - \mathbf{x}'$. The functions $G_A(\mathbf{R}, \mathbf{r})$, $G_N(\mathbf{R}, \mathbf{r})$ are Fourier transformed with respect to \mathbf{r} to yield $G_A(\mathbf{R}, \mathbf{k})$, $G_N(\mathbf{R}, \mathbf{k})$. Finally spherical symmetry is exploited to describe correlations in the space $R = |\mathbf{R}|$, $k = |\mathbf{k}|$ and $\alpha = \angle(\mathbf{R}, \mathbf{k})$. We now also have to transform the equations of motion. In terms like $\left[|\phi(\mathbf{x})|^2 + |\phi(\mathbf{x}')|^2 + \bar{G}_N(\mathbf{x}) + \bar{G}_N(\mathbf{x}') \right] G_A(\mathbf{x}, \mathbf{x}')$ of Eq. (2.48), we assume $|\phi(\mathbf{x})|^2 = |\phi(\mathbf{x}')|^2$ and $\bar{G}_N(\mathbf{x}) = \bar{G}_N(\mathbf{x}')$ within the square brackets. Then we let $\mathbf{x} \rightarrow \mathbf{R}$. In this manner, we avoid convolution integrals in the equations of motion. This approximation was also used in Ref. [82] and is justified as long as the length scale of correlations, i.e. values of r for which G_A and G_N are significant, is short compared to the length scale of variations in the condensate cloud.

As initial checks of our code we reproduced the results of Milstein *et al.* [82] and Holland *et al.* [127]. This verification step was greatly simplified by following the above parametrisation of correlations, rather than the one employed earlier and detailed in appendix B.

To apply the resonance theory to the exact experimental situation, the initial state for the molecular field needs to be carefully adjusted. We chose $\phi_m(\mathbf{x}, 0)$ such that it obeys Eq. (3.13). This is a natural choice, even if approximate, related to the ground state of the Hamiltonian in the homogenous case [128]. Fig. 3.9 shows that for such a molecular initial state, the molecular density performs rapid oscillations around $(g/(2\nu))^2 |\phi_a(\mathbf{x}, t)|^4$. The time averaged effect on the interaction terms in the modified GP equation (2.61) is thus just the generation of an effective atom-atom interaction of strength U_{eff} . This supports the view presented in Ref. [45], that off-resonance the molecular field is not a crucial part of the physics. A complete simulation for the case $a = -20a_0$ as in section 3.4.1 shows that after 1.5 ms the condensate depletion in our resonance theory simulations is 4 times higher than in a corresponding simulation with atoms only. These are still not enough uncondensed atoms to affect the mean-field dynamics.

We believe that even this factor of four is more likely evidence that the incorporation of molecules into HFB quantum theory must be done with more care rather than a genuine molecular field effect: Due to the large atom-molecule coupling g , the product $|g\phi_m|$ is of the order of $U|\phi_a|^2$ even for small molecular population as in Fig. 3.9. To be consistent, it might therefore be necessary to include quantum fluctuations of the molecular field, as sketched at the end of section 2.4.4. Also the approximation assuming small condensate variation

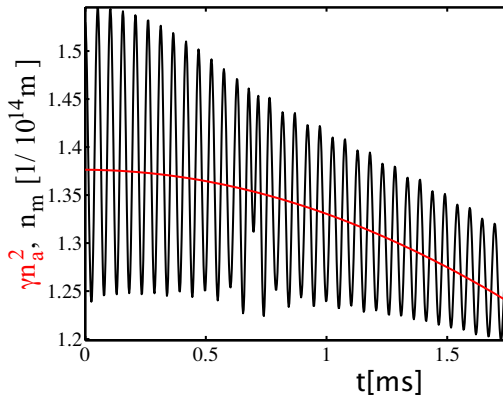


Figure 3.9: Rapid population oscillations of the molecular condensate. (black) Density of the molecular condensate n_m at a selected reference point. (red) Instantaneous value of $\gamma^2 n_a^2$, where n_a is the density of the atom condensate at the same location and $\gamma = g_0/2\nu_0$.

within the correlation length is not safely fulfilled, as we find numerically. We did not pursue this path any further. Nonetheless a more careful implementation of the molecular field for other interesting, spherically symmetric non-equilibrium problems might be a subject for further studies.

3.4.3 Discussion

Hartree-Fock-Bogoliubov theory indicates that the condensate depletion during a Bosenova collapse is insufficient to have a measureable influence on the dynamics of the mean field. This result is reinforced by agreement with the analytical predictions of Yurovsky [121]. Our studies of resonance theory show that molecular effects can also not explain the discrepancy between experimental and theoretical collapse times. The results of Hartree-Fock-Bogoliubov simulations of collapsing condensates presented so far have been published in the Physical Review [129].

In theoretical studies of the Bosenova, the growth of the uncondensed fraction by elastic collisions (quantum evaporation) has been pointed out [111, 124]. This might also play an important role in a case (ii) collapse. Elastic collisions with a single atom transferred to the uncondensed fraction do not occur in the HFB theory, since the creation of pairs can be identified as the leading contribution to the production of uncondensed atoms in the limit of weak coupling U_o . This

does not mean that relevant physics is missing in the HFB method, as a coherent elastic collision process with one atom scattering into a previously uncondensed mode might transfer coherence into that region of Hilbert space [130]. In that case the above process would not populate G_N since we define the quantum field $\hat{\chi}$ to have zero expectation value. Elastic collisions of the quantum evaporation type are thus in our framework part of the nonlinear dynamics of the GP mean field.

A further step could be to employ a different factorisation scheme for the correlation functions, for example the method of non-commutative cumulants put forward in [74] which differs from ours in its truncation method. To determine the rate of spontaneous production of uncondensed atoms in that formalism we would need to include the higher order correlation functions in our simulations.

The two biggest approximations involved in the HFB treatment presented so far are the use of spherical symmetry and the factorisation of correlation functions. Stochastic truncated Wigner theory can be used to close these loopholes in our approach. We described in section 2.5, how truncated Wigner theory of a three-dimensional Bose gas is formulated in terms of the three-dimensional stochastic wave function. Despite requiring solutions of the equation of motion for a possibly large number of trajectories, this method is much more tractable than handling the five dimensional correlations functions of an HFB study in cylindrical symmetry. The study of collapsing condensates with the Wigner method allows us to employ a somewhat complementary approximation scheme for the quantum evolution, and to simultaneously extend our studies to the exact experimental geometry.

3.5 Quantum Corrections in the Truncated Wigner Framework

Previously in his chapter, we showed that quantum corrections in the framework of time dependent Hartree-Fock-Bogoliubov theory do not accelerate the collapse of a BEC in a spherically symmetric trap. We now investigate the collapse in a cigar shaped trap, exactly like in the experiment. The cylindrical situation can be tackled in the truncated Wigner approximation (TWA), using accurate experimental parameters. This method is explained in detail in section 2.5. We find that the inclusion of quantum effects also in this approach does not yield results in agreement with the experiment.

We also show that the initial presence of a thermal cloud increases the production rate of uncondensed atoms, i.e. depletion. The resulting reduction in the condensate population just before collapse could, in principle, appear as a slightly accelerated collapse. However, we will explain below why this effect would be difficult to detect in an experiment. Irrespective of measurability, even for temperatures about three times higher than the experimental temperature of $T = 3 \text{ nK}$, the acceleration of the collapse due to depletion is insufficient to bring the theoretical and experimental results into agreement.

In the experiment, the measured atom number was deduced from counting atoms in the central region of the trap. In our simulations the uncondensed atoms are produced in the same spatial region as the BEC. Since the experimental method did not distinguish between condensed and uncondensed atoms, we conclude that the experiment was not sensitive to the above described temperature effect. We note that, for $T \neq 0$, the evolution of the *total* number of atoms is essentially unchanged compared to the GP results.

3.5.1 Numerical Method

The aim of this section is to point to the relevant elements of the theory in chapter 2, and to clarify the basis of the conclusions drawn from our stochastic simulations.

We present solutions of the Wigner SDE (2.88) in section 2.5, modelling the Bosenova experiment without any significant free parameters. Recall from section 2.5 that in the stochastic treatment, the equation of motion is very similar to the GPE, with additional noise η added to the initial state and, in the presence of three-body losses, a dynamical noise term $d\xi$ in the equation of motion.

For reasons given in section 2.5.6, it is advantageous to solve the stochastic equation of motion for Bosenova collapse scenarios in the harmonic oscillator basis. A brief description of the method and definitions for condensed and uncondensed component in this case can also be found in that section.

Eqns. (2.95)-(2.99) show the form of the stochastic GPE in the energy basis, including the required overlap integrals. It has been outlined in Refs. [103, 104] how these integrals can be exactly computed on an appropriately chosen non-equidistant spatial grid. Different spatial grids would however be necessary for the exact solution of integrals involving different powers of the wave function. To remain computationally efficient we chose a grid which allows the exact calculation of Eqns. (2.96) and (2.98). We checked that our results are invariant under

a variation of the grid used for evaluation of the integrals

Finally, a comment is in order regarding our definition of the condensed component of the stochastic field in section 2.5.6, using the expectation value of the field operator. A more rigorous definition is given by the Penrose-Onsager criterion [131]. Exemplary applications of this method can be found in [104, 132]. However to employ the criterion, we would have to average and subsequently diagonalize the one-body density matrix of size $N_{\text{modes}} \times N_{\text{modes}}$, which is not feasible in our case as will be explained very shortly in this section.

Throughout our truncated Wigner studies of collapsing condensates, we use three different levels of approximation of Eq. (2.95):

- GP evolution: Gross-Pitaevskii evolution only. In this case both the noise on the initial state and dynamical noise are omitted ($\eta = 0$, $d\xi = 0$).
- TWA with initial noise: Truncated Wigner evolution without dynamical noise ($d\xi = 0$).
- TWA with dynamical noise: Complete truncated Wigner evolution ($\eta \neq 0$, $d\xi \neq 0$).

The reasons for studying the GP evolution are two-fold and similar to those motivating section 3.3. Firstly it aids the determination of the required number of oscillator modes by comparison with the established position space results [30]. Secondly it allows us to quantify differences between the classical and quantum field simulations.

For the determination of the required mode numbers, the GP equation is solved in the harmonic oscillator basis to reproduce the atom number curve of Fig. 3.2 (b). In doing so, we have encountered a limitation of the oscillator-basis: Due to the extremely narrow peak of the condensate wave function at the collapse time, described in section 3.3, numerically accurate simulations beyond this point require a very large number of modes $\gtrsim 10^6$. The condensate evolution beyond the moment of collapse is therefore not feasible⁸. Fortunately it is possible to recognise a potential acceleration of the collapse from the total atom numbers and the maximum of $|\phi|^2$ (peak density) until a time shortly before the collapse. This approach was already taken when we interpreted the results of our HFB simulations.

⁸Note that in the oscillator basis we cannot make use of the FFT algorithm, and hence the tractable mode numbers are lower than for position grid methods.

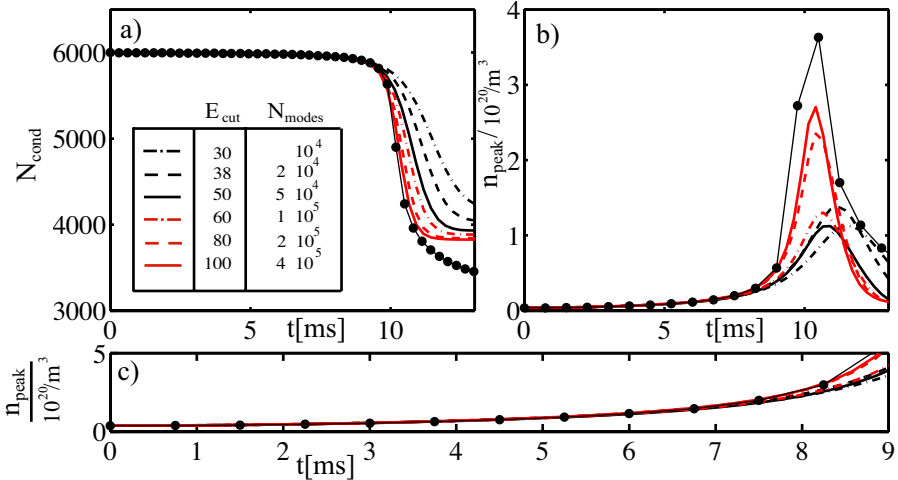


Figure 3.10: GP evolution only. (a) Atom number N_{cond} in the condensate during a collapse with $a_{\text{collapse}} = -10a_0$, where a_0 is the Bohr radius. (●) Results obtained on a spatial grid [30]. Thick lines correspond to solutions of Eq. (2.88) in the energy basis. The inset is a table with the number of modes for different E_{cut} and a legend. As E_{cut} increases, the atom number curves approach the correct position basis solution. The position space data presented has a low number of temporal samples, but suffices for the point we make here. (b) Time evolution of the peak density n_{peak} of the condensate. Labels as in (a). (c) Close up of peak density for the initial stage only.

Fig. 3.10 (a) shows the number of atoms remaining in the condensate for different numbers of oscillator modes employed. In the case of 4×10^5 modes, the result appears close to convergence against the solution of the GP obtained on a spatial grid [30]. However, we can conclude from the evolution of the peak densities in panel (b) that a cutoff as big as $E_{\text{cut}} \sim 150$, corresponding to about 1.5×10^6 modes, would be required to evolve through the collapse.⁹ We find that the evolution until ~ 8 ms can be accurately represented in a basis which is tractable also in the stochastic multi-trajectory treatment ($\sim 5 \times 10^4$ modes, $E_{\text{cut}} = 50$). This can be seen in Fig. 3.10 (c).

We outlined in section 2.5.3 under which conditions the truncation in the Wigner approach is justified. The requirement was that the condensate density n_{cond} be larger than the mode density in the volume where the condensate density is significant. This criterion, Eq. (2.83), depends on the type of basis and on

⁹The height of the narrowest possible peak in a restricted mode basis is proportional to the cutoff E_{cut} .

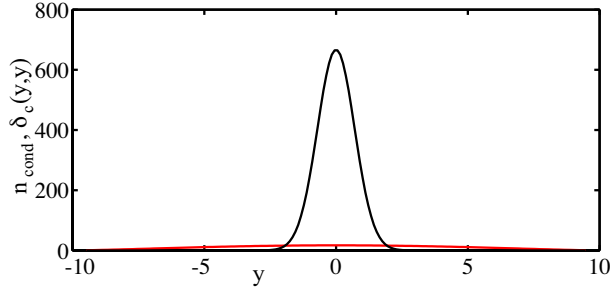


Figure 3.11: Comparison of BEC density n_{cond} (black) and restricted modespace commutator $\delta_c(\mathbf{x}, \mathbf{x})$ (red) along the y -axis at $t = 0$. Plots are for $E_{cut} = 50$. As t increases, so does the condensate density, resulting in an even better justified truncation approximation. The values for E_{cut} are given in units of the oscillatory energy $\hbar\omega_x$ throughout the rest of this chapter.

the employed mode number. For the Bosenova problem it can be fulfilled in the oscillator basis but not in the position basis. We explicitly verified that our choice $E_{cut} = 50$ safely fulfills Eq. (2.83). Fig. 3.11 shows the comparison between the condensate density of the initial state of our simulation and the mode density δ_c . Everywhere but in a negligible region on the cloud surface the criterion is fulfilled.

3.5.2 Collapse of a Cigar Shaped Condensate

Here we present truncated Wigner results for a collapse with $a_{collapse} = -10a_0$, for which the experimentally measured $t_{collapse}$ is (6 ± 1) ms [28, 83] in the full cylindrical experimental geometry. We find that only very few uncondensed atoms are created prior to the actual collapse, see Fig. 3.12 (a). This result qualitatively agrees with our studies of a spherically symmetric geometry with the HFB method in section 3.4.1. Due to the very small depletion in the initial phase, the collapse is not accelerated, as can be seen from the identical peak densities in Fig. 3.12 (b) for cases with and without quantum fluctuations. As discussed in the previous section, despite the numerical limitations we can thus conclude that the inclusion of zero temperature quantum depletion does not result in agreement between theory and experiment. We also see that the inclusion of dynamical noise in the

evolution is important for quantitative details in the uncondensed atom number, Fig. 3.12 (a), but not for the bulk collapse, Fig. 3.12 (b). We have checked

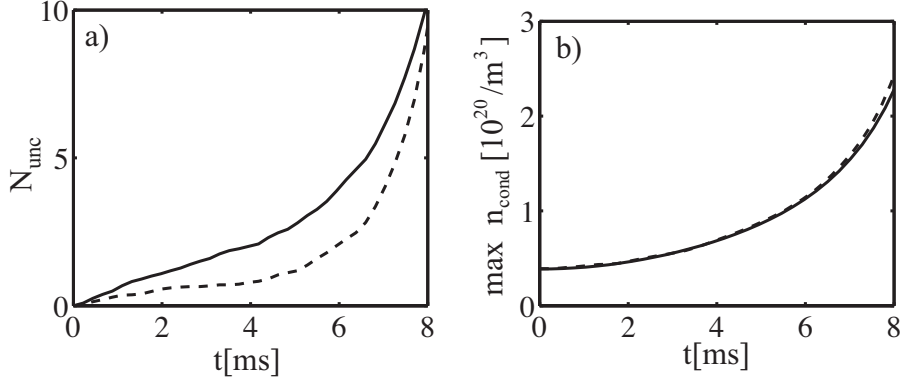


Figure 3.12: Initial 8 ms of evolution after the change in scattering length from 0 to $a_{\text{collapse}} = -10a_0$. (a) N_{unc} for the solutions with dynamical noise (solid) and initial noise only (dashed). (b) Condensate peak density for GP evolution (solid) and TWA with dynamical noise (dashed). The result is unchanged, hence no acceleration of the collapse occurred before 8 ms, which exceeds the experimental collapse time of (6 ± 1) ms. In both (a) and (b) $E_{\text{cut}} = 50$.

that these results are qualitatively unchanged for other scenarios, i.e. where the attractive interaction is changed to $a_{\text{collapse}} = -6a_0$ and $a_{\text{collapse}} = -25a_0$. In the latter case, we have observed a larger production of uncondensed atoms just before collapse, but it did not significantly accelerate the collapse.

3.5.3 Inclusion of a Thermal Cloud

As the final step towards more accurate modelling of the experiment we include initial thermal population in the uncondensed modes. We will show that, if temperature effects are taken into account, the precise results for the measured collapse times might depend on whether N_{cond} or N_{tot} is measured.

In the oscillator basis representation, detailed in section 2.5.6, the initial state for nonzero temperature is [98]

$$c_{lmn} = \psi_{0,lmn} + \eta_{lmn} \left[2 \tanh \left(\frac{\epsilon_{lmn} - \mu}{2k_B T} \right) \right]^{-1/2}. \quad (3.16)$$

Here ϵ_{lmn} are the energies of the oscillator modes with quantum numbers l, m, n . T is the temperature of the cloud and $\psi_{0,lmn}$ are the corresponding expansion coefficients of the GP ground state. The η_{lmn} are complex Gaussian noises obeying

$\overline{\eta_{lmn}^* \eta_{l'm'n'}}$ = $\delta_{ll'}\delta_{mm'}\delta_{nn'}$. Although the temperature in the Bosenova experiment was measured to be 3 nK, in Fig. 3.13 we present our results for a few different temperatures: $T = 0$, $T = 3$ nK, $T = 5.3$ nK and $T = 8$ nK. We plot the final 2 ms of simulated time. This corresponds to the collapse stage and exceeds the time of ~ 8 ms for which we can employ sufficiently many modes. Nonetheless we would like to draw some qualitative conclusions from these simulations of ‘‘BEC collapse in a restricted mode space’’: If the collapse time was deduced from the condensate atom number alone, which is shown in Fig. 3.13 (a), it appears to be shorter for increased temperature. The reduction by ~ 0.75 ms for the experimental temperature of 3 nK is however not nearly enough to reach agreement with the experimental collapse time value of (6 ± 1) ms. The reduction in condensate atom number just before collapse compared to the GP dynamics results from stimulated transitions to uncondensed modes rather than an increased total atom loss, which can be deduced from an inspection of N_{unc} and N_{tot} . These *qualitative* features are independent of the employed value of E_{cut} . However we point out that the *quantitative* details of the evolution of condensed and uncondensed fractions for the times presented in Fig. 3.13 depend on E_{cut} . Fig. 3.13 (b) shows that the acceleration of collapse is much smaller, if only the total atom number is taken into account. We point out that the increased population of the uncondensed modes just before collapse occupies the same spatial region as the condensate atoms. For reasons given in the introduction to section 3.5, the experiment therefore did probably not capture the temperature effect described here.

3.6 Hartree-Fock-Bogoliubov vs. Wigner: Comparison of the Methods for a Spherical BEC

We now proceed to the direct comparison of the two quantum field theories featured in this thesis, applied to a Bosenova collapse. Both rely on approximations to achieve a numerically tractable description of the quantum evolution. However, the mathematical formalism of each method and the approximations involved differ greatly, as outlined in the theory chapter. The *quantitative* agreement between the uncondensed number evolution of both methods that we present in this section is thus a strong indication of the results’ validity.

As described in section 3.3, HFB simulations are not feasible in the case of

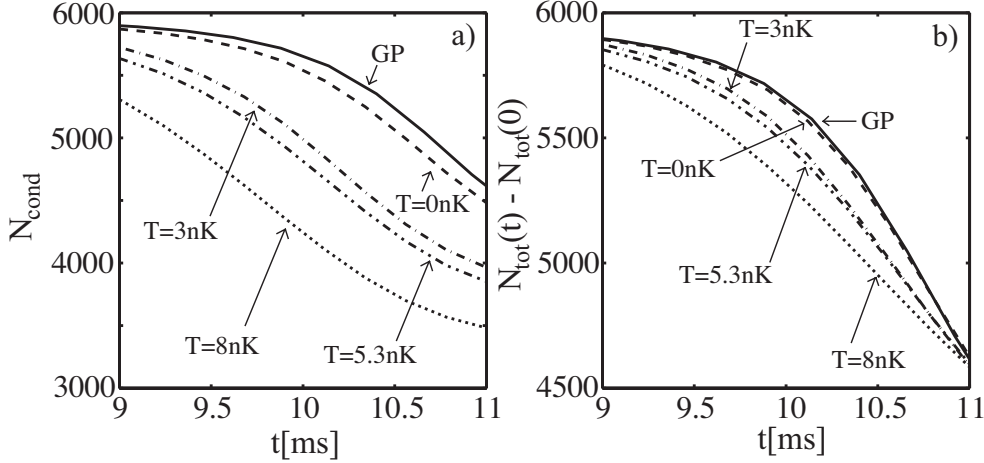


Figure 3.13: Slight acceleration of the collapse due to initial thermal atoms. (a) Time evolution of N_{cond} around the collapse. (b) The total number of atoms for the same period of the evolution. The sampling errors of all these results are less than 1%. We determine the sampling error from the difference between the average of 75% of the trajectories and all of them. We used $E_{\text{cut}} = 50$ for all graphs in this figure.

the cylindrically symmetric experimental situation, as the correlation functions G_A and G_N are then five dimensional. In section 3.4.1, we have thus considered a spherical trap for HFB studies. Similarly, we compare here the TWA and HFB methods for a range of temperatures of the initial thermal cloud and a spherical geometry. In the HFB approach, we take finite temperature into account by using correlation functions corresponding to a thermal population of oscillator states at $t = 0$:

$$G_N(\mathbf{x}, \mathbf{x}') = \sum_{lmn} \frac{1}{e^{\frac{\epsilon_{lmn}-\mu}{k_B T}} - 1} \varphi_{lmn}^*(\mathbf{x}') \varphi_{lmn}(\mathbf{x}), \quad (3.17)$$

$$G_A(\mathbf{x}, \mathbf{x}') = 0. \quad (3.18)$$

Here $\varphi_{lmn}(\mathbf{x}) \equiv \varphi_l(x)\varphi_m(y)\varphi_n(z)$. For the finite temperature TWA simulations we have used $E_{\text{cut}} = 40$.

We find excellent agreement between the uncondensed atom numbers predicted by HFB and TWA for the initial 5 ms of the collapse¹⁰ and a range of temperatures, as shown in Fig. 3.14. The higher the temperature, the larger

¹⁰For this period the evolution can be obtained with $\sim 5 \times 10^4$ modes, allowing multi-trajectory solutions.

the initial uncondensed population $N_{\text{unc}}(0)$, which causes more stimulated transitions to the uncondensed fraction. As reported in [97] an increase in temperature of the initial state also requires more trajectories for the sampling error to be satisfactorily small.

The TWA and HFB in the spherical case both qualitatively confirm the results presented in section 3.5.3 for cylindrical geometry: Higher temperature thermal clouds yield an increased creation of uncondensed particles just before collapse. This appears like an accelerated collapse on the curve for N_{cond} . In contrast inspection of the total atom number shows almost no acceleration.

Validity timescale: We believe that for the time-period we consider, the approximations involved in both methods are justified and therefore a comparison is useful. However, while it is known that the truncation in the TWA and the factorisation of correlation functions in the HFB are valid for short times only, both methods suffer from a lack of quantitative knowledge about this timescale. For the situation of a BEC in an optical lattice within the tight binding (Bose-Hubbard) regime, the validity timescales for TWA and HFB have been shown to coincide. There they are given by $t \ll J/U$, where J and U are the Bose-Hubbard hopping strength and on-site interaction respectively [99, 133].

Numerical performance: We find that both methods for the quantum field treatment of Bose gases, HFB and TWA, agree in a direct comparison of the uncondensed atom number evolution during a BEC collapse. The TWA is advantageous for spatially asymmetric problems, as the increased dimensionality of the correlation functions renders the HFB method numerically intractable. However, in a spherically symmetric case the HFB is advantageous. This is because the correlation functions G_N and G_A are only three dimensional due to the spatial symmetry. Meanwhile the truncated Wigner evolution has to be always modelled in the full three dimensions as the quantum fluctuations cannot be assumed to be spherically symmetric. The quantum evolution in the HFB approach is obtained with a single solution of equations (2.47), (2.48) and (2.49), compared to averaging over many realisations of Eq. (2.88) in the TWA. Our simulations consequently showed that for the spherical case the HFB requires vastly shorter CPU times. As an example: For the result shown in Fig. 3.14 (b), the HFB took 26 CPU hours (using parallel computation), while the required 200 trajectories of the TWA took 450 CPU hours.

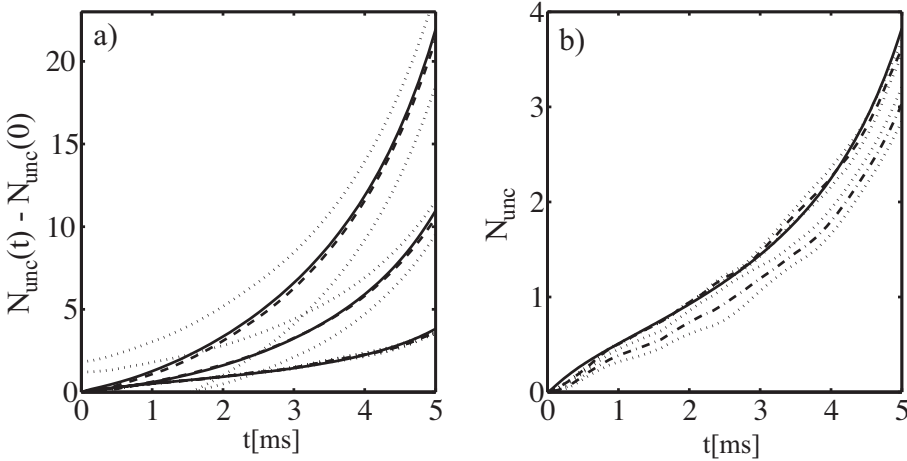


Figure 3.14: Increase in uncondensed atom number $N_{\text{unc}}(t) - N_{\text{unc}}(0)$ during the first stages of a spherical collapse with $a_{\text{collapse}} = -12a_0$ for the TWA and HFB. (a) The TWA results with dynamical noise (dashed) are in excellent agreement with the HFB result (solid) for (from lowest to highest curve) $T = 0, 3, 5.3 \text{ nK}$. Dotted lines indicate the sampling error. (b) Close-up of the result for $T = 0$. The TWA with initial noise only (dot-dashed) agrees less with the HFB (solid) than the result of the TWA with dynamical noise terms (dashed).

3.7 Parallels to Cosmology

We have described in section 2.3.4, how under certain conditions the behaviour of fluctuations of the condensate is analogous to the physics of quantum fields in the curved space-time of general relativity. The implications of this result have been first mentioned in section 1.3. If applied to the collapsing BEC scenario, the analogy provides us with a system in which to study key features of the effect of cosmological inflation [29] on vacuum fluctuations of quantum fields. This aspect of the Bosenova collapse has been studied by Calzetta and Hu [45, 46], who explain many of the features of the Bosenova experiment considering the behaviour of quantum fluctuations around a fixed condensate evolution.

One prediction arising from their considerations of quantum test fields riding on the condensate background is that the atoms in jets [28] are in a phase squeezed quantum state [45]. The consequently large atom number fluctuations in the jets agree well with experimental observations [28]. A measurement of the quantum statistics in these jets would thus allow some verification of the ideas of particle creation in cosmological space-times that were applied to derive the result.

However as explained in section 3.2.2 many of these features have equally

well been understood within semi-classical Gross-Pitaevskii theory. For instance, Bao *et al.* can explain number fluctuations in jets within GP theory, as a result of strong sensitivity to minor experimental deviations from a perfectly centered initial state [119]. Hence, while there seems to be consensus in the literature that not all effects which appear in the experiment can be explained on the semi-classical level, the extent and way in which quantum effects become important remains unclear.

To find a quantum approach that allows us to identify clearly where quantum effects play a role, and where they are irrelevant, the collapse time should be the ideal starting point. It is a far simpler concept than the other, more extensively studied effects like bursts and jets. Thus if quantitative agreement cannot be reached for this simple observable, as we showed in this chapter, it seems unlikely to be reached for observables like quantum mechanical number variances in the ejected jets.

3.8 Conclusions and Outlook

In this chapter we compared the predictions of two candidate quantum theories with experimental results for the collapse time t_{collapse} of Bose-Einstein condensates collapsing under self-attraction. While these theories could have been expected to explain the disagreement between experimental results and theoretical predictions [30], we found that the inclusion of quantum effects has no positive effect on the level of agreement.

We studied the collapse time rather than many of the more intricate effects of the experiment, such as bursts and jets, because it represents by far the simplest observable for which precise data exists. It is also an observable which is sensitive solely to physics before the moment of collapse, thus avoiding uncertainties regarding a potential break down of our very first assumption, the s-wave scattering approximation Eq. (2.4) under the extreme conditions of the collapse¹¹.

Our three dimensional stochastic simulations of the “Bosenova” experiment on collapsing BECs [28] have shown a moderate acceleration of the collapse if an initial thermal cloud is taken into account, although the effect is not large enough to quantitatively account for the discrepancy between experimental and theoretical collapse times. The predictions of HFB and TWA theories for collapse

¹¹A simple estimate using Eq. (1.9) for the case in Fig. 3.4 (a) gives $n_{\text{peak}}|a_s|^3 \sim 7 \times 10^{-7}$, not suggesting problems in this (weakly attractive) case.

in a spherically symmetric case agree very well with each other.

The origin of the collapse time discrepancy thus remains unknown. We conjecture that it arises from quantum correlations not captured by our description. Although a Gaussian initial state is physically reasonable, high order correlations could arise during collapse which are beyond the scope of the methods employed here. To understand the discrepancy better, it would be desirable to conduct an experiment to measure the collapse times and correlation functions for a larger range of scenarios and with even more precision.

Our results of truncated Wigner simulations of collapsing condensates and the comparison between TWA and HFB have been accepted for publication in the Physical Review [134].

Chapter 4

Topological Structures in Bose-Einstein Condensates

In section 1.3 we already hinted that certain topological structures of interdisciplinary interest can be created in a BEC. A broad range of physics has been uncovered in the study of line vortices [35, 38, 135], which are rather simple topological objects. By adding internal degrees of freedom (section 1.2.1) to produce multi-component topological defects, such as coreless vortices [136] and Skyrmions, we can reveal further interesting phenomena. Skyrmions, which are the subject of the first part of this chapter, were first introduced in particle physics [21–24], where their application [25] has recently triggered a controversial search for penta-quarks [137]. We will give a brief overview of Skyrmions in particle physics in section 4.1.3.

In a BEC, a Skyrmion can be most easily described as a line vortex threaded into a ring vortex, as we describe in more detail in section 4.1.2. It has been shown that Skyrmions can be energetically stable in a harmonically trapped two component BEC [27], and that the Skyrmion topology can be seeded by phase imprinting techniques [138, 139]. However their experimental realisation remains to be achieved. In order to facilitate this, we have surveyed the relevant parameter space and identified regimes in which Skyrmions are stable. The results are presented in section 4.2. In particular we aimed to find Skyrmions with lower atom numbers than demonstrated previously [27], as the high atom number Skyrmions of Ref. [27] would be accessible only for experiments specifically designed to operate with large BECs [140].

In the second part of this chapter, section 4.3, we demonstrate a trapping configuration that can enable the controlled study of multiple stationary vortex rings

in a BEC. Ring vortices can also be seeded by phase imprinting techniques [141]. Unsupported ring vortices are however energetically unstable against contraction [142] and have so far been only observed in non-stationary situations, for example as the decay product of dark solitons or in soliton collisions [143, 144]. In contrast, our method could enable the stabilisation of a stack of up to nine parallel vortex rings under realistic experimental conditions. The creation of stationary vortex rings would also aid studies of their interactions [145] and represent a stepping-stone towards the creation of Skyrmions, as a Skyrmion is build from a line and a ring vortex (see section 4.1.2). Furthermore, in the proposed trapping configuration the BEC is flowing through an optical tunnel with velocities close to the speed of sound. This suggests their applicability to analogue gravity studies (chapter 5).

4.1 Introduction to Skyrmions

We first introduce concepts and methods relevant for the investigation of Skyrmions. In section 4.1.1 we provide some basics of topology, section 4.1.2 defines the topological object to which we refer as “Skyrmion”, section 4.1.3 gives an overview of the historical origin of Skyrmions and their recent application in particle physics, while section 4.1.4 explains the corresponding objects in gaseous BECs. The latter section also details the method employed throughout the chapter to find stationary states.

4.1.1 Topological Solitons

Mathematically, two spaces are deemed topologically equivalent if they can be continuously deformed into one another. Hence, topological structures in a BEC are states with interesting properties, which cannot be continuously deformed into a trivial condensate. A simple example is the line vortex [38], where the phase of the condensate wave function $\phi(\mathbf{x})$ changes by $2\pi q$ ($q \in \mathbb{N}$) on a closed loop around the location of the vortex (termed singularity). Assuming cylindrical coordinates with the z axis co-aligned with the vortex singularity, the function $\Lambda(r, z, \varphi) = \phi(\mathbf{x})/|\phi(\mathbf{x})| = \exp(iq\varphi)$ defines a continuous map $\Lambda : \mathbb{R}^3 \rightarrow U(1)$ from physical space onto the group $U(1)$ [146]. According to Eq. (2.11) section 2.2.1, this phase circulation corresponds to a circular flow field. Because the map Λ is “wound” around the unit circle in the complex plane defined by $U(1)$, we cannot continuously deform it to a map $\Lambda_0(r, z, \varphi) \equiv \text{const.}$ describing a BEC

at rest.

A fundamental result of homotopy theory is that all mappings such as Λ can be classified by an integer topological invariant, the winding number W [146]. For the line vortex example, a winding number is given by $W = \int_0^{2\pi} \frac{d\arg \Lambda}{d\varphi} \frac{d\varphi}{2\pi}$. Evaluating the integral, we obtain $W = q$ and can identify the winding number with the vortex charge [38].

Finally, we briefly define a topological soliton. Solitons are extended wavelike solutions of nonlinear wave equations, which (i) can propagate without change of shape and (ii) preserve shape after collisions with other such objects [146]. These are referred to as topological solitons, if they carry a nontrivial value of some topological charge. While it certainly would be an interesting field of further research, collisional properties of BEC Skyrmions have not yet been investigated. In this thesis, we succumb to the common habit of referring to solitary waves, for which only property (i) has to hold, as solitons as well.

4.1.2 Skyrmiон Topology

Skyrmions are topological solitons. While a structure with the topology of a line vortex can still exist in two dimensions, Skyrmions are intrinsically 3D objects. Further they require a two component wave function, which can be realised in a BEC by simultaneously trapping two different hyperfine states (section 1.2.1). An important property of a Skyrmiон is that the atomic field approaches a constant value at spatial infinity: for a trapped BEC this means sufficiently far from the trap centre. Then we can identify all points at infinity, turning the domain of our wave function into the compact space S^3 , the three dimensional spherical surface in four dimensions. The two component wavefunction of the BEC $(\phi_1, \phi_2)^T$ at a particular position can be represented by the $SU(2)$ matrix $U(\mathbf{x})$ which maps a standard state, such as $(1, 0)$, into it:

$$\begin{pmatrix} \phi_1(\mathbf{x}) \\ \phi_2(\mathbf{x}) \end{pmatrix} = \sqrt{n(\mathbf{x})} U^\dagger(\mathbf{x}) \begin{pmatrix} 1 \\ 0 \end{pmatrix}. \quad (4.1)$$

Here the total density of atoms is denoted by $n(\mathbf{x}) = |\phi_1(\mathbf{x})|^2 + |\phi_2(\mathbf{x})|^2$. The function Λ defined as $\Lambda = U(\mathbf{x})$ now represents a mapping $\Lambda : S^3 \rightarrow SU(2)$ due to the above mentioned identification of all points at infinity. In this case, homotopy theory again predicts an integer winding number [27, 146].

Any $SU(2)$ matrix $U(\mathbf{x})$ can be parametrised as $U = \exp(i\sigma \cdot \omega(\mathbf{x}))$, where σ is the vector of Pauli matrices and $\omega(\mathbf{x})$ a finite rotation. We now choose

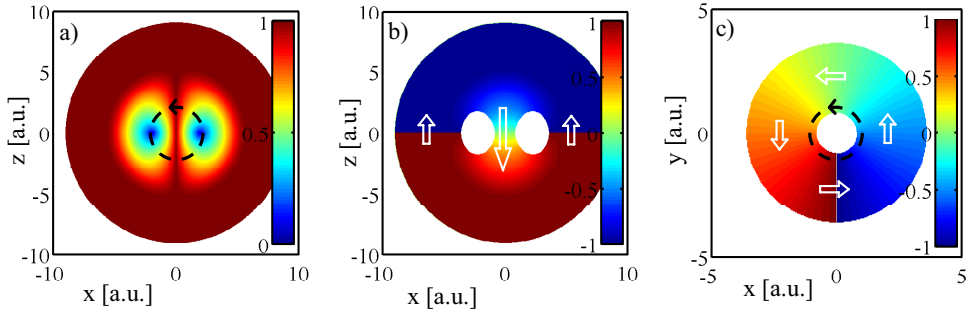


Figure 4.1: Skyrmion topology given by Eq. (4.3). For simplicity we assume a step function density profile n with radius $R_{sph} = 8$. (a) Relative magnitude of the ring component (component one) $n_r = |\phi_1|/(|\phi_1| + |\phi_2|)$ in the xz plane. The 3D structure is rotationally symmetric around the z axis. The dashed black line indicates a circumference along which n_r changes twice fully from 0 to 1. This demonstrates the equivalence of spatial rotations and component space rotation. (b) Phase ϑ_1 of the ring component in the xz plane in units of π . Regions with $n_r < 50\%$ are shown in white. (c) Phase ϑ_2 of the line component (component two) in the xy plane in units of π . Regions with $n_r > 50\%$ are shown in white and the plotted domain differs from (a) and (b). The dashed black line indicates a spatial rotation which is equivalent to a line component phase rotation. In (b) and (c) the BEC flow associated with the phase structure via $\mathbf{v}_i = \hbar \nabla \vartheta_i / m$ is indicated by white arrows.

$\omega(\mathbf{x}) = \lambda(\mathbf{x})\hat{\mathbf{x}}^{(m)}$, for some function λ and the unit vector

$$\hat{\mathbf{x}}^{(m)} = (\cos(m\varphi) \sin \theta, \sin(m\varphi) \sin \theta, \cos(\theta))^T. \quad (4.2)$$

$\hat{\mathbf{x}}^{(m)}$ is given in spherical polar coordinates r, φ, θ and reduces to the radial unit vector for $m = 1$. In any case, we can see that physical rotations as well as radial translations are now equivalent to rotations in “component space”.

Explicitly the wave function (4.1) can be written in our coordinates as:

$$\begin{pmatrix} \phi_1(\mathbf{x}) \\ \phi_2(\mathbf{x}) \end{pmatrix} = \sqrt{n(\mathbf{x})} \begin{pmatrix} \cos[\lambda(\mathbf{x})] - i \sin[\lambda(\mathbf{x})] \cos \theta \\ -i \sin[\lambda(\mathbf{x})] \sin \theta \exp(im\phi) \end{pmatrix}. \quad (4.3)$$

λ determines the detailed shape of the wavefunction, but as long as it meets the boundary conditions $\lambda(0) = 0$ and $\lambda(\infty) = n\pi$, the topology will be that of a Skyrmion. The resulting wavefunctions are visualised for $n = 1, m = 1$

in Fig. 4.1. If we consider the BEC flow, associated via Eq. (2.11) with the phase profiles shown in Fig. 4.1, we can see that a Skyrmion consists of a line vortex carried by component two, which is threaded into the low density region of component one, which carries a ring vortex. Component one hence circulates around component two and through the line vortex core, see Fig. 4.2 for a 3D illustration.

We will therefore refer to component one as the *ring component* and component two as the *line component*. It can be seen in Fig. 4.1 (a) that a spatial rotation on the dashed line is equivalent to a rotation in the two dimensional component space. Other rotations, such as indicated in Fig. 4.1 (c), correspond to phase rotations of one of the components. In general it can be seen that any $SU(2)$ transformation of the state Eq. (4.3) corresponds to another Skyrmion with rotated symmetry axis (which was the z -axis for the case in Fig. 4.1) [139]. In this sense for a Skyrmion, spatial and $SU(2)$ rotations are equivalent.

If we vary the position \mathbf{x} over all space, the wave function $(\phi_1, \phi_2)^T$ “winds” over the whole of $SU(2)$. Similar to the example in the previous section, it is thus not possible to continuously deform the Skyrmion wave function into one with a simpler topology, such as a coreless vortex (A line vortex, whose core is filled by a second, nonflowing Hyperfine component). Our quest for stable Skyrmions later in this chapter is essentially a search for functions $\lambda(\mathbf{x})$, for which Eq. (4.3) corresponds to a local minimum of energy.

The Skyrmion winding number can be most conveniently written as [27]:

$$W = \frac{\epsilon_{\alpha\beta\nu}}{24\pi^2} \int d^3\mathbf{x} \text{Tr} [U(\partial_\alpha U^\dagger)U(\partial_\beta U^\dagger)U(\partial_\nu U^\dagger)], \quad (4.4)$$

where $\epsilon_{\alpha\beta\nu}$ is the completely antisymmetric tensor and repeated indices have to be summed. For the practical implementation it is more useful to write this expression in terms of the individual components, however the result is unwieldy and hence banished into appendix C.

For the topological structure given by Eq. (4.3) with the appropriate boundary conditions for $\lambda(\mathbf{x})$, W evaluates to $W = nm$. This is just the product of the charge m of the line vortex in component two with the charge n of the ring vortex in component one. Higher winding number Skyrmions are thus obtained by increasing the vortex charge in either component.

There are more topological structures that can be realised in multi-component BECs besides line vortices, ring vortices and Skyrmions. Further examples are Dirac monopoles [147] and Alice rings [148], but these are not studied in this thesis.

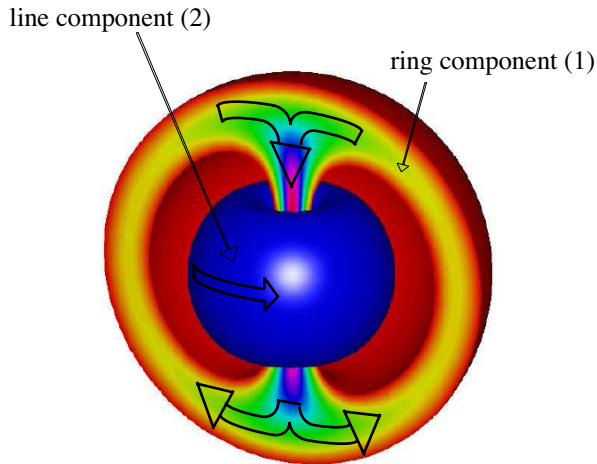


Figure 4.2: 3D illustration of a Skyrmion in a ^{87}Rb BEC (taken from Ref. [27]). The central (blue) torus is an isosurface of the line component. An isosurface of the ring component (red) is shown for $x < 0$: on the y - z plane between the isosurface sections the ring component density is indicated by a colormap from red (lowest) to purple (highest). The circulation associated with each vortex is indicated by the arrows. Each component consists of 4.5×10^6 atoms within a 7.8 Hz spherical harmonic trap.

4.1.3 Skyrmions in Particle Physics

The concept of Skyrmions was introduced by T.H.R. Skyrme around 1960 in the context of particle and nuclear physics. He proposed a meson field theory which is able to correctly classify the spectrum of light Baryons that were found experimentally and hence bring some order into the zoo of newly discovered particles [21, 22]. This was before the strong interactions responsible for this particle zoo were explained in much more detail within the framework of quantum chromodynamics (QCD) and the quark picture [69, 71]. According to this now well established part of the standard model of elementary particle physics, the bosonic mesons (such as π -mesons and kaons) are bound states of quarks and antiquarks, while fermionic baryons (such as the proton and neutron) consist of three quarks.

In contrast, Skyrme considered directly the classical properties of a multi-component meson field, describing the π^0 , $\bar{\pi}^0$, π^+ , π^- mesons. These carry the so-called isospin quantum number [34], in the quark model related to their content of “up” and “down” quarks¹. Skyrme showed that this meson field possesses solitonic solutions with topology as given by Eq. (4.3). Similarly to the correspon-

¹All pions have isospin $I = 1$, with isospin z -components I_z : $\pi^0:0$, $\pi^+:1$, $\pi^-:-1$

dence between spatial rotations and BEC component rotation that we illustrate in Fig. 4.1, in the particle physics Skyrmion spatial rotations are connected to isospin rotations. Interestingly, the soliton solutions possess properties appropriate for the description of Baryons, among them a winding number W which can be interpreted as the integer Baryon number.

One can now proceed to quantise the simultaneous spin and isospin rotations of the skyrmion, yielding a rotational energy $E_{rot} = \hbar^2 J(J+1)/2I$ [25] for a quantum number J which refers to both, isospin and angular momentum, which are equal due to the equivalence of spatial and isospin rotations. I is the soliton's moment of inertia. Given J , the model predicts $(2J+1)^2$ degenerate states.² For each J these states form a baryon multiplet, an arrangement that is indeed observed in nature for $J = 1/2$ and $J = 3/2$. The theory also gives quantitative predictions regarding these light baryons which are satisfied to a few percent [25].

It was later shown by E. Witten how the success of Skyrme's model can be understood in the context of QCD. The Lagrangian that Skyrme employed to obtain the Skyrmion solutions can be derived as a low energy limit of the full QCD Lagrangian [23, 24].

Diakonov *et al.* used the Skyrme model to go beyond the description of light baryons and considered higher rotational excitations with $J = 5/2$ [25]. The resulting symmetry multiplet is shown in Fig. 4.3. They conjectured that the right-most particle in the second row of the multiplet corresponds to the experimentally observed nucleon resonance $N(1710)$ [149], which allowed them to predict energies, decay widths and branching ratios of other members of the multiplet. Of particular interest are the particles at the corners of the pyramid: To realise their quantum numbers in the quark model, they have to be made of at least 5 constituents (4 quarks and an anti-quark). Of these, the member at the top of the pyramid, later called Θ^+ , has received most attention as it should be experimentally accessible. The prediction of the penta-quark Θ^+ by Diakonov *et al.* was followed some years later by the first experimental evidence precisely at the anticipated energy [26].

A number of experiments have since reported similar results, however other experiments did not find a Θ^+ resonance where they were expected to [137]. There are qualitative differences between the experiments reporting the Θ^+ and some delivering null results, because of which these null results do not necessarily

²We have $(2J+1)$ possibilities for the z component quantum number of each: spin and isospin.

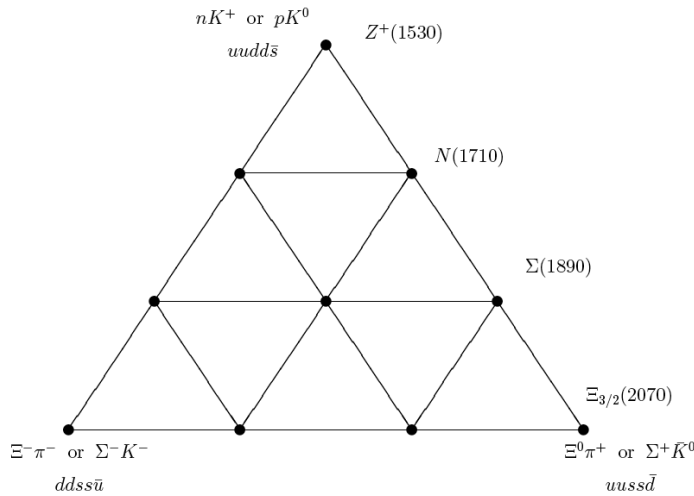


Figure 4.3: Anti-decuplet of particle states predicted by Skyrme theory in Ref. [25]. For example $\Sigma(1890)$ denotes a Σ hyperon with mass 1890 MeV. The x and y axes in the diagram correspond to isospin z -component (up and down quark content) and hypercharge (strange quark content), respectively. The particles at the corners of the diagram cannot be realised as a conventional baryon with three quarks. Instead they must represent exotic states, with minimal pentaquark content as indicated (u : up, d : down, s : strange, \bar{s} -anti strange etc.). The exotic particle candidate Z^+ is now known as the Θ^+ .

falsify the reports of discovery. However some originally positive results have since been revised and retracted, leaving the existence of the Θ^+ in considerable doubt (page 1019 of Ref. [149]).

Nonetheless the tremendous theoretical and experimental efforts [137] triggered by the application of Skyrme theory underlines the fundamental nature of the concept of topological solitons.

4.1.4 Skyrmiions in Bose-Einstein Condensates

We have seen that a Skyrmiion in a BEC can be realised if at least two hyperfine states are available in a 3D system. If these states are chosen such that collisions allow interconversion between them, we refer to the gas as a spinor condensate. Multi-component condensates in which spin changing collisions are energetically suppressed can also be created [150]. In either case it is of central importance for the experimental observation of Skyrmiion structures whether they are energetically and dynamically stable (see section 2.3.3).

Literature overview

Skyrmions in spinor condensates have been studied for example by Al Khawaja *et al.* [151, 152] and Herbut *et al.* [153]. It was found that spinor Skyrmions are generally energetically unstable. They are also dynamically unstable, however their lifetimes can under some circumstances exceed the lifetime of the condensate [151, 152], which is limited by inelastic collisions (section 1.2.2).

It has been suggested in Ref. [139] that for two hyperfine BEC components in which the atom numbers are separately conserved, energetically stable states might be possible due to phase separation (section 2.2.4). The basic principle can be understood on the basis of Fig. 4.1. The primary instability mechanism of the Skyrmion is contraction of the ring vortex. Ring vortices carry an energy per unit length, making it energetically favourable for them to be shorter [154]. However if the core region of the ring component is filled by a second hyperfine component carrying a line vortex, the mutual repulsion between these components due to phase separation allow the line component filling to prevent the vortex ring contraction.

The first numerical studies of such Skyrmions were undertaken by Battye *et al.* [60, 155]. They found that phase-separation indeed allows energetically stable Skyrmions within a homogenous background condensate. However for the stabilisation to succeed, the relative fraction of atoms in the line component cannot be too small. Ref. [155] also reports briefly on spatially propagating Skyrmions.

Savage *et al.* considered $W = 1$ Skyrmions in realistic, trapped condensates [27]. They found that stable Skyrmions require fairly large numbers of atoms. The confined Skyrmion essentially fills the entire harmonic trap and is thus considerably affected in its shape by the external potential. Fig. 4.2 shows an example of such a large Skyrmion, containing 4.5×10^6 atoms in each component. Several new energetic instability mechanisms that are not present in a homogenous system are also reported in Ref. [27]. They have to be countered if the Skyrmion is to be created in a realistic trapped system. Understanding the physical reasons for these instabilities more deeply is a central goal of this chapter, as it is important for the experimental creation of Skyrmions.

Finally Ruostekoski studied Skyrmions with winding numbers $W > 1$ in a trapped BEC [156]. He states that stable Skyrmions with line charges greater than one can be found for $N < 10^7$ in ^{87}Rb only if the scattering lengths are modified compared to the measured values. For unmodified parameters the multiply

quantised line singularities split into multiple single charge vortices, a known effect for single component condensates [38]. For the modified scattering lengths (corresponding to stronger surface tensions as we explain in section 4.2.5), Skyrmions with multiply quantised line vortices are found. Skyrmions with ring charge $n = 2$ are found in 7×10^6 atoms without scattering length modification.

Model and parameters

Skyrmion stability depends crucially on the exact physical parameters employed. We used the specific case of the magnetically trappable ^{87}Rb hyperfine states $|1\rangle \equiv |F = 1, m_f = -1\rangle$, $|2\rangle \equiv |F = 2, m_f = 1\rangle$, as Rubidium is the most common atom for BEC experiments. The employed atomic mass was $m = 1.4432 \times 10^{-25}$ kg.

To determine the energetic stability of Skyrmions, we numerically solve the Gross-Pitaevskii equation (GPE) in imaginary time, as described in section 2.2.2. For skyrmion drift stabilisation, which is discussed in section 4.2.4, we consider the application of a rotating trap. Combining the equations of section 2.2.2 and section 2.2.3 for the case of a two-component BEC we arrive at the coupled imaginary time equations for our two component system in a frame rotating with angular velocity $\boldsymbol{\Omega}$ compared to the lab frame:

$$\hbar \frac{\partial}{\partial t} \phi_i(\mathbf{x}) = - \left(-\frac{\hbar^2}{2m} \nabla^2 + V(\mathbf{x}) + \sum_{j=1,2} U_{ij} |\phi_j(\mathbf{x})|^2 - \boldsymbol{\Omega} \cdot \mathbf{L} \right) \phi_i(\mathbf{x}), \quad (4.5)$$

where ϕ_i for $i = 1, 2$ denote the BEC wavefunctions of the two components, normalised to the number of atoms in each component, N_1 and N_2 . For later reference we define $N_{tot} = N_1 + N_2$ and $N_r = N_2/N_{tot}$. The potential

$$V(\mathbf{x}) = \frac{1}{2} m (\omega_\perp^2 (x^2 + y^2) + \omega_z^2 z^2) \quad (4.6)$$

is that of a cylindrically symmetric harmonic trap, and m is the atomic mass. The interaction parameters U_{ij} are proportional to the scattering lengths for intra- (U_{11}, U_{22}) and inter-component (U_{12}) interactions: $U_{ij} = 4\pi\hbar^2 a_{ij}/m$. \mathbf{L} is the angular momentum operator, $\mathbf{L} = i\hbar(y\partial_x - x\partial_y)$ in cartesian coordinates.

To work out the relevant parameters in this model more clearly, it is helpful to rewrite Eq. (4.5) in dimensionless form. Using $\tilde{\mathbf{x}} = \mathbf{x}/a_z$, $\tilde{t} = \omega_z t$, $\tilde{\phi}_i = \phi_i a_z^{3/2} / \sqrt{N_i}$, $\tilde{\boldsymbol{\Omega}} = \boldsymbol{\Omega} / \omega_z$, $\tilde{\mathbf{L}} = \mathbf{L} / \hbar$, where $a_z = \sqrt{\hbar/m\omega_z}$ is the harmonic oscillator

scale length, Eq. (2.24) becomes³:

$$\begin{aligned} \frac{\partial}{\partial \tilde{t}} \tilde{\phi}_i(\tilde{\mathbf{x}}) = & - \left[-\frac{1}{2} \tilde{\nabla}^2 + \frac{1}{2} \left(\frac{\omega_{\perp}^2}{\omega_z^2} (\tilde{x}^2 + \tilde{y}^2) + \tilde{z}^2 \right) \right. \\ & \left. + \sum_{j=1,2} \lambda_{ij} \left| \tilde{\phi}_j(\tilde{\mathbf{x}}) \right|^2 + i\tilde{\Omega} \left(\tilde{x} \frac{\partial}{\partial \tilde{y}} - \tilde{y} \frac{\partial}{\partial \tilde{x}} \right) \right] \tilde{\phi}_i(\tilde{\mathbf{x}}), \end{aligned} \quad (4.7)$$

with interaction coefficients

$$\lambda_{ij} = 4\pi N_j a_{ij} \sqrt{m\omega_z/\hbar}. \quad (4.8)$$

In a spherical nonrotating trap the physics is fully determined by the λ_{ij} .

Early measurements gave the ^{87}Rb scattering lengths: $\bar{a}_{11} = 5.67$ nm, $\bar{a}_{22} = 5.34$ nm, $\bar{a}_{12} = \bar{a}_{21} = 5.5$ nm [150] for the hyperfine states $|1\rangle$ and $|2\rangle$. After the bulk of our numerical work was done, we became aware of revised values for the scattering lengths: $a_{11} = 5.315$ nm, $a_{22} = 5.052$ nm, $a_{12} = a_{21} = 5.191$ nm [157, 158]. These differ from the \bar{a}_{ij} primarily by an overall scale factor. Choosing this to be $\bar{a}_{11}/a_{11} = 1.067$, according to Eq. (4.8) this is equivalent to an increase in atom numbers by the same factor, or by about 7%. The residual differences, although small, are significant. Therefore, our major results are presented for both sets of scattering lengths: early (\bar{a}_{ij}) and revised (a_{ij}).

In magnetic traps the two states will in general have slightly different trap frequencies due to the differential Zeeman effect [37, 157], which is discussed in section 4.2.3. Taking gravity into account, this results in a small offset of the trap centres for each component which, for weak traps, can become comparable to the Skyrmion length scale $a_z \propto \omega_z^{-1/2}$. We report in section 4.2.4 that this effect can and should be minimised, and therefore, unless otherwise stated, we assume identical spherical traps with $\omega = \omega_z = \omega_{\perp} = 2\pi \times 7.8$ Hz for both hyperfine components. In contrast, the change in the dimensionless non-linear interaction coefficients due to the actual different trap frequencies themselves is negligible.

Although we present our results for specific trap frequencies, the scaling Eq. (4.8) implies that our results apply for different trap frequencies provided the atom number is adjusted to keep the λ_{ij} constant. For example, if the trap frequencies are increased by a factor of four, the atom number decreases by a factor of two. This scaling applies provided the Gross-Pitaevskii equation is valid, and hence fails if the density becomes too high.⁴

³We assumed already $\tilde{\boldsymbol{\Omega}} = \tilde{\Omega} \hat{\mathbf{z}}$, which will be our later choice.

⁴At very high BEC densities the s-wave approximation (see section 1.2.2) might break down.

Numerical scheme

The steps involved in determining Skyrmion stability are the following: We fix the atom numbers in both components and create an initial state with the topology of a $W = 1$ Skyrmion in a harmonic trap. We use Eq. (4.3) with n and λ as given in appendix C. This initial state is then evolved in imaginary time according to Eq. (4.7).

In the renormalisation step of the imaginary time algorithm, we usually separately constrained N_1 and N_2 . The numerical solution of Eq. (4.7) in the Skyrmion case is however computationally challenging, prompting us to search for improved methods. We tested some of the alternate prescriptions mentioned in section 2.2.2 and Ref. [56], such as fixing chemical potentials μ_1 and μ_2 instead of the atom number and combining either method with the use of Sobolev gradients. None of these modifications was found to be better suited to our problem than the conventional method with fixed atom number.

If an energetically stable Skyrmion state exists in the vicinity of our initial trial solution, the method converges towards this state. In the case of energetic instability, the state evolving in imaginary time leaves the topological class of a Skyrmion, indicated by a decay of the winding number from the initial value of one. The winding number is monitored throughout the imaginary time evolution, and numerical runs are usually aborted once $W \neq 1$. According to the arguments of Ref. [64] (see section 2.3.3), whenever we find an energetically stable state it is likely to also be dynamically stable. For several examples we explicitly confirmed this by solving the real time equivalent of Eq. (4.5).

In our numerical survey of the BEC parameter space three dimensional spatial grids with 64^3 grid points were used. However the specific results presented in this paper were verified on bigger grids. To solve the GPE in imaginary time we used both the RK4IP algorithm [159] and the corresponding first order interaction picture method. We found that the lower order method was faster. Typical imaginary timesteps were $\Delta\tau = 10^{-5}$ s. The simulations were done with the aid of the high level programming language XMDS [160].

Experimental creation scheme

The experimental sequence envisaged for actual Skyrmion creation would look as follows. One would first phase imprint a state in the $W = 1$ topological class onto the BEC [138, 139, 141]. This would then relax towards the ground state of the class, such as the Skyrmion states that we find later in this chapter, by

means of thermal dissipation.

4.2 Stability of Trapped Skyrmions in Condensates

We are now ready to present our results from a detailed numerical stability analysis of Skyrmions in a harmonically trapped BEC. We show that the stability of three-dimensional Skyrmions in trapped Bose-Einstein condensates depends critically on scattering lengths, atom numbers, trap rotation and trap anisotropy. In particular, for the ^{87}Rb $|F = 1, m_f = -1\rangle$, $|F = 2, m_f = 1\rangle$ hyperfine states stability is sensitive to the scattering lengths at the 2% level, where it is the differences between them that are crucial. Our smallest example of a stable Skyrmion, in a slightly cigar shaped trap, has slightly more than 2×10^6 atoms, a number which scales with the inverse square root of the trap frequency. These can be stabilised against drift out of the trap by laser pinning.

Our stability analysis can be roughly divided into two segments: In the first, sections 4.2.1 - 4.2.3, we consider stability with respect to cylindrically symmetric perturbations (atom number variations and trap offset in the z direction). In the second stage, reported in section 4.2.4, we consider stability against non-cylindrically symmetric perturbations, in particular against drift of the line vortex singularity out of the trap. We finish with non-spatial perturbations such as scattering length variation.

4.2.1 Atom Numbers in a Skyrmion

Previous work had discovered stable Skyrmions in a BEC with total atom numbers of the order of 10^7 [27]. A major motivation for the work reported here was to find stable Skyrmions with fewer atoms. While we showed in section 4.1.4 how large atom numbers are in fact physically equivalent to tighter *spherical* trapping potentials, tight spherical confinement also poses experimental challenges.

The atom numbers in a Skyrmion are constrained by two main instability mechanisms: collapse of the ring vortex and deconfinement of the line component. In the latter case, the density of the line component drops off more slowly than the ring component at the edge of the condensate. Consequently the phase variation associated with the line vortex extends to infinity and the wavefunction there cannot be identified with a single point in $SU(2)$. Thus the topological

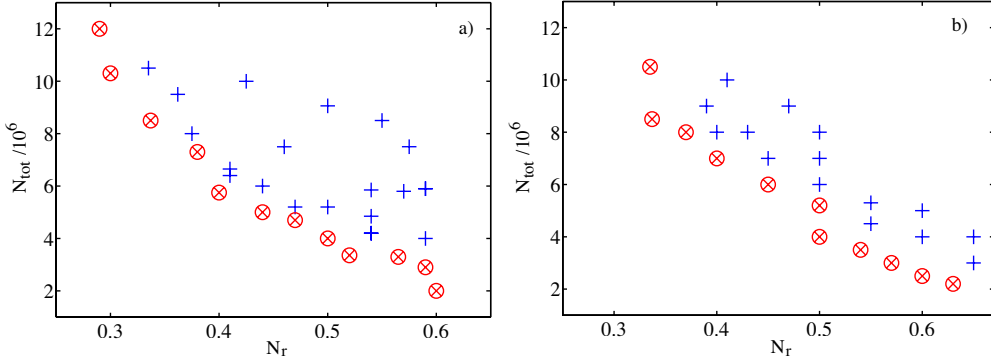


Figure 4.4: Skyrmiion stability diagram against cylindrically symmetric perturbations, in a spherical trap: (+ blue) stable, (\otimes red) unstable. The axes are the total atom number $N_{tot} = N_1 + N_2$ and relative line component fraction $N_r = N_2/N_{tot}$. (a) \bar{a}_{ij} set of scattering lengths. For $N_r > 0.6$ all tested cases were unstable. (b) a_{ij} set of scattering lengths. For $N_r > 0.65$ all tested cases were unstable.

classification of wavefunctions into classes with integer winding number fails. Numerically this is indicated by the calculated winding number not being an integer.

The results of our stability survey regarding atom number variations are summarised in Fig. 4.4. Points on the plots indicate whether a Skyrmiion with the corresponding N_r , N_{tot} values is stable (+) or not (\otimes). The two panels show the results for the two different sets of scattering lengths introduced in section 4.1.4. As expected from the discussion in that section, the revised scattering lengths require slightly more atoms for stability with given N_r . The unstable cases with slightly too few atoms have imaginary time evolution for which the ring singularity, most easily visible in Fig. 4.8, moves inwards until it reaches the Skyrmiion core. We define the core as the narrow volume where the ring component flows through the line vortex core. While the ring singularity drifts inwards, the flow velocity through the core increases. Eventually, the flow velocity, Eq. (2.11), exceeds the local two component speed of sound, see Eq. (2.25) (section 2.2.4), and the ring vortex collapses, destroying the ring circulation. The imaginary time evolution of the Mach number in such a scenario is shown in the movie `skyrmiion_corebreak_imagtime.mov` on the CD.

As the filling of the vortex-ring by the line component can hinder the collapse of the ring vortex, we find stable Skyrmiions with smaller N_{tot} if the relative fraction of the filling N_r is increased, as shown in Fig. 4.4. However, this works only up to $N_r \sim 0.65$. For higher N_r the line component escapes confinement by the ring component, with the associated phase variation on the BEC surface

leading to a breakdown of the topological structure.

In summary, Fig. 4.4 shows a region with stability bounded towards lower N_{tot} by ring vortex collapse, and towards higher N_r by breakdown of the global topological structure. The lowest Skyrmion atom number allowed by these two constraints is $N_{tot} \sim 3 \times 10^6$ for the revised scattering lengths.

4.2.2 Skyrmion Core Flow

The increase in central flow speed associated with the collapse of the ring vortex, in imaginary time evolution, led us to consider configurations in which this velocity was reduced. The flow speed is high through the core because it is narrow, its width being determined by the healing length. The return flow speed of the ring component through the outer shell of the Skyrmion is typically orders of magnitude slower because it occurs through a correspondingly greater cross sectional area, see Fig. 4.5.

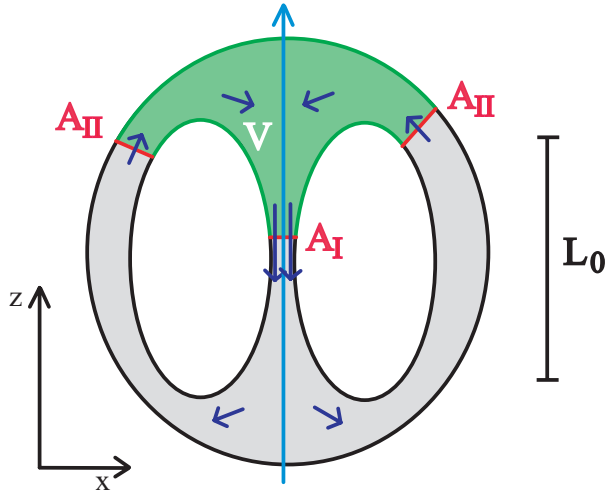


Figure 4.5: Sketch of the flow geometry within the ring component. Shown is a slice in the xz plane, the 3D structure is rotationally symmetric around the axis indicated in blue. The gray and green shaded areas are occupied by the ring component, confined from the outside by the trapping potential and from the inside by the line component. The flow direction is indicated by blue arrows. The green area is the cross section with the volume V explained in the text. Red lines are intersects with the surface area through which the ring component streams into and out of V . Taking the 3D structure into account, the available cross sectional area in the core (A_I) is much smaller than on the outer shell (A_{II}).

Mathematically we can see this from the continuity equation (2.12), using $\dot{n} = 0$ for a stationary state. We can use Gauss' theorem to integrate $\nabla \cdot (n_1 \mathbf{v}_1) = 0$ over the green volume V in Fig. 4.5:

$$\begin{aligned} 0 &= \int d^3\mathbf{x} \nabla \cdot (n_1 \mathbf{v}_1) = \int_A n_1 \mathbf{v}_1 \cdot d\mathbf{A} = \int_{A_I + A_{II}} n_1 \mathbf{v}_1 \cdot d\mathbf{A} \\ &\sim (n_1 v_1)_{A_I} A_I - (n_1 v_1)_{A_{II}} A_{II} \end{aligned} \quad (4.9)$$

A denotes the surface of V and $d\mathbf{A}$ an outside oriented surface element. The third equality arises because on all segments of A besides A_I and A_{II} the flow velocity is tangential to the surface. In the final expression $(n_1 v_1)_{A_I}$ denotes the product of averaged density and velocity ($v_1 = |\mathbf{v}_1|$) on the surface A_I . A_I itself denotes the area of the surface.

Due to the geometry evident in Fig. 4.5 $A_{II} \gg A_I$. The densities of the ring component on either surface are comparable, resulting in $v_{1,I} \gg v_{1,II}$ from Eq. (4.9).

Further, the quantisation of the circulation for a charge one ring vortex requires the velocity \mathbf{v}_1 to satisfy

$$\oint_{\mathcal{C}} \mathbf{v}_1 \cdot d\mathbf{l} = \frac{h}{m}, \quad (4.10)$$

where \mathcal{C} is any closed path around the ring singularity [34]. Due to the high flow speeds through the core dictated by Eq. (4.9), most of the circulation accumulates there. The above equation thus approximately becomes:

$$\int_{-L_0/2}^{L_0/2} v_z(r = 0, z) dz = \frac{h}{m} q, \quad (4.11)$$

where L_0 denotes the length of the core of the Skyrmion in the z direction (see Fig. 4.5).

Elongating the core, by stretching the trap into a cigar shape, should therefore slow the core flow as the circulation is generated over a greater length of core. This is indeed what we found. However, decreasing the atom numbers for which stable Skyrmions exist by stretching the trap reaches a limitation as the outer shell of the ring component thins and the line component pushes through to the outside.

To prevent this we decreased a_{22} by 2%, imagining for example an optical Feshbach resonance [161]⁵. This increases the surface tension and hence strengthens

⁵It will become clear in section 4.2.3 that it might be necessary to create Skyrmions at a specific magnetic bias field strength, ruling out conventional magnetic Feshbach resonances.

phase separation, as will be described in section 4.2.5, and simultaneously makes the line component denser and more localised. For parameters modified thus, we found a stable Skyrmion containing $N_{tot} = 2.13 \times 10^6$ atoms at $N_r = 0.6$ in a trap with anisotropy $\eta \equiv \omega_\perp/\omega_z = 1.3$, $\omega_\perp = 2\pi \times 7.8$ Hz.

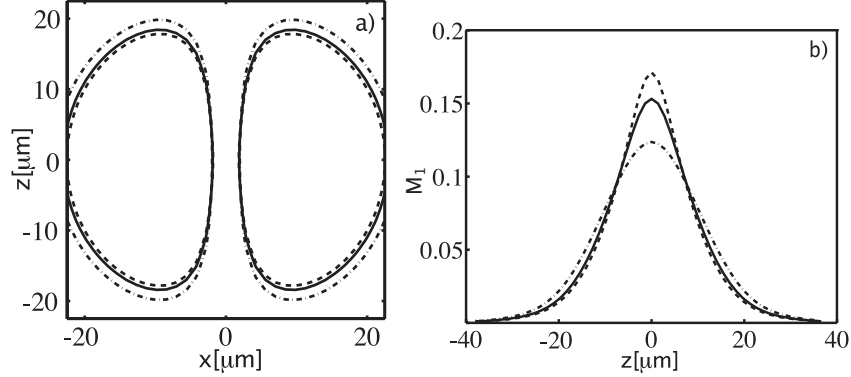


Figure 4.6: Influence of changes in N_r on the core ($N_{tot} = 5 \times 10^6$): (Dashed) $N_r = 0.47$, (solid) $N_r = 0.5$, (dot-dashed) $N_r = 0.58$. Scattering lengths \bar{a}_{ij} . a) Shape of the core. Shown is the cross section of an isosurface of the density of the line component ($n_2 = 2.5 \times 10^{-19} \text{ m}^{-3}$) with the xz plane. b) Mach number of the ring component M_1 along the core for $x = 0$, $y = 0$.

We also observed that increasing the fraction of line component N_r , which has the stabilising effect described in section 4.2.1, lowers the central flow speed: Fig. 4.6 shows how the shape of the core changes for small changes in N_r and the effect of this variation on the flow speed.

It is well known that for a superfluid the relation of the flow velocity to the local speed of sound has important implications for stability, the superflow breaking down once the speed of sound is exceeded [162]. We now investigate this relation for Skyrmions. As long as the features of the Skyrmion are sufficiently larger than the wavelength of the sound-modes considered, we can approximate the background two component BEC as locally homogeneous and apply the result for the speed of low energy excitations that we give in Eq. (2.25). In the phase separated regime, the c_- branch of Eq. (2.25) is imaginary. We argued in section 2.2.4 that this causes the components to separate, removing the possibility of c_- excitations. Hence we consider here only the c_+ branch of the speed of sound. Inspection of Eq. (2.25) shows that this branch essentially smoothly interpolates between the single component sound velocities $c_1 = \sqrt{U n_1 / m}$ and $c_2 = \sqrt{U n_2 / m}$ (see section 2.2.1) in the regions where the BEC composition is changing from dominated by component 1 to dominated by component 2.

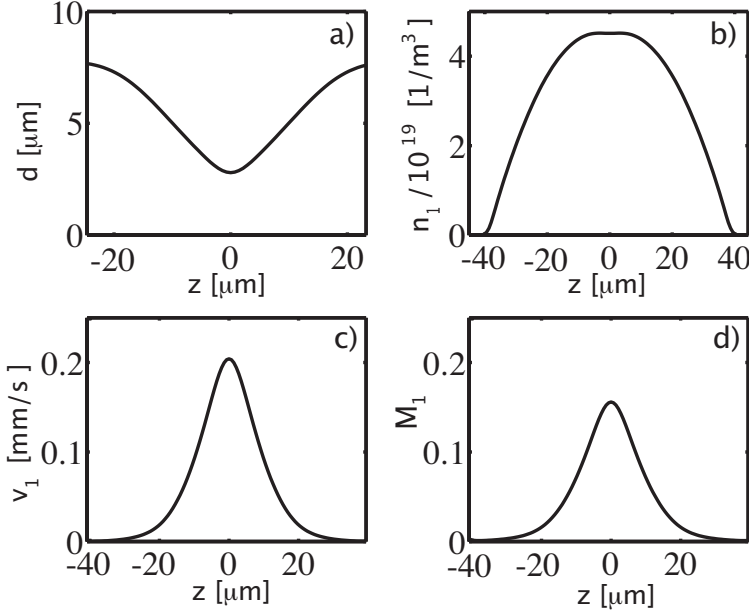


Figure 4.7: Skyrmion core properties ($N_{tot} = 5 \times 10^6$ and $N_r = 0.5$). Scattering lengths \bar{a}_{ij} . (a) Core width d defined in the text. (b) Density of ring component. (c) Flow velocity v_1 . (d) Mach number M_1 of the ring component along the core.

We define the Mach numbers $M_i = v_i(\mathbf{x})/c_+(\mathbf{x})$. For a typical Skyrmion close to the stability boundary, Fig. 4.7 shows M_1 along the Skyrmion core, its density, the flow speed and the core width

$$d(z) = \left\{ \frac{\int (x^2 + y^2) |\phi_1|^2 dx dy}{\int |\phi_1|^2 dx dy} \right\}^{1/2} \quad (4.12)$$

where the integration is over the inner core area only. The speed of the ring component though the thin vortex core of the line component has a sharp peak in the centre and reaches $M_1 \sim 0.15$. The two dimensional structure of the Mach number in the yz plane is shown in Fig. 4.8. It supports the conclusions drawn from Fig. 4.5.

4.2.3 Gravitational Sag

We now outline how the magnetic field dependence of the magnetic moments of the hyperfine states constituting the Skyrmion in general leads to different trap frequencies for different states. This results in differential gravitational sag, and hence slightly offset traps.

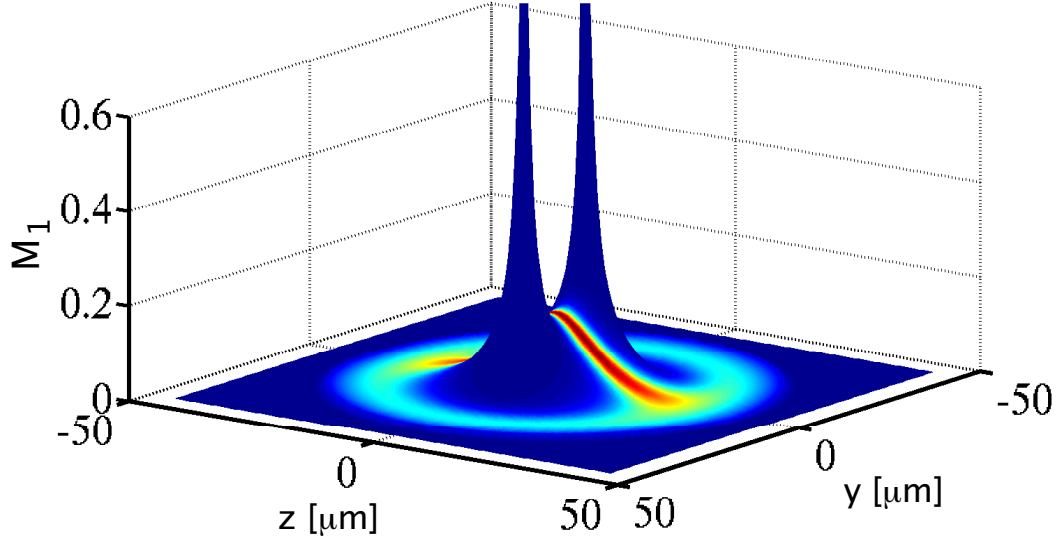


Figure 4.8: Mach number of ring component in the yz plane for a case near the stability boundary with $N_{tot} = 5 \times 10^6$ and $N_r = 0.5$. The superimposed colormap shows the ring component density (blue - lowest density, red - highest density). The peaks are at the location of the ring singularity. Scattering lengths a_{ij} .

The energy of an atom in the hyperfine state $|F, m_F\rangle$, with electronic spin $1/2$, in an external magnetic field B is given by the Breit-Rabi equation [37, 163]

$$E(F, m_F, B) = -\frac{\Delta_{hf}}{2(2I+1)} - g_I \mu_B m_F B \pm \frac{\Delta_{hf}}{2} \left(1 + \frac{2m_F}{I + \frac{1}{2}} x + x^2 \right)^{1/2},$$

$$x = \frac{(g_I + g_J)\mu_B}{\Delta_{hf}} B. \quad (4.13)$$

The nuclear spin for ^{87}Rb is $I = 3/2$. Here Δ_{hf} is the hyperfine splitting at zero magnetic field, g_I and g_J are the gyro magnetic ratios of electron and nucleus respectively and μ_B is the Bohr magneton. x is a dimensionless magnetic field and the upper sign applies for states with $F = I + 1/2$, the lower one for states with $F = I - 1/2$. For ^{87}Rb [164, 165]

$$\Delta_{hf} = 6834.68261090434(3)\text{MHz}, \quad (4.14)$$

$$g_I = 0.9951414(10) \times 10^{-3},$$

$$g_J = 2.00233113(20). \quad (4.15)$$

For these parameters, the energies given by Eq. (4.13) are shown in Fig. 4.9.

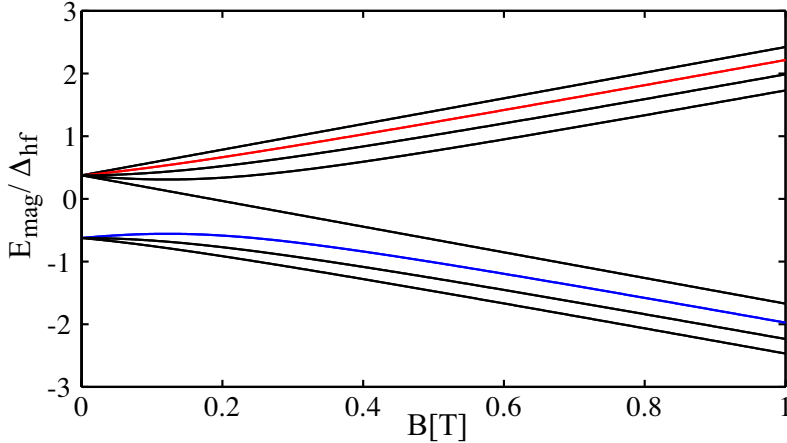


Figure 4.9: Magnetic field dependence of the hyperfine energy levels of ^{87}Rb , calculated from Eq. (4.13). The two states which are magnetically trappable at low fields and are used in our simulations are colored red (line) and blue (ring). It can be seen that the quadratic Zeeman-effect causes deviations from a linear magnetic field dependence of the energies.

The following discussion of the consequences of this behaviour for magnetic trapping is kept one dimensional (dimension x) for simplicity. We assume the magnetic trap has the form

$$B = B_0 + B_2 x^2, \quad (4.16)$$

where B_0 is the bias field. We can expand Eq. (4.13) around some B_0 as

$$E(i, B) = E_0^{(i)}(B_0) + E_1^{(i)}(B_0)(B - B_0) + E_2^{(i)}(B_0)(B - B_0)^2 + \mathcal{O}(B^3), \quad (4.17)$$

where all information concerning the state has been gathered in the collective index i . Inserting the magnetic field, we obtain the following potential for atoms in state i

$$V(x)^{(i)} = E_0^{(i)}(B_0) + E_1^{(i)}(B_0)B_2 x^2 + \mathcal{O}(x^4). \quad (4.18)$$

The ratio of trap frequencies for atoms in states i and j at bias field B_0 is therefore

$$\frac{\omega_{(i)}^2}{\omega_{(j)}^2} = \frac{E_1^{(i)}(B_0)}{E_1^{(j)}(B_0)} \quad (4.19)$$

A gravitational acceleration g will displace the equilibrium position in the trap from $x = 0$ by $X_0^{(i)} = g/\omega_{(i)}^2$. The fractional difference in the gravitational sag

between the two hyperfine states is then

$$\frac{|X_0^{(j)} - X_0^{(i)}|}{X_0^{(j)}} = \left| 1 - \frac{\omega_{(j)}^2}{\omega_{(i)}^2} \right| = \left| 1 - \frac{E_1^{(j)}(B_0)}{E_1^{(i)}(B_0)} \right|, \quad (4.20)$$

If we apply this result to the 7.8 Hz trap and hyperfine states considered in this paper, the resulting offset is about $11\mu\text{m}$ at a bias field of 1 Gauss. Eq. (4.13) predicts zero offset at a bias field $B_0 = B^*$ with [157]

$$B^* = 3.22946 \text{ Gauss}. \quad (4.21)$$

The offset is about $2\mu\text{m}$ at $B_0 = 2.85$ Gauss and about $0.1\mu\text{m}$ at $B_0 = 3.21$ Gauss.

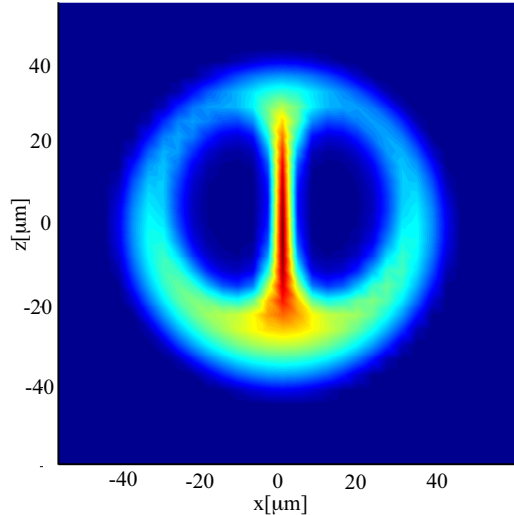


Figure 4.10: Effect of a slight offset $d = 0.1\mu\text{m}$ between the trap centres for the line and the ring component. There is a much greater centre of mass asymmetry between the two components than the offset of the trap centres, due to the strong surface tension between the components. Other Skyrmion parameters are as in Fig. 4.2.

We numerically investigated the effect of offsets of this order by shifting the traps felt by the two components with respect to one another in the z -direction $\mathbf{d} = d\hat{\mathbf{z}}$ (from now on we return to three dimensions). We found for a Skyrmion far from the stability boundaries of Fig. 4.4 b) ($N_{tot} = 9 \times 10^6$ and $N_r = 0.5$ [27] with a radius of approximately 40 microns) that an offset of $d = 2\mu\text{m}$ produced instability. The centres of mass of the hyperfine components spatially separate

significantly and the topological structure breaks down. However, with an offset of $d = 0.1 \mu\text{m}$ the Skyrmion remained stable, albeit with a spatial profile perturbed on length scales much greater than $0.1 \mu\text{m}$, see Fig. 4.10.

This strong influence of slightly offset trap centres of the spatial profiles in a multi-component BEC is a generic feature as was shown analytically in Ref. [166]. The effect was also demonstrated experimentally [150].

We did not thoroughly investigate offsets the x or y directions⁶. The Skyrmion structure suggests greatest resilience against trap offsets in the z -direction and a single verification run does not contradict this assumption. It showed instability of a Skyrmion for a trap offset of $0.1 \mu\text{m}$ in the x direction.

Since the offset scales as ω_z^{-2} , it can always be made sufficiently small compared to the Skyrmion length scale $a_z \propto \omega_z^{-1/2}$ by using a tighter trap. Skyrmions in tight traps also require lower atom numbers, by the scaling argument given in section 4.1.4. The other option we have seen, is to operate at the magnetic bias field B_0 where the states experience the same trapping frequencies, Eq. (4.21). Finally, it might be advantageous to create Skyrmions in a tight optical trap, avoiding magnetic fields entirely, which would also widen the range of suitable hyperfine states to include $|F = 2, m_f = 2\rangle$ and $|F = 1, m_f = 1\rangle$, between which exists an interspecies Feshbach resonance [167].

If the gravitational sag effect on Skyrmions is to be countered by adjusting the trap bias field to the value B^* of Eq. (4.21), our results show that magnetic field stability on the level of 10 mG is required. This can presently be achieved experimentally [168].

4.2.4 Stabilisation against Drift

Line vortices in single component trapped BECs are unstable towards drift out of the trap under the influence of dissipation. The physical origin of this effect is simple: The atomic density near the vortex core is low, hence it is energetically favourable if the vortex is located in regions of higher potential energy and lower background density. This drift can be prevented by a rotation of the trap [38, 169].

The Skyrmion line vortex component behaves in a very similar fashion [27]. If we slightly shift the Skyrmion initial state (4.3) from the centre of the trap

⁶The trap offset is always in the direction of gravity. But the Skyrmion's line vortex, whose orientation defines our z -axis, can be spatially oriented at will. Offsets in the x and y direction are challenging numerically, as trap rotation has to be additionally considered for stabilisation, see section 4.2.4).

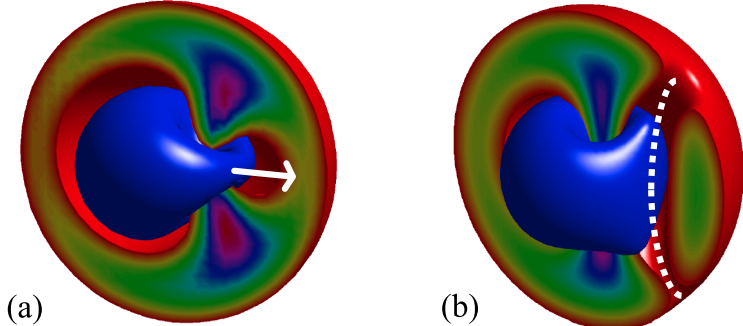


Figure 4.11: Illustration of Skyrmion instabilities for non-cylindrically symmetric perturbations. In both cases the trap is rotated. (a) If the rotational velocity is insufficient to stabilise the line vortex, the Skyrmion core drifts out of the trap towards the edge. The arrow indicates vortex motion in imaginary time. (b) For too high rotational velocities, an additional line vortex is seeded in the *ring* component in this example. The white dashed line shows the approximate location of the new line singularity.

(non-cylindrically symmetric perturbation), the Skyrmion core drifts out of the trap in the imaginary time evolution, see Fig. 4.11 (a), unless the trap is rotated sufficiently fast.

Rotational stabilisation

As there is no obvious experimental way to rotate the components independently, we rotate both. While the filled vortex in the line component is stabilised by rotation faster than a critical value $\Omega_{c,l}$, there is a destabilising effect on the toroidal flow in the ring: for rotation frequencies Ω bigger than a critical value $\Omega_{c,r}$, the imaginary time evolution creates an additional line vortex in the ring component. A snapshot in imaginary time of this is shown in Fig. 4.11 (b). The complete evolution is captured in the movie `skyrmion_ringbreak_imagtime.mov`. Due to the associated phase variation of the ring vortex on the Skyrmion surface, the topological equivalence of \mathbb{R}^3 and S^3 breaks down and with it the Skyrmion.

Therefore stabilisation requires $\Omega_{c,l} < \Omega < \Omega_{c,r}$. The critical frequencies $\Omega_{c,l}$ and $\Omega_{c,r}$ are determined numerically. To establish whether there is a stable Skyrmion for a given rotation frequency, we shift a previously obtained stable cylindrically symmetric state both parallel and perpendicular to the line vortex and evolve it in imaginary time. We observe either stabilisation close to the original symmetry axis, or vortex drift out of the trap, or the disruption of the ring

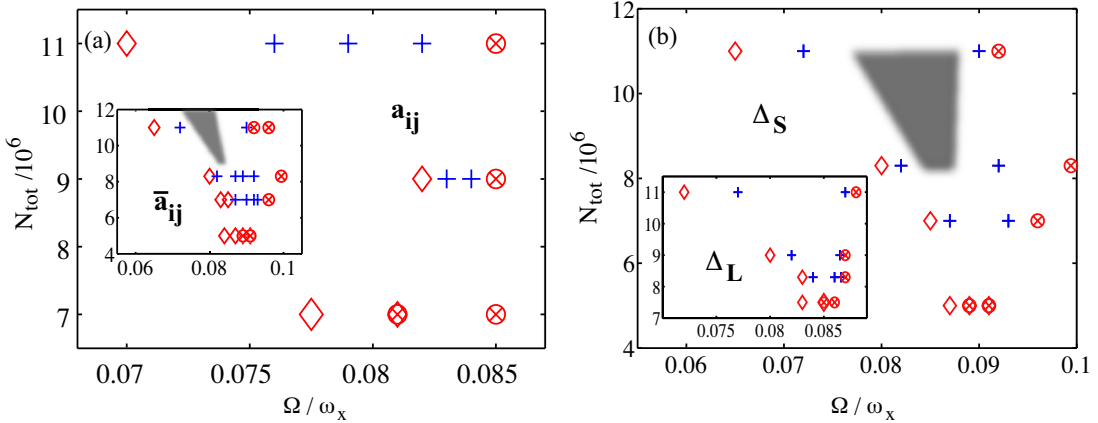


Figure 4.12: Windows of stable rotation frequency for various total atom numbers; $N_r = 0.5$ throughout. (+ blue) stable, (\otimes red) unstable against additional vortex creation in the ring component, (\diamond red) unstable against line vortex drift out of the trap. (a) Comparison of scattering lengths sets. Main diagram: a_{ij} set of scattering lengths. Inset: \bar{a}_{ij} set of scattering lengths. The grey shaded area indicates the location of the stability region for the a_{ij} values. The small offset Δ_S was used. (b) Comparison of different offsets for the \bar{a}_{ij} scattering lengths. Main diagram: Small offsets Δ_S . Inset: Large offsets Δ_L . The grey shaded area indicates the location of the stability region for large offsets.

component circulation due to the creation of additional vortices. The response to trap rotation is studied for both sets of scattering lengths and varies significantly between the a_{ij} and \bar{a}_{ij} parameter sets. Two different offsets were employed: (i) $\Delta_{Sx} = 2\mu\text{m}$ $\Delta_{Sz} = 2\mu\text{m}$ and (ii) $\Delta_{Lx} = 10\mu\text{m}$ $\Delta_{Lz} = 10\mu\text{m}$. Large perturbations might occur during Skyrmion initialisation. The resulting windows of stable rotation frequencies are shown in Fig. 4.12, with the shape of the data points distinguishing the different behaviour in imaginary time outlined above. The critical rotation frequency for stabilisation of the line vortex increases with decreasing atom number, as is the case for an unfilled line vortex in a pancake trap [169], while the critical rotation frequency for disturbances in the ring component decreases slightly for smaller numbers. Therefore the window that allows the stabilisation of Skyrmions by rotation closes around $N_{\text{tot}} = 7 \times 10^6$ for the early set of scattering lengths (\bar{a}_{ij}) and around $N_{\text{tot}} = 9 \times 10^6$ for the revised ones (a_{ij}), see Fig. 4.12.

Stabilisation by optical pinning

For low atom numbers, Skyrmions can be stabilised by a laser pinning potential [170], without the need for rotation. A repulsive external potential at the location of the line singularity makes a density depression there energetically favourable. This depression is naturally realised around the vortex core, hence the pinning potential prevents drift of the vortex towards the edge of the cloud. The potential generated for the BEC by off-resonant interaction with a laser beam, as described in section 1.2.1, is proportional to the light intensity and has the form [171]:

$$V(\mathbf{x}) = V_0 \left(\frac{w_0}{w(z)} \right)^2 \exp \left[-2(x^2 + y^2)/w(z)^2 \right],$$

$$w(z) = w_0 \sqrt{1 + \left(\frac{z}{z_r} \right)^2}, \quad z_r = \pi \left(\frac{w_0}{\lambda} \right) w_0, \quad (4.22)$$

where λ is the wavelength of the laser and w_0 , V_0 are constants that describe its width at the focal point and intensity, respectively. Using the early scattering lengths \bar{a}_{ij} , we found a stable Skyrmion with $N_{tot} = 2 \times 10^6$ and a pinning potential of $V_0 = 10\hbar\omega_x$, $w_0 = 1.3\sigma_x$ ($\sigma_x \equiv (\hbar/m\omega_x)^{1/2}$) and $\lambda = 450$ nm.

However, the pinning laser beam can also have a destabilising effect on the Skyrmions: it reduces the density of the ring component in the core, increasing the flow velocity, which can lead to collapse of the ring vortex. If laser pinning and rotation are used together, it appears to be possible to limit the disrupting effects of both methods.

Figures 4.14 and 4.13 show an example, with the pinning amplitude reduced to $V_0 = 6.5\hbar\omega_x$, and trap rotation of $\Omega = 0.06\omega_x$. The scattering lengths here are also the early values, \bar{a}_{ij} . We verified that this case is stable for independent perturbation of any one of the parameters mentioned above by 3%. For the revised a_{ij} scattering lengths, the small Skyrmion reported in section 4.2.2 may be stabilised with combined rotation and pinning. We found that this Skyrmion could also be stabilised with a pinning potential of strength $V_0 = 10\hbar\omega_x$ alone.

4.2.5 Variation of the Scattering Lengths

Due to experimental uncertainties in the ^{87}Rb (revised) scattering lengths, we investigated the effect of changing them on Skyrmion stability. Ref. [157] does not contain uncertainties for the presented a_{ij} . The calculation of these uncertainties from those given for the underlying singlet and triplet scattering lengths (a_S , a_T)

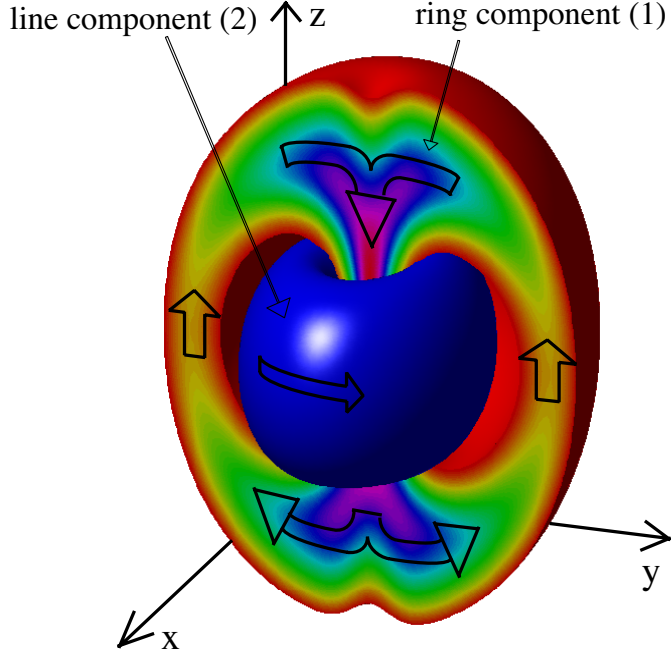


Figure 4.13: Three dimensional density profiles for a Skyrmion with $N_{tot} = 2 \times 10^6$, $N_r = 0.6$ in the presence of a pinning potential ($V_0 = 6.5\hbar\omega_x$, $w_0 = 1.3\sigma_x$, see Eq. (4.22)) and in a rotating trap ($\Omega = 0.06\omega_x$). The anisotropy of the trap is $\omega_\perp/\omega_z = 1.3$ and the scattering lengths are the \bar{a}_{ij} . See text for definitions of symbols and for values of other parameters. The central (blue) torus is an isosurface of the line component. An isosurface of the ring component (red) is shown for $x < 0$: on the y - z plane between the isosurface sections the ring component density is indicated by a colormap from red (lowest) to purple (highest). The circulation associated with each vortex is also indicated.

in Ref. [158], involves a coupled channels calculation beyond the scope of our thesis [172]. This also prevented us from using the even more recent values for a_S and a_T of Ref. [173] for our analysis. However, the uncertainty for the a_{ij} should be roughly the same as for a_S and a_T [172], which leaves us with an experimental scattering lengths uncertainty of $\sim 0.3\%$.

For a case with 9 million atoms we found that variations of a_{11} by 5% resulted in Skyrmion instability. For increased a_{11} this was due to disruption of phase separation. For decreased a_{11} the line component moved outward through the ring component. This is because the relative magnitude of a_{11} and a_{22} determines which component surrounds the other. In the Skyrmion configuration a_{11} is larger and hence lower densities of the ring component are energetically favorable. We

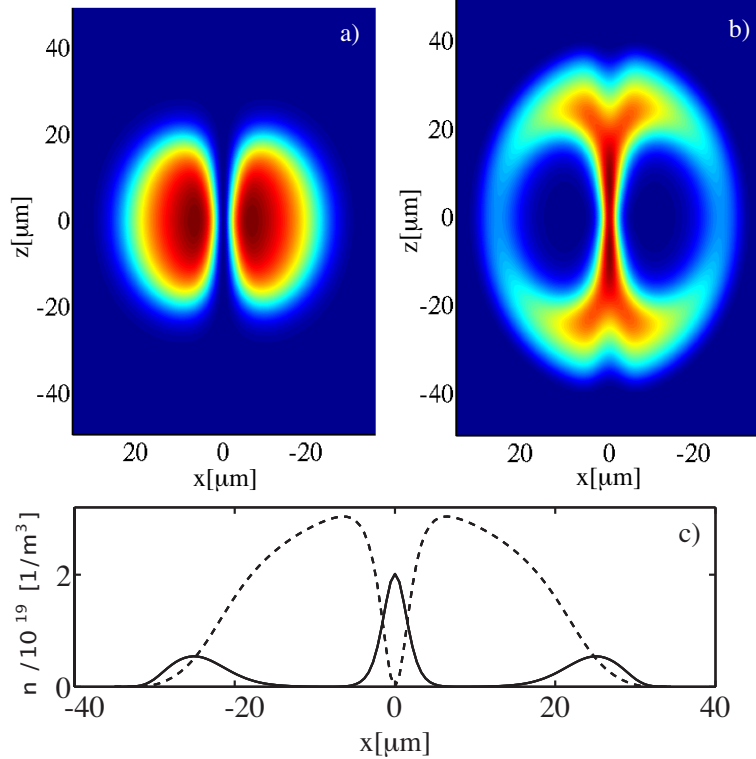


Figure 4.14: Small Skyrmion with $N_{tot} = 2 \times 10^6$ and $N_r = 0.6$, stabilised against drift with rotation and pinning. Scattering lengths \bar{a}_{ij} . (a) Colormap of line component density (blue - lowest density, red - highest density) in the xz plane. (b) Ring component density. (c) Density profiles of the line (dashed) and ring components (solid) along the x -axis ($y = 0, z = 0$). Parameters as for Fig. 4.13.

did not find that increases in a_{12} were destabilising. However, decreases of 2% caused instability, again due to loss of phase-separation. Similarly, decreases in a_{22} were benign, but increases of 2% lead to instability. To verify some of these results we used numerical grids with 256^3 points.

Rescaling the new scattering lengths to $\tilde{a}_{ij} = ca_{ij}$ with $c = 1.067$ results in $\tilde{a}_{11} = 5.67$, $\tilde{a}_{22} = 5.39$, $\tilde{a}_{12} = 5.54$ and thus achieved $\tilde{a}_{11} = a_{11}$, compare section 4.1.4. The constant c can be absorbed into a minor rescaling of the atom numbers. The older values \bar{a}_{ij} then arise from the \tilde{a}_{ij} by a 1% decrease in \tilde{a}_{11} and a 0.7% decrease in \tilde{a}_{12} . As we expect the same stability properties for the \tilde{a}_{ij} values as for the a_{ij} , we conclude that the old scattering lengths \bar{a}_{ij} lie within the stability domain. Explicit simulations confirm that Skyrmions are stable with the \bar{a}_{ij} scattering lengths, with almost unchanged surface tension compared to the a_{ij} .

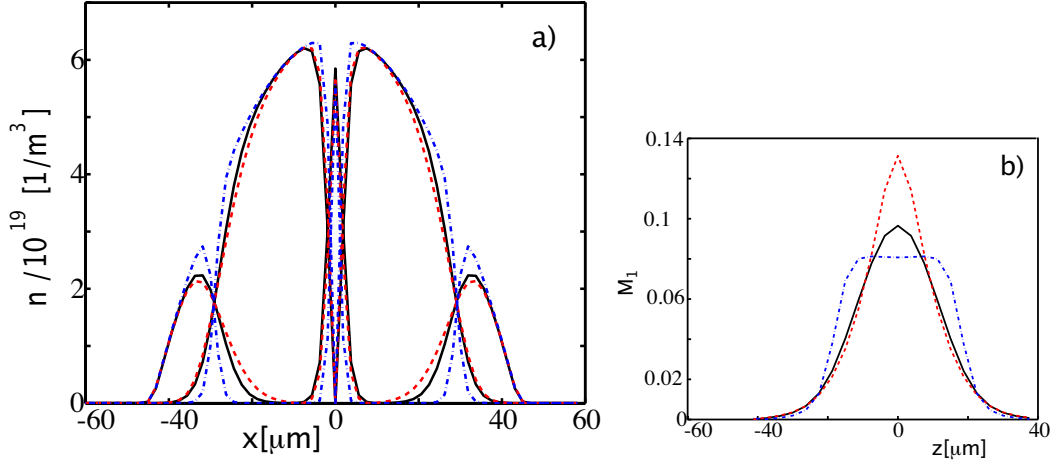


Figure 4.15: Skyrmion with $N_{tot} = 9 \times 10^6$ and $N_r = 0.5$ for different surface tensions σ . (solid black) normal σ : \bar{a}_{ij} set of scattering lengths. (dashed red) low σ : \bar{a}_{11} increased by 2%. (dot-dashed blue) high σ : \bar{a}_{12} increased by 5%. (a) Densities of the line- and ring components across the core ($z = 0, y = 0$). (b) Mach number ($M_1 = v_1/c_+$) of the ring component along the core ($x = 0, y = 0$).

The sensitivity of Skyrmion stability to the scattering lengths can be understood in terms of the phase separation criterion or more generally in terms of the surface tension σ at the component interface [60, 61]. For an interface within a homogeneous background, and in the limit of $U_{11} = U_{22}$, [61] σ is

$$\sigma = n_2 \sqrt{\frac{\hbar^2}{2m} \left(\frac{U_{12}}{\sqrt{U_{11}U_{22}}} - 1 \right)} \frac{U_{22}}{n_1}. \quad (4.23)$$

The derivative of this with respect to U_{11} has a pole where σ has a zero (the critical value for phase separation). It then predicts large variations in surface tension for small variations in U_{11} . Even though we find significant deviations from the homogeneous results, like stable Skyrmions in the regime $U_{12}^2 < U_{11}U_{22}$, this qualitative prediction from the homogeneous case holds. The zero of σ is shifted from $U_{12}^2 = U_{11}U_{22}$ in the trapped case, but our simulations show big changes in surface tension for small changes in the U_{ij} , as displayed in Fig. 4.15. Fig. 4.15 a) illustrates the variation in the size of overlap regions between the line and ring components. Fig. 4.15 b) shows the Mach number. The qualitative differences result from changes in the shape of the core.

4.2.6 Supersonic Core Instability?

The explanation given in section 4.2.1 of the Skyrmion decay in imaginary time for low line component atom numbers, was that the line component then has insufficient strength to prevent contraction of the ring singularity. However, if a more hydrodynamic view point is taken, we would expect stability to depend on local properties of the flow pattern, rather than the global topological structure.

Since supersonic flow in a BEC is energetically unstable [162], Eq. (4.11) together with the requirement $M_1 < 1$ imposes an upper limit on the minimal atom number in a Skyrmion: Lower numbers result in smaller Skyrmions with shorter corelength L_0 (Fig. 4.5). This results in higher flow velocities in the core. If these exceed the speed of sound we must expect Skyrmion instability.

However the limitation towards lower atom numbers that we numerically found in Fig. 4.4 seems to have a different origin. We deduce this from two facts: (i) A simple estimate of the minimal atom number obtained from requiring subsonic core flow turns out an order of magnitude too low.⁷ (ii) Despite thorough numerical searches, we were not able to find Skyrmions with Mach numbers in the core in excess of $M_1 \sim 0.25$.

It is possible that despite observation (ii) a parameter region in which a stable core flow would be faster exists, but is narrow. Alternatively, energetic instability towards the emission of another kind of excitation than phonons could explain these results, if the phase velocity of these excitations is less than the phonon velocity. A candidate are surface waves on the interface between the components [175]. These could be a reason for the apparent critical velocity around $M \sim 0.25$ that we find numerically. Using the result for an interface between two large, asymptotically homogeneous BEC components [175], the phase velocities of the longest wavelength interface waves fitting into the Skyrmion core turn out about an order of magnitude slower than the observed flow velocities, Fig. 4.7 (c). Landau's criterion [162] predicts energetic stability for flow velocities less than the phase velocity of the lowest energy excitations. However, the cylindrical shape and narrow width of the overlap region between the two Skyrmion components in its core, could easily cause large deviations from the results of Ref. [175].

A final verdict about whether the excitation of surface waves can be drawn upon as an additional explanation for the lower limit on the size of Skyrmions

⁷To obtain a criterion, we estimated the length of the narrow segment of the Skyrmion core based on the work of Ref. [174], and assumed a primitive triangular velocity profile (compare Fig. 4.7).

would thus require more detailed studies.

4.2.7 Summary and Outlook

Some useful conclusions may be drawn from our study regarding the experimental prospects for producing stable Skyrmions in trapped BECs. The situation is more optimistic than initial work might have suggested [27], as we have shown that substantially less atoms are required for stable Skyrmions to exist. After the completion of our work on Skyrmions for this chapter, experimental progress towards creating BEC traps for much larger atom numbers than required for Skyrmions has been reported [176]. These traps contain typically 2×10^7 atoms.

However, we have also found that the windows of stability can be rather small, and that they are sensitive to the precise values of the scattering length ratios. The ability to manipulate the scattering lengths, for example using optical Feshbach resonances, would improve the robustness and flexibility of experiments. Stabilisation techniques such as laser pinning are also likely to be useful.

If Skyrmions are finally created in a BEC experiment, it would be interesting to consider whether they might address questions occurring in low energy QCD by means of the correspondence described in section 4.1.3.

4.3 High Charge Ring Flows in Bose-Einstein Condensates

We have shown in section 4.2 that the BEC flow through the core of a Skyrmion becomes rather fast, up to one quarter of the speed of sound. Despite the fact that energetic instability due to the flow velocity itself is only expected for supersonic flow, we did not find any Skyrmions with higher Mach numbers than about 0.25 in the core. In the second part of this chapter, we investigate whether higher Mach numbers can be achieved in the ring component if the line component is effectively replaced by an optical potential. The remaining topological structure is just a ring vortex, without any complications arising from two component BEC physics.

We will show that even high charge ring flows can indeed be stabilised by optical potentials and that the flow velocity in their core is only limited by the speed of sound as expected. The optical potential with which this can be achieved is that of a laser beam containing an optical vortex, which we describe in section 4.3.1.

By tightly focussing such a laser beam blue-detuned from an atomic resonance, it is possible to create a finite length *optical tunnel* for the BEC, defined by the “dark” region of the beam in the vortex core (section 4.3.2).

4.3.1 Optical Vortices

In order to replace the line component of a Skyrmion by an optical potential, we require a repulsive light field with a toroidal topology. This can in fact be realised by a focussed, blue-detuned laser beam that contains an *optical vortex*. An optical vortex has an electric field that possesses a phase circulation on any slice plane perpendicular to its propagation axis. This phase structure is reminiscent of a line vortex in a BEC (section 4.1.1). One obtains an overall helical phase structure if the entire laser beam is considered [177]. The electric field has to vanish at the centre of this beam.

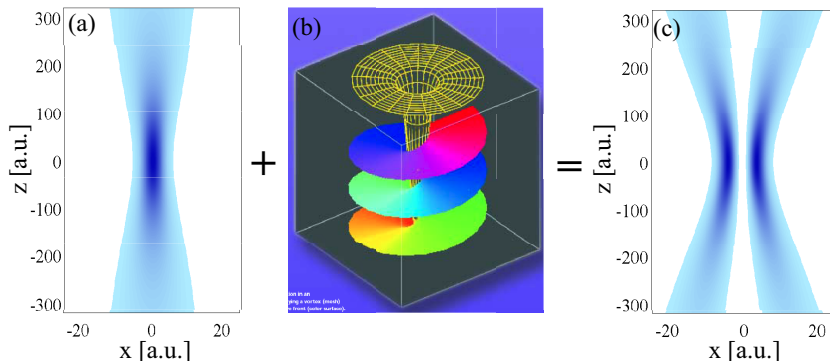


Figure 4.16: Schematic of a focussed laser beam containing an optical vortex. (a) Intensity profile in the xz plane of an ordinary laser propagating along the z -axis, according to Eq. (4.22). Darker blue indicates higher intensity. (b) Helical phase fronts of an optical vortex. The mesh frame indicates the intensity profile dictated by the phase singularity at the centre (this image is taken with kind permission from Ref. [177]). (c) Resulting intensity profile of a focussed laser beam containing an optical vortex according to Eq. (4.25). Color scheme as in (a). If the rotational symmetry around the z axis is taken into account, one can see that the high intensity region (dark blue) is of toroidal topology.

Common methods of creating optical vortices are using holograms [178, 179], spiral phase plates [180] or uniaxial crystals [181]. Previous uses for optical vortices in the context of cold atom physics include writing a waveguide into an atom cloud [182] or helping to guide atoms in an optical fibre [183]. Further

details regarding optical vortices and methods of their creation can be found in the review [184].

By tightly focussing the beam, it is possible to create a region of high light intensity that is of toroidal shape (Fig. 4.16), with a low light intensity region at the centre, thus forming an *optical tunnel*.

4.3.2 Potentials and Method

We now numerically show that an optical vortex laser beam can stabilise a BEC ring flow, using realistic parameters for both the BEC and the optical vortex. To determine energetic stability of the BEC, we use the imaginary time method as in the first half of this chapter, but without complications due to two components or rotation. Hence we can directly solve the basic imaginary time GPE (2.18).

Using cylindrical coordinates r, z, φ , we model a BEC cloud in a cigar-shaped trap with frequencies ω_r radially and ω_z longitudinally. In this second part of the chapter, we can assume that the wave function ϕ of the sole remaining BEC component does not depend on φ , hence $\Delta = \frac{\partial^2}{\partial r^2} + \frac{1}{r} \frac{\partial}{\partial r} + \frac{\partial^2}{\partial z^2}$. The interaction coefficient U is related to the s-wave scattering length a_s as usual: $U = 4\pi\hbar^2 a_s/m$, where m is the atomic mass. Both parameters⁸ are taken for ⁸⁷Rb: $m = 1.44 \times 10^{-25}$ kg and $a_s = 5.67$ nm.

For the external potential $V(\mathbf{x})$, which appears in Eq. (2.18) we assume two contributions, a harmonic trap V_t and an optical potential V_v , i.e. $V = V_t + V_v$. The building blocks are individually given by:

$$V_t(r, z) = \frac{1}{2}m(\omega_r^2 r^2 + \omega_z^2 z^2), \quad (4.24)$$

$$V_v(r, z) = V_0 r^{2l} w(z)^{-(l+1)} w_0^2 \exp\left(-\frac{r^2}{w(z)^2}\right), \quad (4.25)$$

$$w(z)^2 = w_0^2 + \frac{(z - z_{f0})^2}{k_0^2 w_0^2}. \quad (4.26)$$

As explained in section 4.3.1, the repulsive potential V_v can be generated by a blue-detuned optical vortex laser beam [185]. The charge of the optical vortex l is taken to equal 2 for all our numerical solutions. The propagation direction of the laser beam coincides with the long trap axis z . Further, w_0 is a parameter

⁸The scattering length is \bar{a}_{11} in the notation of the Skyrmion section. We started with work on the optical vortex system before we became aware of the a_{ij} ⁸⁷Rb scattering length values. As we only consider a single component from now on, variations of the scattering length on the 7% level are irrelevant, in contrast to the Skyrmion scenario.

describing the waist of the laser beam at its focus, k_0 is the wave number of the light and z_{f0} controls the position of the beam focus. For the results presented here we used $k_0 = 1.4 \times 10^7 \text{ m}^{-1}$ and $z_{f0} = 0$. For $l = 0$, Eq. (4.25) is just the potential of an ordinary focussed laser that we already encountered⁹ in Eq. (4.22).

Fig. 4.17 shows the combined potential of the harmonic trap and the optical vortex $V = V_t + V_v$. An equal energy contour is indicated by the white lines. A condensate ground state treated in the Thomas-Fermi approximation [34], where $|\phi|^2 = (\mu - V)/U > 0$, would fill the volume within the white line for a chemical potential $\mu = 20.9\hbar\omega_r$.

In three dimensions, the tight focus of the laser beam generates a circular local maximum, whose intersection with the rz plane yields the peaks situated symmetrically around the origin at $|r| \sim 5\mu\text{m}$, see Fig. 4.17. For a suitable

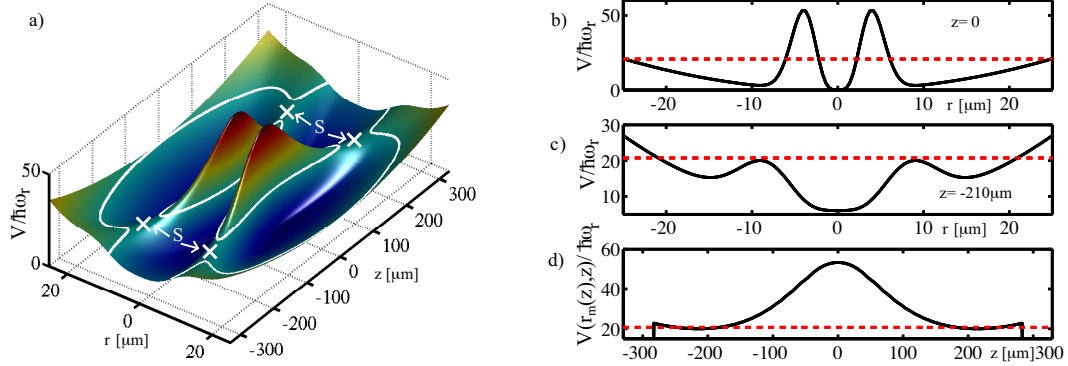


Figure 4.17: Combined harmonic trap V_t and optical vortex potential V_v for $V_0 = 99\hbar\omega_r$, $w_0 = 2.8\mu\text{m}$, $q = 9$. Trap frequencies: $\omega_r = 7.8 \times 2\pi \text{ Hz}$ and $\omega_z = 0.5 \times 2\pi \text{ Hz}$. (a) $V = V_t + V_v$. Saddle points of the potential are indicated by S . The white line is an isocontour $V = \mu_0$ at $\mu_0/(\hbar\omega_r) = 20.9$. (b, c) Radial cross sections of the potential at $z = 0$ (b) and at $z = -210\mu\text{m}$ (c). Dotted lines indicate μ_0 . (d) Dependence of the height of the potential “ridge” (local maximum) of V_{tot} on z . This corresponds to the function $V(r_m(z), z)$ described in the text. For $|z| > 280\mu\text{m}$ the local maximum disappears for the parameters chosen.

choice of parameters the combined potential exhibits saddle points, marked S in Fig. 4.17 (a). If the chemical potential is above the potential value at the saddle points, the BEC can “wrap” around the intense region of the optical vortex.

We find parameter sets for which the saddle points exist as follows: First we

⁹For exact equivalence we need to rescale $w_0 \rightarrow \sqrt{2}w_0$ and $V_0 \rightarrow 2V_0$ in Eq. (4.22).

determine the position of the maximum with respect to r of the vortex potential in Eq. (4.25), with z fixed, by solving

$$\frac{\partial}{\partial r} V_v(r, z) = 0. \quad (4.27)$$

for r . We ignore the harmonic trap in this step. The solution of Eq. (4.27) is:

$$r_m(z) = \sqrt{l} \sqrt{w_0^2 + \frac{z^2}{k_0^2 w_0^2}}. \quad (4.28)$$

The height of the potential “ridge” visible in Fig. 4.17 (a) is then approximately given by $V(r_m(z), z)$, where V_t is now taken into account. Fig. 4.17 (d) shows $V(r_m(z), z)$. The saddle points must be minima of this function if they exist. For $V(r_m(z), z)$ to have extrema besides the obvious maximum at $z = 0$, the quartic expression

$$\left(\frac{\partial}{\partial z} V(r_m(z), z) \right) / z = -\frac{2e^{-l} l^l V_0 w_0^4}{k_0^2} \left(w_0^4 + \frac{z^2}{k_0^2} \right)^{-2} + \frac{l m \omega_z^2}{k_0^2 w_0^2} + m \omega_z^2 = 0 \quad (4.29)$$

must have real roots. After selecting the optical vortex parameters and ω_r , equation Eq. (4.29) yields a useful approximation for the strongest axial confinement ω_z allowed.

In order to find energetically stable ring flows we solve Eq. (2.18) with $V = V_t + V_v$ in imaginary time exactly as we did for the Skyrmions. The initial trial function for the imaginary time algorithm is one which now has the same topological structure as the target ring flow: We multiply an amplitude $\sqrt{n(r, z)}$ obtained from the Thomas-Fermi approximation [34] with a phase factor $\exp(i\eta(r, z))$:

$$\psi(r, z, \phi) = \sqrt{n(r, z)} \exp(i\eta(r, z)), \quad (4.30)$$

$$\eta(r, z) = q \arccos \left(\frac{|z| (D-r)}{s(r, z)} \right), \quad (4.31)$$

$$s(r, z) = \sqrt{(z^2 + (D-r)^2)}. \quad (4.32)$$

On any closed loop threaded through the *single* circular ring singularity implicit in Eq. (4.31), the phase η varies by $2\pi q$, where q is the ring vortex charge. The initial state thus contains one charge q ring vortex. Its singularity is located at $r = D$, $z = 0$ in our coordinates.

4.3.3 Stabilisation of High Charge Ring Flow

The low density region of a vortex ring in a BEC has a toroidal shape, which matches the shape of the high intensity region of a focussed optical vortex laser

beam. In the presence of the optical vortex potential, it becomes energetically favorable for the BEC ring singularity to be located at the maximum of laser light intensity. This prevents the contraction of the vortex ring. This mechanism is similar to the stabilisation of line vortices within a harmonically trapped BEC cloud by laser pinning, which we applied to Skyrmions in the second part of section 4.2.4.

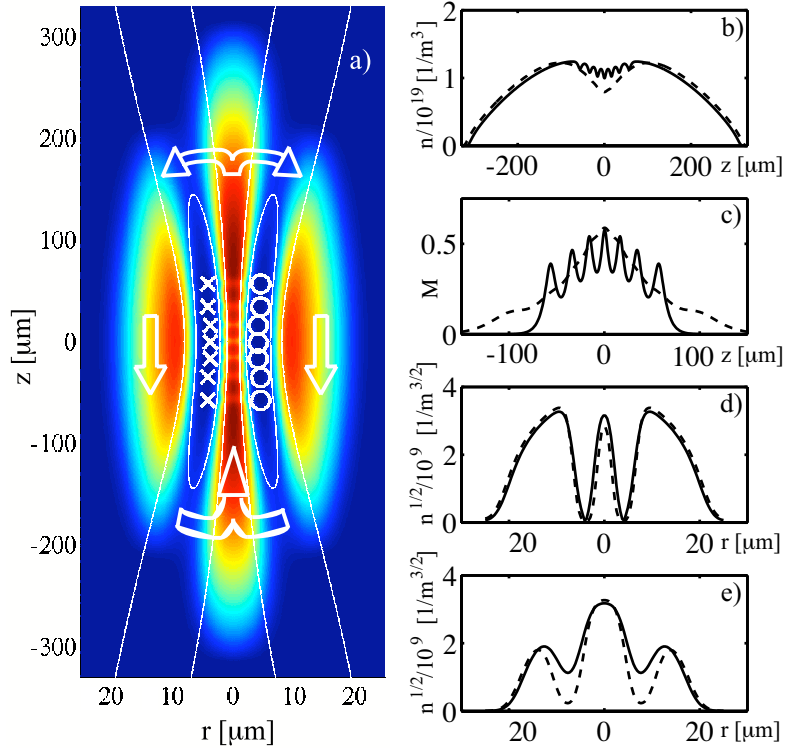


Figure 4.18: Cross-sections of density and velocity structures for different stationary ring flows. In (a) the shape of the optical vortex potential is also shown. Parameter set for case (i): $V_0 = 48\hbar\omega_r$, $w_0 = 3\mu\text{m}$, $q = 7$, indicated by solid lines in (b-e). Parameter set for case (ii): $V_0 = 99\hbar\omega_r$, $w_0 = 2.8\mu\text{m}$, $q = 9$, indicated by dashed lines in (b-e). (a) Shows the BEC density (red highest, blue lowest) in the r - z plane for case (i). The arrows indicate the BEC flow, thin white lines are isocontours of the optical vortex potential at $V_v = 1 \times 10^{-32}\text{J}$ (outer lines) and $V_v = 1 \times 10^{-31}\text{J}$ (inner lines). The intersection of ring singularities with the r - z plane is marked by \times (\circ) for mathematically positive (negative) circulation. (b) BEC density and (c) Mach number M at $r = 0$ along z axis. (d) BEC amplitude in radial direction at $z = 0$. (e) BEC amplitude in radial direction at $z = 170\mu\text{m}$.

Examples of stationary states resulting from the imaginary time evolution are shown in Fig. 4.18. In a harmonic trap with $\omega_r = 7.8 \times 2\pi$ Hz and $\omega_z = 0.5 \times 2\pi$ Hz the BEC contains 2.2×10^6 atoms. The subplots are for two different sets of optical vortex parameters and ring flow charges: case (i) and case (ii) as given in the caption. Case (ii) represents the more intense optical vortex. It can be seen in Fig. 4.18 (a) that the single charge 7 ring singularity that was present in the initial state has broken up into a regular stack of seven unit charge ring singularities. It is known for vortex structures in BEC, that multiple unit charge vortices are usually energetically favoured over a single high charge vortex [38]. For case (i) the seven individual ring singularities are responsible for the multi-peak structure of the Mach number shown in Fig. 4.18 (c). If the parameters are altered towards those of case (ii), the influence of the singularities on the flow in the tunnel is reduced. This corresponds to the transition from the solid to the dashed lines in Fig. 4.18 (b-c). The overall topological structure of the high light intensity region surrounded by a BEC ring flow in a harmonic trap (Fig. 4.18) is reminiscent of that of a Skyrmi n and can thus be thought of as an ‘‘Atom-Light Skyrmi n ’’.

By the same argument used in section 4.2.2 for the case of Skyrmi n s, the integral along the z axis of the flow velocity is directly connected to the ring vortex charge q . The quantization condition for our high charge ring flow is $\oint_{\mathcal{C}} \mathbf{v} \cdot d\mathbf{l} = \frac{\hbar}{m}q$, where \mathcal{C} denotes any closed contour threading through all the ring singularities. In this case Eq. (4.11) becomes:

$$\int_{-L_o/2}^{L_o/2} v_z(r=0, z) dz = \frac{\hbar}{m}q, \quad (4.33)$$

where L_o here denotes the length of the optical tunnel in the z direction, which is implicitly governed by the beam waist parameter w_0 of the optical vortex in Eq. (4.25).

The method we propose for stabilising the ring singularities by pinning should be experimentally realisable with present technology. The procedure to form the ring flow consists of initially creating a BEC at rest, already in the presence of the optical vortex. Then a ring flow structure with high vorticity is seeded by means of phase imprinting, using the suggestion that exists for the ring component of a Skyrmi n [139]. In the presence of dissipation the BEC is expected to evolve towards stationary states, like those in Fig. 4.18.

As can be seen in Fig. 4.18 (c) the flow velocity through the tunnel in the core of the optical vortex can be much higher than those we found in the core of a Skyrmi n (compare section 4.2.6). There are two main possibilities to increase

the core flow velocity from a given state: (i) We can shorten the optical tunnel by reducing the focal width w_0 in equations (4.25) and (4.26). A shorter tunnel increases the velocity according to Eq. (4.33). The variation can be done in a continuous fashion numerically, by using a previously found stable ring flow as initial state of simulations with a shortened tunnel. (ii) We can increase the vortex charge q . However this is only possible in a discrete fashion and, in contrast to (i), numerically requires a complete new imaginary time solution of Eq. (2.18) from a suitable initial state. The highest core Mach number that we numerically found was $M = 0.87$.

As expected [162], supersonic flows turned out to be energetically unstable. This manifested itself in the imaginary time evolution as a decay of the total ring flow charge from q_1 to $q_2 < q_1$, whenever the parameters were such that a final state with charge q_1 would breach the speed of sound.

4.3.4 Summary and Outlook

We have introduced a novel arrangement for the study of persistent ring flows in a BEC. It utilises optical vortices, laser beams with a phase singularity at the centre and hence a zero intensity hollow core. If tightly focussed, the highest intensity region of the optical vortex can fit into the low density region of the matter-wave ring vortex in the BEC and hence stabilise it against contraction. We showed numerically that energetically stable BEC states with ring flows of charges up to $q = 9$ exist in such a system.

If a Skyrmion is viewed as a method to stabilise the ring vortex component, the optical vortex stabilisation introduced in the second part of this chapter is more flexible. Even the stabilisation of a charge 2 ring flow in a skyrmion requires 7×10^6 atoms [156]. According to our discussion of the relation between flow quantisation, core flow velocity and minimal Skyrmion size in sections 4.2.2, 4.2.6 and 4.3.3, we expect this number to increase for higher ring charges. In comparison, case (ii) of section 4.3.3 represents a stable charge 9 ring flow in a condensate of only 2.2×10^6 atoms.

We have also demonstrated that in the proposed trapping configuration the BEC is flowing through the optical tunnel with velocities close to the speed of sound. No supersonic energetically stable flows were found, as expected. However despite the energetic instability, it is not necessary that a supersonic flow is also dynamically unstable [64]. As we are interested in supersonic flows in a BEC for the purpose of analogue gravity, introduced in section 1.3, we investigated whether

it is possible to dynamically bring the optical tunnel flow into the supersonic regime to create an analogue black hole. This research is described in chapter 5.

4.4 Conclusion

This concludes the part on topological structures of this thesis. The creation of ring vortices is an integral part of the creation of Skyrmions. Experimental efforts towards Skyrmion creation in BECs are thus provided with an intermediate target by the separate stabilisation of ring vortex structures demonstrated in the second part of this chapter. The final step of creating stable Skyrmions is surely facilitated by our extensive stability analysis and discussion of several mechanisms by which a Skyrmion would decay in the presence of dissipation.

Our stability analysis of Skyrmions has been published in the Physical Review [186]. The proposal for the creation of stable high charge ring flows in a BEC is submitted for publication [187].

Chapter 5

Supersonic Bose-Einstein Condensates for Analogue Gravity

Bose-Einstein condensates are a promising physical system to realise the ideas of analogue gravity [17], such as the observation of analogue Hawking radiation [16], analogue cosmological particle production [50] and matter-wave superradiance [51]. While Skyrmions, subject of the previous chapter, are difficult to access in nuclear physics, at least certain ideas of Skyrme theory were experimentally verified [47]. In contrast, the Hawking effect [48, 49], whose study by means of analogy is at the heart of analogue gravity, has not been observed experimentally. Indeed it has dim prospects of observation in astronomy for decades to come. Detecting analogue Hawking radiation in a BEC would thus not only represent yet another success of cold atom physics, but realise a milestone for the field of quantum field theory in curved spacetime. Accordingly, our goal in this chapter is to identify experimentally feasible setups with sonic horizons (see section 1.3), in which a measurable analogue Hawking effect is expected. We aim to show that present technology suffices.

It is clear that a sonic horizon is required for analogue Hawking radiation. What is less clear, is which of the horizon properties used in the literature are physical prerequisites for the Hawking effect, and which serve the simplification of its derivations. We will briefly discuss these issues, however the theory of the analogue Hawking effect itself is not our main topic. We thus move on to propose several experimentally realisable setups for horizon creation in a BEC. Depending on, for example, the detection method that one envisaged for analogue Hawking

phonons, any of those can turn out to be most suitable.

We begin with some introductory remarks about quantum field theory in curved spacetime (section 5.1). In section 5.2 we define sonic horizons and review the relevant literature. Following that, we collect properties that are believed necessary for a sonic horizon to emit analogue Hawking radiation, adding our own thoughts to the topic (section 5.3). The rest of the chapter is taken up by our results regarding three distinct schemes for horizon creation: sonic horizons in optical tunnels (section 5.4), sonic horizons in the parent condensate of an atom-laser (section 5.5) and sonic horizons in the exit nozzle of a BEC reservoir (section 5.6). The main features of all these ideas are summarised in section 5.7. Based on the criteria outlined in section 5.3 we also assess the suitability of each of these scenarios for analogue Hawking radiation.

5.1 Introduction

5.1.1 General Relativity

In Einstein's classical theory of gravitation, general relativity (GR), spacetime is significantly curved in the proximity of extremely compact and massive objects like neutron stars and black-holes. On very large scales, such as the size of the Universe itself, curvature also becomes important. We now briefly introduce some concepts of GR to aid the motivation of our work, however detailed general relativistic formalism is not required for this thesis.

The curvature of spacetime due to the presence of mass-energy is expressed in the language of differential geometry. An important element of GR is the spacetime metric $g_{\mu\nu}(x)$. An infinitesimal distance element (in spacetime) ds^2 is given in terms of infinitesimal displacements dx^μ as

$$ds^2(x, dx) = g_{\mu\nu}(x)dx^\mu dx^\nu. \quad (5.1)$$

Here x denotes a four-vector¹ $(t, x, y, z)^T$ and Greek indices appearing as superscript and subscript² have to be summed over the 4 spacetime coordinates.

A useful concept is the light-cone, as it is in special relativity: For any given event x in the spacetime, we can segregate directions dx according to whether

¹The speed of light is $c = 1$, but throughout this section only.

²Sub and superscript distinguish whether a quantity transforms like a derivative (subscript) or like a differential (superscript) under coordinate transformations.

$ds^2(x, dx) < 0$, these are called time-like, or $ds^2(x, dx) > 0$, these are called space-like³. The separatrix between these classes, the set of dx with $ds^2(x, dx) = 0$, forms a three dimensional cone, the light cone. Displacements on this cone are called null or light-like.

Under the influence of gravity only, particles move on geodesics in the curved spacetime, which are extremal lines between two (non-null separated) events. These geodesics can be found from a second order ordinary differential equation if the initial tangential vector of the geodesic is known. This “geodesic equation” is determined by $g_{\mu\nu}(x)$ and contains its derivatives. Massive objects move on time-like and massless ones on light-like geodesics⁴.

It is the mass-energy distribution that causes spacetime to warp, according to the Einstein equations. These are a set of coupled, second order, nonlinear partial differential equations for the metric $g_{\mu\nu}$, involving the energy-momentum tensor $T_{\mu\nu}$.

An important prediction of GR is the existence of black-holes: The metric that solves Einstein’s equations for the energy-momentum distribution of a compact object of mass M possesses a surface which causally disconnects its inside and outside regions. This surface, called an event-horizon, is located at a radius $R_S = 2M$ from the centre of mass⁵. The light cones, expressed in Minkowski coordinates of the universe’s rest frame, appear warped behind the event horizon such that all time-like geodesics are pointing towards the centre, see Fig. 5.1 (a). For a particle that passes the event-horizon of such a black-hole, no future exists but to fall into the centre. The most massive stars are believed to collapse to a black-hole after ending their fusion processes: The mass is concentrated beyond the event-horizon, almost in a singular point.

5.1.2 Quantum Field Theory in Curved Spaces

Quantum field theory (QFT) can be formulated in a relativistically invariant fashion and naturally arises as the theory for a consistent unification of quantum mechanics and special relativity [32, 71]. A similar merging of general relativity with quantum mechanics turned out to be much harder. So far, a consistent theory of quantum gravity does not yet exist. It is however possible to proceed

³The convention for our flat space Minkowski metric is $\text{diag}(-1, 1, 1, 1)$.

⁴A geodesic is light-like if its tangential vector is everywhere light-like.

⁵We assume spherical symmetry. $R_S = 2GM/c^2$ if units are restored, where G is the gravitational constant.

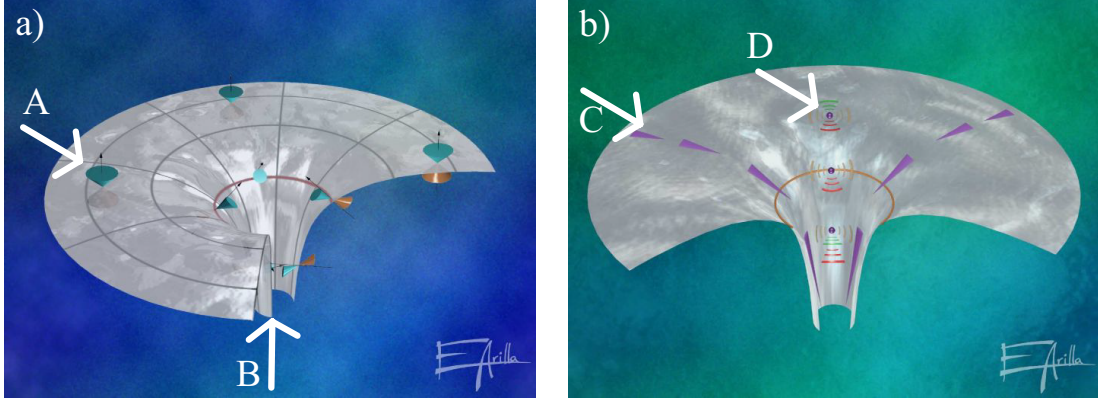


Figure 5.1: (a) Illustration of the tipping of light-cones (A) in the curved spacetime around a black hole (B). The red line is the event horizon. (b) Illustration of wave propagation in the flowing background around an analogue black hole. The length of violet arrows indicates the velocity of the flow (C). The colored arcs indicate in which directions (in the lab frame) waves can propagate (D). The yellow line is the sonic horizon. Both images are reproduced with kind permission from Ref. [17].

with a semiclassical approach, in which the spacetime metric enters classically but the matter fields are quantised. This might be appropriate for lengths and times that stay well clear of the Planck scales⁶ [66]. Far above these scales, we are in the realm of quantum field theory in curved spacetime (QFTCS) or semi-classical gravity.

Taking usual quantum field theory as the starting point, we write our field equations but use the general relativistic metric $g_{\mu\nu}$ instead of the Minkowski metric for all scalar products. For example the Klein-Gordon equation for a scalar field $\phi(x)$ of mass m can in curved spacetime be written as:

$$[\sqrt{-g}\partial_\mu (\sqrt{-g}g^{\mu\nu}\partial_\nu) + m^2] \phi(x) = 0, \quad g = \det(g_{\mu\nu}). \quad (5.2)$$

The change appears innocent, but already if viewed as a classical wave equation, Eq. (5.2) is vastly more involved than the flat spacetime version $(-\partial_t^2 + \nabla^2 +$

⁶Beyond the Planck length $(G\hbar/c^3)^{1/2} = 1.6 \times 10^{-35}$ m and Planck time $(G\hbar/c^5)^{1/2} = 5.4 \times 10^{-44}$ s, quantum gravity is believed to become crucial.

$$m^2)\phi(x, t) = 0.$$

When quantising this curved space field theory further complications arise. In flat Minkowski space where $g_{\mu\nu} = \text{diag}(-1, 1, 1, 1)$, Eq. (5.2) can be solved by separation of variables in any inertial frame. Mathematical solutions can be unambiguously divided into positive and negative frequency ones⁷, and the field operator solution can be expanded in a complete set $u_i(x)$ of positive frequency modes

$$\hat{\phi}(x) = \sum_i \left[\hat{a}_i u_i(x) + \hat{a}_i^\dagger u_i^*(x) \right]. \quad (5.3)$$

The expansion Eq. (5.3) defines the annihilation and creation operators \hat{a}_i , \hat{a}_i^\dagger , which define the vacuum $|0\rangle$ by $\hat{a}_i|0\rangle = 0$. As the property of a mode having positive frequency is invariant under Poincaré transformations [66], so is the vacuum.

In curved space such a preferred set of (inertial) coordinates does not exist, and given one expansion of the field operator as in Eq. (5.3), we might equally well expand the field in a basis that has positive frequencies with respect to other coordinates $\hat{\phi}(x') = \sum_i \left[\hat{a}_i \bar{u}_i(x') + \hat{a}_i^\dagger \bar{u}_i^*(x') \right]$. The vacuum defined by the \hat{a}_i in general does not agree with the one previously obtained. As a result of this, the particle content of a field is observer dependent and loses some of its meaning in curved spaces [66].

An important prediction using QFTCS was made by S. Hawking in the 1970s. He considered the effect of a star collapsing to a black hole on a field described by Eq. (5.2). Hawking found an emission of thermal radiation by the black hole and accompanying loss of black hole mass [48, 49]. The effect has been subsequently re-derived by a variety of means, also for scenarios where an ‘‘eternal black hole’’ always existed [66].

We now outline the essential features of the original derivation. Consider a scalar quantum field in the Heisenberg picture, i.e. the mode-solutions of the quantum field operator in Eq. (5.3) contain the entire time dependence and the quantum state is ‘‘eternal’’. We employ a spherical coordinate system with radial coordinate r , in which the centre of mass of the star and later the black hole stays at $r = 0$. Imagine incoming, spherical, positive frequency waves at early times and far from $r = 0$ (past infinity). These waves travel inwards, are affected by the changes in the metric resulting from the gravitational collapse of the star and subsequently propagate outwards. Some waves are trapped inside the event

⁷A positive frequency mode $u(x, t)$ with respect to t fulfills $\partial_t u(x, t) = -i\omega t$ with $\omega > 0$.

horizon of the black hole (BH) and can never escape to spatial infinity. A wave packet can pass through $r = 0$ early enough, so that it can just escape before the event horizon develops. Depending on its distance to the horizon when the latter is formed, it can take the packet arbitrarily long to escape to spatial infinity. It is found that due to this process, a mode that started off with positive frequency at past infinity, is in general not a positive frequency mode at future infinity⁸.

So far we have thought about a classical wave propagation problem, but now the ambiguity of quantum states in QFTCS comes into play. Because the space time contains an event horizon, we cannot find modes that are at all points positive frequency. However we can employ a set of modes that is positive frequency in a domain of spacetime where it seems sensible to define the vacuum $|0\rangle$. The logical domain is past infinity. Now we consider an observer at future infinity. Far from the black hole, spacetime is flat and the observer employs usual (spherical) plane wave modes to expand the field operator. The vacuum defined by those, $|\bar{0}\rangle$, disagrees with $|0\rangle$. For the observer, our quantum state hence contains particles. Their spectrum is found to be thermal [48, 49] at the Hawking temperature $T_H = \frac{\hbar}{2\pi k_b c} \kappa$, where κ is the acceleration due to gravity on the event horizon of the black hole. Importantly, the central results of the derivation depend exclusively on the behaviour of the metric at the horizon, parametrised by κ . A crucial ingredient is the exponential decrease in the wavelength of an outgoing spherical mode traced backwards in time to the horizon.

This derivation appears to have little in common with the more popular explanation of the Hawking effect's physics: Vacuum pair fluctuations are turned from virtual to real at the horizon; the negative energy member of the pair falls into the BH, lowering its mass, while the other escapes, constituting the Hawking radiation. However, it is a useful way of thinking about the Hawking effect, and derivations using the idea exist [188].

The exponential blue shift mentioned above seems to render the effect sensitive to physics on arbitrarily small length scales [16]. It has later been shown that Hawking radiation is insensitive to alterations of the dispersion relation at high frequencies [189, 190]. Nonetheless, even our brief outline shows that the theory of the Hawking effect is far from straight-forward. W. Unruh suggested how the correspondence between excitations of a moving fluid and quantum fields in curved spacetime could be exploited to study the principles of the Hawking effect [16]. The theoretical and experimental study of the analogue can, if not

⁸Late times and far from the location of the black hole.

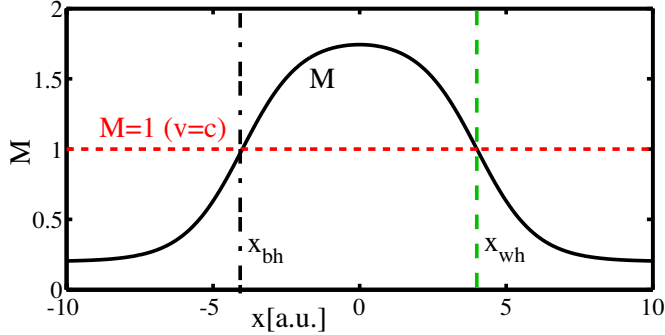


Figure 5.2: Example of a Mach number profile (solid black) belonging to a right-flowing fluid. The flow contains a sonic black hole horizon (black, dot-dashed) at $x = x_{bh}$ and a sonic white hole horizon (green, dashed) at $x = x_{wh}$.

confirm the astrophysical effect itself, at least deepen our understanding of, and confidence in, the physical effects at play. For the particular case of a BEC we have outlined the main part of the derivation of the analogy in section 2.3.4. In order for quantum effects in both systems to be analogous, we also need the field operators in the field equation to bosonic commutation relations [17]. This is the case in a BEC. A simple sketch of how the analogue Hawking effect arises in a fluid is given in the next section.

5.2 Analogue Gravity

Let us consider a fluid in one dimension x , flowing from left to right, schematically depicted in Fig. 5.2. The flow is subsonic ($M < 1$) for $x < x_{bh}$. It accelerates, and exceeds the speed of sound at x_{bh} . It later returns to subsonic velocities. Excitations in this fluid are sound waves (phonons). Once they have passed x_{bh} to the right, they can never return to $x < x_{bh}$ because they propagate with the speed of sound, c . In this sense, x_{bh} is an event horizon for phonons, which we call a sonic black hole horizon. In two dimensions, the situation is depicted in Fig. 5.1 (b). In more complicated 3D situations, the horizon is a surface on which the *normal* component of the flow exceeds the speed of sound. Phonons also cannot enter the region left of x_{wh} from the right, and we call x_{wh} the sonic white hole (WH) horizon. The analogous object in GR is less well known than the black hole, but has been studied theoretically and is speculated to exist around the singularity of an electrically charged (Reissner-Nordström) black hole [191].

Further, we can quantise the phonon excitations. Consider vacuum phonon

pair production near x_{bh} . It can occur that one partner of the pair is trapped in the supersonic region and swept downstream (in the direction of flow) and the other propagates against the flow to the left. This idea closely resembles the second, “popular” picture of the Hawking effect given above. A detailed derivation shows that the spectrum of phonons emitted upstream is thermal at the “analogue Hawking temperature” [16]. In a BEC experiment we expect to observe a thermal cloud of uncondensed atoms, precisely with the Hawking temperature of the established sonic horizon.

The possibility of an analogue Hawking effect was first noticed by W. Unruh [16]. Since then, much work has gone into refinement of the theory, determination of further systems exhibiting this analogy and discovery of spacetimes that can be realised in them. A comprehensive review is Ref. [17]. Among these studies, we focus here on those that considered the analogue Hawking effect in a fluid, in particular a BEC. For the remainder of this section, we give an approximately chronological summary of the theoretical developments underpinning the present chapter in this thesis.

After the initial idea by W. Unruh, the details of analogue gravity in fluid systems were first worked out by M. Visser [192]. The article, for example, introduced ergoregions in analogue systems. Ergoregions arise in GR around rotating black holes. A phonon in the ergoregion cannot remain motionless with respect to an observer at infinity, it could however escape to infinity. In this sense spacetime is “dragged around” with the rotating hole. The ergoregion boundary of a fluid is the surface on which the velocity-modulus exceeds the speed of sound. Unless the flow is normal to this surface, the ergoregion is distinct from the sonic horizon defined above. Visser also extended Unruh’s result for the analogue Hawking temperature T_H to take into account spatially varying sound speeds. He found:

$$T_H = \frac{\hbar g_h}{2\pi k_B c}, \quad g_h = \frac{1}{2} |\mathbf{n} \cdot \nabla (c^2 - v^2)| \Big|_{S_H} = c^2 |\mathbf{n} \cdot \nabla M| \Big|_{S_H}, \quad (5.4)$$

where the directional derivatives have to be evaluated at a point \mathbf{x} on the horizon S_H , c is the speed of sound and M the Mach number as usual.

Together with S. Liberati and S. Sonego, Visser then considered fluid dynamical requirements for horizons to occur [193]. They pointed out that transsonic flows require special conditions to be satisfied for a regular flow at the horizon. We discuss these in section 5.3.1.

The first to explicitly take a BEC perspective were Garay *et al.* [194, 195]. They analysed the stability of sonic black holes or BH-WH pairs in concrete

systems, using the Bogoliubov equations; see section 2.3.3. A BH-WH configuration in a 1D ring trap and a double BH in an atom laser-like system are considered. In both systems the spectral analysis shows dynamical instabilities, but in certain regimes these are weak enough to allow the adiabatic creation of quasi-stable transsonic flows. Due to their relevance for our work, the extensions and clarifications of this study in Refs. [196, 197] are discussed in some detail in section 5.3.2.

Following the work by Garay *et al.*, C. Barceló, Liberati and Visser also considered BEC in detail [65], extending their analysis of Ref. [193]. They in particular showed how corrections to the analogue metric arise if the full Bogoliubov equations are employed, as we hinted in section 2.3.4. They provided a simple estimate for the analogue Hawking temperature in a BEC to be of the order of $T_H \sim 1$ nK.

In their next article on the topic, the same team studied a double de-Laval nozzle for a BEC [198]. Such a construction is used in supersonic wind tunnels in aerodynamics. They pointed out that the sonic horizon must be established at the throat of the first nozzle, and derived the analogue Hawking temperature for a situation where either the cross section of the nozzle *or* the external potential are varying. We will extend this result in section 5.3.1 to cases where both vary. In Ref. [198], T_H was estimated to lie around 7 nK. However the authors suggested its improvement to 70 nK using Feshbach resonances, which can increase the speed of sound. We argue in section 5.3.4 that Feshbach resonances are unlikely to help in practice. We also propose a way to realise a double de-Laval nozzle for a BEC and point out difficulties with the dynamic creation of a transsonic flow in such a setup in section 5.4.

Ref. [199] by Barceló *et al.* presents a “zoo” of possible analogue spacetimes containing black holes, white holes or both and discusses their causal structure. Ref. [50] covers mostly another analogue gravity effect, cosmological particle creation, but we mention the article due to its detailed derivation of the analogue Klein-Gordon equation. Recently, the same team found that a sonic horizon theoretically does not have to be formed at finite time, but can be rapidly asymptotically approached, but never quite realised [200, 201]. It is unclear whether such a feat is any easier to accomplish experimentally than establishing a stable horizon at finite time.

Important foundations for our work are also due to U. Leonhardt *et al.* They developed a Bogoliubov theory of unstable excitations and first pointed out the generic instability of sonic white holes [197]. They then considered the analogue

Hawking effect using the full Bogoliubov theory [202]. Importantly, the hydrodynamic approximation “predicts its own demise”: As an outgoing phononic mode is traced back through time towards the horizon, its wavenumber increases (blue shifts) and mathematically diverges as the horizon is approached. According to our discussion in section 2.3.2, such a BEC excitation necessarily enters the particle like part of the Bogoliubov spectrum and is no longer a phonon. The apparent involvement of arbitrarily short wavelengths in hydrodynamic theory is in perfect analogy with the astrophysical problem. However, in the BEC the physics that takes over at short wavelengths, i.e. Bogoliubov theory, is well understood. Leonhardt *et al.* showed that the analogue Hawking effect persists even if the full Bogoliubov spectrum is taken into account, further corroborating the independence of Hawking’s effect from modified dispersion at short wavelengths [189, 190]. From this viewpoint the sonic horizon only exists for certain modes and is slightly delocalised.

S. Giovanazzi *et al.* proposed a simple way to realise a black hole horizon without a white hole, in a BEC [203]. The basic idea is to let a condensate flow out of a reservoir under the influence of an optically generated piston. It all takes place under tight transverse confinement. We will study this proposal in more detail throughout section 5.6.1.

5.3 Experimentally Utilisable Sonic Horizons

We have already given the basic definitions of black and white hole sonic horizons. Now we take a look at how horizons can be engineered in a BEC and what the underlying hydrodynamical equations of the condensate can tell us about horizon properties. First we will develop the hydrodynamic description of condensates from section 2.2.1 a little further, then we discuss horizon stability and later the rapidity with which the flow can be allowed to vary. Finally we derive bounds on the achievable analogue Hawking temperatures and mention the signatures by which the effect could be detected.

Most of the detail is gathered from throughout the literature. Exceptions are the equation for the analogue Hawking temperature for varying cross-section and potential (5.11), and most importantly, the limits on the temperature due to three-body losses, which constitute the main result of this section.

5.3.1 Sonic Horizons

As we have discussed in section 2.2.1, a BEC in the hydrodynamic regime obeys the continuity (2.12) and Bernoulli's equation (2.13) without the quantum pressure term p_q (hereafter, we will refer to this approximation just as “the hydrodynamic equations”). These equations describe any viscosity-free, irrotational fluid. Recall that neglecting p_q requires the condensate not to vary on length scales shorter than the healing length $\xi = 1/\sqrt{8\pi n a_s} = \hbar/(\sqrt{2}mc)$. The hydrodynamic regime for the BEC *and its excitations* is also required for the exact analogy to hold (section 2.3.4). Nonetheless we know that in general the condensate has to be described by the hydrodynamic equations plus the quantum-pressure term or equivalently using the full GPE (2.10). As we aim for realism, we generally solve the GPE, but the hydrodynamic equations provide useful guidance. We report to what extent predictions of the hydrodynamic theory have been fulfilled by numerical solutions of the GPE.

Often the physical situation allows us to describe the fluid flow effectively in one dimension x . We consider stationary or quasi stationary situations. For our purposes, we define the latter as a flow which allows us to neglect $\partial n/\partial t$ and $\partial v/\partial t$ in the hydrodynamic equations. These assumptions allow us to obtain a simple set of hydrodynamic equations⁹:

$$J = n(x)v(x)A(x), \quad (5.5)$$

$$\mu = \frac{1}{2}mv^2(x) + Un(x) + V(x). \quad (5.6)$$

Here μ is the chemical potential, J the particle current and v the flow speed. As previously, the local speed of sound is $c = \sqrt{Un/m}$ and the Mach number $M = v/c$. We have two situations in mind: (i) BEC flowing in a narrow, tube-like confining potential with longitudinal coordinate x and effective cross-section $A(x)$. Such a potential could be created by a red-detuned (attractive) laser beam as employed to form optical lattices. These beams can produce tight confinement in the transverse directions. Another example for point (i) is the optical tunnel proposed in chapter 4. (ii) Spherically symmetric, radial flow in d dimensions ($d = 2, 3$), where x is the radial coordinate¹⁰ and $A(x) = 2(d - 1)\pi x^{(d-1)}$. For example imagine a BEC in a flat, pancake shaped trap ($d = 2$), which is coupled out of the trap at the centre and hence flows radially inwards.

⁹To transform the continuity equation one uses Gauss's law, assuming constant v and n along other dimensions than x .

¹⁰We use x instead of r here, to unify notation with situation (i).

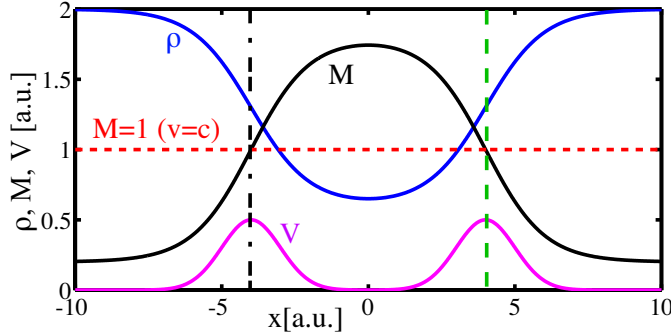


Figure 5.3: Physical reason for transonic flow. Sketch of Mach number (black), density (blue) and external potential (V) of a BEC flowing to the right. Other features as in Fig. 5.2.

One can derive a particularly instructive equation for the spatial acceleration $a = vv'$ of the flow (f' denotes $\partial f/\partial x$ here and in the following). Differentiating Eqs. (5.5) and (5.6) with respect to x , eliminating n' between the two and replacing $v' \rightarrow a/v$ we get

$$a = \frac{v^2}{v^2 - c^2} \left(c^2 \frac{A'}{A} - \frac{V'}{m} \right). \quad (5.7)$$

It can be seen that for finite acceleration at the location where the speed of sound is reached (x_h), we require

$$\left(c^2 \frac{A'}{A} - \frac{V'}{m} \right) \Big|_{x=x_h} = 0. \quad (5.8)$$

That is, $M = 1$ can only occur at the potential peak¹¹ if $A = \text{const.}$ or at the narrowest point of a constriction if $V = \text{const.}$ [193].

Eq. (5.7), the so-called “nozzle-equation”, also implies an important difference of condensate (fluid) behaviour between sub and supersonic flows. Fig. 5.3 sketches the Mach number profile required by Eq. (5.7). We assume that $A = \text{const.}$, the BEC is manipulated through an external potential V only. While subsonic, the BEC becomes faster as the potential rises ($V' > 0$). Once supersonic, it accelerates *further* as the potential again decreases ($V' < 0$). The flow only becomes subsonic again, if a second potential hump exists as shown in the sketch. The double hump setup depicted in Fig. 5.3 is analogous to the double constrictions used in supersonic wind tunnels for aircraft manufacturing (double de-Laval nozzle). The first constriction is there referred to as a “sonic throat” and

¹¹To exclude potential minima, we require the reasoning of the next paragraph.

the second one as a “diffuser”. In Eq. (5.7), a potential hump fulfills essentially the same role as a cross-sectional constriction.

In a transsonic viscous fluid, the divergence in a that would arise from violations of Eq. (5.8) is regulated by the viscosity, with interesting implications for the analogue Hawking temperature [193]. However, the viscosity in a BEC is zero, hence in the hydrodynamic and stationary regime (5.8) must hold. We find in our numerical simulations that the flow obeys the condition even if slowly varying in time or varying in space faster than allowed for a safe application of the hydrodynamic approximation. Eq. (5.8) thus is a useful tool to determine existence and location of sonic horizons in a BEC.

In most scenarios considered here, we make use of potential humps to create sonic horizons, as they seem easier to realise in a BEC than constrictions.

The hydrodynamic equations can be used to obtain the complete condensate flow if the potential $V(x)$ and cross section $A(x)$ are known. To this end we follow [203]. Combining Eqns. (5.5) and (5.6), we can write

$$q(x)M(x)^{2/3} - \frac{1}{2}M^2(x) = 1, \quad (5.9)$$

$$q(x) = \frac{\mu - V(x)}{ms(x)^2}, \quad s(x) = \left(\frac{JU}{A(x)m} \right)^{1/3}. \quad (5.10)$$

The function $q(x)$ now contains all information about the trapping configuration and $s(x)$ becomes the speed of sound at the horizon $s(x_h) = c(x_h)$, see Eq. (5.5). Solutions of the cubic equation (5.9) for M are usually unwieldy. However, a useful quantity that can be derived from Eq. (5.9) is the analogue Hawking temperature (5.4).

Differentiating Eq. (5.9) with respect to x , solving for $M'(x)$ and applying L'Hôpital's rule ,we obtain for a location at the horizon $x = x_h$:

$$\begin{aligned} T_H &= \frac{\hbar c}{2\pi k_B} |M'| = \frac{\hbar c}{2\pi k_B} \left| \frac{3Mq'}{3M^{4/3} - 2q} \right| \\ &= \frac{\hbar c}{2\pi k_B} \left| \frac{5q' \pm \sqrt{25q'^2 + 48M^{4/3}q''}}{8M^{1/3}} \right| = \frac{\hbar c}{2\pi k_B} \frac{\sqrt{3q''}}{2}. \end{aligned} \quad (5.11)$$

For the final step we have used $M(x_h) = 1$, $q(x_h) = 3/2$, see Eq. (5.9), and $q'(x_h) = 0$ [203]. The latter implies Eq. (5.8).

From Eq. (5.10) we get:

$$q'' = \frac{1}{s^2} \left(\frac{\mu - V}{m} (\log A)'' - \frac{V''}{m} - \frac{4}{3} (\log A)' \frac{V'}{m} \right). \quad (5.12)$$

While analytic expressions for the horizon temperature in the cases $V = \text{const.}$ or $A = \text{const.}$ have been obtained before [198], Eqs. (5.11) and (5.12) constitute to our knowledge the first expression valid where both vary.

While the equations here were derived assuming a stationary state, we can often approximately use them for condensates subject to time dependent manipulations. Most obviously, this is the case when the manipulations are sufficiently slow so that the BEC flow adiabatically follows its ground state. This allows one to devise schemes for the adiabatic creation of a transsonic flow from a subsonic one, see [194, 195].

5.3.2 Stability

We have now established how sonic horizons can be created in principle. The next question is under which circumstances they are dynamically stable.

The most comprehensive stability analysis of black and white holes was done by Garay *et al.* in Refs. [194–196]. As argued in these papers, a stability analysis must be based on the full Bogoliubov equations (2.31), as the hydrodynamic approximation is not valid for excitations as the horizon is approached. This can be seen by a Taylor expansion in ξq of the dispersion relation for excitations in a flowing homogeneous condensate [196]. In the rest frame of the condensate there is no flow, and we can simply rewrite the Bogoliubov dispersion relation (2.35) using $\omega' \equiv \epsilon_q/\hbar$:

$$\omega'^2 = c^2 q^2 \left(1 + \frac{\xi^2 q^2}{2} \right). \quad (5.13)$$

Transforming this expression to the laboratory frame yields a doppler shifted frequency $\omega = \omega' + vq$:

$$(\omega - vq)^2 = c^2 q^2 \left(1 + \frac{\xi^2 q^2}{2} \right). \quad (5.14)$$

Expanding in ξq we finally obtain:

$$\omega \simeq (v \pm c)q + \frac{1}{4}c \xi^2 q^3 + \mathcal{O}(\xi^4 q^5). \quad (5.15)$$

In the hydrodynamic approximation we neglect all terms but the first. However, we can see that the relative importance of the first and second terms, given by their ratio $\frac{c}{4(v \pm c)} \xi^2 q^2$, depends not only on ξq but also on $1/(v \pm c)$, which can become infinite at the horizon. Again, this is just another derivation of the appearance of short wavelength physics as waves are traced towards the horizon.

As we have seen that the excitation spectrum near the horizon is significantly influenced by physics beyond the hydrodynamic approximation, the stability of a given transsonic flow must be determined from the full Bogoliubov equations (2.31). For concrete examples, which capture the essence of a flow with a black hole, white hole, or both, see Ref. [196]. They found:

- Black hole - white hole pairs (such as in Fig. 5.3) are dynamically stable only if special boundary conditions, for example *particular* periodic boundary conditions, are imposed. By engineering a system such that these are met, stable BH-WH pairs can be created [194].
- Black holes by themselves are dynamically stable, *unless* specific boundary conditions are imposed.
- White holes by themselves are dynamically unstable, *unless* specific boundary conditions are imposed. Also for the BH-WH pair, the instability can be traced to the white hole component.

This summary neglects some details contained in Ref. [196], but suffices for the interpretation of our numerical simulations. All scenarios containing a white hole showed dynamical instabilities at the white hole, while all flows with only a black hole were stable. In effectively one-dimensional scenarios, the dynamical instability at the white hole takes the form of an emission of grey solitons. This fact can already be found in Ref. [195], but becomes more clearly visible in the numerical data we show. That the breakdown of superfluid flow beyond the critical velocity leads to the creation of soliton trains has also been found in studies of superfluid behaviour, e.g. [204, 205]. There, the obstacle potential used to make the flow supersonic was usually small, and no distinction between BH and WH was made. Generic instability of the white hole is further supported by the work of Leonhardt *et al.* [197].

To improve the chances of an observation of the analogue Hawking effect, we require a stable horizon temperature. As this depends on $M'|_{x=x_h}$, the slope of the Mach number at the horizon, instabilities near the black hole that would cause variations of this slope cannot be tolerated.

Previous studies also required a stable white hole [194, 195] or at least instabilities too weak to develop over relevant timescales. According to our stability summary, this demand would rule out most flows containing a white hole. In this thesis we nonetheless take a closer look at two particular scenarios with a white hole, explaining along the way why they might be relevant: In the first case a

BH-WH pair is realised *within* a single emitted grey soliton, which remains immobile for a long period (section 5.4.3). In the second case the soliton emission takes place in a region well separated from the black hole horizon and does not affect the horizon structure (section 5.5.3).

5.3.3 Rapidity of Flow Variation

Having established under which circumstances we expect a stable horizon, we now ask how rapidly (spatially) the flow can or should become supersonic. In the following, we will refer to $\partial M/\partial x$ as the “rapidity” of flow variation. Considering the 1D equivalent of Eq. (5.4) we see that a large rapidity results in a large analogue Hawking temperature. However that equation requires the conditions for the conventional derivation of the analogue Hawking effect to be fulfilled, most notably the validity of the hydrodynamic approximation for the background BEC at the horizon. Thus a too rapid variation in the flow is forbidden.

We will now give a brief overview of what appears to be the state of the literature regarding the requirements for the analogue Hawking effect.

Let us first consider conditions *local* to the horizon. In writing the analogue metric (2.42) we neglected the derivative operator (see section 2.3.4):

$$D_2 \hat{n}_1(\mathbf{x}) = -\frac{1}{2} \frac{\nabla^2 \sqrt{n(\mathbf{x})}}{\sqrt{n(\mathbf{x})}^3} \hat{n}_1(\mathbf{x}) + \frac{1}{2} \frac{1}{\sqrt{n(\mathbf{x})}} \nabla^2 \left(\frac{\hat{n}_1(\mathbf{x})}{\sqrt{n(\mathbf{x})}} \right). \quad (5.16)$$

Neglecting the first term requires the quantum pressure to be small, and is justified if the hydrodynamic approximation for the *background condensate* holds at the horizon. Neglecting the second term requires the excitation modes to have phononic wavenumbers at the horizon. As shown in section 5.3.2 this is impossible. Nonetheless, the analogue Hawking effect has been shown to persist [202]. Hence, this element of the approximation appears to be unnecessary. Finally, for most derivations of the effect, one uses the eikonal approximation to treat wave propagation near the horizon [65, 206]. This is a high momentum approximation, and due to the blue shift *improves* as the mode approaches the horizon.

Extending the view to aspects of the global flow, derivations also usually assume that the eikonal approximation continues to hold out to future infinity. This allows the concrete prediction of the spectrum of particles observed far from the (real or sonic) black hole in the asymptotically flat region. However as the Hawking phonons originate from the horizon, the validity of this assumption can no longer affect their principal presence. Hence violating it would merely distort

the spectrum¹².

Let us now consider what happens if the background BEC flow strongly varies spatially at the horizon, such that the hydrodynamic approximation is not strictly justified. There are several consequences: (i) We can no longer rely on Eq. (5.9) to determine the location of the horizon. This is not a crucial point; let us assume that a horizon is established somewhere. (ii) It is not justified to neglect the first term of Eq. (5.16). It has been shown in Ref. [65], that this introduces a position dependent correction to the speed of sound. We would however still expect to be able to create an effective space time with a horizon. (iii) Modes for which we can use the eikonal approximation at the horizon have small wavelength and cease being phonons. It is thus not justified to neglect the second term of Eq. (5.16). Ref. [65] suggests how corrections to the metric could be included in such a case. These would however depend on the wavelength. It is not entirely clear, at least to this author, how the apparent problem, point (iii), co-exists with the persistence of the Hawking effect in Ref. [202].

It seems not safe to conclude that quantum particle creation for a rapidly varying flow does not exist. However, what is sure, is that the theoretical situation becomes more complicated and our confidence in the existence of an effect is lowered. Our reasons for questioning whether the approximations employed in existing derivations of radiation by sonic horizons are physically required or mathematically convenient, will become clear in the next section. As the pursuit of a conclusive answer to this question is outside of the main line of this thesis, we react to the lack of clarity by proposing realistic experimental systems for either case: With Mach number variation within the constraints of the hydrodynamic approximation and beyond.

5.3.4 Limits on the Analogue Hawking Temperature

We now show that for a horizon in the hydrodynamic regime the achievable analogue Hawking temperature is considerably limited by three-body loss processes in the condensate. For the flow to remain in the hydrodynamic regime, we demand

$$\left| \frac{\partial M}{\partial x} \right| \Bigg|_{x=x_h} \lesssim \frac{1}{D\xi}, \quad (5.17)$$

¹²We found indications that the eikonal approximation would in fact be violated for an important special case in the BEC: A sonic horizon created by a Gaussian hump potential. Following this issue further did however not lie within the direction of research of this thesis.

for $D \gg 1$. Linearising around the horizon, we thus allow M to vary by a fraction $1/D$ within one healing length ξ . Inserting Eq. (5.17) and the expression for ξ (section 2.2.1), into Eq. (5.4) we obtain

$$T_H \lesssim \frac{mc^2}{\sqrt{2}\pi k_B D} = \frac{Un}{\sqrt{2}\pi k_B D}. \quad (5.18)$$

All quantities have to be evaluated at the horizon. We immediately see that once the rapidity (i.e. D) is fixed, the only other continuously tunable parameter remains the condensate density. High analogue Hawking temperatures thus require dense condensates. However, as noted in sections 1.2.2 and 2.1.1 and demonstrated in chapter 3, losses from inelastic atomic collisions become increasingly important at high densities.

To determine a quantitative limit imposed on the analogue Hawking temperature, we investigate the effect of the loss in some more detail. We consider a flow that is harmonically confined with frequency ω_\perp in the transverse direction r , and in either of two regimes: We call the condensate quasi-one dimensional (Q1D) when $\mu \ll \hbar\omega_\perp$. In this case transverse excitations are “frozen”, and we can factor the BEC wave function into a longitudinal and transverse part $\phi(\mathbf{x}) = \phi_{1D}(x)\psi_\perp(r)$, where the transverse part $\psi_\perp(r)$ remains in the oscillator ground state [207]. The velocity in this case is exclusively in the longitudinal x direction. Our second regime is $\mu \gg \hbar\omega_\perp$, we label it “transverse Thomas-Fermi” (TTF). Under these condition we can consider the flow in the Thomas-Fermi approximation [34] and the velocity can in general have a transverse component. To get a handle on the effect of loss in either case, we assume the density profiles

$$n_{\text{q1d}}(x, r, t) = n_0(x, t) \exp\left(-\frac{r^2}{\sigma_r^2}\right) \quad (5.19)$$

in the Q1D and

$$n_{\text{ttf}}(x, r, t) = n_0(x, t) - \frac{1}{2} \frac{m\omega_r^2 r^2}{U} \quad (5.20)$$

in the TTF regime. $n_0(x, t)$ is the time dependent peak density in either case. We consider $n_{\text{ttf}}(x, r, t)$ only where the given expression is positive.

Now we take the part of the GPE (2.27) concerned with losses only¹³. If we assume that the transverse structure of the condensate is always well described by either of the profiles defined above, we can integrate out the transverse coordinates. In this case, the effective loss-equation for the peak density that we

¹³We neglect kinetic, potential and interaction terms.

obtain reads:

$$\frac{\partial n_0(x, t)}{\partial t} = -\frac{1}{\alpha_1} K_1 n_0(x, t) - \frac{1}{\alpha_2} K_2 n_0(x, t)^2 - \frac{1}{\alpha_3} K_3 n_0(x, t)^3, \quad (5.21)$$

with loss constants K_i as before, and effective loss parameters $(\alpha_1, \alpha_2, \alpha_3) = (1, 2, 3)$ in the Q1D and $(\alpha_1, \alpha_2, \alpha_3) = (2, 3, 4)$ in the TTF regimes.

In the situations of interest here, three-body losses are always dominant, hence we consider only those in what follows. For short times or weak loss, we can approximate Eq. (5.21) by a finite difference equation. We now demand that losses shall not reduce the peak density by more than a fraction f of the initial value within a time interval Δt . This corresponds to

$$\frac{K_3}{\alpha_3} n_0^3 \Delta t \lesssim f n_0. \quad (5.22)$$

We hence define the maximal allowed peak density under these conditions:

$$n_{\max} = \sqrt{\frac{\alpha_3 f}{K_3 \Delta t}}. \quad (5.23)$$

Finally we substitute this for the density into Eq. (5.18) and obtain:

$$T_H \lesssim \frac{U}{\sqrt{2\pi k_B D}} \sqrt{\frac{\alpha_3 f}{K_3 \Delta t}}. \quad (5.24)$$

It is apparent from Eq. (5.24) that for given criteria ($D, f, \Delta t$), the temperature is strongly dependent on atomic parameters (U and K_3).

Comparison of BEC-Atom Species

In the light of the results above, we now compare atomic species commonly employed in BEC experiments: ${}^4\text{He}$, ${}^{23}\text{Na}$, ${}^{87}\text{Rb}$ and ${}^{137}\text{Cs}$. The relevant parameters for these atoms are listed in table 5.1.

The scattering length a_s , and hence the interaction U , can be tuned towards higher, more favourable values with the use of Feshbach resonances. However in the large a_s regime the three-body loss rate increases as a_s^4 [211]. According to Eq. (5.24) this rules out an improvement of T_H using Feshbach resonances.

Let us now calculate concrete numbers from Eq. (5.24). A value of $D = 20$ just about places the sonic horizon in the hydrodynamic regime¹⁴. Further, Eq. (5.24)

¹⁴Note that to use the eikonal approximation around the horizon, the background should vary little within one wavelength $\lambda = 2\pi/q$, where q is the wavenumber. To be a phonon, the wavenumber must fulfill $\xi q \ll 1$. For the shortest wavelength phonons $1/q \sim \xi$. Hence we require small Mach number variations within $\lambda \sim 2\pi\xi$, rendering $D = 20$ a rather bold choice.

| atom | a_s [nm] | m/m_p | $K_2 \times 10^{20}$ [m^3/s] | $K_3 \times 10^{42}$ [m^6/s] |
|-------------------|------------|---------|----------------------------------|----------------------------------|
| ^4He | 7.5 | 4 | 2, Ref. [208] | 9000, Ref. [208] |
| ^{23}Na | 2.8 | 23 | 0.053, Ref. [209] | 2.12, Ref. [209] |
| ^{87}Rb | 5.5 | 86.3 | 150, Ref. [210] | 32, Ref. [173] |
| ^{137}Cs | 11.1 | 133 | small | 130, Ref. [211] |

Table 5.1: Parameters for atomic species. The values for cesium assume a magnetic field of 23 G, where the ratio of scattering length to three-body loss is most favourable [211].

is fairly weakly dependent on the parameters whose suitable values we can only estimate: f and Δt . Let us allow the loss of 10% of the peak density ($f = 0.1$) within a time $\Delta t = 50$ ms. The achievable analogue Hawking temperatures using these criteria are listed in table 5.2.

| atom | $n_{max}/(10^{19}/m^3)$ | $\xi[\mu\text{m}]$ | T_H [nK] | T_H/T_{crit} |
|-------------------|-------------------------|--------------------|------------|-----------------------|
| ^4He | 3.0 | 0.42 | 3.8 | 0.10% |
| ^{23}Na | 194 | 0.086 | 16 | 0.15% |
| ^{87}Rb | 50 | 0.12 | 2.2 | 0.19% |
| ^{137}Cs | 25 | 0.12 | 1.4 | 0.30% |

Table 5.2: Achievable Hawking temperatures according to Eq. (5.24), calculated using $\alpha_3 = 4$, $\Delta t = 0.05$ s, $f = 0.1$ and $D = 20$. Also shown are the condensate densities and associated healing lengths allowed by criterion (5.23). The temperatures are also given in relation to the critical temperature (1.1) (section 1.2).

We see that the values vary strongly between the atomic species, with sodium exhibiting the highest temperature. We also give T_H in relation to the condensation temperature¹⁵.

The temperatures are mostly smaller than the early optimistic estimate of 70 nK [198] but compare well with the 15 nK given for sodium in [203]. The values are low in spite of the rather radically optimistic parameters Δt , D and f that we have used. To be on the safe side, they all would need to be adjusted in the direction of decreasing temperature.

¹⁵Expression (1.1) shall suffice. In fact it is modified by interactions and confinement, but these modifications are small.

These low limits motivate the question posed in section 5.3.3: Is the hydrodynamic approximation a necessity for any kind of quasi-particle creation by the horizon, or is it merely an analytical convenience? It is very likely that without the hydrodynamic approximation the spectrum is no longer thermal. Thus it is an entirely open question whether leaving the hydrodynamic regime would facilitate the detection of horizon radiation, even *if* the effect exists then. But since the low temperatures of table 5.2 will make a detection within the hydrodynamic regime extremely challenging, the possibility should not be entirely neglected.

Another direction that seems worth considering is a possible suppression of inelastic collisions [212].

5.3.5 Signature of the Analogue Hawking Effect

In this section we point out that further theoretical work determining the detailed experimental signature of the analogue Hawking effect in a BEC is called for. Possible complications arise as the created phonons are indistinguishable from thermal excitations of the BEC.

It is sometimes assumed that the analogue Hawking effect will be detected in the form of a thermal cloud with temperature T_H . For such a feature not to be covered by existing thermal fluctuations, T_H must be larger than the condensate temperature. We further require thermalisation, which takes a certain time. Our results of the preceding section indicate that in particular the combination of the two, high temperatures over a long time, might be problematic.

A complementary detection option is the recently suggested spectroscopic measurement of phonons [213]. This is however experimentally not yet established, in contrast to well known techniques to determine the thermal cloud shape by time of flight methods and absorption imaging [34]. Nonetheless, we see advantages in such a scheme, as it would allow fast phonon detection, which reduces the importance of atom-losses.

Given the anticipated small Hawking effect within a large background of thermal phonons and depletion, an experimental setup in which minor changes can switch the condensate flow between sub and transsonic could be advantageous. The difference between the observed uncondensed spectra in these two cases will provide a cleaner signal.

We finally mention that for the observation of an actual thermal spectrum, an asymptotically flat region is required, with vanishing condensate velocity. This corresponds to the flat Minkowski spacetime, far away from the black hole in

astrophysics.

5.3.6 Outlook

Let us briefly summarise some important facts regarding sonic horizons in BECs. To create a globally dynamically stable flow, one should avoid a white hole. The flow at the black hole horizon must be in the hydrodynamic regime to justify the application of conventional derivations of the analogue Hawking effect. Under these conditions the Hawking temperature is strictly limited by the maximal achievable density. This in turn is limited by three-body loss processes, more strongly so for heavier atoms.

Due to several questions that arose in this section, seeking an answer to which lies not within the scope of this thesis, we in the following present multiple experimentally realisable setups for the creation of sonic horizons: We begin with the use of the optical tunnels of chapter 4. In them sonic horizons beyond the hydrodynamic regime can be established. As outlined above, in such a case traditional theory does not apply. Next we consider atom laser systems, where we find BH-WH pairs with the expected dynamical instabilities. Under some special circumstances these might be tolerable. If so, this system allows the simple switching between subsonic and transsonic flow mentioned above. Finally we consider outflow from a reservoir. This is the most flexible approach. We numerically show that for realistic parameters a stable transsonic flow can be achieved. It realises the maximal analogue Hawking temperature derived here.

5.4 Supersonic Optical Tunnel

To begin our presentation of systems for the creation of sonic horizons, we now return our attention to the one that was proposed at the end of chapter 4: high-charge ring flows through an optical tunnel. It was the ultimate result of section 4.3 that stationary high-charge ring flows exist in a condensate within a combination of a harmonic trap and the repulsive potential of an optical vortex. The condensate flows through the core of the optical vortex just as through an optical tunnel and was shown to reach velocities of up to 0.7 of the local speed of sound there. We also reported that stationary states with $M > 1$ do not exist due to the energetic instability of supersonic flows. However as outlined in section 5.3.2, dynamically stable supersonic flows may exist.

5.4.1 Flow Acceleration

We evolve the stationary state for case (ii) in table 5.3, obtained with the imaginary time method in section 4.3.3, using the real time Gross Pitaevskii equation in cylindrical coordinates (see section 2.10 and section 4.3.2). The parameters and formulation of the equations are essentially the same as in the previous chapter. A dynamical increase of the flow velocity through the optical tunnel could be achieved by slowly decreasing the laser focal width w_0 , reducing the length of the tunnel. The explanation given in section 4.3.3 for the imaginary time evolution holds also for adiabatic real time manipulations. While we found this method to have the desired effect, the variation of the potential affects the whole condensate cloud. In order to reduce perturbations of the bulk BEC, manipulation had to be very slow, requiring uncomfortably long computer run times.

The flow velocity in the optical tunnel can also be increased by suddenly or slowly ramping up a localised additional hump potential in the tunnel flow of the BEC. Recall that the potential of the optical vortex shaping the tunnel is given by Eq. (4.25) (section 4.3.2):

$$V_v(r, z) = V_0 r^{2l} w(z)^{-2(l+1)} w_0^2 \exp\left(-\frac{r^2}{w(z)^2}\right), \quad (5.25)$$

$$w(z)^2 = w_0^2 + \frac{(z - z_{f0})^2}{k_0^2 w_0^2}, \quad (5.26)$$

with parameters: beam waist w_0 , laser wave number k_0 , focus z -coordinate z_{f0} and optical vortex charge l .

The additional hump potentials can also be created by laser beams, but without optical vortex charge:

$$V_{h,i}(r, z) = V_i w_i(z)^{-2} w_{i,0}^2 \exp\left(-\frac{r^2}{w_i(z)^2}\right), \quad (5.27)$$

$$w_i(z)^2 = w_{i,0}^2 + \frac{(z - z_{f,i})^2}{k_i^2 w_{i,0}^2}. \quad (5.28)$$

The “hump” potentials (5.27) describe laser beams shone down the z -axis of our system and focussed onto the point $r = 0$, $z = z_{f,i}$. We use the subscript i to distinguish several of these laser beams. These potentials are similar to Eq. (5.25) with $l = 0$. Again, the $w_{i,0}$ describe the waist of the laser beams at their foci, k_i are the wave numbers of the light and $z_{f,i}$ control the position of the beam foci. For the results presented here we used $k_i = k_0 = 1.4 \times 10^7 \text{ m}^{-1}$ and $z_{f,i} = z_{f0} = 0$, except where otherwise stated.

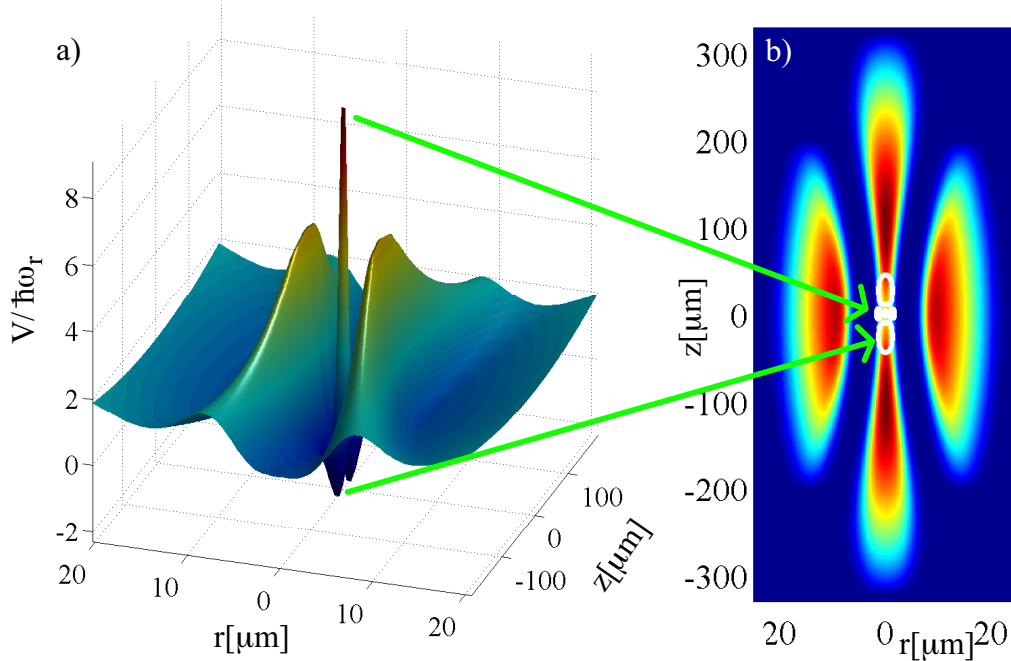


Figure 5.4: Placement of additional hump potentials in the optical tunnel system. (a) Surface plot of $\frac{1}{10} [V_v(r, z) + V_t(r, z)] + V_{h,1}(r, z) + V_{h,2}(r, z)$, i.e. the trap and vortex potentials are scaled down to make the hump potential more visible. Parameters are as for scenario B in table 5.3. Due to the combination of an attractive and a repulsive obstacle potential, the hump potential for scenario B has a maximum and two minima. (b) Color map of condensate density in the ground state, as in Fig. 4.18. White: iso-contours of $V_{h,1}(r, z) + V_{h,2}(r, z)$ for $V = 6\hbar\omega_r$ and $V = -\hbar\omega_r$. The green arrows point to the approximate location of maximum and minimum of the hump potential.

Fig. 5.4 shows how exemplary hump potentials are situated in the global trapping and flow structure.

The tunnel flow responded to additions of such potentials with acceleration, similar to the case of changing the whole optical vortex, but with tractable numerics. The small disruption by a sudden ramp-up of the additional potential is due to the small overall volume that is affected by the potential change, see Fig. 5.4 (b).

Whether slow (adiabatic) or sudden, all investigated ramps had in common that, once the BEC flow exceeds the speed of sound, our simulations showed the emission of single or multiple grey solitons. The frequency of the soliton emission

| | $\frac{V_0}{\hbar\omega_r}$ [J] | w_0 [\mu m] | q | $\frac{V_{h1}}{\hbar\omega_r}$ [J] | $\frac{V_{h2}}{\hbar\omega_r}$ [J] | w_1 [\mu m] | w_2 [\mu m] |
|------------|---------------------------------|---------------|-----|------------------------------------|------------------------------------|---------------|---------------|
| case (i) | 48 | 3 | 7 | | | | |
| case (ii) | 99 | 2.8 | 9 | | | | |
| scenario A | 99 | 2.8 | 9 | 7.7 | 0 | 2 | |
| scenario B | 99 | 2.8 | 9 | -8.5 | 18.8 | 1.2 | 0.7 |
| scenario C | 99 | 2.8 | 9 | -8.5 | 12.5 | 1.2 | 0.7 |

Table 5.3: Overview of potential parameters used for real time manipulation, see Eqns. (5.25)-(5.28). In all cases $k_i = k_0 = 1.4 \times 10^7/m$ and $l = 2$.

depends on the strength, width and position of the hump. This behaviour qualitatively agrees with previous studies in one dimension [204, 214]. In the following we report on a couple of interesting examples, the potential parameters used to achieve the acceleration in each case are summarised in table 5.3.

According to our discussion in section 5.3.1, a hump potential with a single peak does not allow a (quasi) stationary transsonic flow which is subsonic at both ends. Such a flow requires the realisation of a double de-Laval nozzle: we would need either two constrictions or two humps. We numerically examined a variety of *dynamical* sequences, inserting double de-Laval nozzles into the existing ring flow. The result always was the same: The speed of sound is breached initially at the downstream hump (the farthest in the direction of BEC flow), consequently not achieving the desired effect. The results presented in the following are thus just for a single peak potential.

5.4.2 Dynamical Instability

Train creation, scenario A

An example of a scenario resulting in a train of grey solitons is presented in Fig. 5.5. In this simulation we linearly ramp up a hump laser beam, centred at $z_{f,1} = -20\mu\text{m}$ over a time of 1s, with parameters as given in table 5.3. The obstacle accelerates the BEC flow, shown in Fig. 5.5 (b).

It can be seen that the z coordinate at which the flow first becomes supersonic does not coincide with the maximum of our hump potential $V_{h,1}$, as we might expect considering the potential at $r = 0$ alone. The reason is the interplay between the varying width of the narrow channel in the core of the optical vortex with the variations in the combined trapping and hump potential on the z axis:

It follows from the regularity condition at the horizon, Eq. (5.8), that A' and V' need to have the same sign there. Due to the symmetry of the optical vortex potential under $z \rightarrow -z$, we have $A' < 0$ for $z < 0$ and $A' > 0$ for $z > 0$. The sign of the potential slope V' at $r = 0$ can be found from Fig. 5.5 (d). Taking into account that at point X in Fig. 5.5 (d) the flow is not yet sufficiently accelerated, it can only become supersonic near point Y, where the sign condition can again be fulfilled. This is indeed what is found in the dynamics.

Once the local speed of sound is reached, localised density dips develop and propagate downstream (towards positive z , in the direction of BEC flow). We observe that the flow through the narrow optical tunnel remains quasi-one dimensional at all times, i.e. the flow velocity there depends only on z . When the first soliton reaches the outer region of the trap, it decays. The decay excites oscillations of the whole cloud. In Fig. 5.5 (c) we compare the solitons emitted in our simulations with the analytical expression for grey solitons [215, 216] given by $n_{sol} = n_{bg}(z) |u(z, z_0)|^2$, where

$$u(z, z_0) = B \tanh[B(z - z_0)/\xi] + iD, \quad (5.29)$$

with D and B related by $D^2 + B^2 = 1$. The wavefunction n_{sol} represents a dip to a fraction D^2 of the inhomogeneous background density n_{bg} at $z = z_0$. B describes the soliton's width. The background healing length ξ is evaluated at the location of the soliton (z_0): $\xi = 1/\sqrt{4\pi n_{bg}(z_0)a_s}$. After adjusting n_{bg} , z_0 and D , the width of the soliton is fixed, and the excellent agreement shown in Fig. 5.5 (c) thus demonstrates the applicability of 1D theory.

Transverse effects of soliton propagation, scenario B

Despite the success of one-dimensional soliton theory in describing the grey solitons in our optical tunnel, the core of the optical tunnel is merely a part of our three-dimensional atom-light skyrmion. We will hence take a quick look at the BECs behaviour in the dimensions transverse to the tunnel axis. Fig. 5.6 shows density color maps in the rz plane and locations of ring singularities at the initial time $t = 0$ and at 0.555 s after adding a hump potential. In scenario B, two grey solitons are emitted. Following the evolution in the rz plane, we find that the solitons propagate without connection to the initial ring singularities. Those singularities slowly shift their position in time, to reflect changes of the overall flow structure along the z -axis. However we also see the temporary creation of additional ring vortex-antivortex pairs, not present in the initial flow. These always

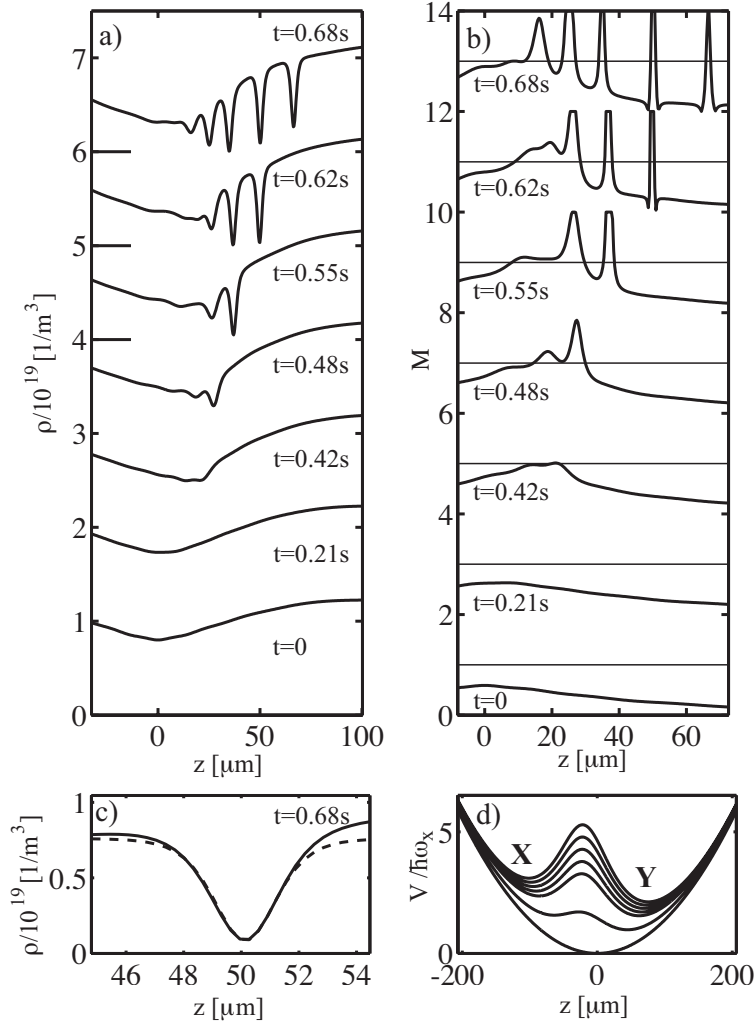


Figure 5.5: Generation of a grey soliton train. The initial state is that of case (ii) in table 5.3. A potential hump centred at $z = -20 \mu\text{m}$ is ramped up over 1 s. (a) Time evolution of condensate density along the z -axis. The graphs for subsequent time samples are shifted upwards by 1 unit. The zero of density is indicated with an elongated tick mark for the last three samples. (b) Evolution of the Mach number. Successive samples are shifted by 2. Thin horizontal lines indicate $M = 1$ for each time sample. The peaks are cut off at $M = 2$; their amplitude is as high as 600 for almost dark solitons. (c) Fit of the functional shape described in the text (dashed grey) onto a soliton in the train (solid black). The fit parameters are $n_{\text{bg}} = 7.6 \times 10^{18}/\text{m}^3$ and $D = 0.33$. (d) Monotonically increasing hump potential for the same time samples as in panel (a). The symbols X and Y indicate locations in the flow relevant to the discussion in this section.

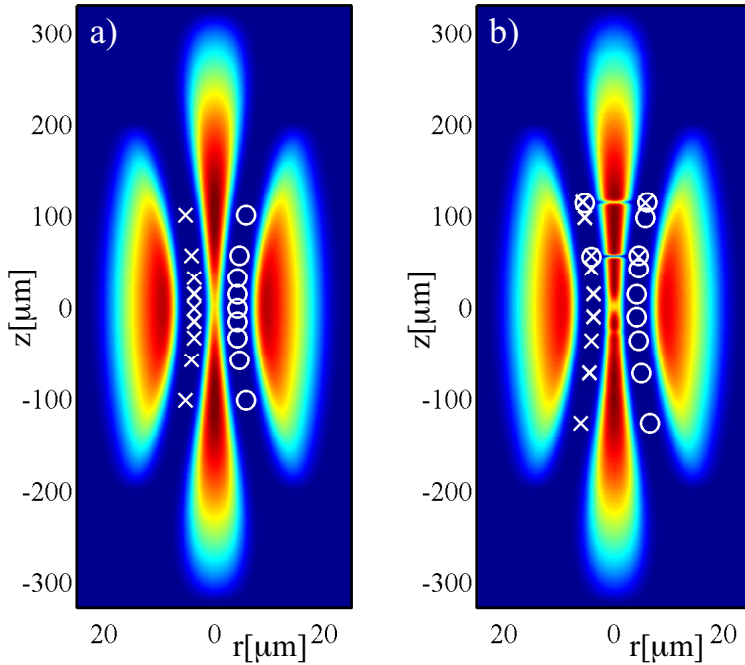


Figure 5.6: BEC density in the r - z plane (red highest, blue lowest). The intersection of ring singularities with the r - z plane is marked by \times (\circ) for mathematically positive (negative) circulation. (a) Initial state for case (ii) in table 5.3. (b) Situation 0.555 s after the sudden addition of the obstacle potential for scenario B in table 5.3. The density dips belonging to the two emitted grey solitons are visible in the core. For this snapshot, each is surrounded by a ring vortex-antivortex pair. While the 9 ring singularities of the initial state have slightly shifted position to reflect changes in the overall flow structure, they are not found to be connected to soliton movement.

appear at the same z -coordinate as the solitons and co-propagate with them for short times. After that they are annihilated again. Radially, the singularity pairs appear within the low BEC density region where the optical vortex potential is strong. The whole evolution for this case, including creation and destruction of singularities, is shown in the movie `soliton_ring_hybrids?-gpe.mov` on the CD.

Following the ring pair creation up lay outside the scope of this thesis. Previous work on the 3D structure of BEC excitations in tight, quasi-one dimensional confinement, however, suggests that our solitons evolve into soliton vortex-ring hybrids [217]. These have already been observed experimentally [144]. The optical tunnel would present a clean system for their study.

5.4.3 Single Soliton Horizons

Scenario C

We created a soliton that was immobile in the lab-frame for a long time by the sudden addition of an obstacle potential shaped as in Fig. 5.7 (d), with parameters listed under scenario C in table 5.3. Once the flow exceeds the speed of sound, a single grey soliton is emitted and for time spans as long as 0.58 s it remains located near $z = 0$, see Fig. 5.7. Only after that time does the grey soliton begin to accelerate.

Again, we observe that at all times the flow speed in the tunnel is a function of z only, i.e. it remains quasi-one dimensional. Extending our previous considerations, the behaviour of the soliton after its creation can be well understood with the aid of the 1D Lagrangian approach [215, 216]. We apply the time dependent Ansatz $\phi(z, t) = \sqrt{n_{\text{bg}}(z)} e^{-i\mu t/\hbar} u(z, t)$, where μ is the chemical potential, $u(z, t)$ the soliton wavefunction and $n_{\text{bg}}(z)$ denotes the background condensate density. We work in a frame of reference that moves with the speed of the background flow (v_{bg}) at the soliton centre (z_0). This speed is allowed to vary slowly in time. The ansatz for $u(z, t)$ is $u(z, t) = B(t) \tanh[B(t)(z - z_0(t))/\xi(t)] + iD(t)$ as before, but $D(t)$ and $B(t)$ are now time dependent. $\xi(t)$ denotes the healing length at $z_0(t)$. The leading order result for the soliton equation of motion, following [215, 216], is:

$$\frac{\partial^2 z_0}{\partial t^2} = \frac{U}{4m} \left(1 + \frac{U}{\mu} n_{\text{bg}} \right) \frac{\partial n_{\text{bg}}}{\partial z} \Big|_{z=z_0} + \frac{\partial v_{\text{bg}}}{\partial t}. \quad (5.30)$$

We find that this equation describes the trajectories of solitons in our simulations well, within uncertainties arising from the numerical extraction of n_{bg} and v_{bg} . In particular, Eq. (5.30) explains the immobility of the soliton shown in Fig. 5.7 (a-b). In the vicinity of the soliton's initial position the effective potential for the solitons, given by the background density, is approximately flat. This implies that the final travel direction of the soliton can be manipulated between positive and negative z , by using potentials which are slightly asymmetric along the z axis, as we have confirmed numerically. The BEC density increases on the side with the deeper well, making it the favoured escape direction.

Prospects for soliton horizon radiation

Finally, we analyse whether and how grey solitons could play a role in analogue gravity studies. Our goal here is not a rigorous and complete account, but on the

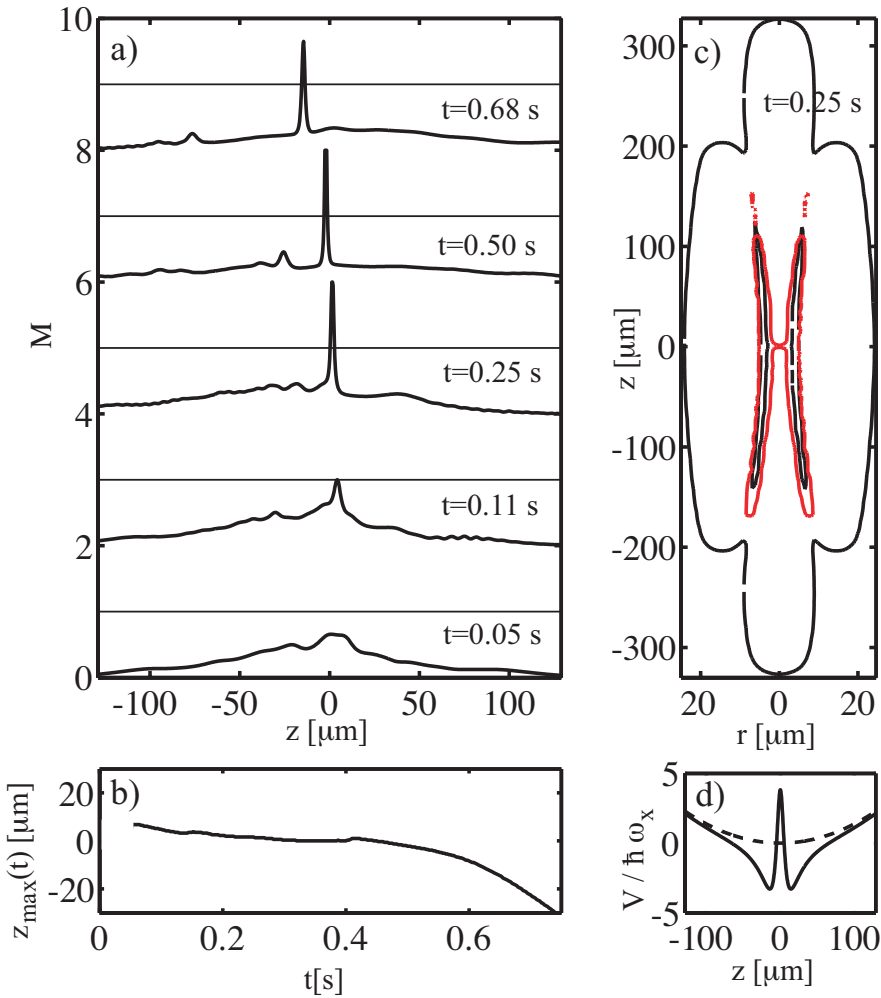


Figure 5.7: Scenario of long-time immobile soliton as sonic horizon, following a sudden change in the potential as shown in (d). (a) Time evolution of the Mach number M . Graph layout as in Fig. 5.5. (b) Position of the maximum of M . (c) (red) Shape of the ergoregion, see section 5.2, and (black) the BEC cloud (shown is an isocontour at $n = 3 \times 10^{16} \text{ m}^{-3}$). Where the ergoregion surface intersects $r = 0$, the flow is normal to the surface and we have a horizon. (d) The potential is suddenly modified (at $t = 0$) from the shape indicated by the dashed line to the solid line.

contrary to present basic ideas and stimulate further interest.

The grey solitons of section 5.4.3 possess a sonic black hole horizon where the BEC flow past them becomes supersonic. They also carry a white hole horizon. The separation between the black-hole and white-hole horizons d depends on the soliton size, dictated by the healing length. We numerically find $d \sim 2\xi$. This

places the BH-WH pair well outside the hydrodynamic regime.

There exist interesting phenomena in analogue gravity, which crucially involve white holes in addition to black holes, such as the black hole laser effect [218]. We stated in section 5.3.2 that BECs with a widely separated black- and white-hole pair are usually dynamically unstable [194, 196]. As the grey solitons here already represent the end-product of dynamical instability, the black and white holes contained *within* them are stable as long as the soliton exists. Given the complications of creating well separated BH-WH pairs, compared to the ease with which one can obtain grey solitons, it seems worthwhile to direct further research towards the question, whether features of the Hawking or black-hole laser effects persist in this rather rapidly varying flow. Another motivation is the strict analogue Hawking temperature limit in the hydrodynamic regime.

It has been stated that the core ingredients of Hawking radiation are exclusively the existence of an apparent horizon and the validity of the eikonal approximation there [206]. The Mach number around the long time immobile soliton of Fig. 5.7 becomes as high as 600. The group velocity v_g of Bogoliubov excitations with wave number k is given by [65]:

$$|v_g| = \frac{c^2 + \frac{\hbar^2}{2m^2} k^2}{\sqrt{c^2 k^2 + \left(\frac{\hbar}{2m} k^2\right)^2}} |k|. \quad (5.31)$$

Inserting numbers for our case, we see that only wave packets localised around wavelengths as short as $g\xi$ with $g = 0.015$ have a group velocity in excess of $600c$. There is thus a window of wave numbers, $\pi/\xi \ll k \ll 2\pi/(g\xi)$, for which a point of no return exists *and* the eikonal approximation should be valid in its vicinity. The location of this “horizon” varies depending on the major wavelength of the wave packet. Due to the steep Mach number profile, the “horizons” for different wavelengths are spatially close. Quantum emission of quasi-particles by the horizon thus appears conceivable for wave numbers within the window.

The velocity of the bulk BEC beyond the tunnel is effectively zero, see Fig. 4.18 (c). This provides a region of flat space for the detection of quasi-particles emitted by the horizon. The steering of the soliton’s escape direction could be an advantage for spectroscopic detection of horizon radiation [213]. The horizon-soliton can be made to travel towards $z > 0$, while the generated quantum excitations are spectroscopically detected in the bulk BEC at $z < 0$ before the soliton reaches the cloud edge.

One of the advantages of the analogue gravity program over the astrophysical original, is the ability to push the studied system to the validity limits of existing

derivations of horizon radiation. This allows the segregation of essential premises from merely analytically convenient assumptions. In this sense the optical tunnel system might one day complement more conventional analogue gravity setups along the lines proposed in Refs. [194, 195, 203, 219, 220].

5.4.4 Summary

In this section, we have studied the response of the high charge ring flows that we found in chapter 4 to dynamical potentials which drive the flow into the supersonic regime. This realises a supersonic optical tunnel for the BEC. Our simulations generically show the creation of quasi-one dimensional grey solitons in the tunnel, once the speed of sound is exceeded. As an aside, we have pointed out a possible connection to soliton-vortex-ring hybrids. Finally we discussed the prospects of using a single, stabilised soliton as an analogue gravity tool. We argue that whilst the Mach number around the realised horizon varies too rapidly to expect the usual form of analogue Hawking radiation, it might be suited to probing the physical boundaries for quantum emission from a horizon. Many subtleties appear in traditional derivations of Hawking radiation [221]. Thus studies of analogue gravity should make full use of their ability to study the effect, theoretically and experimentally, under diverse conditions.

5.5 Sonic Horizons in Atom Lasers

Atom lasers [168] produce a moving BEC. The atoms emitted in an atom laser are usually free falling under gravity and those in the original condensate move to replenish the loss due to outcoupling. Hence atom lasers have already been suggested for studying the analogue Hawking effect [195].

We consider a parent BEC cloud, in which the atoms are outcoupled only within a small fraction of the condensate volume. This could, for example, be achieved by employing a Raman laser outcoupling mechanism [168] and focussing the lasers responsible for the outcoupling onto a small region of the cloud. In such a case we have three principally different options to create supersonic flows: (i) The atoms falling under the influence of gravity in the atom laser beam will eventually become supersonic. (ii) The bulk BEC streaming towards the outcoupling region to replenish lost atoms can be made supersonic. (iii) If the outcoupling is strong enough it will create a localised condensate density depression, which can cause the BEC in the parent cloud to become supersonic.

However, atom laser beams are typically several orders of magnitude less dense than BEC clouds. Option (i) thus will give rather small Hawking temperatures by the arguments of section 5.3.4. Further, from Eq. (5.8) with $A = \text{const.}$ we see that a stationary horizon in the beam would require the addition of an additional hump potential to achieve $V' = 0$ (The slope of the gravitational potential $V'_{\text{grav}} = mg$ is everywhere positive). As atoms falling under gravity accelerate fast, the additional hump would also serve the purpose to move the horizon significantly away from the parent BEC cloud. We did not further consider this option and will instead take a closer look at (ii) and (iii).

5.5.1 Dimensionless Formalism

In the remainder of this chapter we frequently vary the external potential for the BEC and also the atomic species considered. To facilitate this, we now present those aspects of the formalism that do not change from section to section. We also use a dimensionless formulation of the GPE.

To this end we measure lengths in the oscillatory units of the transverse harmonic confinement $a_{\text{osc}} = \sqrt{\hbar/(m\omega_{\perp})}$. Harmonic confinement in the transverse direction r is a feature of all scenarios that follow. The timescale is set by $1/\omega_{\perp}$. Hence $\tilde{t} = t\omega_{\perp}$, $\tilde{\mathbf{x}} = \mathbf{x}/a_{\text{osc}}$ and $\tilde{\Psi} = \Psi a_{\text{osc}}^{3/2}$. Eq. (2.10) then becomes

$$i\frac{\partial\tilde{\phi}(\tilde{x}, \tilde{r}, \tilde{t})}{\partial\tilde{t}} = \left(-\frac{1}{2}\tilde{\nabla}^2 + \frac{1}{2}\tilde{r}^2 + \tilde{V}(\tilde{x}) + \tilde{U}_{3D}|\tilde{\phi}|^2 - i\frac{\tilde{K}_3}{2}|\tilde{\phi}|^4 \right) \tilde{\phi}. \quad (5.32)$$

Here $\tilde{U}_{3D} = U/(\hbar\omega_{\perp}a_{\text{osc}}^3) = 4\pi\frac{a_s}{a_{\text{osc}}}$ and $\tilde{K}_3 = K_3/(a_{\text{osc}}^6\omega_{\perp})$. $\tilde{V}(\tilde{x})$ denotes longitudinal components of the potential measured in units of $\hbar\omega_{\perp}$. We also define the dimensionless Hawking temperature $\tilde{T}_H = \frac{\tilde{c}}{2\pi}\frac{\partial M}{\partial\tilde{x}}$, related to $T_H = \omega_{\perp}\hbar\tilde{T}_H/k_B = \omega_{\perp}7.6 \times 10^{-12} \tilde{T}_H$.

For some cases we employ an ω_{\perp} large enough so that transverse dynamics can be ignored. Then we can reduce the dimensionality of the GPE. For sufficiently low chemical potential $\mu \ll \hbar\omega_{\perp}$, see e.g. Eq. (2.19), we can assume that the transverse wavefunction $\psi_{\perp}(r)$ remains in the oscillator groundstate $\psi_{\perp}(r) = \mathcal{N} \exp(-r^2/2a_{\text{osc}}^2)$. We then again make the Ansatz $\phi(x, r, t) = \psi_{\perp}(r)\phi_{1D}(x, t)$ and demand $2\pi \int_0^\infty dr r |\psi_{\perp}(r)|^2 = 1$, which results in $\mathcal{N} = 1/\sqrt{\pi a_{\text{osc}}^2}$ [207]. We insert this Ansatz into Eq. (5.32) and project onto the transverse ground state component, i.e. we multiply Eq. (5.32) by ψ_{\perp} and then integrate $2\pi \int_0^\infty dr r$. After

conversion to dimensionless units, we obtain

$$i \frac{\partial \tilde{\phi}_{1D}(\tilde{x}, \tilde{t})}{\partial \tilde{t}} = \left(-\frac{1}{2} \frac{\partial^2}{\partial \tilde{x}^2} + \tilde{V}(\tilde{x}) + \tilde{U}_{1D} |\tilde{\phi}_{1D}|^2 - i \frac{\tilde{K}_{3,1D}}{2} |\tilde{\phi}_{1D}|^4 \right) \tilde{\phi}_{1D}, \quad (5.33)$$

with $\tilde{U}_{1D} = \tilde{U}_{3D}/(2\pi) = 2\frac{a_s}{a_{\text{osc}}}$ and $\tilde{K}_{3,1D} = \tilde{K}_3/3\pi^2$. Note that in the chosen scheme the actual central density in the tight trap is $\tilde{n}_{3D} = \tilde{n}_{1D}/\pi = |\tilde{\phi}_{1D}|^2/\pi$.

When considering the corresponding 1D reduction of the time independent GPE, one finds a chemical potential $\tilde{\mu}_{1D} = \tilde{\mu}_{3D} - 1$. The system is quasi one dimensional, i.e. the one dimensional description is accurate, when $\tilde{\mu}_{1D} \lesssim 1$.

We usually give a physical situation (i.e. atomic species and transverse trap frequency) that we have in mind for any given set of dimensionless parameters. It is however often possible to find different physical parameters corresponding to the same situation, at least for scenarios without loss ($K_3 = 0$).

The formalism just defined is also used in section 5.6, however the detailed shape of $\tilde{V}(\tilde{x})$ varies from case to case. In captions of graphs we aimed to indicate by tildes whether a parameter is dimensionless. However we did not exercise the same rigour with coordinates, which are dimensionless throughout this section despite occasional use of untilded “ x ” and “ t ”.

5.5.2 Horizon due to Strong Outcoupling

To begin, we investigate whether the outcoupling process by itself gives rise to sonic horizons in the parent condensate cloud of an atom laser. We assume a long and tight cylindrical trap where the outcoupled atoms fall in a perpendicular direction, so that they disturb the parent BEC as little as possible. Thus we do not have to model the beam. Assuming tight confinement we use Eq. (5.33) with

$$\tilde{V}(x) = \frac{1}{2} \eta^2 x^2 + W \exp\left(-\frac{x^2}{2\sigma^2}\right) - i \frac{\gamma}{2} O(x). \quad (5.34)$$

The aspect ratio of the trap is $\eta = \omega_x/\omega_\perp$. We optionally consider an additional repulsive Gaussian potential of width σ and amplitude W . The outcoupling is modelled by the imaginary contribution to $\tilde{V}(x)$. It takes essentially the form of a spatially dependent one-body loss term with profile $O(x) = B \exp[-2(x - x_{\text{oc}})^2/\sigma_{\text{oc}}^2]$. The strength of the outcoupling is denoted by γ . The normalisation B ensures $\int dx O(x) = 1$. We imagine $O(x)$ to arise from the transverse profile with width σ_{oc} of a Raman outcoupling laser slicing the condensate and centered on x_{oc} . For now we consider $\tilde{K}_{3,1D} = 0$.

We can easily obtain a rough estimate of the flow generated by the “sink” in the outcoupling region defined by $O(x)$. The outcoupling modifies the equation of continuity:

$$\frac{\partial|\phi|^2}{\partial t} = -\frac{\partial}{\partial x}(v|\phi|^2) - \gamma O(x)|\phi|^2. \quad (5.35)$$

We assume the BEC density near x_{oc} is approximately constant $n = n_{oc}$. Integrating Eq. (5.35) over the interval $(x_{oc} - L, x_{oc} + L)$ then gives:

$$\frac{\partial N(L)}{\partial t} = v n_{oc}|_{x=x_{oc}-L} - v n_0|_{x=x_{oc}+L} - \gamma n_{oc}, \quad (5.36)$$

provided that L is large enough for the interval to accommodate the Gaussian profile $O(x)$. $N(L)$ denotes the number of atoms within the chosen interval. If we assume that the atoms lost due to outcoupling are approximately replenished by a flow of atoms into the interval, we can use $\frac{\partial N(L)}{\partial t} = 0$. Assuming equal and opposite velocities at $x = x_{oc} \pm L$ we get: $|v(x_{oc} \pm L)| = \gamma/2$. The inflow velocity is thus just given by the outcoupling strength. The expression holds for weak outcoupling where our assumptions are reasonable. The resulting Mach number is $M = \frac{\gamma}{2\sqrt{U_{n_0}}}$. To improve the Hawking temperature, we need high densities, but to achieve high Mach numbers we then require large γ with consequently more loss of atoms.

We now numerically investigate the flow profiles created by the outcoupling mechanism in more detail. Our simulations begin from a ground state of Eq. (5.33) with chemical potential $\tilde{\mu}_{1D}$, in which the BEC does not move. This state is found by imaginary time evolution. Then the outcoupling is slowly switched on to transfer the condensate into a state with steady inflow into the sink. For $W = 0$, no sonic horizon is established due to the shape of the parabolic trapping potential, which yields a flow structure that becomes faster away from the origin. From Eq. (5.8) we can see that in this situation a stable horizon is impossible, as there is no location with $V' = 0$ besides the origin.

For strong outcoupling, we found that a local density dip appears around the outcoupling region. In this dip, the Mach number becomes large. However, values of γ high enough to create supersonic flow in this manner result in massive disruptions of the BEC cloud. In order to reduce these disruptive effects, we place a repulsive Gaussian potential into the same region as the outcoupling. Fig. 5.8 (b) shows the result of smooth creation of a horizon that lies within the outcoupling region. Its dimensionless Hawking temperature is $\tilde{T}_H = 0.07$. For that to correspond to, say 10 nK, we require $\omega_\perp = 3000 \times 2\pi$ Hz. Under these

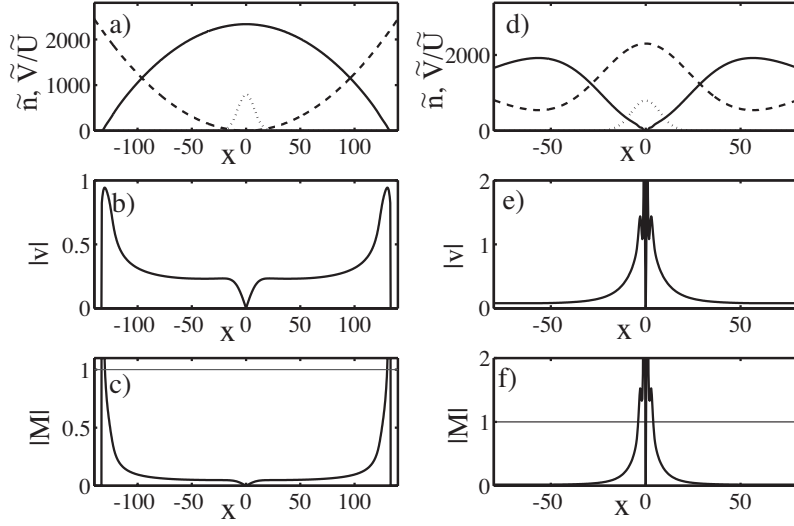


Figure 5.8: (a)-(c) No horizon is established for weak outcoupling within a harmonic trap only. For the figure we ramped γ to 0.5. (a) density (solid), $\tilde{V}(x)/\tilde{U}_{1D}$ (dashed) and shape of outcoupling region (dotted). (b) Velocity $|v|$. Near the sink $v \sim 0.25 = \gamma/2$ as predicted. (c) Mach number (black). The grey line indicates $M = 1$. Other parameters were $x_{oc} = 0$, $\sigma_{oc} = 15$, $\tilde{U}_{1D} = 0.01$, $\tilde{\mu}_{1D} = 25$, $\eta = 0.05$. (d)-(f) We can create a sonic horizon for stronger outcoupling. To limit disrupting effects on the BEC cloud, the outcoupling region is placed within a repulsive potential. We used $W = 23$, $\sigma = 24$ and a final $\gamma = 4$.

conditions the actual densities would be 1-2 orders of magnitude higher than the limits in table 5.2.

The horizons within this setting appeared generically inside of the outcoupling region. This can be understood from Eqs. (5.7) and (5.8), which are valid outside of this region: Besides the origin, there is only one location with $V' = 0$ and the acceleration a on either side has the wrong signs for the flow to become supersonic. Within the outcoupling region however, the continuity equation (5.35) must be used and Eq. (5.7) is no longer valid. This allows the flow to become transsonic.

There are no dynamical instabilities visible in our simulations, despite the presence of white holes deep in the outcoupling region. The BEC density there is very small. Either this, damping due to the outcoupling, or an effective boundary condition resulting from the symmetry which requires $v(x = 0) = 0$ appears to remove dynamical instabilities.

For horizons within the outcoupling region, the influence of the outcoupling

on Hawking phonons might have to be considered. Also analytical estimates of the analogue Hawking temperature in this scheme are complicated by the modified continuity equation. In the following, we pursue schemes allowing horizon creation away from the outcoupling, rather than study this case in more detail.

5.5.3 Horizon due to Obstacle

The flow towards the sink in the parabolic parent BEC cloud of an atom laser does not establish a sonic horizon outside of the outcoupling region, because of unsuitable conditions for a quasi-stationary sonic horizon. We can change these conditions by using an additional potential hump and turn the BEC flow supersonic. Fig. 5.9 illustrates a cigar shaped BEC cloud. The cloud is sliced by a Gaussian blue detuned (repulsive) laser sheet at the centre¹⁶. Our localised outcoupling mechanism is now placed near the long end of the cigar trap. Due to the outcoupling, the bulk BEC will flow towards that end of the trap to replenish the loss. This flow v and the outcoupled beam of atoms are symbolised by arrows in the sketch 5.9.

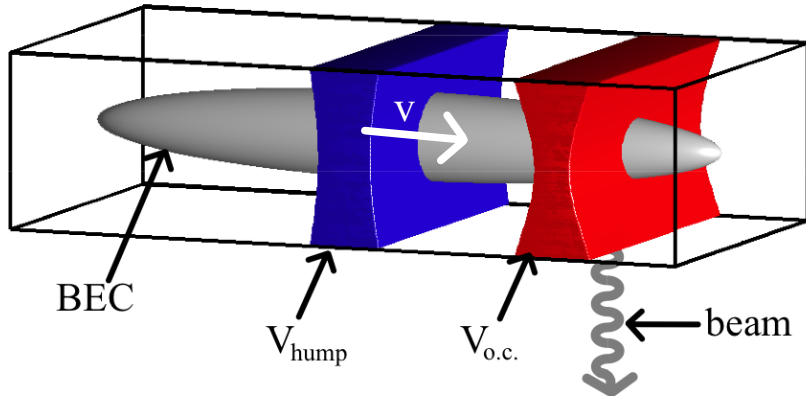


Figure 5.9: Setup for sonic horizon creation in BEC flow over a hump potential. We imagine the repulsive potential and outcoupling laser of Eq. (5.34) to be realised as laser sheets so that their potentials are (approximately) independent of r .

If the outcoupling is initiated slowly, we expect a quasi-stationary flow after an initial transient period. We can then use the formalism of section 5.3.1 to

¹⁶The effect of the potential on the condensate is not shown in the sketch.

predict the behaviour of the flow. The outcoupling strength γ fixes the flux J of the outflow according to $J = \gamma n_0/2$.

According to Ref. [203], the parameter $q(x)$, Eq. (5.10), takes its minimal value at the horizon. If this exceeds the critical value $3/2$ the flow will remain subsonic. The critical outcoupling strength γ_{crit} is found from $q(0) = \frac{\mu - W}{m(\frac{JU}{m})^{2/3}} = \frac{3}{2}$, as

$$\gamma_{\text{crit}} = \frac{\left[\frac{2}{3}(\mu - W)\right]^{3/2}}{\sqrt{m}Un_0}. \quad (5.37)$$

If this is exceeded, the flow turns supersonic at the crest of the potential [203]. As established in section 5.3.1, to return the flow to subsonic velocities, a second hump would be required. We soon explain why a double hump structure in the considered setup cannot be advantageous for the *dynamical* creation of a transsonic flow. For now we ignore our gloomy prediction and just investigate the behaviour of a flow that breaches the speed of sound at the obstacle by means of numerical solutions of Eq. (5.33). We shall find that our impudence is rewarded with an interesting discovery.

Narrow Obstacle Potential

For our results here we will employ realistic parameters unlike in section 5.5.2. We continue our use of the 1D GPE, as the dynamics that we will encounter would render higher dimensional simulations extremely challenging. However the parameter regime is one where the one dimensional equation should be a good approximation.

We compare two cases. First, we aim to realise the maximal Hawking temperature presented in section 5.3.4. The atom of choice is hence sodium, the peak density chosen according to table 5.2 ($\tilde{n}_{1D} = 100$) and the width of the obstacle is $\sigma = 12 = 35\xi$, for the appropriate healing length. Further we assume tight transverse confinement with $\omega_\perp = 6800 \times 2\pi$ Hz, which results in $a_{\text{osc}} = 0.25$ μm , $\tilde{U}_{1D} = 0.022$. We use the Thomas-Fermi approximation [34] to estimate $\tilde{\mu}_{1D} = \tilde{n}_{1D}\tilde{U}_{1D} = 2.2$. Finally we employ $\gamma = 0.8$ ($\gamma_{\text{crit}} = 0.3$).

The result of a numerical solution of Eq. (5.33) for these parameters is shown in Fig. 5.10. Initially, the region of nonvanishing outflow velocity spreads with the speed of sound. Once this perturbation of the wave function reaches the hump potential at the centre, the flow breaches the speed of sound at the potential crest as expected. No quasi-stationary flow is established, in agreement with our expectations. Instead there is a white hole, which emits a train of gray solitons as

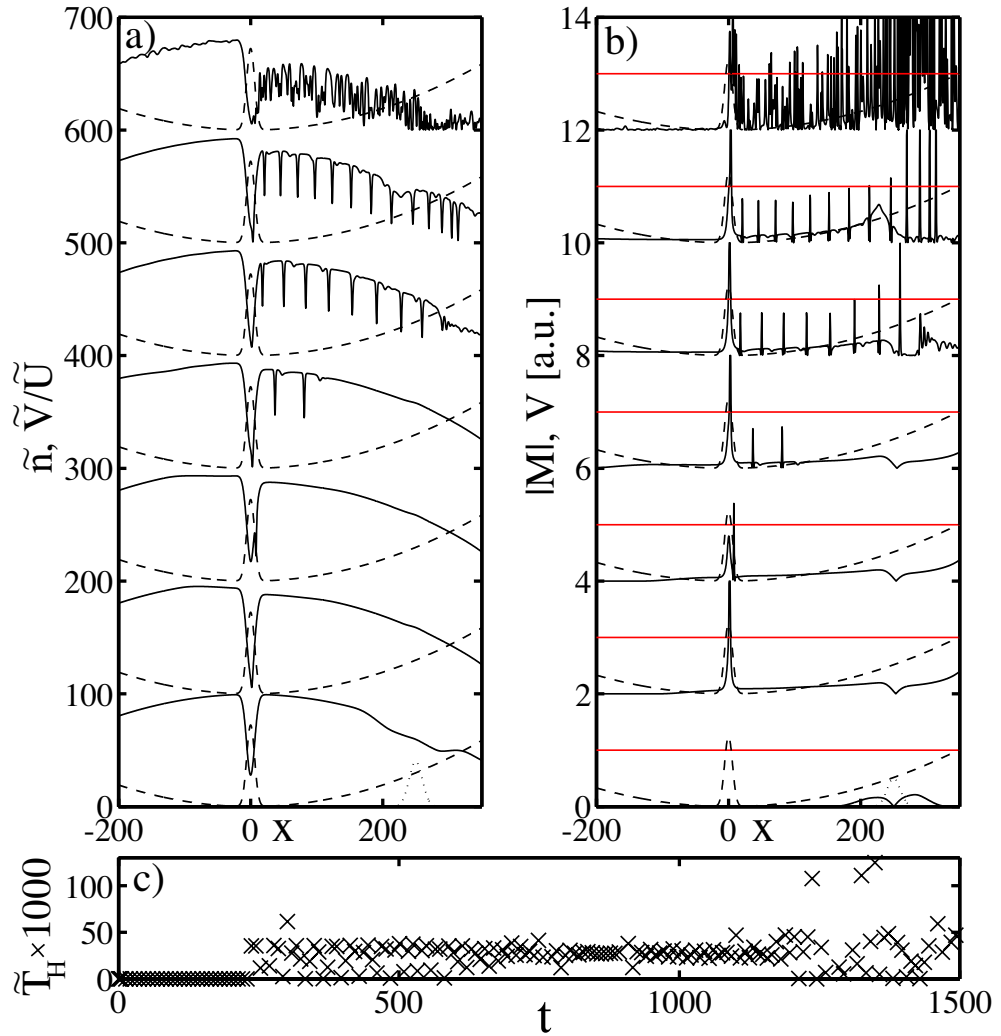


Figure 5.10: Dynamical evolution of BEC flow over an obstacle potential with $\sigma = 12$. (a) density (solid), \tilde{V}/\tilde{U} (dashed), outcoupling region $O(x)$ [a.u.] (dotted, at the bottom to the right). Successive samples are moved upwards by 100. Snapshots are at $\tilde{t} = 56, 240, 256, 320, 496, 616, 2376$. $\tilde{t} = 621$ corresponds to 15 ms. (b) Mach number (solid, black). Successive samples are moved upwards by 2. Red line indicates $M = 1$. Scaled potential (dashed). (c) Analogue Hawking temperature \tilde{T}_H . $\tilde{T}_H = 0.04$ corresponds to $T_H = 13$ nK.

we have seen in section 5.4. Each time a soliton is created the black hole horizon is strongly perturbed, the third sample in Fig. 5.10 (b) was chosen to show this. As a result, even though the instability originates from the white hole, the numerically determined analogue Hawking temperature exhibits large variations in time. The evolution for this case is also captured in the movie `humpflow_q1d_bad_gpe.mov` on the CD.

Note that in contrast to our studies of the optical tunnel, here we are not interested in the sonic horizons associated with the solitons themselves. We only study the horizons of the background flow.

Wide Obstacle Potential

We get a more interesting result when the width of the hump potential is increased to $\sigma = 60$. The evolution is shown in Fig. 5.11. We see soliton train emission as before, however in contrast to the previous case, the black hole horizon stays unperturbed by the dynamical instability of the white hole. As already stated in section 5.4, the soliton width is determined by the condensate healing length ξ . For a sufficiently wide obstacle potential, the black and white holes are separated further than ξ . Hence solitons can form at the white hole and propagate downstream without affecting the black hole sonic horizon. As a consequence, also the analogue Hawking temperature remains constant over long times, Fig. 5.10 (c).

The whole left hand side of the condensate remains stable for the time span shown in the figure, while the right hand side becomes increasingly turbulent. The left side is shielded by the “analogue event horizon” of the black hole. However as we know, this is only true for phononic excitations. Wavepackets from the particle like, high momentum part of the Bogoliubov spectrum can reach the left side and after times longer than $\tilde{t} \sim 1200$ the black hole is perturbed and the BEC at $x < 0$ also suffers turbulence.

A careful inspection of the numerical data shows that the onset of perturbations in the previously stable left hand region coincides with a wave reflection from the right cloud edge reaching the black hole. In the movie `humpflow_q1d_gpe.mov` on the CD this can also be seen. We conjecture that the reflection effect could be avoided in practice by further extending the BEC cloud in the x -direction. Our x domain was limited by numerical constraints: The simulation presented used 8192 points and has been verified on a doubled grid. As the grid spacing is fixed by the requirement to be smaller than the healing length, a sufficiently large x domain would require vastly more points. These limitations do not apply to an

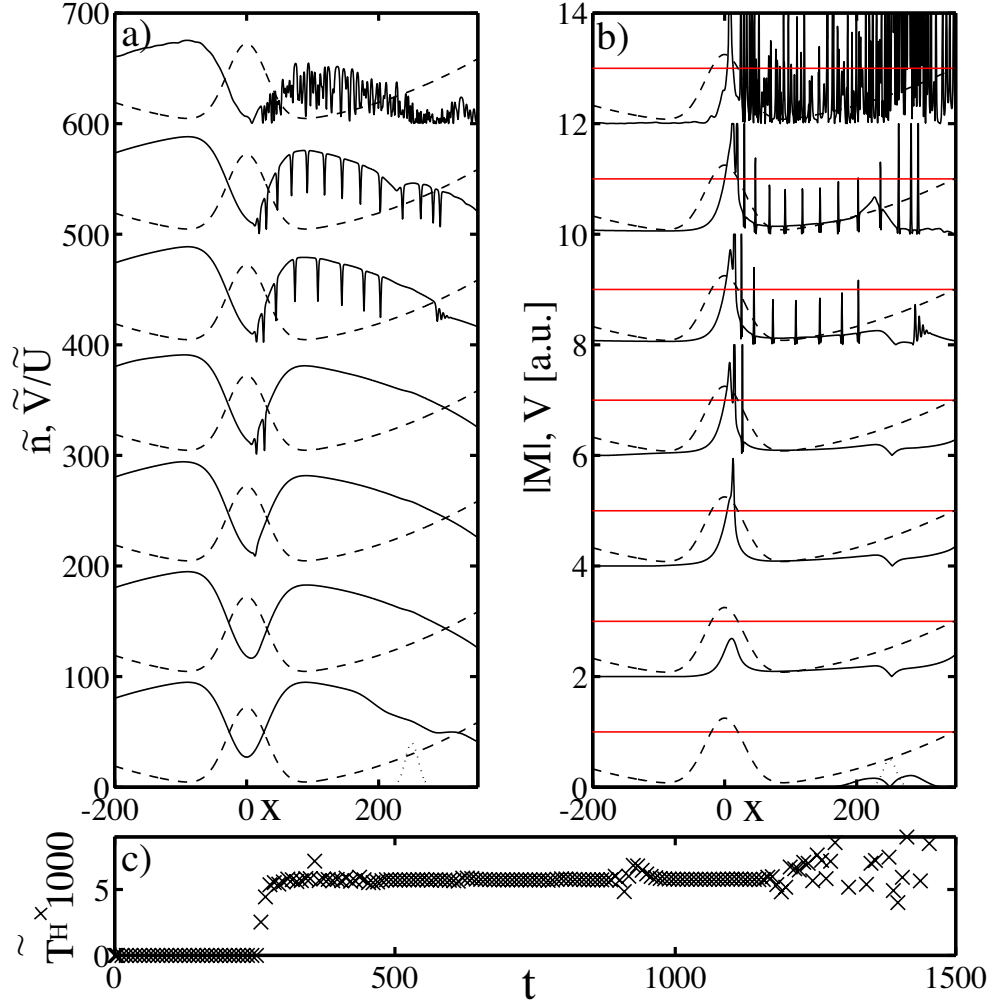


Figure 5.11: Graph as Fig. 5.10 but for $\sigma = 60$. (c) In contrast to Fig. 5.10, the analogue Hawking temperature remains almost constant until $\tilde{t} \sim 1200$. The value $\tilde{T}_H = 6 \times 10^{-3}$ corresponds to $T_H = 1.9$ nK.

experiment. The condensate simulated contains only 55000 atoms, an experiment could easily accommodate an order of magnitude more. We added another movie to the CD, `humpflow-gpe.mov`, which shows an even less perturbed black hole horizon, albeit for less realistic parameters.

Comparing the results for $\sigma = 12$ and $\sigma = 60$, we see that with the requirement of shielding the black hole from the white hole instability, a Hawking temperature as given in table 5.10 cannot be achieved. The value $\sigma = 12$ is not even as

narrow as $\sigma = 20\xi$, but yet the width is already too small. Besides not being able to reach the temperature limit, this scenario would have another drawback in practice: In the hydrodynamic regime the condensate only flows over the hump as long as $\tilde{U}_{1D}\tilde{n}_{1D,bg} > W$, see Eq. (5.6). In this expression we refer to the peak background density away from the hump as $\tilde{n}_{1D,bg}$. Due to three-body losses at high densities, $\tilde{n}_{1D,bg}$ will decrease, inescapably violating the condition at some time. It is possible that the problem could be overcome by dynamically reducing W by the same rate as $\tilde{n}_{1D,bg}$ decreases. Alternatively the detection of analogue Hawking phonons has to be fast.

Finally, there should also be a special advantage to this scenario. We can vary it between transsonic and supersonic flows by minimal variation of the parameter γ , as long as we are near γ_{crit} . This might be helpful for the removal of the measurement background as discussed in section 5.3.5. However, we did not explicitly verify this feature. Since we strictly do not have a stationary flow, Eq. (5.37) might only be approximately valid.

We still owe an account of complications that occur in attempting to dynamically establish flow over a double hump structure, realising a double de-Laval nozzle. Consider two Gaussian humps in the flow, with the outcoupling region to the right of them. The region of non-vanishing flow velocity spreads from the outcoupling region and reaches the rightmost hump first. The flow will first become supersonic there, and encounters no further hump downstream to act as a diffuser. Thus the scheme is doomed to fail.

5.5.4 Summary

We have now considered sonic horizons in the parent BEC cloud of an atom laser, a much simpler system than the supersonic optical tunnel. We can create sonic horizons either by strong outcoupling or by the addition of a repulsive hump potential in the way of the flow. In the first case, we establish effectively black holes only, however these necessarily appear inside the outcoupling region. This is an undesired feature. In the second case, we establish a BH-WH pair. We see dynamical instabilities at the white hole similar to those in section 5.4. However, using realistic parameters for a quasi-1D sodium condensate, we numerically showed that for wide humps the soliton emission does not perturb the black hole horizon for times up to $t = 30$ ms. The realised analogue Hawking temperature corresponds to $T_H = 1.95$ nK. We conjecture that the unperturbed time span can be further extended if the cloud size is increased beyond that which we can

feasibly simulate.

5.6 Reservoir Outflow

We have seen violent consequences of a white hole and its dynamical instabilities. Knowing that sonic black holes by themselves are dynamically stable, the obvious way to proceed is to try to create a transsonic flow without a white hole. In such a case, the BEC that has become supersonic must remain so. A simple suitable scenario was suggested by Giovanazzi *et al.* [203]: outflow of a condensate from a reservoir. They showed, using one-dimensional simulations without losses, that their proposed setup allows dynamically stable horizon formation. We will now explore this system in greater detail. To structure our analysis, we first outline the physical setup and subsequently investigate several details of the proposed experiment. At the end of this section, we will put all the pieces together and present a complete 3D simulation covering all aspects of the outflow scenario.

5.6.1 Outflow Scenario

Let us imagine a BEC reservoir from which the condensate is allowed to flow out¹⁷. For example, consider the atoms confined between two potential humps in one dimension. If one of these humps is chosen slightly too weak for true confinement, the condensate can leak out. When exiting the reservoir, the BEC turns supersonic and remains so, avoiding a white hole. The flow at this “exit-hump” is very similar to that near the hump in the atom laser, section 5.5.3. However, now there will be no initial BEC density on the outer side of the hump. As we will soon see, this difference is crucial and leads to a stable transsonic flow.

We can compare the outflow scenario of this section and the flow over the hump in the atom laser of the previous section with a hydrodynamic de-Laval nozzle. The latter can be operated above or below a critical exit pressure [222]: A single de-Laval nozzle can create a stable transsonic flow if the exit pressure is below a critical value. The flow then remains supersonic. If the exit pressure exceeds this critical value, one obtains an exit shock: a surface where hydrodynamic quantities vary discontinuously, and behind which the flow is again subsonic. To bring the flow back to subsonic speeds without a shock, at the same pressure

¹⁷This system can in fact be viewed as an atom laser as well. In this thesis, we use the label “atom laser” for the proposals involving an active outcoupling mechanism presented in the previous section.

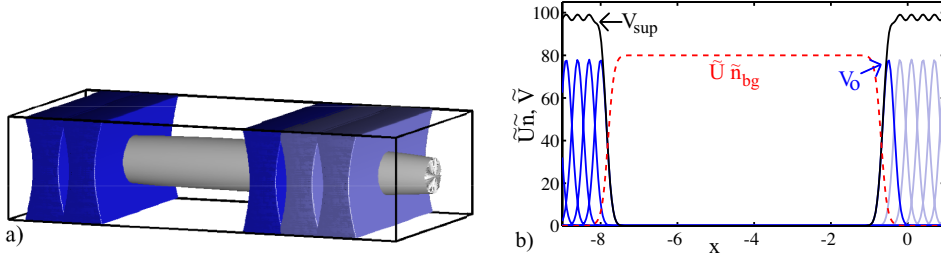


Figure 5.12: (a) Schematic of a cigar shaped BEC (grey, ends are cut off in the figure), sliced by multiple blue detuned laser sheets (blue). (b) These sheets (blue) add up to form barriers (black), which are impenetrable for the condensate (red-dashed, shown is $\tilde{U}\tilde{n}$). The left sheets act as permanent endcap. To initiate supersonic outflow from this reservoir, the optical potentials sketched in light blue in panels (a) and (b) are suddenly removed. This changes the right hand side barrier from the black line to the dark blue line. $\tilde{U}\tilde{n}_{bg}$ exceeds the height of the last remaining hump by a small margin, and the condensate is allowed to leak out.

that it had before the nozzle, a second nozzle (diffuser) is required as already mentioned before. The derivative terms in the GPE would quickly destroy any discontinuous structure, thus a condensate cannot form a discontinuous shock. Instead it forms a dynamically unstable white hole¹⁸.

Let us now proceed to consider the reservoir outflow. Here we extend the idea of Ref. [203] in several ways. First, we simulate the horizon in 3D, exploiting cylindrical symmetry. In particular we do not always assume a quasi 1D situation, allowing $\mu \gtrsim \hbar\omega_\perp$. In such cases it makes sense to study the transverse structure of the horizon. Secondly, as our discussion in section 5.3.4 showed the importance of three-body losses for our problem, we included them in our simulations. Finally, we evaluate whether the optical piston described in Ref. [203] is required in practice.

A sketch of the outflow scenario is given in Fig. 5.12, containing the modification we suggest compared to [203]: Barriers constructed by potential superposition and outflow initiation by barrier reduction. The condensate is initially confined in an elongated, cigar shaped trap, sliced by blue detuned laser sheets which act as endcaps. This defines our reservoir. The sheets superimpose to

¹⁸Dispersive shocks have been studied in condensates, see e.g. Ref. [223].

achieve approximately top-hat shaped potentials. The height of this superposition potential V_{sup} is larger than the bulk condensate interaction energy $\tilde{U}\tilde{n}_{bg}$, hence the atoms are confined. \tilde{n}_{bg} is the background density within the reservoir, i.e. where the potential vanishes. The confinement follows from the hydrodynamic equation for the initial stationary state, Eq. (5.6), using $\tilde{\mu} = \tilde{U}\tilde{n}_{bg}$ and $\tilde{n} > 0$. To initiate outflow, all but one of the right-hand sheets are suddenly removed. The height of the remaining single sheet V_0 is less than that required for confinement so that the BEC starts to stream out. The purpose of the superposition method, is to avoid a rapid temporal change in the potential within the region where the condensate density is significant. Otherwise we would cause disruptions. In an experiment one could just let the condensate propagate supersonically along the waveguide created by the transverse confinement, once it has exited the reservoir. The numerical treatment requires a damping technique at the grid edge, for which we employ an outcoupling potential.

Taking all these elements together, the potential that we apply for our dynamics is

$$\begin{aligned} \tilde{V}(r, x, t) = & \frac{1}{2}r^2 + \sum_{n=0}^{15} V_g(V_0, x_l(t) - nd, \sigma) + V_g(V_0, x_r, \sigma) \\ & + V_g(-i\gamma, x_{oc}, \sigma_{oc}) + \theta(-t) \sum_{n=1}^{15} V_g(V_0, x_r + nd, \sigma), \\ V_g(W, x_0, \sigma_0) \equiv & W \exp(-2(x - x_0)^2/\sigma_0^2). \end{aligned} \quad (5.38)$$

V_0 denotes the amplitude and σ the width of an individual Gaussian sheet. $x_l(t)$ is the position of the innermost sheet in the left barrier and x_r the same on the right. d is the separation between the sheets. Usually $x_l(t) = x_l = \text{const.}$ The outcoupling is parametrised by γ , x_{oc} and σ_{oc} . The potential $V_g(V_0, x_r, \sigma)$ is separated from the other members of the right top-hat array, as it is the one that remains. We will refer to this sheet as the “hump potential”. $\theta(-t)$ denotes the Heavyside step function.

In several simulations we use the one dimensional GPE (5.33). In these cases the potential is given by Eq. (5.38) for $r = 0$;

Instead of initiating outflow by lowering the barrier on the right, we can also proceed in closer analogy to Ref. [203]. We use a hump potential just high enough to confine the BEC by itself. Then, simultaneously with the change in potential, we use the left sheets as a moving “optical piston”: We let $x_l = x_l(t) = x_l(0) + v_p t$. The sheets move with the velocity v_p to the right and press the condensate out

of the reservoir. In modelling this, we additionally phase imprint the velocity v_p onto the condensate (see section 1.2.1). The latter is not necessary to create outflow, but in our experience makes it smoother. Initiation of outflow by a piston is probably more difficult to implement experimentally than the simple, abrupt lowering of the right barrier. In particular the moving optical potential might involve noisy, mechanical manipulations of optical instruments. For this reason we investigate a possible alternative.

The left potentials are kept on throughout evolution and could in practice be replaced by one wide, intense beam. On the left hand side, no modifications of the potential are intended, hence there is no motivation for using the top-hat shape there. For computational reasons, we however often simulate the horizon formation using a small x domain, necessitating a left end cap with a sharp edge. We thus use the top-hat construction on both ends.

In this section we will consider Gross-Pitaevskii dynamics in 3D, Eq. (5.32), and 1D, Eq. (5.33). For the former, we consider Eq. (5.32) using cylindrical coordinates r, x, φ . Besides small details in the shape of the laser sheets, which can be seen in Fig. 5.12 (a), our problem is cylindrically symmetric. We neglect these and assume independence of the wave function of φ . The simulations are thus done on a two dimensional grid. Nonetheless we refer to them in what follows as “3D simulations”, as their results should pertain to the fully three-dimensional scenario due to the approximate symmetry. We find the condensate initial state by imaginary time evolution according to Eq. (2.19). This is done in the potential of harmonic trap and end cap laser sheets.

If we consider the effective cross-sectional area $A(x)$ to be constant, the dimensionless analogue Hawking temperature at the hump potential (for $t > 0$) can be readily evaluated from Eqns. (5.4), (5.11) and (5.38). One finds [203]:

$$\tilde{T}_H = \frac{1}{2\pi} \sqrt{-\frac{3}{4} \frac{\partial^2 V}{\partial x^2}} = \frac{1}{2\pi} \sqrt{\frac{3V_0}{\sigma^2}}. \quad (5.39)$$

We know from section 5.3 that high Hawking temperatures require high densities. This seems not to be the case in Eq. (5.39), however there is a disguised dependence on n : The equation was derived in the hydrodynamic approximation where V (and therefore V_0) cannot exceed μ . Thus $V_0 \leq \mu = Un_{bg}$.

Our results are grouped into 4 sections. First we present the most important conclusions from our 3D simulations (section 5.6.2), then we present our results regarding the necessity of the optical piston (section 5.6.3), next we numerically implement three-body losses (section 5.6.4) and finally, combining all aspects, we

perform a complete simulation of sonic horizon formation under realistic experimental conditions (section 5.6.5).

5.6.2 Transverse Horizon Shape

To begin, we show that a stable horizon is also formed if the transverse dimension is taken into account. We further show that the formation is robust, by employing our initiation scheme without an optical piston. We present results regarding the transverse structure of the horizon under Q1D and TTF conditions.

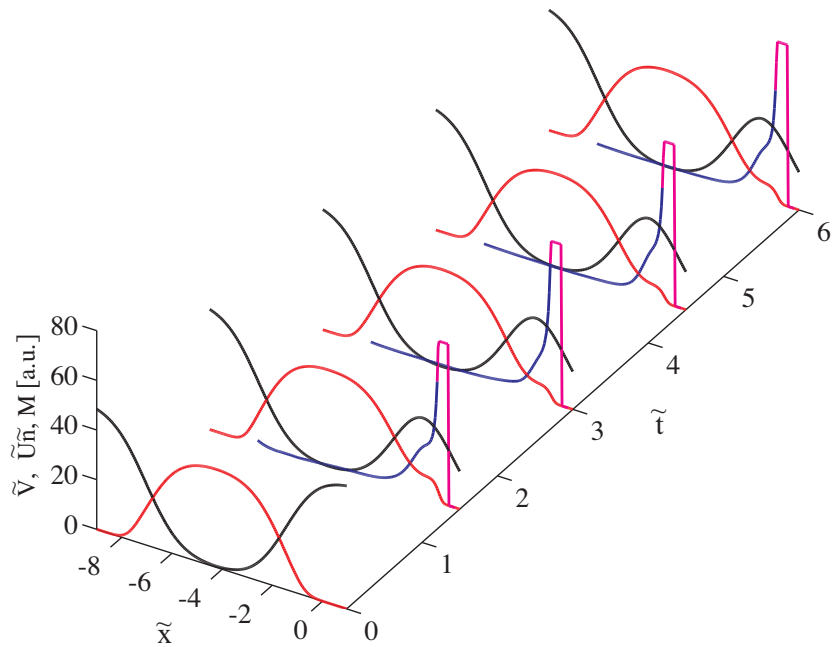


Figure 5.13: Sudden outflow initiation in the TTF regime as described in the text. The simulation is 3D, but quantities are shown at $\tilde{r} = 0$. Interaction energy (red), potential (black) and Mach number (blue and violet). For $M > 1$ the Mach number is shown in violet. It is also cut above $M > 1.3$.

We now employ parameters corresponding to helium. In the TTF case we take $\omega_{\perp} = 200$ Hz which gives $a_{\text{osc}} = 3.5 \mu\text{m}$ and $\tilde{U}_{1D} = 0.027$. For the Q1D case we take $\omega_{\perp} = 6800$ Hz hence $a_{\text{osc}} = 0.60 \mu\text{m}$ and $\tilde{U}_{1D} = 0.16$. The resulting

bulk densities in either case correspond to the limiting values shown for helium in table 5.2.

To give an idea of the scale of the perturbation resulting from the sudden initial change of potential under TTF conditions, we show Fig. 5.13. Perturbations in the density are not visible on the scale of the figure. It can be seen that the Mach number profile needs some time to settle. Numerical constraints force us to use a small x domain. Larger domains should only lead to smoother horizon formation. The horizon is actually not established exactly at the hump. This is due to interplay between $A(x)$ and $V(x)$, similar to that discussed for Fig. 5.5. In a similar Q1D simulation, the horizon is established precisely at the hump. The initial evolution of BEC flowing out of a reservoir is also shown in the movie `outflow_gpe.mov` on the CD.

The flow settles and then becomes slowly varying in time as the reservoir is drained. Let x_h denote the location of the horizon on the x -axis. Fig. 5.14 shows the radial variation of density, Mach number and horizon temperature at $x = x_h$, and the two dimensional shape of the BEC in the rz plane.

The Mach number increases further from the trap axis, located at $r = 0$. This is largely due to the density decrease while the velocity is approximately independent of r . The analogue Hawking temperature appears to be constant on the shown slice¹⁹. We find that the qualitative shapes presented in Fig. 5.14 (b) and (d) look similar at other time samples than those shown (see movie on the CD: `outflow_ooo_transverse.mov`).

Interestingly the slice at constant x does not coincide with the sonic horizon. Finding the exact horizon location is a non-trivial endeavour. The violet line in Fig. 5.14 (a) and (c) is the intersection with the surface where $M = 1$, which is the boundary of the *ergoregion*, as explained in section 5.2. There the flow velocity exceeds the speed of sound, but since the flow is not perpendicular to the surface indicated by the violet line, the velocity's normal component does not. The true horizon lies somewhere between the violet and white lines.

In a Q1D case, the transverse shape of the horizon should not be meaningful. We know transverse excitations to be frozen out for the BEC, and similarly would expect them to play no role for the phonon field. Propagating excitations are thus plane waves in the x direction times a transverse oscillator ground state. For these modes the horizon should essentially be defined at $r = 0$ or in some radially averaged sense. However under TTF conditions, where the healing length ξ is

¹⁹It is constant to the extent that we suspect a physical principle at work, however time constraints towards the end of the PhD did not allow us to pursue this matter further.

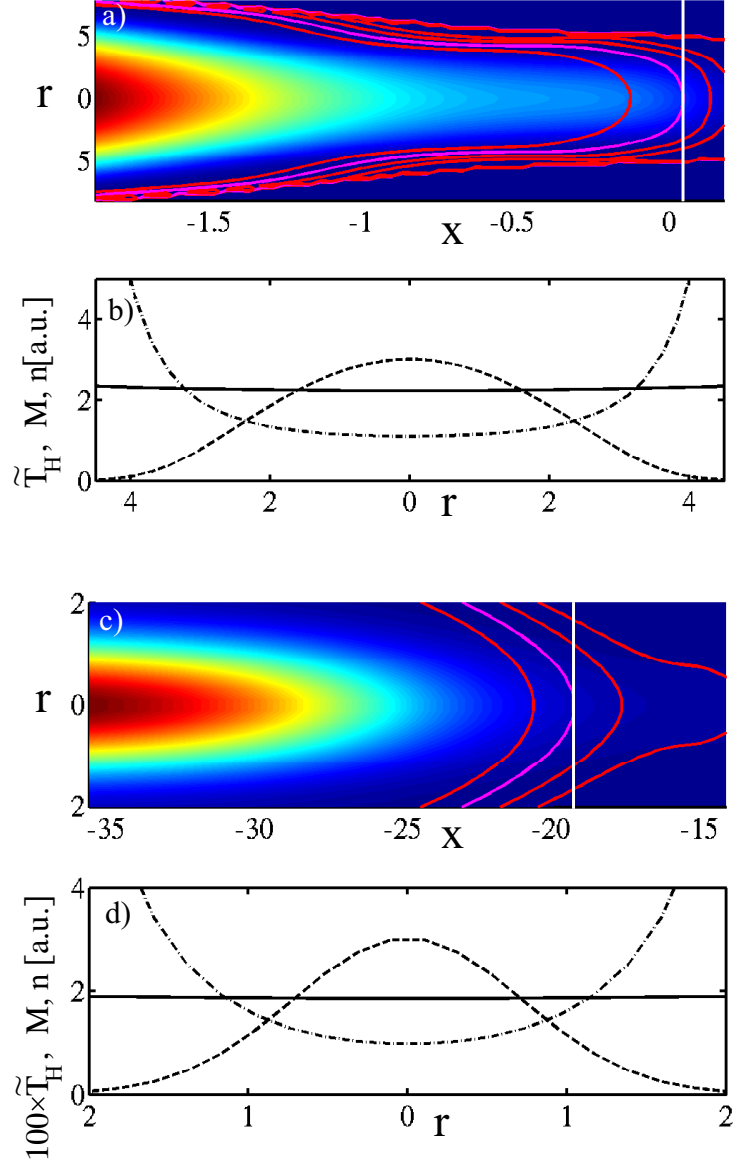


Figure 5.14: Transverse structure of the BEC with horizon. (a)-(b) TTF regime with $\tilde{\mu} = 40$, $V_0 = 32$, $\tilde{n}_{bg} = 1480$, $\xi = 0.11$ and $\sigma = 2.4 \simeq 22\xi$. The snapshot is taken at $\tilde{t} = 6$ (5 ms after initiation). Other parameters $x_r = -0.5$, $x_l = -8$, $d = 0.8\sigma$. (a) Colormap of density in r - z plane (red highest, blue lowest). Superimposed are contours (red) of equal Mach number at $M=(0.5, 2, 4, 8)$. $M = 1$ is marked violet. (b) Dependence of Mach number M (dot-dashed), density n (dashed) and analogue Hawking temperature \tilde{T}_h (solid) on r at $x = x_h$. This slice through the condensate is indicated by the white line in (a). (c)-(d) Q1D regime with $\tilde{\mu}_{3D} = 1.64$, $V_0 = 32$, $\tilde{n} = 1480$, $\xi = 0.7$ and $\sigma = 14 \simeq 20\xi$. The snapshot is taken at $\tilde{t} = 64$ (1.5 ms after initiation). Other parameters $x_r = -20$, $x_l = -90$, $d = \sigma$. The temperature shown in panel (d) is scaled. The colors and lines in (c) and (d) have the same meaning as in (a) and (b).

shorter than the radial cloud extension, the complicated horizon shape might be significant. We left this issue for further studies.

To conclude the present section, we underline that the outflow horizon is stable even in three dimensions, whether or not the confinement is tight. For a condensate beyond the Q1D regime we however find that the transverse horizon shape is non-trivial, requiring further investigation.

5.6.3 Maintaining Pressure

We now investigate whether the “optical piston” proposed in Ref. [203] is necessary for a useful reservoir outflow. The piston’s purpose is to maintain the reservoir “pressure” $\tilde{U}\tilde{n} = V_0$ so that outflow can occur. In the proposal of [203], it is also used to initiate outflow in the first place. However we have already seen that stable outflow can be initiated with a sudden jump in V to $V_0 < \tilde{U}\tilde{n}$ (Fig. 5.13). In such a situation, the density decreases if no piston is used because the reservoir empties. However, for a large reservoir the density decrease will be small. Due to strong three-body losses in the high density regime, required for a high T_H , we expect some degree of density reduction in any case. This makes it unclear whether an optical piston is in fact beneficial for our purpose. Let us now see if numerical results confirm these thoughts.

The points we wish to make in this section do not require 3D simulations and further necessitate large x domains. For now, we thus base our argumentation on solutions of the 1D GPE (5.33). We employ parameters for helium, $\omega_\perp = 6800 \times 2\pi$ Hz and a bulk density corresponding to $n_{3D} = 3.6 \times 10^{19}$, roughly as in table 5.2.

Fig. 5.15 highlights the differences between outflow initiation with and without piston. Due to the requirements of either scheme, we ran the piston case with $\tilde{\mu}_{1D} = V_0$ and the other case with $\tilde{\mu}_{1D} > V_0$, see the parameters given in the figure.

Consider panel (a). When the barrier at $x_r = 80$ is suddenly reduced, the interaction energy $\tilde{U}\tilde{n}$ exceeds V_0 and the BEC streams out. A wave within the reservoir resulting from the sudden change of the potential propagates left, hits the barrier there and reflects. At the last sample, $t = 490$, the reflection has reached the black hole. At this moment the density at the exit jumps down. Before, while the flow perturbation was propagating to the left and back, the density at the exit stayed roughly constant. Consequently, the Hawking temperature for this scenario, shown as the crosses in panel (d), remains constant until

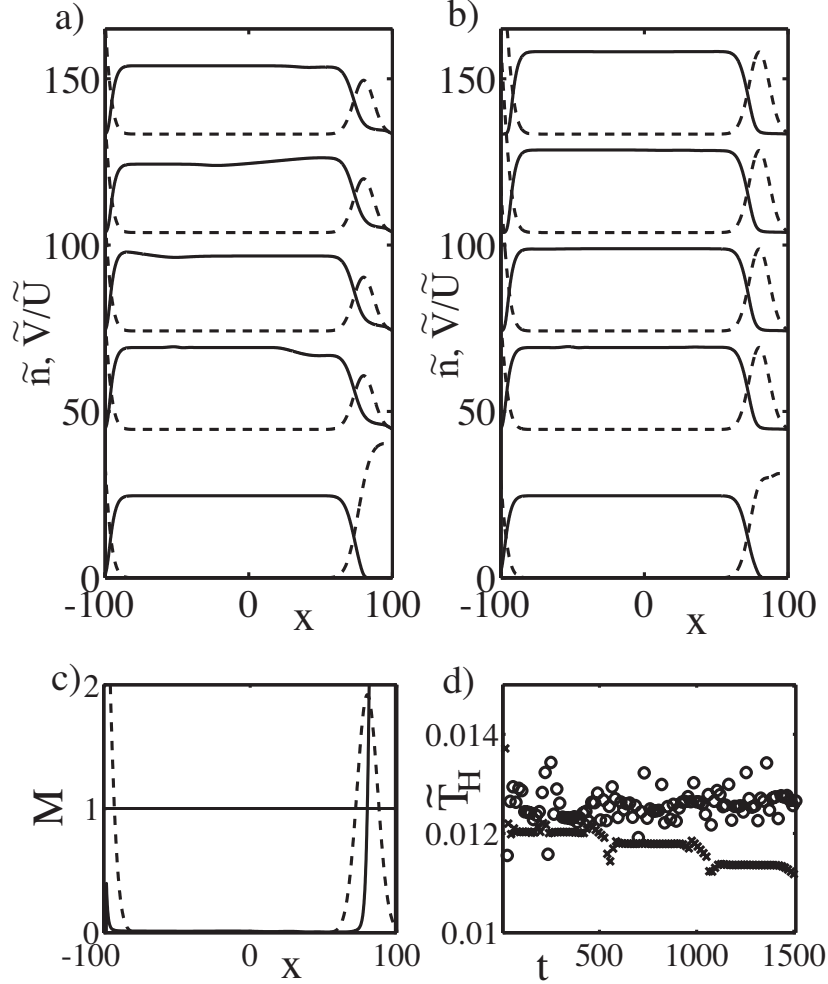


Figure 5.15: Initial time evolution of the condensate in the reservoir after initiation of the outflow. (a) Density (solid) and $\tilde{V}(x)/\tilde{U}_{1D}$ (dashed) for outflow with no piston. $\tilde{\mu}_{1D} = 0.61$, $\xi = 0.64$, $\sigma = 14 \simeq 22\xi$, $V_0 = 0.4$, $x_r = 80$, $x_l = -110$, $d = 0.5\sigma$. The time samples are $\tilde{t}=0, 60, 210, 390, 490$. They were chosen to illustrate the evolution as described in the text. Later time samples are shifted upwards as necessary. The zero of the common axes for \tilde{n} and \tilde{V} for later time samples can be deduced from $\tilde{V}(0) = 0$. (b) The same as in (a), but using the left potential as moving optical piston with $\tilde{v}_p = 0.01$. Also $\tilde{V}_0 = 0.61$, $\tilde{d} = \sigma$, all other parameters are as in panel (a). (c) Sample Mach number profile (solid, thick) for the case with piston. The thin black line indicates $M = 1$. (d) Comparison of analogue Hawking temperatures with (\circ) and without (\times) piston.

the reflected perturbation has returned to the hump. At this point it decreases suddenly to reflect the jump in density, only to again remain constant until the next reflection arrives. Over long times, \tilde{T}_H exhibits a step like profile.

In contrast, when the piston is used, the Hawking temperature remains on average at its initial value, but exhibits much stronger fluctuations. Both differences can be understood. The piston keeps the density at the hump approximately constant, hence the temperature does not reduce as in the no-piston case. However in the piston case $\tilde{\mu}_{1D} = V_0$. Because of this the density at the exit is a factor of four lower rendering it more susceptible to small perturbations.

Having traced the step like reduction of \tilde{T}_H in the absence of a piston to the arrival of a reflected flow perturbation from the hump potential, we argue that the reduction would not occur for sufficiently short times in a larger reservoir. As previously mentioned, larger reservoirs in a Q1D case should be much easier to realise experimentally than numerically²⁰. If a measurement is possible on short time scales, we would conclude from the results in this section that the piston is not required.

5.6.4 Effects of Three-Body-Loss

We know from section 5.3.4 that losses are a limiting factor for the analogue Hawking temperature, but we have not yet taken them into account in our simulations. This is done now, in simulations spanning a longer time and using a much larger x -domain than in the preceding section.

The intention is to minimise density reduction due to drain, in order to assess density reduction due to losses. For a reservoir of size 2200, the perturbation resulting from the outflow that we have seen in the preceding section does not reach the exit hump in the simulated time span of $t = 5000$. The parameters ω_\perp and \tilde{U}_{1D} are as before. We concentrate on the time evolution of the analogue Hawking temperature.

Also for these long times and in the presence of losses, we see no discernible advantage of the piston setup over free outflow, see Fig. 5.16. As predicted in section 5.3.4, three-body loss effects noticeably decrease the analogue Hawking temperature on the time scale of 50 ms, due to their influence on the condensate density. Note that the bulk interaction energy density of the initial state condensate $\tilde{U}_{1D}\tilde{n}_{bg} = \mu_{1D} = 0.61$ is significantly larger than the exit barrier height

²⁰We do not imply that an experiment is easier to do than a computer simulation. Only that *once* the experiment is set up, it can naturally realise large x domains in a tight waveguide.

$\tilde{A} = 0.5$, giving some room for a reduction of condensate density due to losses without an interruption of outflow²¹.

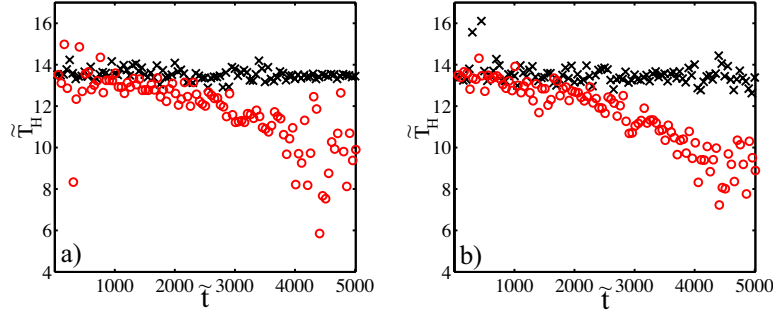


Figure 5.16: Time evolution of analogue Hawking temperature \tilde{T}_H for $\tilde{\mu}_{1D} = 0.61$, $V_0 = 0.5$. (a) Left end barrier acts as piston with $\tilde{v}_p = 0.01$. (\times -black) $\tilde{K}_{3,1D} = 0$. (\circ -red) $\tilde{K}_{3,1D} = 1.4 \times 10^{-7}$ (from table 5.1). (b) Left end barrier does not move. (\times -black) $\tilde{K}_{3,1D} = 0$. (\circ -red) $\tilde{K}_{3,1D} = 1.4 \times 10^{-7}$. $t = 5000$ corresponds to 117 ms.

5.6.5 Optimal Outflow Operation

As the culmination of this chapter, we performed a 3D simulation including loss, which shows the principal feasibility of the proposed experiment. The parameters were chosen to represent the optimal case according to table 5.2. Thus we consider a sodium condensate with $\omega_{\perp} = 6800 \times 2\pi$ Hz ($a_{\text{osc}} = 2.5 \times 10^{-7}$), resulting in $\tilde{n}_{3D} = 30$, which corresponds to $n_{3D} = 1.8 \times 10^{21}/m^3$. This gives $\tilde{\mu}_{3D} = 4.3$, which places the simulation between a Q1D case and a TTF. Further parameters were $V_0 = 2.8$, $\sigma = 6.8$. The sizes of our simulated BEC cloud were about 4 units or 1 μm diameter and 70 units or 17.5 μm length.

We find stable outflow with $\tilde{T}_H = 0.07$, in good agreement with the expectation of $\tilde{T}_H = 0.068$ from Eq. (5.39). For the assumed transverse confinement this equals 23 nK and thus realises the promised maximal achievable temperature. It decays slightly over the timespan of $\tilde{t} = 600$ or 14 ms of our simulation, largely due to the outflow loss. This reduces the density stronger than it would in an experiment due to our small x domain, forced by numerical limitations. A comparison of the atom number evolution with and without loss separates the three-body loss contribution to the reduction of the atom number from that due

²¹Interruption would occur once $\tilde{n}_{1D} < \tilde{A}/\tilde{U}_{1D}$.

to outflow. We find that 5% of our initial atoms are lost due to three-body recombination. This is in fair agreement with the expectation from our estimates in section 5.3.4, considering the more complicated situation here, arising from a density reduction due to the outflow itself. A movie of the transverse dynamics for this outflow scenario, `outflow_ooo_transverse.mov`, is included on the CD.

This simulation suggests that the Hawking temperatures proposed in table 5.2 can be realised under realistic conditions. The transverse confinement is tight but does *not* put the condensate completely into the Q1D regime.

5.6.6 Summary

In this last section of the thesis, we studied BEC flow out of a reservoir. We extended the result of [203], showing that a stable black hole horizon is formed in three dimensions. We have also shown this for cases that are far from quasi one-dimensional. Important observables were found to be robust with respect to perturbations propagating in the condensate cloud. We highlighted interesting properties of the transverse horizon shape. To simplify the proposed experiment, we considered an alternative to the optical-piston. Finally, we numerically investigated the effect of three-body loss on the proposed ideas.

Our final simulation, including all these features and valid for full three-dimensions, shows sonic horizon creation with the maximal achievable Hawking temperature under realistic conditions.

5.7 Conclusions

This concludes our quest to find the most suitable experimental setup for the task of detecting analogue Hawking radiation. To this end we have first rendered existing estimates regarding the achievable Hawking temperatures in a BEC more precisely and in particular pointed out the large differences in these limits between common BEC atom species. We have also compiled a list of desirable horizon properties.

We then embarked on the exploration of several concrete scenarios for horizon creation. Supersonic optical tunnels, a subject of chapter 4, were never before studied. We showed that they can provide grey solitons, which are for long times immobile in the lab frame, and exhibit supersonic flow. We put forward the speculative idea to utilise the associated sonic horizons to probe the validity boundaries of the Hawking effect: These horizons are immersed in too rapidly

varying a flow for a sonic horizon in the hydrodynamic regime, but the low limits on hydrodynamic Hawking temperatures motivate us to seek alternatives.

For the remainder of the chapter we studied simpler systems that can be reduced to effectively one dimension. There we demonstrated that outcoupling induced horizons in an atom laser cloud appear within the outcoupling region. If the outcoupling region is adjacent to an optically generated hump potential, a potentially interesting scenario can occur: We highlighted a case with a black and white hole pair, in which the dynamical instabilities of the white hole do not perturb the black hole for long times.

Finally, we concentrated on what appears to be the cleanest system for analogue Hawking radiation: simple outflow from a reservoir. We performed simulations including the transverse dimension, and found that the value for the maximal analogue Hawking temperature that we derived should be realisable in such a system, under realistic conditions despite loss effects.

Along the way, we learnt that we are not yet in a position to answer the question: “Which is the most suitable experimental setup for the detection of analogue Hawking radiation?”. This is because we discovered or clarified several issues that require further investigation before reaching a conclusive answer. More research is particularly required on the detailed method with which to detect the analogue Hawking effect and the most general physical conditions for horizon radiation to occur. However, due to the breadth of ideas that we propose, a realistic experiment for most possible answers to these questions might be among them. If a switching between sub and supersonic flows turns out to be crucial for a detectable analogue Hawking signature, the atom laser hump flow of section 5.5.3 is the setup of choice. For the highest possible Hawking temperature in the hydrodynamic regime reservoir outflow appears most flexible, section 5.6. Finally, if further studies predict quantum particle creation by a sonic horizon outside of the hydrodynamic regime, the immobile soliton of section 5.4 provides a system where these can be studied without condensate drain. Tolerating the drain, non-hydrodynamic horizons would also be created more easily in a reservoir outflow.

Altogether, experimental physics might be in a position to answer some of the open questions regarding the analogue Hawking effect.

Despite the open questions, we can draw some concrete conclusions: Either the analogue Hawking temperatures will be low, or the phonon detection must be fast, so that losses do not have enough time to affect the experiment, section 5.3.4. The choice of atom is here an important one. Due to dynamical instabilities of white holes, the reservoir outflow proposed by Giovanazzi *et al.* [203] appears to

be the simplest and most robust way to create a sonic horizon. We have shown, in simulations valid for three dimensional setups, that analogue Hawking temperatures of about 23 nK should be achievable in sodium condensates. However, losses affect the signal by more than 10% over 50 ms.

The results showing the creation of grey soliton trains in the optical tunnel created by an optical vortex, as well as the long time immobile single soliton, have been submitted together with our work on stabilised high-charge ring flows for publication [187]. The remaining results of this chapter are currently being prepared for publication.

Chapter 6

Conclusions

In this thesis we studied how Bose-Einstein condensates can be used for the simulation of physical phenomena that are difficult to access in their natural habitats. In particular we addressed three questions: Is our understanding of the quantum-field theory for ultracold atoms good enough to use collapsing condensate experiments as quantitative analogue systems for the inflationary epoch of the Universe's expansion? Do present day experiments allow the creation of Skyrmions in BECs, objects originating from the realm of particle physics? Can analogue Hawking radiation be realised in present day BEC experiments?

Throughout the thesis significant progress has been made towards the answers to all three questions. In chapter 3, we found that the time it takes a condensate with attractive interactions to collapse is presently not captured by our theory. Further experimental and theoretical research to solve the mystery would be necessary, before quantitative use of the analogy between cosmic inflation and collapsing BECs can be made. Qualitative studies might however already be possible, using the methods that we have demonstrated.

According to chapter 4, Skyrmions can be created within present day experiments, but not without overcoming some challenges. Skyrmions prove to be structures that are highly sensitive to a variety of experimental parameters, which have to be carefully adjusted for stable Skyrmions to exist. Because of this, our detailed investigations of the relevant parameter space will be invaluable for any serious attempt to create Skyrmions. Since we have performed our investigations the experimental feasibility of Skyrmions has been continuously increasing. Instabilities become generally easier to control as the Skyrmion gets bigger, and experimentally tractable atom numbers are rising all the time. Our studies also strengthen the case for experimental studies of Skyrmions, by showing the rich-

ness of the system. Effects of the breakdown of superfluidity, surface tension and vortex generation can all be found within Skyrmions. Furthermore, we have found a stepping stone towards Skyrmion creation. We proposed a novel method to stabilise ring vortices in a BEC, which are an integral part of a Skyrmion. This method can further stabilise ring flows with high charges.

The final question, as to the most suitable experiment for the detection of analogue Hawking radiation, proved the most challenging. A conclusive answer requires deeper studies of suitable detection schemes for the analogue Hawking effect, and the minimal set of conditions under which it occurs. These studies do not fit into the scope of this thesis. However, we were able to propose a whole array of setups, catering for various outcomes of future research into these open questions. In devising the schemes, we were continuously cautious about experimental realisability. Within chapter 5 we have reached two main conclusions: Firstly, three-body loss effects will play a major role in any kind of analogue Hawking radiation experiment, limiting the horizon temperatures to about 20 nK, and rendering light atomic species better suited for our cause. Secondly, within these constraints, our simulations show the possibility of dynamical sonic horizon creation by outflow from a reservoir, including loss effects and a transverse dimension.

Our research should contribute to the future applications of Bose-Einstein condensates in interdisciplinary physics. Experiments in three subject areas are shown to be feasible with present technology. We hope that such endeavours will benefit from the investigations that we have performed.

We have also seen that even though we started out to study classical and quantum field theory of Bose-Einstein condensates, our research took us beyond these from quantum scattering theory, to cosmology and particle physics, to nonlinear physics and atomic physics, and further to general relativity and fluid mechanics. It is our hope, that the reader enjoyed this tour through physics as much as we did.

The End

Appendix A

Renormalisation of Resonance Theory using Feynman Diagrams

In section 2.4.4 we introduced a non-relativistic quantum field theory of coupled atoms and molecules. Since the couplings between the atoms and between atoms and molecules are of a contact type, the resulting local quantum field theory will suffer from ultraviolet divergences. Renormalisation absorbs these divergences into the parameters of the Hamiltonian, such that all calculated physical parameters are finite. The starting point is the renormalisation condition: We require that the quantum scattering of low energy atoms has the correct resonant behavior near a Feshbach resonance.

Let's consider the quantum scattering of atoms which are at time $t = -\infty$ in the state $|\Psi\rangle = |\mathbf{p}_1, \mathbf{p}_2\rangle$, with momenta \mathbf{p}_1 and \mathbf{p}_2 (the state is assumed appropriately symmetrized). The evolution of $|\Psi\rangle$ through the scattering event is determined by the time evolution operator $\hat{U}(t_i, t_f)$ [31]. We now define the S-matrix \hat{S} by $\hat{S} = \lim_{\substack{t_f \rightarrow +\infty \\ t_i \rightarrow -\infty}} \hat{U}(t_f, t_i)$ [31]. Let $S(k)$ denote the matrix element of \hat{S} between the states $|\Psi\rangle$, where k denotes the wave number of the scattering particles in the centre of mass frame. It is customary to split off the trivial part containing no interactions by defining the T-matrix $T(k) = \frac{2\pi\hbar^2 i}{mk} (S(k) - 1)$ [71, 80].

In terms of the matrix element of interest, the renormalisation condition can be written as:

$$T(k) = U_{bg} + \frac{g^2/2}{(E + \nu)}. \quad (\text{A.1})$$

Here U_{bg} is the strength of nonresonant atomic background interactions, ν is the energy difference between the molecular bound state that gives rise to the

Feshbach resonance and a pair of unbound atoms, and E is the centre of mass energy of the scattering atoms. g denotes the strength of the coupling between molecular and free atomic states and therefore controls the width of the resonance.

To carry out the renormalisation, the prediction for the scattering amplitude $T(k)$ of the Hamiltonian (2.1), including the molecular part (2.59), has to be calculated and compared with Eq. (A.1). In [80] this has been done using a coupled channels Schrödinger equation approach. Here we present an alternative but equivalent derivation, using Feynman diagrams of the non-relativistic atom-molecule theory.

A.1 Lagrangian and Feynman Rules

In the following we will present a brief sketch of the application of Feynman diagram techniques. The underlying idea is to expand the time-evolution operator of the system (or equivalently transition matrix elements between scattering states) in the framework of time-dependent perturbation theory. Mathematically this can be done either using canonical quantisation of the fields and an operator formalism [32, 71], or in the path integral formulation of quantum mechanics [31, 32, 71]. Either way one finds a set of rules, which allow us to write down the amplitude for scattering events directly from the Lagrangian of the interacting quantum field theory. These rules are known as Feynman rules. For an in-depth justification we refer the interested reader to Refs. [32, 71].

The Lagrangian corresponding to the Hamiltonian (2.1), including the additional terms (2.59) and assuming a vanishing external potential $V(\mathbf{x})$, is obtained by a Legendre transformation. The result is:¹

$$L = \int d^3\mathbf{x} \left\{ \hat{\Psi}_a^\dagger(\mathbf{x}) \left(i\hbar \frac{\partial}{\partial t} + \frac{\hbar^2}{2m} \nabla_x^2 \right) \hat{\Psi}_a(\mathbf{x}) + \hat{\Psi}_m^\dagger(\mathbf{x}) \left(i\hbar \frac{\partial}{\partial t} + \frac{\hbar^2}{4m} \nabla_x^2 + \nu_0 \right) \hat{\Psi}_m(\mathbf{x}) \right. \\ \left. - \frac{U_0}{2} \hat{\Psi}_a^\dagger(\mathbf{x}) \hat{\Psi}_a^\dagger(\mathbf{x}) \hat{\Psi}_a(\mathbf{x}) \hat{\Psi}_a(\mathbf{x}) - \frac{g_0}{2} \left(\hat{\Psi}_m^\dagger(\mathbf{x}) \hat{\Psi}_a(\mathbf{x}) \hat{\Psi}_a(\mathbf{x}) + h.c. \right) \right\}. \quad (\text{A.2})$$

Particles can scatter via the interaction terms in Eq. (A.2). For a scattering event we draw a so-called *vertex* in our Feynman diagram, as shown in Fig. A.1. Between scattering events particles propagate freely, symbolised by the *propagator* lines in Fig. A.1. These are derived from the free part of Eq. (A.2), which is quadratic in field operators.

¹Note that the definition of ν_0 implicit in Eq. (A.2) differs from that of Ref. [80] by the sign.

As quantum mechanics dictates that all possible intermediate states contribute to a scattering event, we now have to draw all possible diagrams, consisting of propagators connected with vertices, whose initial and final states are consistent with our scattering process. For example, Fig. A.2 lists all possible diagrams with two free atoms in the initial and final states. Such a diagrammatic expansion is most useful, when the coupling constants involved are small. Then we only need to draw a finite number of diagrams for a given precision. It is however possible to use Feynman diagram techniques for large couplings, if the structure of the diagrams allows us to actually identify all possible contributions even if their number is infinite. This is the situation that we encounter for atom-molecule resonance theory.

To finally write down the scattering amplitude corresponding to each diagram we make use of the Feynman rules listed in Fig. A.1. For all propagators and vertices of the diagram, we multiply the corresponding expressions. We impose momentum and energy conservation at each vertex. In diagrams that contain closed loops, the energy and momentum assignment is not fixed by this condition. This creates unconstrained loop wave numbers \mathbf{l} and energies E_l . Summing up all intermediate states, each loop necessitates an integration $\int \frac{dE_l}{(2\pi\hbar)} \int \frac{d^3\mathbf{l}}{(2\pi)^3}$. The overall factors of the vertices have been chosen such that they already incorporate the number of possible connections to external lines.

A.2 Summation of Ladder Diagrams

For the calculation of the amplitude for low energy atom scattering from these Feynman diagrams, it is not sufficient to consider only the lowest order, since the couplings U_0, g_0 are not small for a realistic situation. However the simple structure of the theory makes it possible to sum contributing diagrams to all orders of perturbation theory, thus obtaining a non-perturbative result. Analytically this summation of an infinite number of Ladder diagrams is done by means of the Lippmann-Schwinger equation, depicted diagrammatically in Fig. A.2. We could alternatively sum an infinite number of ladder diagrams by arranging them in a geometric series.

The transition matrix element read off the diagrams in Fig. A.1 using the

propagators:

$$\begin{array}{c} \text{Atom} = \frac{i\hbar}{E - \frac{\hbar^2}{2m}\mathbf{k}^2 + i\epsilon} \\ (E, \mathbf{k}) \end{array} \quad \begin{array}{c} \text{Molecule} = \frac{i\hbar}{E - \frac{\hbar^2}{4m}\mathbf{k}^2 + \nu_0 + i\epsilon} \\ (E, \mathbf{k}) \end{array}$$

vertices:

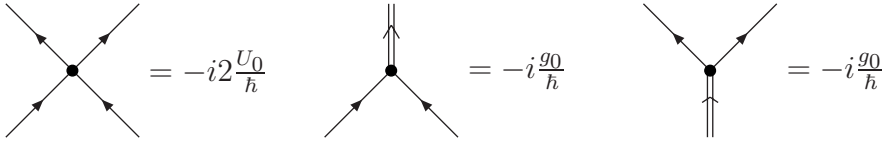


Figure A.1: Momentum space Feynman rules for atom-molecule resonance theory. Single lines represent atoms and double lines molecules. The propagators are obtained as Fourier-transform of the inverse terms quadratic in fields in Eq. (A.2). Interaction vertices follow from the structure of the interaction terms in Eq. (A.2), taking into account the number of possible permutations in the assignment of particles to the external “legs” in the assigned factors. Labels like (E, \mathbf{k}) define the energy and wave number of propagating particles.

momentum space Feynman rules is:

$$\begin{aligned} -\frac{i}{\hbar}T(E, \mathbf{p}, \mathbf{k}) &= -i2\frac{U_0}{\hbar} + \frac{(ig_o)^2 i\hbar}{\hbar^2(E + \nu_o + i\epsilon)} \\ &+ \frac{1}{2} \left(-i2\frac{U_0}{\hbar} + \frac{i\hbar(ig_o)^2}{\hbar^2(E + \nu_o + i\epsilon)} \right) \\ &\times \int \frac{dE_l}{(2\pi\hbar)} \int \frac{d^3l}{(2\pi)^3} \frac{-(i\hbar)^2 \frac{i}{\hbar} T(\frac{E}{2} + E_l, \mathbf{l}, \mathbf{k})}{\left(\frac{E}{2} + E_l - \frac{\hbar^2}{2m}\mathbf{l}^2 + i\epsilon\right) \left(\frac{E}{2} - E_l - \frac{\hbar^2}{2m}\mathbf{l}^2 + i\epsilon\right)}. \end{aligned} \quad (\text{A.3})$$

The contribution from the loop diagrams had to be divided by a symmetry factor of 2. [71].² In Eq. (A.4) we consider the scattering of two distinct particles with energies and momenta $(E/2, \mathbf{p})$ and $(E/2, -\mathbf{p})$.

The energy loop integral can be done with the residue theorem, closing the integration contour in the upper complex plane and picking up the residue at

²We included the number of possible connections to propagators in the vertex factors. In the diagrams in question this overcounts the number of possibilities, as these diagrams are invariant under exchange of the atomic propagators in the loop.

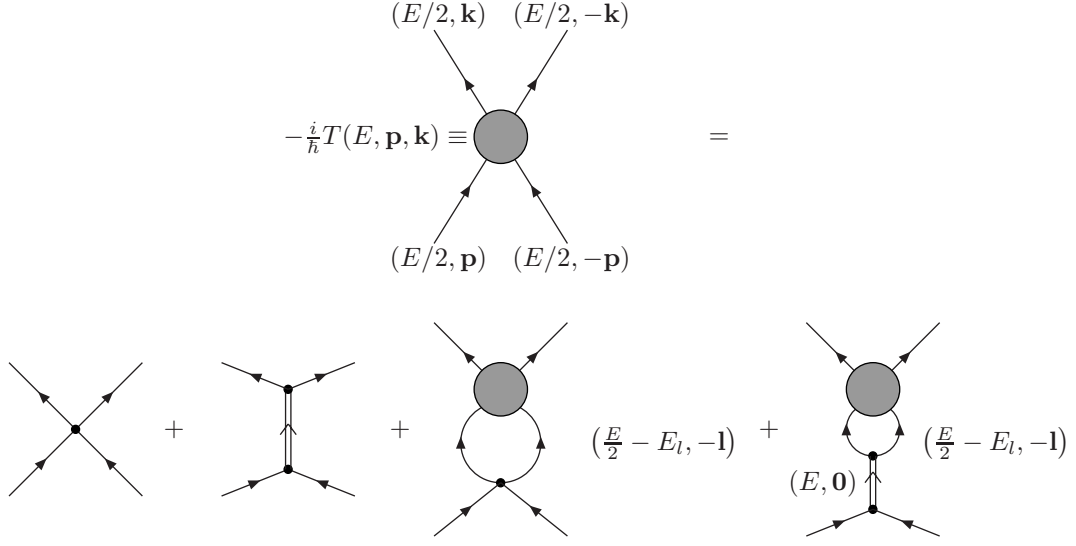


Figure A.2: Lippmann-Schwinger equation for the 2-body scattering amplitude; the shaded circle represents the sum of all possible diagrams with the appropriate external legs. The assignment of energies and momenta to the external legs for all diagrams is as for the first. The last two diagrams contain unconstrained loop variables \mathbf{l} and E_l . In assigning energies and momenta to the propagators, \mathbf{l} and E_l can be assumed to “flow in a loop”. E_l is thus added to the external energy for one of the atomic propagators in the third diagram of the bottom line, and subtracted for the other. The sum yields an implicit integral equation for T .

$E_l = E/2 - \hbar^2/(2m)\mathbf{l}^2 + i\epsilon$. The result is:

$$\begin{aligned}
 & \int \frac{dE_l}{(2\pi\hbar)} \int \frac{d^3\mathbf{l}}{(2\pi)^3} \frac{-(i\hbar)^2 \frac{i}{\hbar} (-1) T(\frac{E}{2} + E_l, \mathbf{l}, \mathbf{k})}{(\frac{E}{2} + E_l - \frac{\hbar^2}{2m}\mathbf{l}^2 + i\epsilon) (E_l - (\frac{E}{2} - \frac{\hbar^2}{2m}\mathbf{l}^2 + i\epsilon))} \\
 &= \int \frac{d^3\mathbf{l}}{(2\pi)^3} \frac{T(E - \frac{\hbar^2}{2m}\mathbf{l}^2, \mathbf{l}, \mathbf{k})}{E - \frac{\hbar^2}{m}\mathbf{l}^2 + i\epsilon} \\
 &= \frac{m}{\hbar^2} \int \frac{d^3\mathbf{l}}{(2\pi)^3} \frac{T(E - \frac{\hbar^2}{2m}\mathbf{l}^2, \mathbf{l}, \mathbf{k})}{\mathbf{p}^2 - \mathbf{l}^2 + i\epsilon}. \tag{A.4}
 \end{aligned}$$

In the last step E was expressed as $\hbar^2\mathbf{p}^2/m$. We now reached an implicit integral equation for T , the Lippmann-Schwinger equation:

$$\frac{i}{\hbar} T(E, \mathbf{p}, \mathbf{k}) = 2 \frac{i}{\hbar} \left(U_0 + \frac{g_0^2}{2(E + \nu_o)} \right) \left(1 + \frac{m}{2\hbar^2} \int \frac{d^3\mathbf{l}}{(2\pi)^3} \frac{T(E - \frac{\hbar^2}{2m}\mathbf{l}^2, \mathbf{l}, \mathbf{k})}{\mathbf{p}^2 - \mathbf{l}^2 + i\epsilon} \right). \tag{A.5}$$

We are interested in scattering only in the s-wave domain (see section 1.2.2), hence T does not have an angular dependence and incoming and outgoing wave numbers are identical. This allows us to write $T(E, \mathbf{p}, \mathbf{k}) \sim T(E, |\mathbf{p}|)$ and approximate $T(E - \frac{\hbar^2}{2m}\mathbf{l}^2, \mathbf{l}, \mathbf{k}) \sim T(E, |\mathbf{p}|)$ [80]. We obtain:

$$\begin{aligned} \frac{i}{\hbar}T(E, |\mathbf{p}|) &= 2\frac{i}{\hbar}\left(U_0 + \frac{g_0^2}{2(E + \nu_o)}\right)\left(1 + \frac{m}{2(2\pi)^3\hbar^2}T(E, |\mathbf{p}|)\int \frac{d^3\mathbf{l}}{(2\pi)^3}\frac{1}{\mathbf{p}^2 - \mathbf{l}^2 + i\epsilon}\right) \\ &= 2\frac{i}{\hbar}\left(U_0 + \frac{g_0^2}{2(E + \nu_o)}\right) \\ &\times \left[1 - \frac{m}{2(2\pi)^3}T(E, |\mathbf{p}|)(4\pi)\left(K - |\mathbf{p}|\operatorname{arctanh}\left(\frac{|\mathbf{p}|}{K}\right) + i\frac{\pi}{2}|\mathbf{p}|\right)\right] \end{aligned} \quad (\text{A.6})$$

In the limit of small $|\mathbf{p}|$, we can solve this to

$$T(E/2, |\mathbf{p}| \sim 0) = 2\frac{U_0 + \frac{g_0^2}{2(E + \nu_o)}}{1 + \left(U_0 + \frac{g_0^2}{2(E + \nu_o)}\right)\frac{m}{2\pi^2\hbar^2}K}. \quad (\text{A.7})$$

When finally comparing Eq. (A.7) with Eq. (A.1) we have to be careful not to double count identical particles in the final state [71]. This removes the overall factor of two in Eq. (A.7).

Our first renormalisation condition is now that Eq. (A.7) be equal to the background scattering strength U , if no molecular bound state is present ($g_0 = 0$), resulting in:

$$U_0 = \frac{U}{1 - \alpha U}, \quad \alpha = \frac{mK}{2\pi^2\hbar^2}. \quad (\text{A.8})$$

Substituting this into Eq. (A.7) gives for $\mathbf{p} \rightarrow 0$:

$$T(E/2, 0) = \frac{(E + \nu_o)\frac{U}{1 - \alpha U} + g_0^2/2}{(E + \nu_o)\frac{1}{1 - \alpha U} + g_0^2\alpha/2} = \frac{U(E + \nu) + g^2/2}{E - \nu}. \quad (\text{A.9})$$

The last equality is our second renormalisation condition, demanding that the low energy scattering matrix should have the resonance shape of Eq. (A.1). If we multiply numerator and denominator of the right hand side with $1/(1 - \alpha U)$ for convenience we achieve equality if

$$g_0 = \frac{g}{1 - \alpha U}, \quad \nu = \nu_o + \alpha\frac{g_0^2}{2}(1 - \alpha U) = \nu_o + \alpha\frac{g_0 g}{2}. \quad (\text{A.10})$$

in agreement with [80].

Appendix B

Implementation of the Hartree-Fock-Bogoliubov Equations for Spherical Symmetry

This appendix provides the link between our original form of the coupled HFB equations for the condensate and atomic correlations, Eqns. (2.47)-(2.49), and the particular adaptation to spherical symmetry that we employ in section 3.4. In line with all our theory in chapter 2, the HFB approach was derived in the full three-dimensions, which leaves us with six dimensional correlation functions. Unless a numerical representation of the correlation dynamics can be achieved with unusually few discrete data points per dimension, PDEs in six dimensions require more than commonly available computational resources.

Our situation of interest, the JILA experiment on collapsing BECs [28], represents a cylindrically symmetric situation, but even exploiting this symmetry the correlation functions are still five dimensional and the equations hence too difficult to solve. As described in section 3.3, we circumvent this problem by modeling the experiment as closely as possible with a spherically symmetric solution. Exploiting spherical symmetry, the correlation functions depend only on three independent variables. The idea behind this dimensionality reduction is sketched in Fig. B.1 and explained in the figure's caption.

The interaction terms in Eqns. (2.47)-(2.49) transform easily into our new set

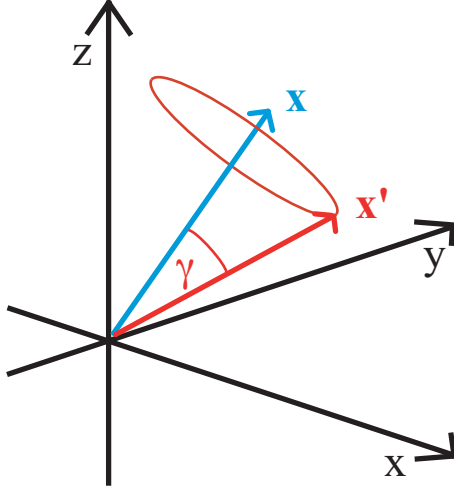


Figure B.1: Simplification of correlation functions in spherical symmetry. The correlation functions in three dimensions are originally parametrised by the vectors \mathbf{x} , \mathbf{x}' . Let us first choose \mathbf{x} (blue). Due to symmetry its orientation is arbitrary; only the length $R = |\mathbf{x}|$ is meaningful. Now we add \mathbf{x}' (red). Having selected a specific \mathbf{x}' and hence $R' = |\mathbf{x}'|$, we can rotate \mathbf{x}' around the axis $\hat{\mathbf{x}}$ as indicated by the red circle, keeping the angle γ between \mathbf{x} and \mathbf{x}' fixed. By symmetry, all these pairs of locations \mathbf{x} , \mathbf{x}' must experience identical atom field correlations. Remembering that the original orientation of \mathbf{x} was also arbitrary, we conclude that in a spherically symmetric system the correlation functions $G_{A/N}(\mathbf{x}, \mathbf{x}')$ depend only on R , R' and γ and write: $G_{A/N}(R, R', \gamma)$.

of coordinates, e.g.

$$\begin{aligned} U_0 \left[\bar{G}_A(\mathbf{x}) G_A^*(\mathbf{x}, \mathbf{x}') - \bar{G}_A^*(\mathbf{x}') G_A(\mathbf{x}, \mathbf{x}') \right] &\rightarrow \\ U_0 \left[\bar{G}_A(R) \bar{G}_A^*(R, R', \gamma) - \bar{G}_A^*(R') \bar{G}_A(R, R', \gamma) \right] \end{aligned} \quad (\text{B.1})$$

More work is required for the transformation of the kinetic energy terms. We first define spherical polar coordinates R , θ , φ for \mathbf{x} and R' , θ' , φ' for \mathbf{x}' . The laplacian ∇^2 in these coordinates is [224]:

$$\nabla_{\mathbf{x}}^2 = \frac{1}{R^2} \frac{\partial}{\partial R} \left(R^2 \frac{\partial}{\partial R} \right) + \frac{1}{R^2 \sin \theta} \frac{\partial}{\partial \theta} \left(\sin \theta \frac{\partial}{\partial \theta} \right) + \frac{1}{R^2 \sin^2 \theta} \frac{\partial^2}{\partial \varphi^2}, \quad (\text{B.2})$$

and similarly for $\nabla_{\mathbf{x}'}^2$. Using the definition $\beta = \cos \gamma$, where γ is the angle between \mathbf{x} , \mathbf{x}' shown in Fig. B.1, we have in the above spherical coordinates:

$$\beta = \cos \theta \cos \theta' + \cos(\varphi - \varphi') \sin \theta \sin \theta'. \quad (\text{B.3})$$

As argued above, correlation functions do not depend on any other combinations of angles. We can thus replace¹

$$\frac{\partial}{\partial\theta} \rightarrow (\cos\theta\sin\theta'\cos(\varphi-\varphi') - \sin\theta\cos\theta')\frac{\partial}{\partial\beta}, \quad (\text{B.4})$$

$$\frac{\partial}{\partial\theta'} \rightarrow (\cos\theta'\sin\theta\cos(\varphi-\varphi') - \sin\theta'\cos\theta)\frac{\partial}{\partial\beta}, \quad (\text{B.5})$$

$$\frac{\partial}{\partial\varphi} \rightarrow -\sin\theta'\sin\theta\sin(\varphi-\varphi')\frac{\partial}{\partial\beta}, \quad (\text{B.6})$$

$$\frac{\partial}{\partial\varphi'} \rightarrow \sin\theta'\sin\theta\sin(\varphi-\varphi')\frac{\partial}{\partial\beta}. \quad (\text{B.7})$$

Using these expressions we can for example write:

$$\begin{aligned} & \frac{1}{\sin\theta R^2}\frac{\partial}{\partial\theta}\left(\sin\theta\frac{\partial}{\partial\theta}\right) \\ &= \frac{1}{\sin\theta R^2}\frac{\partial}{\partial\theta}\left(\sin\theta[\cos\theta\sin\theta'\cos(\varphi-\varphi') - \sin\theta\cos\theta']\frac{\partial}{\partial\beta}\right) \\ &= \frac{1}{\sin\theta R^2}(\cos(2\theta)\sin\theta'\cos(\varphi-\varphi') - 2\cos\theta\cos\theta'\sin\theta)\frac{\partial}{\partial\beta} \\ &+ \frac{1}{R^2}(\cos\theta\sin\theta'\cos(\varphi-\varphi') - \cos\theta'\sin\theta)\frac{\partial}{\partial\theta}\frac{\partial}{\partial\beta}. \end{aligned} \quad (\text{B.8})$$

The derivative $\partial/\partial\theta$ in the last line can also be replaced using Eq. (B.4). Again using the symmetry, we can choose the angles $\theta, \theta', \varphi, \varphi'$ to simplify the problem, knowing that the physics depends only on β . We choose $\theta = \theta' = \pi/2, \varphi = 0$ and $\cos\varphi' = \beta$.

Transforming the remaining part of Eq. (B.2) and using this simplifying choice of angles we finally obtain:

$$\begin{aligned} \nabla_{\mathbf{x}}^2 &= \frac{1}{R^2}\frac{\partial}{\partial R}\left(R^2\frac{\partial}{\partial R}\right) - \frac{2\beta}{R^2}\frac{\partial}{\partial\beta} + \frac{1-\beta^2}{R^2}\frac{\partial^2}{\partial\beta^2}, \\ \nabla_{\mathbf{x}'}^2 &= \frac{1}{R'^2}\frac{\partial}{\partial R'}\left(R'^2\frac{\partial}{\partial R'}\right) - \frac{2\beta}{R'^2}\frac{\partial}{\partial\beta} + \frac{1-\beta^2}{R'^2}\frac{\partial^2}{\partial\beta^2}. \end{aligned} \quad (\text{B.9})$$

The angular parameter β is defined between 1 and -1 . We can thus expand the β -dependence of the correlation functions in terms of Legendre polynomials

¹Formally, partial derivatives with respect to further new angular variables should appear on the right hand side. We ignore those when the derivative operator is acting on correlation functions, as they only depend on β .

$$P_n(\beta)$$

$$\begin{aligned}\tilde{G}_N(R, R', \beta) &= \sum_{n=0}^{M-1} G_N^{(n)}(R, R') P_n(\beta), \\ \tilde{G}_A(R, R', \beta) &= \sum_{n=0}^{M-1} G_A^{(n)}(R, R') P_n(\beta),\end{aligned}\quad (\text{B.10})$$

where M is the number of Legendre polynomials employed. Legendre Polynomials fulfill the relations

$$\int_{-1}^1 P_n(\beta) P_m(\beta) d\beta = \frac{2\delta_{n,m}}{2n+1}, \quad (\text{B.11})$$

$$\left((1 - \beta^2) \frac{\partial^2}{\partial \beta^2} - 2\beta \frac{\partial}{\partial \beta} \right) P_n(\beta) = -n(n+1) P_n(\beta), \quad (\text{B.12})$$

$$(n+1)P_{n+1}(\beta) = (2n+1)\beta P_n(\beta) - nP_{n-1}(\beta), \quad (\text{B.13})$$

$$(\beta^2 - 1) \frac{dP_n(\beta)}{d\beta} = \frac{n(n+1)}{2n+1} (P_{n+1}(\beta) - P_{n-1}(\beta)). \quad (\text{B.14})$$

Using the expansion in Legendre polynomials, the normal and anomalous densities reach a simple form:

$$\begin{aligned}\bar{G}_{N/A}(R) &= \bar{G}_{N/A}(\mathbf{x}) \equiv G_{N/A}(\mathbf{x}, \mathbf{x}) = G_{N/A}(R, R, \beta = 1) \\ &= \sum_{n=0}^{M-1} G_{N/A}^{(n)}(R, R) P_n(1) = \sum_{n=0}^{M-1} G_{N/A}^{(n)}(R, R).\end{aligned}\quad (\text{B.15})$$

In the last step we have used that $P_n(1) = 1 \forall n$.

We now insert Eq. (B.10) into Eqns. (2.47)-(2.49), write the Laplacians in the form Eq. (B.9) and employ the eigenvalue equation Eq. (B.12). In the next step we project onto the equation for the n 'th coefficient in the expansion Eq. (B.10) with the help of Eq. (B.11).

At this point it is useful to define functions $\tilde{\phi}_a(R)$, $\tilde{G}_{N/A}^{(n)}$ by:

$$\phi_a(R) = \frac{\tilde{\phi}_a(R)}{R}, \quad G_{N/A}^{(n)}(R, R') = \frac{\tilde{G}_{N/A}^{(n)}(R, R')}{RR'}, \quad (\text{B.16})$$

and consider equations of motion for these. This redefinition reduces the radial derivatives in Eq. (B.9) to simple second derivatives with respect to R or R' and thus allows the use of much faster interaction picture algorithms for the numerical solution of our final equations.

To reach the final result, Eqns. (3.7)-(3.9) in section 3.4, we have to express the delta function in Eq. (2.48) in our new choice of coordinates. In spherical polar coordinates it becomes

$$\delta(\mathbf{x} - \mathbf{x}') = \frac{1}{2\pi R^2} \delta(R - R') \delta(\beta - 1). \quad (\text{B.17})$$

The normalisation coefficient $1/2\pi R^2$ can be found by integrating the delta function over all space and demanding a unit result.

When we project the relevant part of Eq. (2.48) onto the n 'th Legendre component we get:

$$\begin{aligned} i\hbar \int_{-1}^1 d\beta P_n(\beta) \sum_{m=0}^{M-1} P_m(\beta) \frac{\partial \tilde{G}_A^{(m)}(R, R')}{\partial t} \\ = \dots + U_o \left(\tilde{\phi}(R)^2 + \bar{G}_A(R) \right) \int_{-1}^1 d\beta P_n(\beta) \delta(\mathbf{x} - \mathbf{x}') \Rightarrow \\ i\hbar \frac{2}{2n+1} \frac{\partial \tilde{G}_A^{(n)}(R, R')}{\partial t} \\ = \dots + U_o \left(\tilde{\phi}(R)^2 + \bar{G}_A(R) \right) \frac{1}{2\pi R^2} \delta(R - R') P_n(1) \Rightarrow \\ i\hbar \frac{\partial \tilde{G}_A^{(n)}(R, R')}{\partial t} \\ = \dots + U_o \left(\tilde{\phi}(R)^2 + \bar{G}_A(R) \right) \frac{2n+1}{4\pi R^2} \delta(R - R'). \end{aligned} \quad (\text{B.18})$$

The remaining delta function $\delta(R - R')$ is approximated by a step function of height $1/\Delta R$ on the discrete numerical grid.

An inspection of our final result, Eqns. (3.7)-(3.9), shows that different Legendre components are in fact only coupled via the normal and anomalous densities $\bar{G}_{N/A}(R)$. This feature of the equation renders them particularly suitable for parallel computation. Different Legendre components of the correlation functions can be distributed among separate processors, which then only have to communicate each discrete time step to compute the $\bar{G}_{N/A}(R)$.

The original coordinates R, R', γ that we use here to represent the correlation functions have been previously studied in the Honours thesis of D. Grimm, and we have benefited from these studies. This concludes our summary of the most important technical steps in the actual implementation of Eqns. (2.47)-(2.49) for a spherically symmetric situation.

Appendix C

Topological Structures: Initial States and Winding Numbers

In this appendix, we provide detailed information that will be of use primarily for the reader interested in numerically creating Skyrmion states themselves. The first step is of course the correct creation of a seeding state with the Skyrmion topology for the imaginary time evolution. We use the parametrisation Eq. (4.3). The overall density profile n is chosen reminiscent of the Thomas-Fermi approximation for a single component BEC:

$$n(\mathbf{x}) = \frac{\bar{\mu} - V}{\bar{U}}, \quad (\text{C.1})$$

$$\bar{U} = \frac{U_{11} + U_{22} + 2U_{12}}{4}, \quad (\text{C.2})$$

$$\bar{\mu} = \frac{1}{2^{9/5}} \left(\frac{15}{\pi} (N_1 + N_2) \bar{U} \omega_x \omega_y \omega_z \right)^{2/5}. \quad (\text{C.3})$$

Here V and the other parameters are as defined in section 4.1.4.¹

The Skyrmion profile function $\lambda(\mathbf{x})$ is taken as

$$\lambda(\mathbf{x}) = \pi \left[\frac{2}{\pi} \arctan \left(\frac{\tilde{r}}{2} \right) + (1 - \exp(-\tilde{r}^6)) \left(1 - \frac{2}{\pi} \arctan \left(\frac{\tilde{r}}{2} \right) \right) \right], \quad (\text{C.4})$$

$$\tilde{r} = \frac{1}{\sqrt{2}} \sqrt{\frac{x^2}{\sigma_x^2} + \frac{y^2}{\sigma_y^2} + \frac{z^2}{\sigma_z^2}}. \quad (\text{C.5})$$

¹The use of the averaged quantities $\bar{\mu}$ and \bar{U} is an unnecessary complication as long as the interaction strengths U_{ij} are very similar, as for the Skyrmion values.

For spherically symmetric trap the oscillator widths $\sigma_i = \sqrt{\hbar/m\omega_i}$ coincide and hence the profile function is also spherically symmetric.

As promised, we also give the detailed component decomposition of the Skyrmion winding number Eq. (4.4), which results in the lengthy expression:

$$\begin{aligned}
W = \int d^3x \left\{ & \left[-\Re\phi_2 \left((\partial_y \Im\phi_2)(\partial_z \Re\phi_1)(\partial_x \Im\phi_1) - (\partial_z \Im\phi_2)(\partial_y \Re\phi_1)(\partial_x \Im\phi_1) \right. \right. \\
& + (\partial_z \Im\phi_2)(\partial_x \Re\phi_1)(\partial_y \Im\phi_1) - (\partial_x \Im\phi_2)(\partial_z \Re\phi_1)(\partial_y \Im\phi_1) \\
& \left. \left. - (\partial_y \Im\phi_2)(\partial_x \Re\phi_1)(\partial_z \Im\phi_1) + (\partial_x \Im\phi_2)(\partial_y \Re\phi_1)(\partial_z \Im\phi_1) \right) \right. \\
& + \Im\phi_2 \left((\partial_y \Re\phi_2)(\partial_z \Re\phi_1)(\partial_x \Im\phi_1) - (\partial_z \Re\phi_2)(\partial_y \Re\phi_1)(\partial_x \Im\phi_1) \right. \\
& + (\partial_z \Re\phi_2)(\partial_x \Re\phi_1)(\partial_y \Im\phi_1) - (\partial_x \Re\phi_2)(\partial_z \Re\phi_1)(\partial_y \Im\phi_1) \\
& \left. \left. - (\partial_y \Re\phi_2)(\partial_x \Re\phi_1)(\partial_z \Im\phi_1) + (\partial_x \Re\phi_2)(\partial_y \Re\phi_1)(\partial_z \Im\phi_1) \right) \right. \\
& - \Re\phi_1 \left((\partial_y \Re\phi_2)(\partial_z \Im\phi_2)(\partial_x \Im\phi_1) - (\partial_z \Re\phi_2)(\partial_y \Im\phi_2)(\partial_x \Im\phi_1) \right. \\
& + (\partial_z \Re\phi_2)(\partial_x \Im\phi_2)(\partial_y \Im\phi_1) - (\partial_x \Re\phi_2)(\partial_z \Im\phi_2)(\partial_y \Im\phi_1) \\
& \left. \left. - (\partial_y \Re\phi_2)(\partial_x \Im\phi_2)(\partial_z \Re\phi_1) + (\partial_x \Re\phi_2)(\partial_y \Im\phi_2)(\partial_z \Re\phi_1) \right) \right. \\
& + \Im\phi_1 \left((\partial_y \Re\phi_2)(\partial_z \Im\phi_2)(\partial_x \Re\phi_1) - (\partial_z \Re\phi_2)(\partial_y \Im\phi_2)(\partial_x \Re\phi_1) \right. \\
& + (\partial_z \Re\phi_2)(\partial_x \Im\phi_2)(\partial_y \Re\phi_1) - (\partial_x \Re\phi_2)(\partial_z \Im\phi_2)(\partial_y \Re\phi_1) \\
& \left. \left. - (\partial_y \Re\phi_2)(\partial_x \Im\phi_2)(\partial_z \Re\phi_1) + (\partial_x \Re\phi_2)(\partial_y \Im\phi_2)(\partial_z \Re\phi_1) \right) \right] \\
& / (2\pi^2(|\phi_1|^2 + |\phi_2|^2)^2) \Big\}. \tag{C.6}
\end{aligned}$$

While it is far from obvious from Eq. (C.6) directly, the winding number is crucially sensitive to the BEC flow properties that define a Skyrmion: There must be no phase variation on the surface of the trap and there must be a region of overlap between the azimuthally circulating line component, encircled by the flow of the ring component. The latter is nicely visualised in plots of the topological charge density \mathcal{W} associated with Eq. (C.6) (the integrand), which can be found in [156].

Appendix D

Numerical Methods

The diversity of topics tackled is also reflected in the number of numerical schemes employed. Most of these have been previously developed elsewhere. Hence we only list the methods and programming languages used, and give references to documents with further details (section D.1). However, for two methods we contributed original ideas, presented in appendix B and section D.2.

D.1 Project Overview

D.1.1 Programming

Four types of code have been employed for this thesis. The bulk of our simulations were written in the high-level language **xmds** [225]: The physical problem is formulated in an **xml** script, which essentially specifies the PDE to be solved, the variables to be sampled and the algorithm(s) and numerical grids to be used. **Xmds** then writes a **C++** program for this simulation. Overall, we found **xmds** to be a useful force multiplier. The main advantages of it are the ease with which a simulation can be made more complete by adding extra dimensions or further sampled quantities. Other highlights are the extremely simple transition to parallel computation if a problem proved to demanding for single processor calculations, and the equally simple transition to stochastic calculations. Also, **xmds** writes fast code designed for efficient vectorisation. There are limitations to **xmds** when complicated variables are to be sampled, such as the Skyrmion winding number Eq. (C.6). It is also unpractical for simulations involving functions of different dimensionality, such as the HFB equations. In this case, we resorted to the generation of an incomplete simulation with **xmds**, which was subsequently

completed within **C++**. In retrospect, for the case of the HFB equations, this was a less efficient coding method than writing the **C++** program from scratch. However, the author gained valuable knowledge of the interior workings of **xmds**, which proved beneficial for other projects. The data sampling of **xmds** simulations is designed for **matlab**, hence the data analysis and post processing for this thesis was done with **matlab** scripts. Finally, the simulations of collapsing condensates in the truncated Wigner approximation were done using the **pgpe2** code written by P.B. Blakie and M.J. Davis. This is a powerful program package, based on harmonic oscillator eigenfunctions for the Bose gas evolution in a harmonic trap.

D.1.2 Algorithms

The algorithms employed by order of appearance were:

- Simulation of collapsing condensates with GPE in spherical symmetry: These were initially done using the RK4IP algorithm within **xmds**. RK4IP is a fourth-order Runge-Kutta method in the interaction picture, the latter developed and described in Ref. [226]. To exploit the interaction picture, the rescaling of the wave function as in Eq. (B.16) (appendix B) is crucial. We later implemented the adaptive time step method ARK45, which has since replaced the RK4IP as the workhorse for collapsing condensates. An important point to note here is our handling of the radial variable: In order to use the Fast-Fourier-Transform (FFT) for derivative calculations, we had to artificially extend the radial grid to include negative values. The wave function $\tilde{\phi}_a$ of appendix B was extended anti-symmetrically onto the negative r domain. This ensures the absence of signal propagation between the two halves, by causing the diffusive second derivative in the GPE to be zero at the origin. Care has to be taken with this construction to avoid grid points at or near zero.
- Collapsing condensates with the time dependent Hartree-Fock-Bogoliubov equations: An RK4IP program was generated with **xmds** and then edited within **C++**. Due to the complicated structure (see appendix B), the code required major changes and was parallelised in an original way.
- The imaginary time GPE with the task to find Skyrmion ground states was solved based on an **xmds** script, subsequently modified to sample winding

numbers and do the rescaling step¹. Most simulations used the RK4IP method, however when the trap is rotated, the angular momentum operator terms force the use of the (slower) RK4EX method.

- Stabilised high charge ring flows were found with the same code as Skyrmions, their subsequent real time evolution was simulated entirely within **xmds**.
- The dynamical simulations of sonic horizon formation in chapter 5 make massive use of the adaptive time step ARK45IP and ARK45EX methods in **xmds**. The scripts also contain an initial imaginary time block to ensure our simulations are beginning from a ground state.

D.2 Runge-Kutta Fehlberg Method in XMDS

As part of the work for this thesis, the author implemented the adaptive step size fourth-fifth order Runge-Kutta Fehlberg method in the code generator **xmds**. We originally planned to employ it for imaginary time Sobolev gradient methods, to reduce the runtimes required for Skyrmion research. While this application did not lead to the desired results, the algorithm has been of great use for essentially all subsequent topics of this PhD: Many scenarios of chapter 5 are characterised by calm dynamics until the onset of dynamical instabilities, with subsequently violent condensate evolution. They are thus ideally suited for adaptive step size algorithms. An even more extreme example is a collapsing condensate, as mentioned in section 3.3. However, we implemented the adaptive method after the bulk of work on the Bosenova was completed. For that project, we used the algorithm for comparative 2D and 3D runs in the course of the truncated Wigner studies.

We do not give a detailed description of the Runge-Kutta Fehlberg algorithm ARK45. Several can be found in Refs. [102, 225, 227]. At the heart of the method is the use of a particular set of Runge-Kutta support points k_i (n.b. we use the notation of Ref. [102] where required), from which two solutions of the differential equation of different order can be formed:

$$y_{n+1} = y_n + \sum_{i=1}^6 c_i k_i + \mathcal{O}(h^6), \quad y_{n+1}^* = y_n + \sum_{i=1}^6 c_i^* k_i + \mathcal{O}(h^5). \quad (\text{D.1})$$

¹The rescaling can be done within **xmds** by now.

That is, the solution y is of fifth order in the step size h and y^* of fourth order². A particular sets of coefficients c_i and c_i^* , called “Cash-Karp” coefficients, can be found in Ref. [102, 225, 227]. In Eq. (D.1) the subscript of y labels the discrete time point, i.e. $y_n \equiv y(t_n)$.

A program can compute both solutions from the common set of midpoints and use the difference between them as an estimate of the truncation error due to the finite step size h . If the error was above a previously given tolerance, the step is discarded and recalculated using a smaller step size. Otherwise, based on the error, the size for the next step is adjusted. Remarkably, due to the continuous adjustment of the time step very few steps usually have to be discarded.

So far, what we said applies equally to ordinary differential equations (ODEs) and to partial ones. For partial differential equations the question how to calculate the derivatives arises. **Xmds** offers two options, an interaction picture method, developed in Ref. [226] and an explicit method. The interaction picture method treats the part of the time evolution that is due to the spatial derivative terms exactly, which usually allows much bigger time steps. The method can however only be used if the derivative terms are not multiplied by coordinates.

As reported in Ref. [227], it is not possible to reduce the number of required Fourier transforms in the ARK45 in the same way as in the RK4IP. It is thus best to evolve the wave function in Fourier space, and transform back to position space for the calculation of the non-derivative part of the PDE. During the implementation of ARK45 in the general framework of **xmds**, we contributed two tweaks: memory optimisation and runtime optimisation.

Memory optimisation

The straightforward implementation of the ARK45 method would save the support points k_1 to k_6 as well as y_n , y_{n+1} and y_{n+1}^* . For solving an ODE, this might be fully satisfactory. In contrast, for PDEs each of these variables is a multidimensional function and takes up potentially large amounts of computer memory.

²Note that y^* is another solution, not the complex conjugate. If the solution of an algorithm becomes more accurate by Δ^{n+1} when the step size is reduced by a factor Δ , the method is termed “of order n” [102].

The support points are defined as:

$$\begin{aligned} k_1 &= -i\Delta t f(\psi(t), t), \\ k_2 &= -i\Delta t f(\psi(t) + b_{21}k_1, t + a_2\Delta t), \\ &\dots \\ k_6 &= -i\Delta t f(\psi(t) + b_{21}k_1 + \dots + b_{65}k_5, t + a_6\Delta t), \end{aligned} \quad (\text{D.2})$$

for particular coefficients a_i , b_{ij} , see Ref. [102]. It can be seen that the k_i are obtained by sequential propagation of the initial state for the time step ($\psi(t)$, or a linear combination of the initial state and the support points. The solutions (D.1) can be sequentially assembled from the support points, as these become known. Then, the *incomplete* y'_{n+1} and $y^{*'}_{n+1}$ are at each stage a linear combination of the first M support points, e.g. $y'_{n+1} = y_n + \sum_{i=1}^M c_i k_i$, for $M < 6$. These functions contain the same information as the support point together with the initial state, thus some of these arrays are redundant and can be discarded.

Consider the propagation of a differential equation $i\partial\psi/\partial t = f[\psi, t]$ from time t to $t + \Delta t$. ψ may have spatial dimensions and the functional $f[\psi, t]$ may contain derivatives, so we cover ODEs as well as PDEs.

We devised an algorithm to compute the solutions y_{n+1} and y^*_{n+1} saving only 6 copies of the field. Beyond the continuously assembled y_{n+1} and y^*_{n+1} we require 4 further arrays a_i , a_j , a_k , a_l . We denote a computational assignment by “:=”. It is important that $c_2 = c_2^* = c_5 = 0$ Ref. [102]. The algorithm reads:

$$\begin{aligned} a_i &:= y_n; \\ a_k &:= y_n; \\ a_k &:= f(y_n, t); \\ y_{n+1} &:= a_i + c_1 a_k; \\ y^*_{n+1} &:= a_i + c_1^* a_k; \\ a_j &:= \left(1 - \frac{b_{31}}{c_1}\right) a_i + \frac{b_{31}}{c_1} y_{n+1} + b_{32} a_k; \\ a_j &:= f(a_j, t + a_3 \Delta t); \\ a_l &:= \left(1 - \frac{b_{41}}{c_1}\right) a_i + \frac{b_{41}}{c_1} y_{n+1} + b_{42} a_k + b_{43} a_j; \end{aligned} \quad (\text{D.3})$$

$$y_{n+1} := y_{n+1} + c_3 a_j;$$

$$y_{n+1}^* := y_{n+1}^* + c_3^* a_j;$$

$$a_l := f(a_l, t + a_4 \Delta t);$$

$$y_{n+1} := y_{n+1} + c_4 a_l;$$

$$y_{n+1}^* := y_{n+1}^* + c_4^* a_l;$$

$$a_l := \left(1 - \frac{b_{51}}{c_1}\right) a_i + \frac{b_{51}}{c_1} y_{n+1} + b_{52} a_k + \left(b_{53} - \frac{b_{51}}{c_1} c_3\right) a_j + \left(b_{54} - \frac{b_{51}}{c_1} c_4\right) a_l;$$

$$a_l := f(a_l, t + a_5 \Delta t);$$

$$y_{n+1}^* := y_{n+1}^* + c_5^* a_l;$$

$$a_l := f_1 a_1 + f_2 a_2 + f_3 a_3 + f_4 a_4 + f_5 a_5 + f_6 a_6;$$

$$a_l := f(a_l, t + a_6 \Delta t);$$

$$y_{n+1} := y_{n+1} + c_6 a_l;$$

$$y_{n+1}^* := y_{n+1}^* + c_6^* a_l;$$

In this sequence, the final coefficients f_i are given by the solution of the matrix equation:

$$\begin{pmatrix} 1 & 0 & 0 & 1 & 0 & 1 \\ 0 & 0 & 0 & c_1 & 0 & c_1^* \\ 0 & 1 & 0 & 0 & 0 & 0 \\ 0 & 0 & 1 & c_3 & 0 & c_3^* \\ 0 & 0 & 0 & c_4 & 0 & c_4^* \\ 0 & 0 & 0 & 0 & 1 & c_5^* \end{pmatrix} \begin{pmatrix} f_1 \\ f_2 \\ f_3 \\ f_4 \\ f_5 \\ f_6 \end{pmatrix} = \begin{pmatrix} 1 \\ b_{61} \\ b_{62} \\ b_{63} \\ b_{64} \\ b_{65} \end{pmatrix} \quad (\text{D.4})$$

To motivate this endeavour, consider the spatial grids of size $128 \times 128 \times 128$ that we employed in studies of Skyrmions. Each point carries a complex number for each component of the BEC wave function, with two double precision floating point numbers (2×8 bytes) to a complex number. The whole array thus takes 64 Mb. Present day computer memories are much larger, however for computational performance the relation to CPU cache size is also important. In this respect it can be a significant difference whether 9 or 6 copies of the field have to be stored.

Run time optimisation

We found another trick for the routine to compute the relative truncation error. This error has to be determined after each step, so an efficient implementation is rewarding. The usual criterion for the time step control is to demand that the maximal *relative error* between the fourth and fifth order solutions should be smaller than the given tolerance. We have to thus determine the maximum of the error over the whole spatial grid. However, the solution function, for example the Gross-Pitaevskii wave function, is often only significant on a part of the spatial grid. Towards the grid edge, for example, it naturally has to tend to zero. We wish the relative error in the domains where the function is small to be discarded.

Our routine thus faces a dual task: It has to determine the typical (we chose maximal) value of any given component of the function to be solved for. Then it should determine the maximal relative truncation error for all grid points where the function value is above a given threshold (we chose a cutoff value times the maximal value). The most straightforward method to determine these in a computer code, is by the use of “if-statements”. We list an example that does the described job for a multi-component field on an unspecified grid. The routine is written in C++ and, in a similar form, is executed after each timestep within the ARK45 procedures of **xmds**. It is assumed that the complex arrays `_main_field` and `_check_field` contain the solutions y_{n+1} and y_{n+1}^* respectively. Also note the lines commented `// if statement n *****`, as we will refer to them shortly.

```
/* **** */
double _calculate_timestep_error(complex* _checkfield) {

    // Definition of variables:
    // _mainfield      an array of complex numbers saving the values
    //                  of all functions on all the gridpoints
    // _checkfield     similar to _mainfield but solution of different order
    // _main_size       total number of gridpoints
    // _ncomponents    total number of functions (function components)
    //                  (the total size of _mainfield is thus
    //                  _main_size* _ncomponents complex entries)
    // _cutoff         Down to the fraction _cutoff of the peakvalue of any
    //                  field component, the relative error is considered.

    double _error=1e-24; //initial value smaller than anything expected
    double _result[_ncomponents];
    double _peak[_ncomponents]; // to become peak value in each field component
    for(unsigned long _i0=0; _i0<_ncomponents; _i0++){
        _peak[_i0]=0.0; // initialise all to zero
        _result[_i0]=0.0;
    }
}
```

```

double _temp_error=0.0;
double _temp_mod=0.0;

unsigned long _index_pointer=0;

for(unsigned long _i0=0; _i0<_main_size; _i0++){
    for(unsigned long _i1=0; _i1<_ncomponents; _i1++){
        _temp_mod=mod2(_mainfield[_index_pointer + _i1]);
        if(_temp_mod> _peak[_i1]) // if statement 1 *****
            _peak[_i1]= _temp_mod;
    }
    _index_pointer += _ncomponents;
}

for(unsigned long _i0=0; _i0< _ncomponents; _i0++)
    _peak[_i0]*=_cutoff;

_index_pointer =0;

for(unsigned long _i0=0; _i0<_main_size; _i0++){
    for(unsigned long _i1=0; _i1< _ncomponents; _i1++){
        if(mod2(_mainfield[_index_pointer + _i1])>_peak[_i1]){
            _temp_error=mod(_mainfield[_index_pointer + _i1]
                            -_checkfield[_index_pointer + _i1])
                        /mod(_mainfield[_index_pointer + _i1]);
            if(_temp_error > _error) // if statement 2 *****
                _error = _temp_error;
        }
        _index_pointer+=_ncomponents;
    }
    _result[0]=_error;
    return(_result[0]);
}

```

A problem with this construction is that “if-statements” do not vectorise well. The above code is thus comparatively slow to execute.

We found a simple way to replace two of these “if statements” by simple algebraic equations. “If statements” one and two can be replaced by:

```

_temp_mod=mod2(_mainfield[_index_pointer + _i1]);
_peak[_i1]+= 0.5*(_temp_mod-_peak[_i1] + fabs(_temp_mod-_peak[_i1])) ;

```

and

```

_temp_error=mod(_mainfield[_index_pointer + _i1]
                -_checkfield[_index_pointer + _i1])
                /mod(_mainfield[_index_pointer + _i1]);
_error+= 0.5*(_temp_error - _error +fabs(_temp_error - _error)) ;

```

respectively. In either case we kept the preceding line to provide context. The bracketed expression is nonzero only if the argument `_temp_mod-_peak[_i1]` and `_temp_error - _error` respectively) is nonzero. If it is, the value of the modulus (or error) on the current grid point exceeds the previously determined maximum and the latter is adjusted accordingly. For the trial case provided with

`sech_soliton.xmds` in the `xmds` distribution, we found a useful decrease in computer run time if our construction, with reduced number of if statements, is used.

Our implementation of the ARK45 method in `xmds` has benefited significantly from previous work by M. East.

Bibliography

- [1] S. N. Bose; *Plancks Gesetz und Lichtquantenhypothese*; Z. Phys. **26** 178 (1924); referenced in [228].
- [2] A. Einstein; *Quantentheorie des einatomigen idealen Gases*; Sitzungsber. Kgl. Preuss. Akad. Wiss. page 261 (1924); referenced in [228].
- [3] A. Einstein; *Quantentheorie des einatomigen idealen Gases, Zweite Abhandlung*; Sitzungsber. Kgl. Preuss. Akad. Wiss. page 3 (1925); referenced in [228].
- [4] M. H. Anderson, J. R. Ensher, M. R. Matthews, C. E. Wieman and E. A. Cornell; *Observation of Bose-Einstein Condensation in a Dilute Atomic Vapor*; Science **269** 198 (1995).
- [5] K. B. Davis, M. O. Mewes, M. R. Andrews, N. J. van-Druten, D. S. Durfee, D. M. Kurn and W. Ketterle; *Bose-Einstein Condensation in a Gas of Sodium Atoms*; Phys. Rev. Lett. **75** 3969 (1995).
- [6] C. C. Bradley, C. A. Sackett, J. J. Tollett and R. G. Hulet; *Evidence of Bose-Einstein Condensation in an Atomic Gas with Attractive Interactions*; Phys. Rev. Lett. **75** 1687 (1995).
- [7] D. M. Stamper-Kurn, H. J. Miesner, S. Inouye, M. R. Andrews and W. Ketterle; *Collisionless and hydrodynamic excitations of a Bose-Einstein condensate*; Phys. Rev. Lett. **81** 500 (1998).
- [8] M. Greiner, O. Mandel, T. Esslinger, T. W. Hänsch and I. Bloch; *Quantum phase transition from a superfluid to a Mott insulator in a gas of ultracold atoms*; Nature **415** 39 (2002).
- [9] M. Schellekens, R. Hoppeler, A. Perrin, J. V. Gomes, D. Boiron, A. Aspect and C. I. Westbrook; *Hanbury Brown Twiss Effect for Ultracold Quantum Gases*; Science **310** 648 (2005).

- [10] C.-S. Chuu, F. Schreck, T. P. Meyrath, J. L. Hanssen, G. N. Price and M. G. Raizen; *Direct Observation of Sub-Poissonian Number Statistics in a Degenerate Bose Gas*; Phys. Rev. Lett. **95** 260403 (2005).
- [11] S. Fölling, F. Gerbler, A. Widera, O. Mandel, T. Gericke and I. Bloch; *Spatial quantum noise interferometry in expanding ultracold atom clouds*; Nature **434** 481 (2005).
- [12] A. Öttl, S. Ritter, M. Köhl and T. Esslinger; *Correlations and Counting Statistics of an Atom Laser*; Phys. Rev. Lett. **95** 090404 (2005).
- [13] C. W. Gardiner and P. Zoller; *Quantum Noise*; Springer-Verlag, Berlin Heidelberg, (2004).
- [14] S. A. Morgan, M. Rusch, D. A. W. Hutchinson and K. Burnett; *Quantitative Test of Thermal Field Theory for Bose-Einstein Condensates*; Phys. Rev. Lett. **91** 250403 (2003).
- [15] B. Damski, H. Everts, A. Honecker, H. Fehmann, L. Santos and M. Lewenstein; *Atomic Fermi Gas in the Trimerized Kagomé Lattice at 2/3 Filling*; Phys. Rev. Lett. **95** 060403 (2005).
- [16] W. G. Unruh; *Experimental Black-Hole Evaporation?*; Phys. Rev. Lett. **46** 1351 (1981).
- [17] C. Barceló, S. Liberati and M. Visser; *Analogue Gravity*; Living Rev. Relativity **8** 12 (2005).
- [18] V. Efimov; *Energy levels arising from resonant two-body forces in a three-body system*; Phys. Lett. B **33** 563 (1970).
- [19] V. Efimov; *Weakly-bound states of three resonantly-interacting particles*; Sov. J. Nucl. Phys. **12** 589 (1971).
- [20] T. Krämer, M. Mark, P. Waldburger, J. G. Danzl, C. Chin, B. Enseger, A. D. Lange, K. Pilch, A. Jaakkola, H. Nägerl and R. Grimm; *Evidence for Efimov quantum states in an ultracold gas of caesium atoms*; Nature **440** 315 (2006).
- [21] T. H. R. Skyrme; *A Non-Linear Field Theory*; Proc. Roy. Soc A **260** 127 (1961).

- [22] T. H. R. Skyrme; *A unified field theory of mesons and baryons*; Nucl. Phys. **31** 556 (1962).
- [23] E. Witten; *Global aspects of current algebra*; Nucl. Phys. B **223** 422 (1983).
- [24] E. Witten; *Current algebra, baryons, and quark confinement*; Nucl. Phys. B **223** 433 (1983).
- [25] D. Diakonov, V. Petrov and M. Polyakov; *Exotic anti-decuplet of Baryons:predictions from chiral solitons*; Z. Phys. A **359** 305 (1997).
- [26] T. Nakano *et al.*; *Evidence for a narrow $S=+1$ Baryon Resonance in Photoproduction from the Neutron*; Phys. Rev. Lett. **91** 012002 (2003).
- [27] C. M. Savage and J. Ruostekoski; *Energetically stable pointlike Skyrmions in a trapped Bose-Einstein condensate*; Phys. Rev. Lett. **91** 010403 (2003).
- [28] E. A. Donley, N. R. Claussen, S. L. Cornish, J. L. Roberts, E. A. Cornell and C. E. Wieman; *Dynamics of collapsing and exploding Bose-Einstein condensates*; Nature **412** 295 (2001).
- [29] J. M. Bardeen, P. J. Steinhardt and M. S. Turner; *Spontaneous creation of almost scale-free density perturbations in an inflationary universe*; Phys. Rev. D **28** 679 (1983).
- [30] C. M. Savage, N. P. Robins and J. J. Hope; *Bose Einstein condensate collapse: A comparison between theory and experiment*; Phys. Rev. A **67** 014304 (2003).
- [31] R. Shankar; *Principles of Quantum Mechanics*; Plenum Press, New York (1994).
- [32] S. Weinberg; *The Quantum Theory of Fields, Vol I*; Cambridge University Press (1995).
- [33] R. Baierlein; *Thermal Physics*; Cambridge University Press (1999).
- [34] C. J. Pethik and H. Smith; *Bose-Einstein condensation in dilute gases*; Cambridge University Press (2002).
- [35] F. Dalfovo, S. Giorgini, L. P. Pitaevskii and S. Stringari; *Theory of Bose-Einstein condensation in trapped gases*; Rev. Mod. Phys. **71** 463 (1999).

- [36] J. D. Jackson; *Classical Electrodynamics*; Wiley (1998).
- [37] G. Breit and I. I. Rabi; *Measurement of Nuclear Spin*; Phys. Rev. **38** 2082 (1931).
- [38] A. L. Fetter and A. A. Svidzinsky; *Vortices in a trapped dilute Bose-Einstein condensate*; J.Phys.: Condens. Matter **13** 135 (2001).
- [39] H. Feshbach; *A Unified Theory of Nuclear Reactions 2*; Annals of Physics **19** 287 (1962).
- [40] B. J. Dąbrowska, E. A. Ostrovskaya and Y. S. Kivshar; *Interaction of matter-wave gap solitons in optical lattices*; J. Opt. B: Quant. Semiclass. Opt. **6** 423 (2004).
- [41] B. J. Dąbrowska, E. A. Ostrovskaya and Y. S. Kivshar; *Instability-induced localization of matter waves in moving optical lattices*; Phys. Rev. A **73** 033603 (2006).
- [42] B. J. Dąbrowska-Wüster, S. Wüster, A. S. Bradley, M. J. Davis and E. A. Ostrovskaya; *Quantum effects in the dynamical localization of Bose-Einstein condensates in optical lattices*; cond-mat/0607332 (2006).
- [43] B. J. Dąbrowska, E. A. Ostrovskaya, T. J. Alexander and Y. S. Kivshar; *Multicomponent gap solitons in spinor Bose-Einstein condensates*; cond-mat/0612104 (2006).
- [44] M. Lewenstein, A. Sanpera, V. Ahufinger, B. Damski, A. Sen and U. Sen; *Ultracold atomic gases in optical lattices: Mimicking condensed matter physics and beyond*; cond-mat/0606771 (2006).
- [45] E. A. Calzetta and B. L. Hu; *Bose-Einstein condensate collapse and dynamical squeezing of vacuum fluctuations*; Phys. Rev. A **68** 043625 (2003).
- [46] E. A. Calzetta and B. L. Hu; *Early Universe Quantum Processes in BEC Collapse Experiments*; Int. J. Theor. Phys. **44** 1691 (2005).
- [47] H. Weigel; *Baryons as three-flavor solitons*; Int. J. Mod. Phys. A **11** 2419 (1996).
- [48] S. W. Hawking; *Particle creation by black holes*; Commun. Math. Phys. **43** 199 (1975).

- [49] S. W. Hawking; *Black hole explosions*; Nature **248** 30 (1974).
- [50] C. Barceló, S. Liberati and M. Visser; *Probing semiclassical gravity in Bose-Einstein condensates with widely tunable interactions*; Phys. Rev. A **68** 053613 (2003).
- [51] T. R. Slatyer and C. M. Savage; *Superradiant scattering from a hydrodynamic vortex*; Class. Quant. Grav. **22** 3833 (2005).
- [52] M. W. Jack; *Decoherence due to Three-Body Loss and its Effect on the State of a Bose-Einstein Condensate*; Phys. Rev. Lett. **89** 140402 (2002).
- [53] J. J. Hope; *Quantum field effects in coupled atomic and molecular Bose-Einstein condensates*; Phys. Rev. A **64** 053608 (2001).
- [54] E. P. Gross; *Structure of a quantized Vortex in Boson Systems*; Nuovo Cimento **20** 454 (1961).
- [55] L. P. Pitaevskii; *Vortex Lines in an imperfect Bose Gas*; Sov. Phys. -JETP **13** 451 (1961).
- [56] J. J. García-Ripoll and V. M. Pérez-García; *Optimizing Schrödinger functionals using Sobolev gradients: Applications to quantum mechanics and nonlinear optics*; SIAM J. Sci. Comp. **23** 1315 (2001).
- [57] A. A. Penckwitt, R. J. Ballagh and C. W. Gardiner; *Nucleation, Growth and Stabilization of Bose-Einstein Condensate Vortex Lattices*; Phys. Rev. Lett. **89** 260402 (2002).
- [58] E. M. Lifshitz and L. P. Pitaevskii; *Statistical Physics, Part I*; Oxford: Pergamon (1980).
- [59] T. L. Chow; *Classical Mechanics*; Wiley (1995).
- [60] R. Battye, N. Cooper and P. Sutcliffe; *Skyrmions in Bose-Einstein Condensates*; PrHEP unesp2002/009 (2002).
- [61] P. Ao and S. T. Chui; *Binary Bose-Einstein condensate mixtures in weakly and strongly segregated phases*; Phys. Rev. A **58** 4836 (1998).
- [62] N. N. Bogoliubov; *A new method in the Theory of Superconductivity*; Sov. Phys. JETP-USSR **7** 51 (1958).

- [63] S. A. Morgan, S. Choi, K. Burnett and M. Edwards; *Nonlinear mixing of quasiparticles in an inhomogeneous Bose condensate*; Phys. Rev. A **57** 3818 (1998).
- [64] A. D. Jackson, G. M. Kavoulakis and E. Lundh; *Stability of the solutions of the Gross-Pitaevskii equation*; Phys. Rev. A **72** 053617 (2005).
- [65] C. Barceló, S. Liberati and M. Visser; *Analogue gravity from Bose-Einstein condensates*; Class. Quant. Grav., **18** 1137 (2001).
- [66] N. D. Birrell and P. C. W. Davies; *Quantum fields in curved space*; Cambridge University Press (1982).
- [67] J.-P. Blaizot and G. Ripka; *Quantum Theory of finite systems*; MIT Press (1986).
- [68] J. Goldstone, A. Salam and S. Weinberg; *Broken Symmetries*; Phys. Rev. **127** 965 (1962).
- [69] S. Weinberg; *The Quantum Theory of Fields, Vol II*; Cambridge University Press (1996).
- [70] N. M. Hugenholtz and D. Pines; *Ground-State Energy and Excitation Spectrum of a System of Interacting Bosons*; Phys. Rev. **116** 489 (1959).
- [71] M. E. Peskin and D. V. Schroeder; *An Introduction to Quantum Field Theory*; Perseus Books, Cambridge, Massachusetts (1995).
- [72] A. Griffin; *Conserving and gapless approximations for an inhomogeneous Bose gas at finite temperature*; Phys. Rev. B **53** 9341 (1996).
- [73] N. P. Proukakis, S. A. Morgan, S. Choi and K. Burnett; *Comparison of gapless mean-field theories for trapped Bose-Einstein condensates*; Phys. Rev. A **58** 2435 (1998).
- [74] K. Góral, T. Köhler, T. Gasenzer and K. Burnett; *Dynamics of correlations in atomic Bose-Einstein condensates*; J. Mod. Opt. **51** 1731 (2004).
- [75] T. Köhler and K. Burnett; *Microscopic quantum dynamics approach to the dilute condensed Bose gas*; Phys. Rev. A **65** 033601 (2002).
- [76] D. A. W. Hutchinson, R. J. Dodd and K. Burnett; *Gapless Finite-T Theory of Collective Modes of a Trapped Gas*; Phys. Rev. Lett. **81** 2198 (1998).

- [77] S. A. Morgan; *A gapless theory of Bose-Einstein condensation in dilute gases at finite temperature*; J. Phys. B: At. Mol. Opt. Phys. **33** 3847 (2000).
- [78] D. A. W. Hutchinson, K. Burnett, R. J. Dodd, S. A. Morgan, M. Rusch, E. Zaremba, N. P. Proukakis, M. Edwards and C. W. Clark; *Gapless mean-field theory of Bose-Einstein condensates*; J. Phys. B: At. Mol. Opt. Phys. **33** 3825 (2000).
- [79] S. A. Morgan; *Quantitative test of thermal field theory for Bose-Einstein condensates. II*; Phys. Rev. A **71** 043609 (2005).
- [80] S. J. J. M. F. Kokkelmans, J. N. Milstein, M. L. Chiofalo, R. Walser and M. J. Holland; *Resonance superfluidity: Renormalization of resonance scattering theory*; Phys. Rev. A **65** 053617 (2002).
- [81] D. J. Heinzen, R. Wynar, P. D. Drummond and K. V. Kheruntsyan; *Superchemistry: Dynamics of coupled atomic and molecular Bose-Einstein condensates*; Phys. Rev. Lett. **84** 5029 (2000).
- [82] J. N. Milstein, C. Menotti and M. J. Holland; *Feshbach resonances and collapsing Bose-Einstein condensates*; New J. Phys. **5** 52 (2003).
- [83] N. R. Claussen, S. J. J. M. F. Kokkelmans, S. T. Thompson, E. A. Donley, E. Hodby and C. E. Wieman; *Very-high-precision bound-state spectroscopy near a ^{85}Rb Feshbach resonance*; Phys. Rev. A **67** 060701(R) (2003).
- [84] S. J. J. M. F. Kokkelmans and M. J. Holland; *Ramsey Fringes in a Bose-Einstein Condensate between Atoms and Molecules*; Phys. Rev. Lett. **89** 180401 (2002).
- [85] A. A. Norrie, R. J. Ballagh and C. W. Gardiner; *Quantum turbulence in condensate collisions: An Application of the Classical Field Method*; Phys. Rev. Lett. **94** 040401 (2005).
- [86] P. Deuar and P. D. Drummond; *Correlations in a BEC collision: First-principles quantum dynamics with 150,000 atoms*; [cond-mat/0607831](https://arxiv.org/abs/cond-mat/0607831) (2006).
- [87] C. Lobo, A. Sinatra and Y. Castin; *Vortex Lattice Formation in Bose-Einstein Condensates*; Phys. Rev. Lett. **92** 020403 (2004).

- [88] C. M. Savage, P. E. Schwenn and K. V. Kheruntsyan; *First-principles quantum simulations of dissociation of molecular condensates: Atom correlations in momentum space*; Phys. Rev. A **74** 033620 (2006).
- [89] P. Deuar and P. D. Drummond; *First-principles quantum dynamics in interacting Bose gases: I. The positive P representation*; J. Phys. A.: Math. Gen. **39** 1163 (2006).
- [90] P. Deuar and P. D. Drummond; *First-principles quantum dynamics in interacting Bose gases II: stochastic gauges*; J. Phys. A.: Math. Gen. **39** 2723 (2006).
- [91] J. F. Corney and P. D. Drummond; *Gaussian quantum operator representation for bosons*; Phys. Rev. A **68** 068322 (2003).
- [92] M. J. Steel, M. K. Olsen, L. I. Plimak, P. D. Drummond, S. M. Tan, M. J. Collet, D. F. Walls and R. Graham; *Dynamical quantum noise in trapped Bose-Einstein condensates*; Phys. Rev. A **58** 4824 (1998).
- [93] A. A. Norrie, R. J. Ballagh and C. W. Gardiner; *Quantum turbulence and correlations in Bose-Einstein condensate collisions.*; Phys. Rev. A **73** 043617 (2006).
- [94] A. A. Norrie; *A Classical Field Treatment of colliding Bose-Einstein Condensates*; Ph.D. thesis; University of Otago (2005); URL http://www.physics.otago.ac.nz/research/jackdodd/resources/thesis_page.html.
- [95] C. W. Gardiner; *Handbook of Stochastic Methods*; Springer Verlag (2003).
- [96] P. D. Drummond; *Central partial difference propagation algorithms*; Comp. Phys. Comm. **29** 211 (1983).
- [97] L. Isella and J. Ruostekoski; *Nonadiabatic dynamics of a Bose-Einstein condensate in an optical lattice*; Phys. Rev. A **72** 011601(R) (2005).
- [98] A. Sinatra, C. Lobo and Y. Castin; *The truncated Wigner method for Bose-condensed gases: Limits of validity and applications*; J. Phys. B: At. Mol. Opt. Phys. **35** 3599 (2002).
- [99] A. Pokolnikov; *Evolution of the macroscopically entangled states in optical lattices*; Phys. Rev. A **68** 033609 (2003).

- [100] A. Pokolnikov, S. Sachdev and S. M. Girvin; *Nonequilibrium Gross-Pitaevskii dynamics of boson lattice models*; Phys. Rev. A **66** 053607 (2002).
- [101] A. A. Norrie, R. J. Ballagh, C. W. Gardiner and A. S. Bradley; *Three-body recombination of ultracold Bose gases using the truncated Wigner method*; Phys. Rev. A **73** 043618 (2006).
- [102] W. H. Press, B. P. Flannery, S. A. Teukolsky and W. T. Vetterling; *Numerical Recipes in C*; Cambridge University Press (1992).
- [103] C. M. Dion and E. Cancès; *Spectral method for the time-dependent Gross-Pitaevskii equation with a harmonic trap*; Phys. Rev. E **67** 046706 (2003).
- [104] P. B. Blakie and M. J. Davis; *Projected Gross-Pitaevskii equation for harmonically confined Bose gases at finite temperature*; Phys. Rev. A **72** 063608 (2005).
- [105] M. J. Davis and P. B. Blakie; *Critical temperature of a trapped Bose gas: comparison of theory and experiment*; Phys. Rev. Lett. **96** 060404 (2006).
- [106] S. Hoffmann; *in preparation*; Ph.D. thesis; University of Queensland (2007).
- [107] J. L. Roberts, N. R. Claussen, S. L. Cornish, E. A. Donley, E. A. Cornell and C. E. Wieman; *Controlled collapse of a Bose-Einstein Condensate*; Phys. Rev. Lett. **86** 4211 (2001).
- [108] J. M. Gerton, D. Strekalov, I. Prodan and R. G. Hulet; *Direct observation of growth and collapse of a Bose-Einstein condensate with attractive interactions*; Nature **408** 692 (2000).
- [109] C. C. Bradley, C. A. Sackett and R. G. Hulet; *Bose-Einstein condensation of lithium: Observation of limited condensate number*; Phys. Rev. Lett. **78** 985 (1997).
- [110] N. R. Claussen; *Dynamics of Bose-Einstein condensates near a Feshbach Resonance in ^{85}Rb* ; Ph.D. thesis; University of Colorado (2003).
- [111] R. A. Duine and H. T. C. Stoof; *Dynamics of a Bose-Einstein condensate near a Feshbach resonance*; Phys. Rev. A **68** 013602 (2003).
- [112] L. Santos and G. V. Shlyapnikov; *Collapse dynamics of trapped Bose-Einstein condensates*; Phys. Rev. A **66** 011602 (2002).

- [113] S. K. Adhikari; *Dynamics of collapsing and exploding Bose-Einstein condensate*; Physics Letters A **296** 145 (2002).
- [114] S. K. Adhikari; *Mean-field model of jet formation in a collapsing Bose-Einstein condensate*; J. Phys. B: At. Mol. Opt. Phys. **37** 1185 (2004).
- [115] H. Saito and M. Ueda; *Mean-field analysis of collapsing and exploding Bose-Einstein condensates*; Phys. Rev. A **65** 033624 (2002).
- [116] H. Saito and M. Ueda; *Intermittent Implosion and Pattern Formation of Trapped Bose-Einstein Condensates with an Attractive Interaction*; Phys. Rev. Lett. **86** 1406 (2000).
- [117] H. Saito and M. Ueda; *Power laws and collapsing dynamics of a trapped Bose-Einstein Condensate with an attractive Interaction*; Phys. Rev. A **63** 043601 (2001).
- [118] M. Ueda and H. Saito; *A Consistent Picture of a Collapsing Bose-Einstein Condensate*; J. Phys. Soc. Jpn. Suppl. C **72** 127 (2003).
- [119] W. Bao, D. Jaksch and P. A. Markowich; *Three-dimensional simulation of jet formation in collapsing condensates*; J. Phys. B: At. Mol. Opt. Phys. **37** 329 (2004).
- [120] S. Métens, G. Dewel and P. Borckmans; *Nonadiabatic effects in the dynamics of collapsing Bose-Einstein condensates*; Phys. Rev. A **68** 045601 (2003).
- [121] V. A. Yurovsky; *Quantum effects on dynamics of instabilities in Bose-Einstein condensates*; Phys. Rev. A **65** 033605 (2002).
- [122] J. K. Chin, J. M. Vogels and W. Ketterle; *Amplification of Local Instabilities in a Bose-Einstein Condensate with Attractive Interactions*; Phys. Rev. Lett. **90** 160405 (2003).
- [123] J. L. Roberts, N. R. Claussen, S. L. Cornish and C. E. Wieman; *Magnetic Field Dependence of Ultracold Inelastic Collisions near a Feshbach Resonance*; Phys. Rev. Lett. **85** 728 (2000).
- [124] R. A. Duine and H. T. C. Stoof; *Explosion of a Collapsing Bose-Einstein Condensate*; Phys. Rev. Lett. **86** 2204 (2001).

- [125] R. A. Duine and H. T. C. Stoof; *Microscopic many-body theory of atomic Bose gases near a Feshbach resonance*; J. Opt. B: Quant. Semiclass. Opt. **5** S212 (2003).
- [126] E. A. Donley, N. R. Claussen, S. T. Thompson and C. E. Wieman; *Atom-molecule coherence in a Bose-Einstein condensate*; Nature **417** 529 (2002).
- [127] M. Holland, J. Park and R. Walser; *Formation of pairing fields in resonantly coupled atomic and molecular Bose-Einstein condensates.*; Phys. Rev. Lett. **86** 1915 (2001).
- [128] T. J. Alexander; *Nonlinear waves in Optics and Bose-Einstein condensation*; Ph.D. thesis; Australian National University (2003).
- [129] S. Wüster, J. J. Hope and C. M. Savage; *Collapsing Bose-Einstein condensates beyond the Gross-Pitaevskii approximation*; Phys. Rev. A **71** 033604 (2005).
- [130] M. J. Davis, R. J. Ballagh and K. Burnett; *Dynamics of thermal Bose fields in the classical limit*; J. Phys. B: At. Mol. Opt. Phys. **34** 4487 (2001).
- [131] O. Penrose and L. Onsager; *Bose-Einstein Condensation and liquid Helium*; Phys. Rev. **104** 576 (1956).
- [132] K. Góral, M. Gajda and K. Rzążewski; *Thermodynamics of an interacting trapped Bose-Einstein gas in the classical field approximation*; Phys. Rev. A **66** 051602(R) (2002).
- [133] A. M. Rey, B. L. Hu, E. Calzetta, A. Roura and C. W. Clark; *Nonequilibrium dynamics of optical-lattice loaded Bose-Einstein condensate atoms: Beyond the HFB approximation*; Phys. Rev. A **69** 033610 (2004).
- [134] S. Wüster, B. J. Dąbrowska-Wüster, A. S. Bradley, M. J. Davis, P. B. Blakie, J. J. Hope and C. M. Savage; *Quantum depletion of collapsing Bose-Einstein condensates*; cond-mat/0609417 (2006).
- [135] P. G. Kevrekidis, R. C. Gonzales, D. J. Frantzeskakis and I. G. Kevrekidis; *Vortices in Bose-Einstein Condensates: Some Recent Developments*; Mod. Phys. Lett. B **18** 1481 (2004).

- [136] A. E. Leanhardt, Y. Shin, D. Kielpinski, D. E. Pritchard and W. Ketterle; *Coreless vortex formation in a spinor Bose-Einstein condensate*; Phys. Rev. Lett. **90** 140403 (2003).
- [137] K. H. Hicks; *Experimental search for pentaquarks*; Progr. in Particle and Nucl. Phys. **55** 647 (2005).
- [138] J. Ruostekoski; *Topological phase preparation in a pair of atomic Bose-Einstein condensates*; Phys. Rev. A **61** 041603 (2000).
- [139] J. Ruostekoski and J. R. Anglin; *Creating Vortex-Rings and Three-Dimensional Skyrmions in Bose-Einstein condensates*; Phys. Rev. Lett. **86** 3934 (2001).
- [140] A. Görlitz, T. L. Gustavson, A. E. Leanhardt, R. Low, A. P. Chikkatur, S. Gupta, S. Inouye, D. E. Pritchard and W. Ketterle; *Sodium Bose-Einstein condensates in the F=2 state in a large-volume optical trap*; Phys. Rev. Lett. **90** 090401 (2003).
- [141] J. Ruostekoski and Z. Dutton; *Engineering vortex rings and systems for controlled studies of vortex interactions in Bose-Einstein condensates*; Phys. Rev. A **72** 063626 (2005).
- [142] P. H. Roberts and J. Grant; *Motions in a Bose condensate I. The structure of a large circular vortex*; J. Phys. A: Gen. Phys. **4** 55 (1971).
- [143] B. P. Anderson, P. C. Haljan, , C. A. Regal, D. L. Feder, L. A. Collins, C. W. Clark and E. A. Cornell; *Watching Dark Solitons Decay into Vortex Rings in a Bose-Einstein Condensate*; Phys. Rev. Lett. **86** 2926 (2000).
- [144] N. S. Ginsberg, J. Brand and L. V. Hau; *Observation of Hybrid Soliton Vortex-Ring Structures in Bose-Einstein Condensates*; Phys. Rev. Lett. **94** 040403 (2005).
- [145] J. Ruostekoski and Z. Dutton; *Engineering vortex rings and systems for the controlled studies of vortex interactions in Bose-Einstein condensates*; Phys. Rev. A **72** 063626 (2005).
- [146] R. Rajaraman; *Solitons and Instantons*; North Holland Pub. Comp. (1982).
- [147] C. M. Savage and J. Ruostekoski; *Dirac monopoles and dipoles in ferromagnetic spinor Bose-Einstein condensates*; Phys. Rev. A **68** 043604 (2003).

- [148] J. Ruostekoski and J. R. Anglin; *Monopole core instability and alice rings in spinor Bose-Einstein condensates*; Phys. Rev. Lett. **91** 190402 (2003).
- [149] W. M. Yao *et al.*; *Review of Particle Physics*; J. Phys. G: Nucl. Part. Phys. **33** 1 (2006).
- [150] D. S. Hall, M. R. Matthews, J. R. Ensher, C. E. Wieman and E. A. Cornell; *Dynamics of Component Separation in a Binary Mixture of Bose-Einstein Condensates*; Phys. Rev. Lett. **81** 1539 (1998).
- [151] U. A. Khawaja and H. T. C. Stoof; *Skyrmions in a ferromagnetic Bose-Einstein condensate*; Nature **411** 918 (2001).
- [152] U. A. Khawaja and H. T. C. Stoof; *Skyrmion physics in Bose-Einstein ferromagnets*; Phys. Rev. A **64** 043612 (2001).
- [153] J. F. Herbut and M. Oshikawa; *Stable skyrmions in spinor condensates*; Phys. Rev. Lett. **97** 080403 (2006).
- [154] P. H. Roberts and J. Grant; *Motions in a Bose Condensate I. The structure of the large circular vortex*; J. Phys.A: Gen. Phys. **4** 55 (1971).
- [155] R. A. Battye, N. R. Cooper and P. M. Sutcliffe; *Stable Skyrmions in Two-Component Bose-Einstein Condensates*; Phys. Rev. Lett. **88** 080401 (2002).
- [156] J. Ruostekoski; *Stable particlelike solitons with multiply-quantized vortex lines in Bose-Einstein condensates*; Phys. Rev. A **70** 041601 (2004).
- [157] D. M. Harber, H. J. Lewandowski, J. M. McGuirk and E. A. Cornell; *Effect of cold collisions on spin coherence and resonance shifts in a magnetically trapped ultracold gas*; Phys. Rev. A **66** 053616 (2002).
- [158] E. G. M. van Kempen, S. J. J. M. F. Kokkelmans, D. J. Heinzen and B. J. Verhaar; *Interisotope Determination of Ultracold Rubidium Interactions from Three High-Precision Experiments*; Phys. Rev. Lett. **88** 093201 (2002).
- [159] The RK4IP method is described in the Ph.D. thesis of B.M. Caradoc-Davies which is online at: <http://www.physics.otago.ac.nz/bec2/bmcd/>. This is a pseudo-spectral method with a Runge-Kutta time step.
- [160] Online at www.xmds.org.

- [161] M. Theis, G. Thalhammer, K. Winkler, M. Hellwig, G. Ruff, R. Grimm and J. H. Denschlag; *Tuning the Scattering Length with an Optically Induced Feshbach Resonance*; Phys. Rev. Lett. **93** 123001 (2004).
- [162] L. D. Landau; *Theory of superfluidity of He II*; J. Phys. (USSR) **5** 71 (1941).
- [163] G. K. Woodgate; *Elementary Atomic Structure*; Oxford Science Publications (1980).
- [164] E. Arimondo, M. Inguscio and P. Violino; *Experimental determinations of the hyperfine structure in the alkali atoms*; Rev. Mod. Phys. **49** 31 (1977).
- [165] C. Salomon *et al.*; *Proceedings of the 17th International Conference on Atomic Physics (ICAP 2000)*; American Institute of Physics (2000).
- [166] S. T. Chui, V. N. Ryzhov and E. E. Tareyeva; *Phase separation and vortex states in binary mixture of Bose-Einstein condensates in trapping potentials with displaced centers*; JETP Lett. **75** 233 (2002).
- [167] M. Erhard, H. Schmaljohann, J. Kronjäger, K. Bongs and K. Sengstock; *Measurement of a Mixed Spin Channel Feshbach Resonance in Rubidium 87*; Phys. Rev. A **69** 032705 (2004).
- [168] N. P. Robins, C. Figl, S. A. Haine, A. K. Morrison, M. Jeppesen, J. J. Hope and J. D. Close; *Achieving Peak Brightness in an Atom Laser*; Phys. Rev. Lett. **96** 140403 (2006).
- [169] A. A. Svidzinsky and A. L. Fetter; *Stability of a Vortex in a Trapped Bose-Einstein Condensate*; Phys. Rev. Lett. **84** 5920 (2000).
- [170] C. Raman, J. R. Abo-Shaeer, J. M. Vogels, K. Xu and W. Ketterle; *Vortex Nucleation in a Stirred Bose-Einstein Condensate*; Phys. Rev. Lett. **87** 210402 (2001).
- [171] A. E. Siegman; *Lasers*; Sausalito Calif. University Science Books (1986).
- [172] B. J. Verhaar; private communication (2005).
- [173] A. Marte, T. Volz, J. Schuster, S. Dürr, G. Rempe, E. G. M. van Kempen and B. J. Verhaar; *Feshbach resonances in rubidium 87: Precision measurement and analysis*; Phys. Rev. Lett. **89** 283202 (2002).

- [174] T. H. V. B. Shenoy; *Binary Mixtures of Bose Condensates of Alkali Atoms*; Phys. Rev. Lett. **77** 3276 (1996).
- [175] R. A. Barankov; *Boundary of two mixed Bose-Einstein condensates*; Phys. Rev. A **66** 013612 (2002).
- [176] E. W. Streed, A. P. Chikkatur, T. L. Gustavson, M. Boyd, Y. Torii, D. Schneble, G. K. Campbell, D. E. Pritchard and W. Ketterle; *Large atom number Bose-Einstein condensate machines*; Rev. Sc. Instr. **77** 023106 (2006).
- [177] Y. S. Kivshar and E. A. Ostrovskaya; *Optical Vortices: Folding and twisting waves of light*; Opt. Photon. News **12** 24 (2001).
- [178] N. R. Heckenberg, R. McDuff, C. P. Smith, H. Rubinsztein-Dunlop and M. J. Wegener; *Laser-Beams with Phase Singularities*; Opt. Quantum Electron. **24** 5951 (1992).
- [179] E. Abromochkin, N. Losevsky and V. Volostnikov; *Generation of spiral-type laser beam*; Opt. Commun. **141** 59 (1997).
- [180] M. W. Beijersbergen, R. P. C. Coerwinker, M. Kristensen and J. P. Woerdman; *Helical-wavefront laser beams produced with a spiral phaseplate*; Opt. Commun. **112** 321 (1994).
- [181] V. Shvedov, W. Krolikowski, A. Volyar, D. Neshev, A. Desyatnikov and Yuri Kivshar; *Focussing and correlation properties of white-light optical vortices*; Opt. Express **13** 7393 (2005).
- [182] A. G. Truscott, M. E. J. Friese, N. Heckenberg and H. Rubinsztein-Dunlop; *Optically Written Waveguide in a an Atomic Vapor*; Phys. Rev. Lett. **82** 1438 (1999).
- [183] R. G. Dall, M. D. Hoogerland, D. Thierney, K. G. H. Baldwin and S. J. Buckman; *Single-mode hollow optical fibres for atom guiding*; Appl. Phys. B **74** 11 (2002).
- [184] M. S. Soskin and M. V. Vasnetsov; *Singular Optics*; Progr. Opt. **42** 219 (2001).
- [185] J. Leach, M. R. Dennis, J. Courtial and M. J. Padgett; *Vortex knots in light*; New J. Phys. **7** 55 (2005).

- [186] S. Wüster, T. E. Argue and C. M. Savage; *Numerical Study of the stability of Skyrmions in Bose-Einstein Condensates*; Phys. Rev. A **72** 043616 (2005).
- [187] S. Wüster and B. J. Dąbrowska-Wüster; *Supersonic optical tunnels for Bose-Einstein condensates*; cond-mat/0602108 (2006).
- [188] M. K. Parikh and F. Wilczek; *Hawking Radiation As Tunneling*; Phys. Rev. Lett. **85** 5042 (2000).
- [189] W. G. Unruh; *Sonic analogue of black holes and the effects of high frequencies on black hole evaporation*; Phys. Rev. D **51** 2827 (1995).
- [190] S. Corley; *Computing the spectrum of black hole radiation in the presence of high frequency dispersion: An analytical approach*; Phys. Rev. D **57** 6280 (1998).
- [191] M. P. Hobson, G. Efstathiou and A. Lasenby; *General Relativity*; Cambridge University Press (2006).
- [192] M. Visser; *Acoustic black holes: horizons, ergospheres and Hawking radiation*; Class. Quant. Grav., **15** 1767 (1998).
- [193] S. Liberati, S. Sonego and M. Visser; *Unexpectedly large surface gravities for acoustic horizons*; Class. Quant. Grav., **17** 2903 (2000).
- [194] L. J. Garay, J. R. Anglin, J. I. Cirac and P. Zoller; *Sonic Analog of Gravitational Black Holes in Bose-Einstein Condensates*; Phys. Rev. Lett. **85** 4643 (2000).
- [195] L. J. Garay, J. R. Anglin, J. I. Cirac and P. Zoller; *Sonic black holes in dilute Bose-Einstein Condensates*; Phys. Rev. A **63** 023611 (2001).
- [196] C. Barceló, A. Cano, L. J. Garay and G. Jannes; *Stability analysis of sonic horizons in Bose-Einstein condensates*; Phys. Rev. D **74** 024008 (2006).
- [197] U. Leonhardt, T. Kiss and P. Öhberg; *Theory of elementary excitations in unstable Bose-Einstein condensates and the instability of sonic horizons*; Phys. Rev. A **67** 033602 (2003).
- [198] C. Barceló, S. Liberati and M. Visser; *Towards the Observation of Hawking radiation in a Bose-Einstein Condensate*; Int. J. Mod. Phys. A **18** 1 (2003).

- [199] C. Barceló, S. Liberati, S. Sonego and M. Visser; *Causal structure of acoustic spacetimes*; New J. Phys. **6** 186 (2004).
- [200] C. Barceló, S. Liberati, S. Sonego and M. Visser; *Quasi-particle creation by analogue black holes*; Class. Quant. Grav., **23** 55341 (2006).
- [201] C. Barceló, S. Liberati, S. Sonego and M. Visser; *Hawking-like radiation does not require a trapped region*; Phys. Rev. Lett. **97** 171301 (2006).
- [202] U. Leonhardt, T. Kiss and P. Öhberg; *Bogoliubov theory of the Hawking effect in Bose-Einstein condensates*; J. Opt. B: Quant. Semiclass. Opt. **5** S42 (2003).
- [203] S. Giovanazzi, C. Farrell, T. Kiss and U. Leonhardt; *Conditions for one-dimensional supersonic flow of quantum gases*; Phys. Rev. A **70** 063602 (2004).
- [204] V. Hakim; *Nonlinear Schroedinger flow past an obstacle in one dimension*; Phys. Rev. E **55** 2835 (1996).
- [205] A. Radouani; *Soliton and phonon production by an oscillating obstacle in a quasi-one-dimensional trapped repulsive Bose-Einstein condensate*; Phys. Rev. A **70** 013602 (2004).
- [206] M. Visser; *Essential and inessential features of Hawking radiation*; Int. J. Mod. Phys. D **12** 649 (2003).
- [207] P. J. Y. Louis, E. A. Ostrovskaya, C. M. Savage and Y. S. Kivshar; *Bose-Einstein condensates in optical lattices: Band-gap structure and soliton*; Phys. Rev. A **67** 013602 (2003).
- [208] A. S. Tychkov *et al.*; *Metastable helium Bose-Einstein condensate with large number of atoms*; Phys. Rev. A **73** 031603 (2006).
- [209] A. Görlitz *et al.*; *Sodium Bose-Einstein Condensates in the F=2 State in a Large-Colume Optical Trap*; Phys. Rev. Lett. **90** 090401 (2003).
- [210] S. Dürr, K. W. Miller and C. E. Wieman; *Improved loading of an optical dipole trap by suppression of radiative escape*; Phys. Rev. A **63** 011401(R) (2000).

- [211] T. Weber, J. Herbig, M. Mark, H.-C. Nägerl and R. Grimm; *Three-Body Recombination at Large Scattering Length in an Ultracold Atomic Gas*; Phys. Rev. Lett. **91** 123201 (2003).
- [212] V. A. Yurovsky and Y. B. Band; *Control of Ultra-cold Inelastic Collisions by Feshbach Resonances and Quasi-One-Dimensional Confinement*; physics/0602181 (2006).
- [213] R. Schützhold; *Detection scheme for acoustic quantum radiation in Bose-Einstein condensates*; Phys. Rev. Lett. **97** 190405 (2006).
- [214] C. K. Law, C. M. Chan, P. T. Leung and M. Chu; *Motional Dressed States in a Bose-Einstein Condensate: Superfluidity at Supersonic Speed*; Phys. Rev. Lett. **85** 1598 (2000).
- [215] G. Theocharis, P. Schmelcher, M. K. Oberthaler, P. G. Kevrekidis and D. J. Frantzeskakis; *Lagrangian approach to the dynamics of dark matter-wave solitons*; Phys. Rev. A **72** 023609 (2005).
- [216] Y. S. Kivshar and W. Królikowski; *Lagrangian approach for dark solitons*; Opt. Commun. **114** 353 (1995).
- [217] S. Komineas and N. Papanicolaou; *Vortex Rings and Lieb Modes in a Cylindrical Bose-Einstein Condensate*; Phys. Rev. Lett. **89** 070402 (2002).
- [218] S. Corley and T. Jacobson; *Black hole lasers*; Phys. Rev. D **59** 124011 (1999).
- [219] C. Barceló, S. Liberati and M. Visser; *Towards the observation of Hawking radiation in Bose-Einstein condensates*; Int. J. Mod. Phys. A **18** 3735 (2003).
- [220] M. Sakagami and A. Ohashi; *Hawking Radiation in the Laboratory*; Progr. Theor. Phys. **107** 1267 (2002).
- [221] A. D. Helfer; *Do black holes radiate?*; Rep. Progr. Phys. **66** 943 (2003).
- [222] L. D. Landau and E. M. Lifshitz; *Fluid Mechanics*; Pergamon Press (1959).
- [223] V. M. Pérez-García, V. V. Konotop and V. A. Brazhnyi; *Feshbach Resonance Induced Shock Waves in Bose-Einstein Condensates*; Phys. Rev. Lett. **92** 220403 (2004).

- [224] Gradshteyn and Ryzhik; *Table of Integrals Series and Products*; Boston: Academic Press (1980).
- [225] P. T. Cochrane, G. Collecut, P. D. Drummond and J. J. Hope; *xmds documentation* (2006); URL <http://www.xmds.org/documentation.html>.
- [226] B. M. Caradoc-Davies; *Vortex Dynamics in Bose-Einstein Condensates*; Ph.D. thesis; University of Otago (2000); URL <http://www.physics.otago.ac.nz/research/jackdodd/resources/bmcdthesis.html>.
- [227] M. J. Davis; *Dynamics of Bose-Einstein Condensation*; Ph.D. thesis; University of Oxford (2001).
- [228] A. Pais; *The Science and the Life of Albert Einstein*; Oxford University Press (1982).